Structural Analysis of a Tippler Structure

by

Petrus Johannes Adriaan van Zyl

Submitted in partial fulfilment of the requirements for the degree
MASTER OF MECHANICAL ENGINEERING
in the Faculty of Engineering, Built Environment and Information Technology,
University of Pretoria
Pretoria

Study leader: Mr. NDL Burger
Co-study Leader: Mr. PR de Wet

October 2005

ACKNOWLEDGEMENTS

I wish to thank Mr. B. Murphy and all other personnel of Richards Bay Coal Terminal for all the information and data made available to me in support of this study.

I would also like to thank my study leader Mr. N,D.L. Burger and co-study leader Mr. P.R. de Wet of the University of Pretoria, for all their guidance and advice. Furthermore, I would like to thank Professor. E. Fourie for his inputs and advice on the interpretation of the available data.

Lastly, I would like to thank my family, especially my wife for their support during the completion of the study and my Creator for the opportunity laid before me.

TABLE OF CONTENTS

LIST OF TABLES

LIST OF FIGURES

LIST OF SYMBOLS

RBCT	Richards Bay Coal Terminal	
FEA	finite element analysis	
FEM	finite element model	
sec	sec	
mm	millimetre	
CG	centre of gravity	
σ	stress	[Pa]
σ_{xx}	stress in the x-direction	[Pa]
σ_{xx}	stress in the y-direction	[Pa]
τ_{xy}	shear stress	[Pa]
σ_1	maximum principal stress	[Pa]
σ_2	minimum principal stress	[Pa]
ε	strain	[Unitless]
E	Young's modulus	[Pa]
v	Poisson ratio	
f_{Nyq}	Nyquist frequency	[Hz]
f_s	sample frequency	[Hz]
S'_e	unadjusted endurance limit	[MPa]
S_e	adjusted endurance limit	[MPa]
S_{ut}	ultimate tensile strength	[MPa]
k_a	surface finish factor	
k_b	size factor	
k_c	reliability factor	
k_d	temperature factor	
k_e	shape factor	
k_f	miscellaneous effects	
K_f	fatigue strength reduction factor	
K_t	elastic stress concentration factor	
q_c	notch sensitivity factor	
c	material constant used for Paris equation	
m	material exponent use for Paris equation	
ΔK	range of cyclic stress intensity factor	
k_{scale}	scaling factor for strain gauge data	

ABSTRACT

Tippler structures operate under arduous conditions for most of their operational lives. During routine structural inspections large fatigue cracks were discovered on some of the main structural components of a Tippler structure. These cracks were situated in a safety-critical area of the structure and therefore rendered the structure unsafe for operation. Structural failure could affect throughput enormously as the Tippler forms the first step in a coal terminal's operational process. A high operational availability is therefore expected from these structures.

The complex rotational working of the Tippler structure complicates the analytical evaluation of the structure. A further complication is the ever-changing boundary conditions while the structure rotates, together with the weight reduction of the coal in the wagons when the wagons are offloaded. Both these factors need to be taken into account when determining the stress levels in the structure while operational.

This study identifies the main factors that led to the development of the structural cracks. The analysis process consisted of constructing a linear static finite element model of the Tippler structure and verifying the accuracy of the model by means of strain gauge measurements on the actual structure. From this analysis accurate stress values were obtained for the structure under operational conditions. A short literature study identified additional factors that would have an effect on the fatigue life of the structure under the conditions as experienced at a coal terminal.

In the last part of the study the information obtained form the analysis and literature sources were applied to verify the suitability of the proposed changes made to the structure.

CHAPTER 1

INTRODUCTION

1.1. Background

Richards Bay Coal Terminal (RBCT) is the largest coal export terminal in the world. Established in 1976 with an original capacity of 12 million tons per annum, it has grown into an advanced 24-hour operation, which exports more than 72 million tons of coal a year (Richards Bay Coal Terminal). RBCT is capable of handling more than 700 ships per annum.

Coal is transported by rail to the terminal from the coal mines situated in the Gauteng, Free State and Mpumalanga areas. The coal enters the terminal in train wagons with a capacity of up to 84 tons each. Two wagons at a time enter one of four tandem Tipplers which tip the contents of the wagons onto a moving conveyor. The conveyors transport the coal to the grading plant where the coal is graded before being transported to the stackers and stacker reclaimers, which dump the coal on stockpiles according to grade. When needed, the coal is reclaimed by means of the stacker reclaimers, transported by the conveyor system to the ship loaders and loaded onto the ships. A schematic layout of the complete process is shown in Figure 1.1. Note that the schematic layout only illustrates the process and not the operations layout.

The tandem Tippler, as shown in Figure 1.2, is the first link in the RBCT process. The trains arrive at the terminal in lengths of 200 wagons and are divided into train lengths of 100 wagons. These trains are then moved to the Tipplers by means of a locomotive where the positioner in front of the Tippler takes over. When the offloading cycle starts the positioner pushes the train along and positions two wagons at a time into the Tippler by means of a muscle arm. The Tippler then tips the two wagons. The wagons are fitted with rotational joins between them to allow the wagons on the Tippler to rotate relative to the rest of the train during the tipping process. The emptied wagons are then pushed from the Tippler by the next two loaded wagons. This process repeats itself for all 100 wagons or 50 tip cycles.

This dissertation describes a full structural analysis done on a Tippler structure that developed structural cracks while operating as described above. The severity of the cracks necessitated a redesign of the cracked component to eliminate the possibility of future cracking or structural collapse. However, to be able to verify the validity of the proposed changes the stress cycles as experienced by the Tippler under normal operating conditions had to be determined accurately.

Once the finite element model of the structure was constructed and verified by means of strain gauge results, the proposed changes were incorporated and validated.

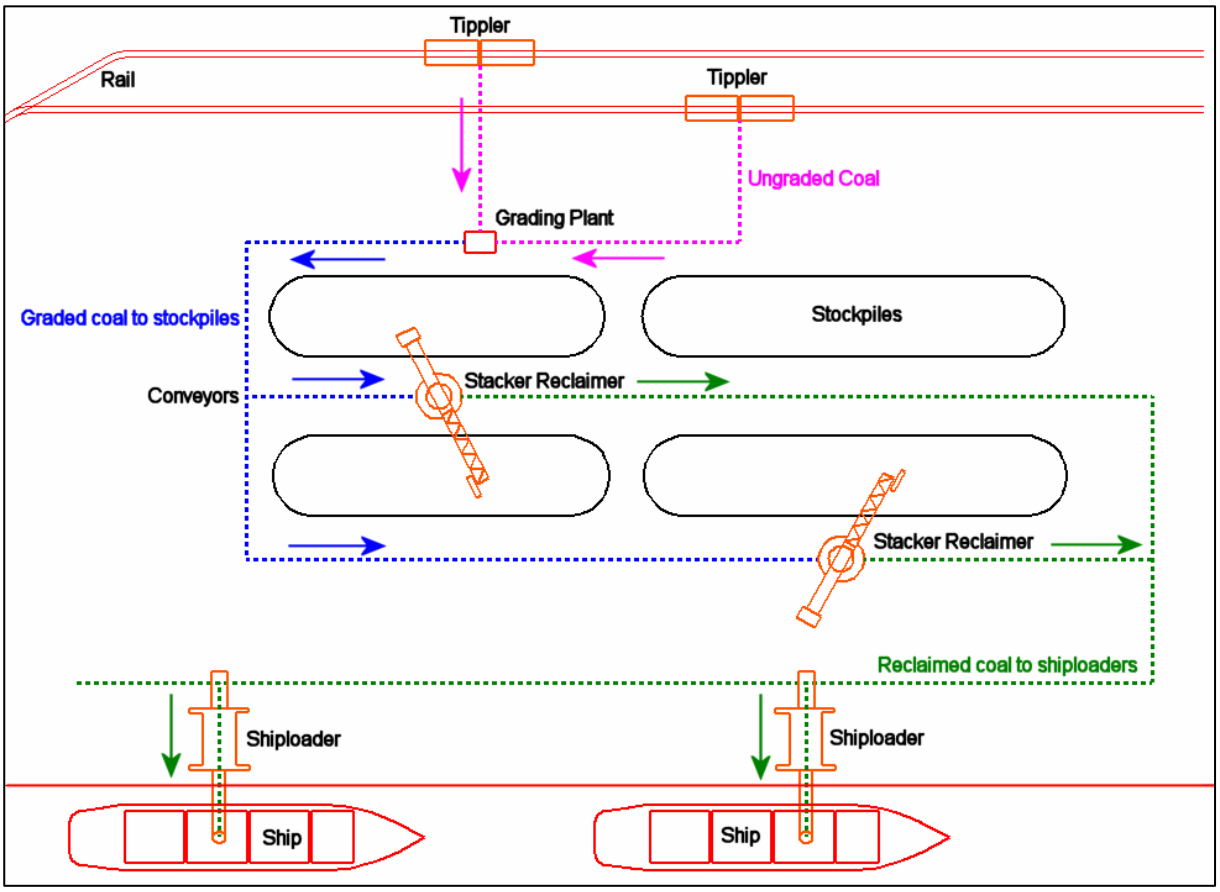

Figure 1.1: Schematic layout of RBCT's operations

Figure 1.2: Tippler with wagons being pushed into position

1.2. Motivation

Coal export terminals receive their coal from various mines by train. To rapidly offload the coal onto conveyors that transport the coal to stockpiles, machines known as Tipplers offload the wagons. This is achieved by passing the train through a drum-like structure, known as a cage, which clamps and overturns one or two trucks at a time. Figure 1.3 shows a schematic layout of a Tippler with two wagons lined up in front of it. Should a Tippler break down, the throughput of coal is seriously affected. High reliability is therefore required. Arduous working conditions and hidden structural weaknesses can adversely affect this objective. By employing the latest finite element analysis (FEA) techniques the structure can be analysed 'dynamically' and the corresponding stress patterns can be examined for high stress areas. By eliminating these high stress areas and by ensuring that the repaired or modified structure has a good safety margin against the development of fatigue cracks, a system with known structural weaknesses can be converted into a highly reliable machine, as demonstrated by this investigation.

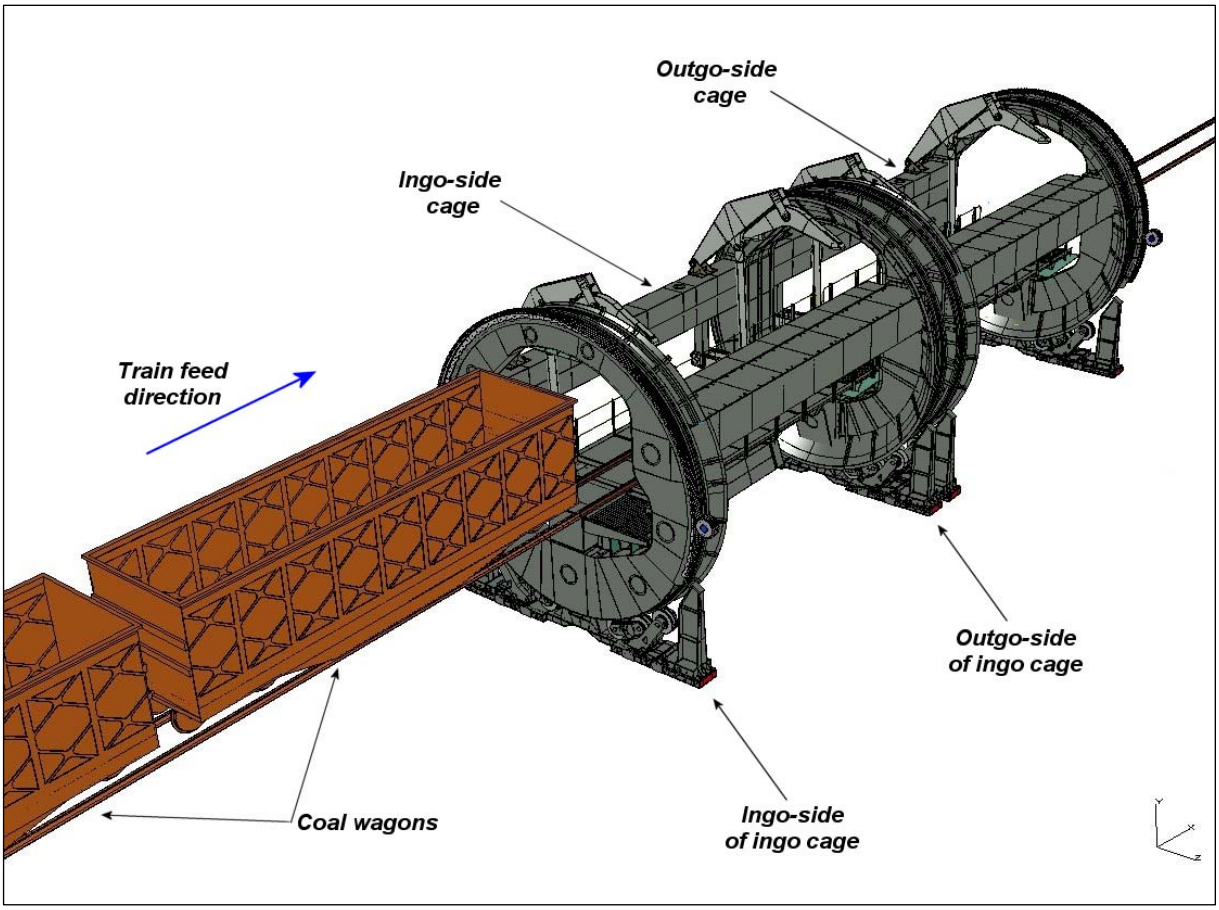

Figure 1.3: Tippler layout with empty wagons

1.3. Problem formulation

The current throughput of 72 million tons of coal a year (Richards Bay Coal Terminal) is handled by four Tipplers of similar construction. Each Tippler performs on average 294 tipping cycles per day, based on a wagon load of 84 tons for 365 days per year. The Tipplers were in operation for approximately 10 (ten) years when the structural cracks were discovered during a maintenance inspection, indicating more than one million tipping cycles per structure. The structure's design should allow for an infinite fatigue life to ensure crack-free operation.

The complex layout and working cycle of a Tippler subject the Tippler's structure to varying torsional and bending forces as indicated in Figure 1.4. A preliminary structural investigation revealed that these forces and the original design layout resulted in sufficiently high stresses in some areas to cause fatigue cracks as experienced by the structure under investigation.

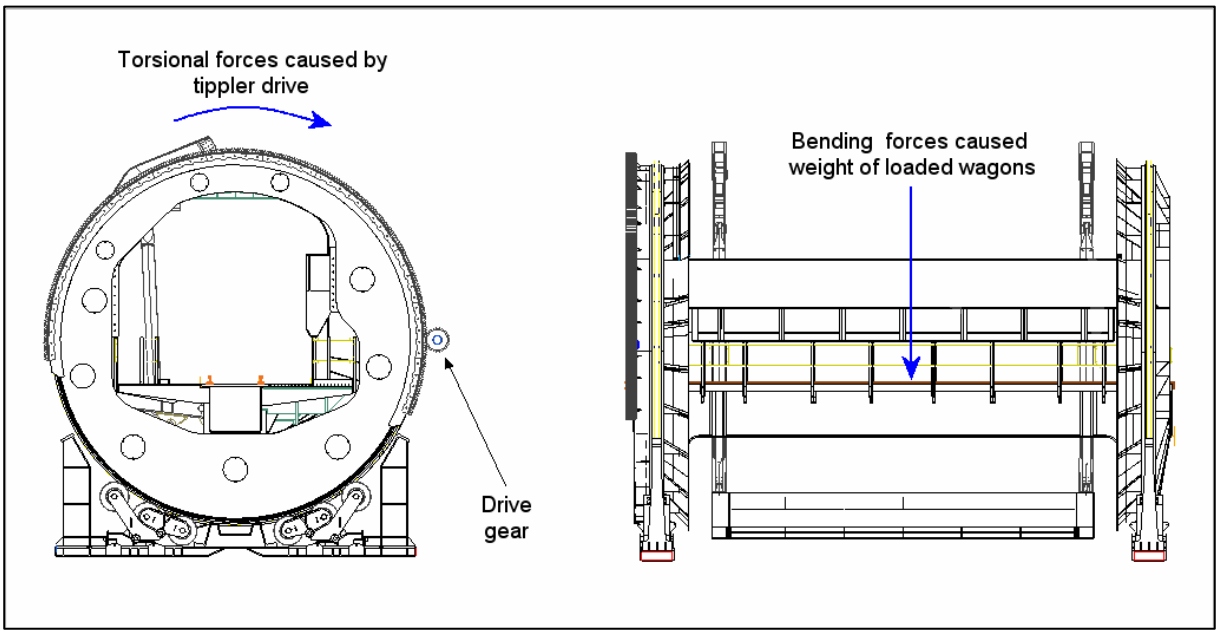

Figure 1.4: Forces experienced on Tippler structure

The crack indicated in Figure 1.5 developed in the corner of the structure platform as indicated in Figure 1.6. The cracks developed in the outgo side corners of the platform of the ingo side cage and similarly in the ingo side, corners of the outgo side platform (see Figure 1.3 for terminology). All the cracks have originated in a fillet weld joining the side and base plates of the platform structures. However, the fact that cracks developed in all four corners as indicated, and not in only one corner indicates that a weld defect may not have been the overwhelming factor but definitely a contributing factor to the crack development. For this reason, all possible contributing factors were investigated.

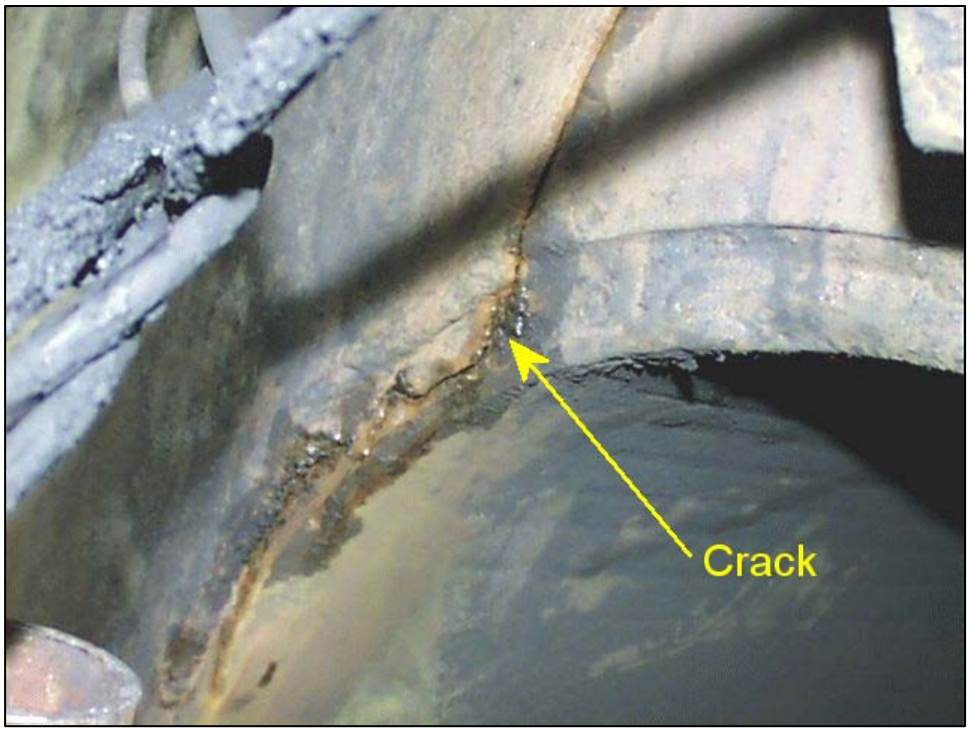

Figure 1.5: Crack in Tippler platform front corner

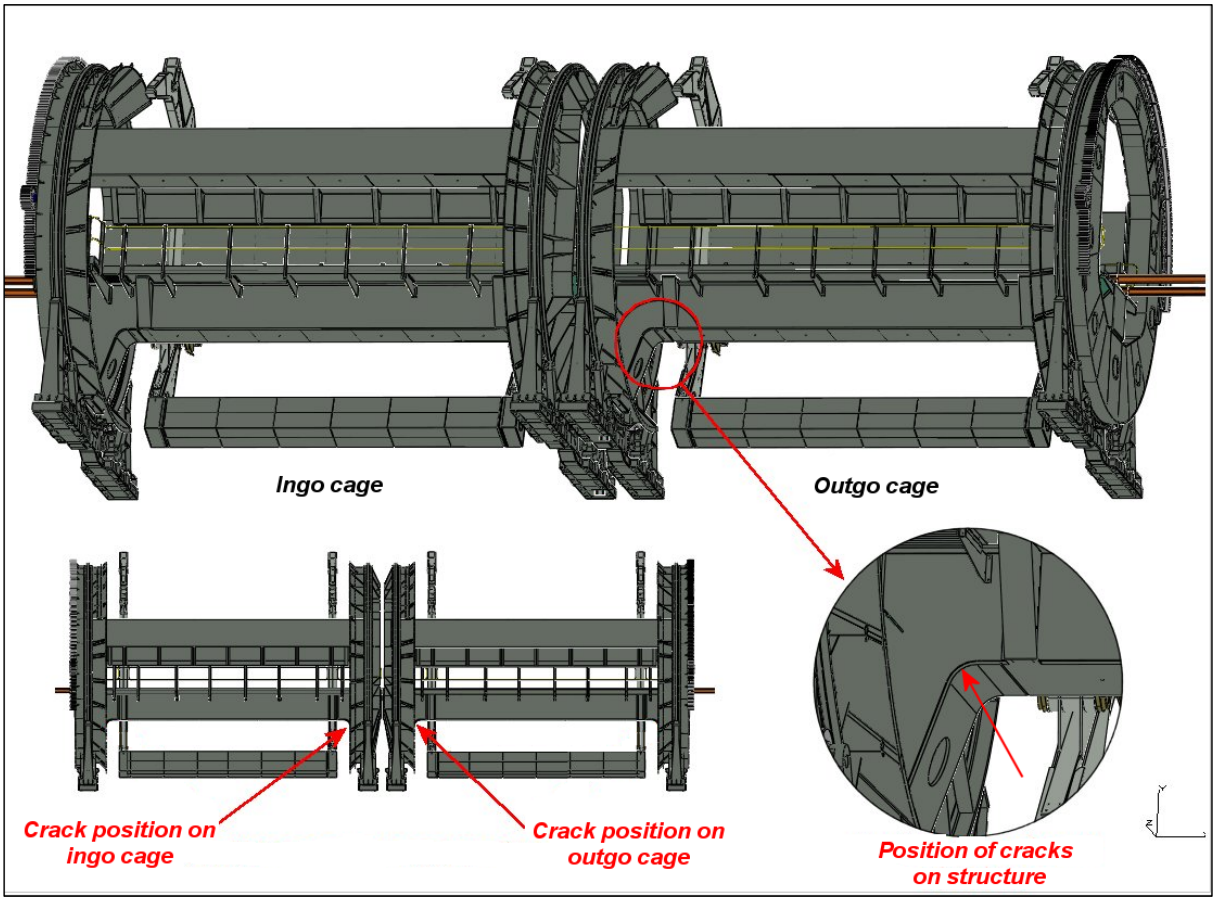

Figure 1.6: Positions on Tippler structure where cracks developed

To determine the external and internal influences on the structure that led to the development of the fatigue cracks as indicated, a structural analysis had to be done on the structure. The difficulty with performing an analysis on a structure of this nature is that the boundary conditions on the structure change with each increment through which the structure is rotated. These ever-changing boundary conditions during the tip cycle need to be simulated during the analysis to obtain accurate and reliable results.

1.4. Problem-solution approach

The analysis on the Tippler structure consists of a literature study that identified the factors that most likely played a role in the formation and growth of the cracks in the platform corners i.e. possible welds defects and corrosion, and furthermore factors that could influence the accuracy of the finite element analysis and strain gauge analysis as applied. From the methods available in the literature evaluation methods and procedures were selected that would provide the most accurate results from the analysis.

The fact that the cracks developed from a weld joining the bottom and side plates of the Tippler platform structure necessitates the use of the fracture mechanics approach to evaluate the structural life as obtained. It is however unclear at which phase of the useful structural life the cracks did develop from the welds and how long it took to grow before they were discovered. A further complication is the presence of corrosion at the weld positions as shown in figure 1.5, as all available literature indicates that the presence of corrosion affects the accuracy of fatigue life estimations. It is however known that the structure as evaluated had a useful life under the prevailing conditions, of approximately 10 years or 1.07 million cycles before the cracks were discovered.

For this reason, an approach was followed whereby a “representative” stress life or S-N curve was constructed from the available data, which provided an equivalent fatigue life of approximately 10-years for the stress cycles as obtained from the finite element analysis and strain gauge data. This S-N curve was then used to evaluate the structural changes as proposed. For evaluation purposes, the fatigue theory for welded and unwelded material was studied.

The analysis as described above was broken down into the following five steps:

i) A literature study on possible aspects that could lead to crack formation or growth on a Tippler structure, or may have an influence on the results

obtained during the investigation. The literature study further included a review of the methods and tools used in the analysis.

ii) A finite element analysis (FEA) on the complete structure to determine the magnitude of the stresses at the positions where the cracks originated. The simulation of the rotational operation of the Tippler was accomplished by using linear static finite element models representing each 10-degree tip angle during the tipping cycle. Each model was constrained and the forces applicable for the specific tip angle were applied to the model. The stresses obtained from the FEA model for each tip angle were compared to the measured stresses as obtained from strain gauge measurements at the specific time the Tippler passed through the corresponding tip angle.

iii) Strain gauge measurements to verify the stress values as obtained from the FEA and to identify any stress variations that may occur in the structure.

iv) An estimation of an equivalent stress life or S-N curve that would closely simulate the actual life achieved by the current structure.

v) A verification of the proposed structural changes by means of the equivalent S-N curve, to determine the validity of the structural changes made to the platform structure.

From the steps listed above, it was possible to determine the effectiveness of the proposed changes. Where differences existed between the strain gauge measurements and the finite element model results, the differences were analysed and, where needed, the necessary adjustments were made to the finite element models.

The similar construction of the ingo and outgo cages of the Tippler (the outgo cage is an almost exact mirror image of the ingo cage – see Figure 1.7), made it possible to focus the investigation on the ingo cage. The results obtained from the ingo cage analysis can be relayed to the outgo cage without the necessity of an additional analysis on the outgo cage.

The limited downtime available on the Tippler necessitated the completion of the strain gauge measurements on the structure before any FEA model existed of the structure. The positions where the strain gauges were applied were therefore determined from knowledge obtained from a previous analysis done on a similar structure and some basic calculations.

The finite element model preparation, analysis and post-processing was done with I-DEAS 11 NX software. The I-DEAS software was also used for the fatigue life calculations and data processing.

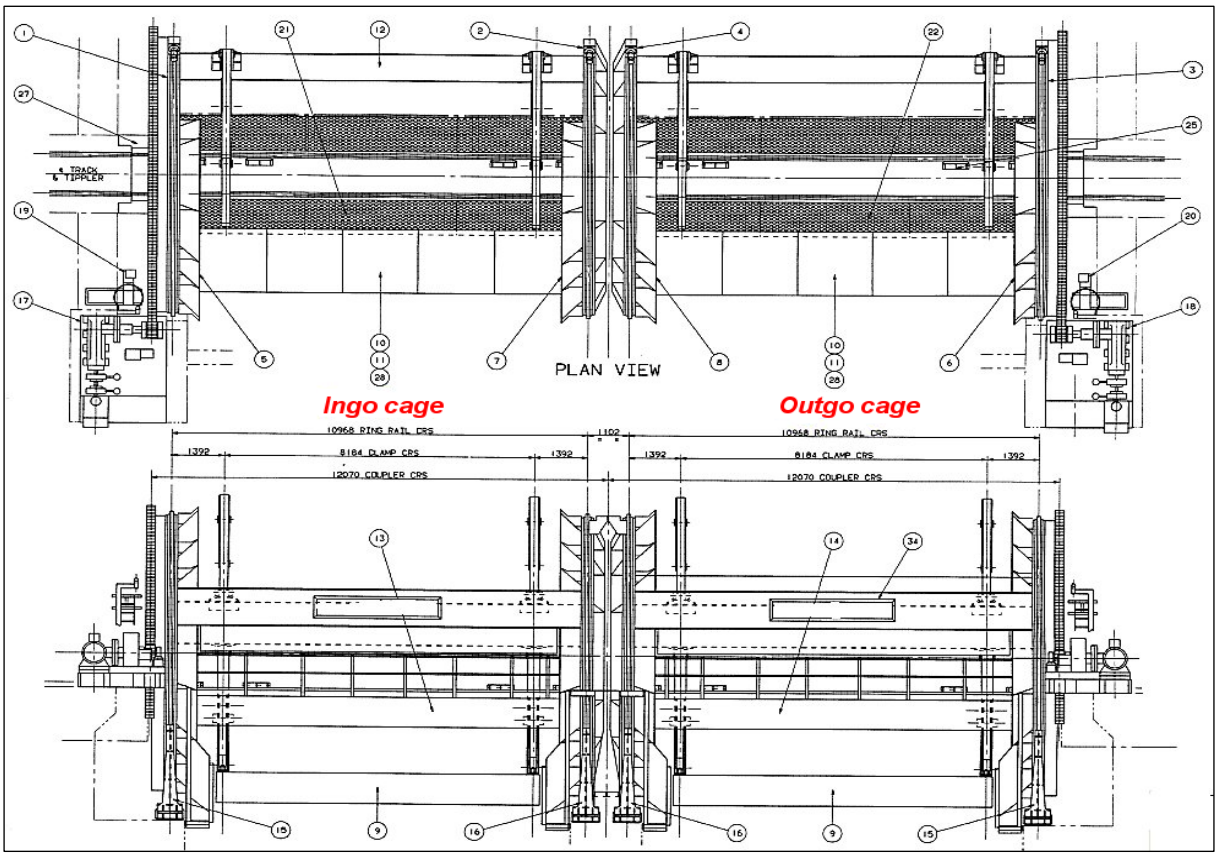

Figure 1.7: Similarity between ingo and outgo cage structures
Source: Extracted from original structural drawing (RBCT)

1.5. Tippler terminology

The Tippler structure consists of two drum-like cages resting on eight support roller assemblies in which the coal wagons are rolled over and tipped to offload the coal. The coal falls onto a conveyor system which transports it to the grading plant. Figure 1.8 shows the layout of the tipping process.

Each cage consists of two end rings, a platform structure, a cross beam at the back and a side beam at the front. Mounted on the cross beam is a clamp assembly that clamps the wagon onto the rail during the tip cycle. The layout of the ingo cage is shown in Figure 1.9.

The two cages are similar in construction and are referred to as the *ingo cage* and the *outgo cage*. Each cage has two end rings, which are referred to the *ingo ingo end ring* for the ingo side end ring on the ingo cage and the *ingo outgo end ring* for the outgo side end ring on the ingo cage. Similarly, the outgo cage's end rings are referred to as the *outgo ingo end ring* for the ingo end ring on the outgo side cage and the *outgo outgo end ring* for the outgo side end ring of the outgo cage.

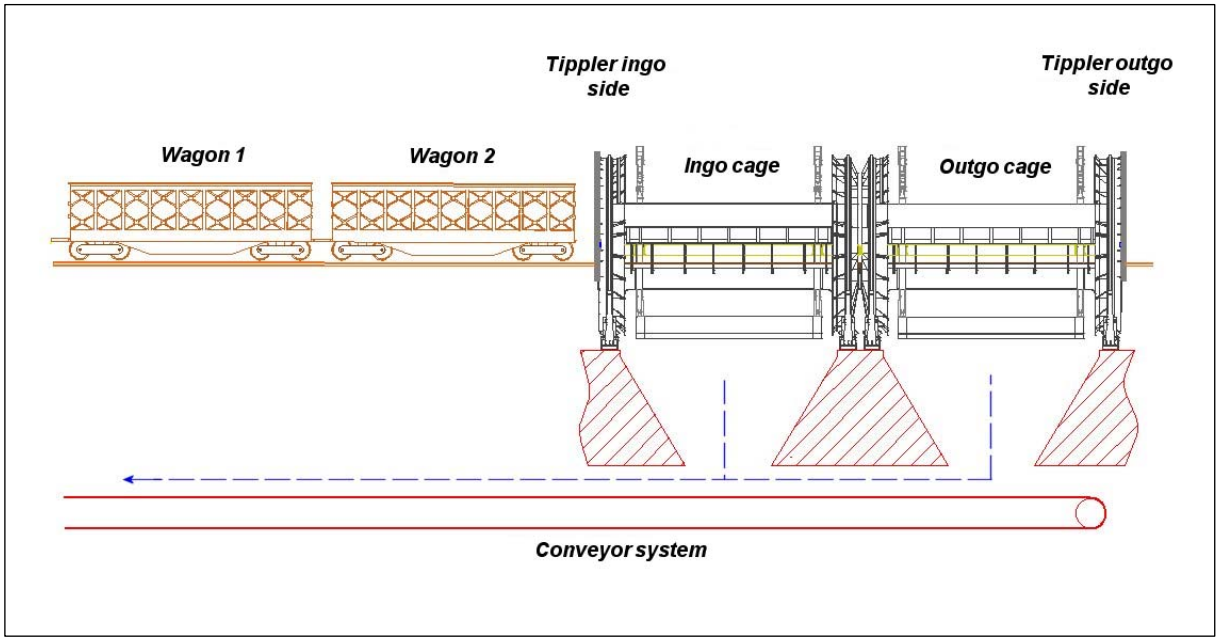

Figure 1.8: Tippler process layout

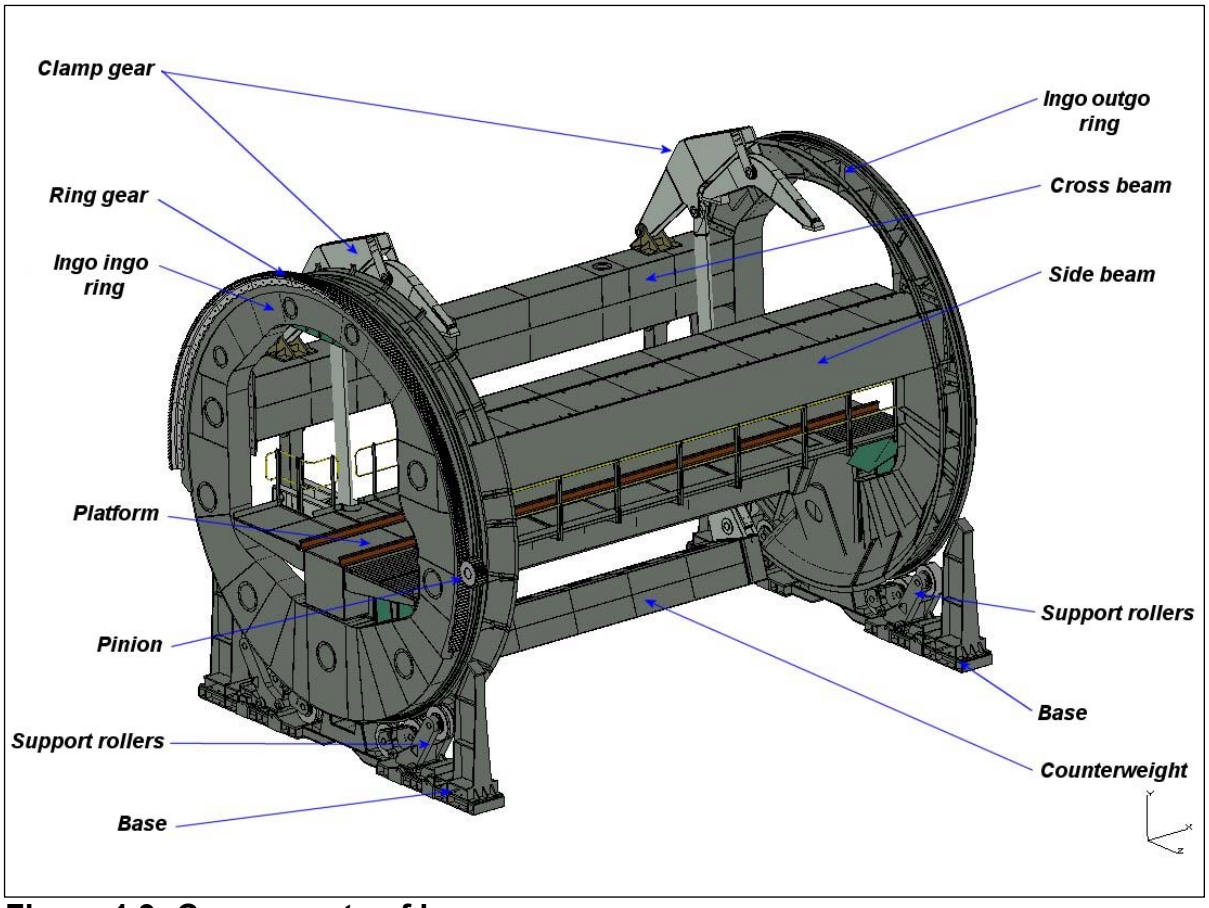

Figure 1.9: Components of ingo cage

The clamp system consists of two clamps mounted on two clamp arms which are in turn mounted to the cross beam at the back. The clamp arm is further connected by means of a tie rod to a clamp mechanism. This clamp mechanism incorporates the

counterweight as shown in Figure 1.10. The clamping process is completely mechanical and there are no outside forces (hydraulic or electrical) that contribute to the clamping action

During the tip cycle the wagons are tipped towards the side beam by means of two pinion gears that drive the two ring gears situated on the ingo ingo end ring and the outgo outgo end ring of the two cages. The drives of the two cages are not mechanically coupled and the two cages can tip separately. The tip angle is through 160 degrees and the total tip cycle takes approximately 40 sec. The complete load and tip cycle takes approximately 110 sec to complete. The terminology as stated was used throughout the study.

The following chapters describe each step listed in paragraph 1.3 in more detail and where necessary literature references were included to explain the results obtained.

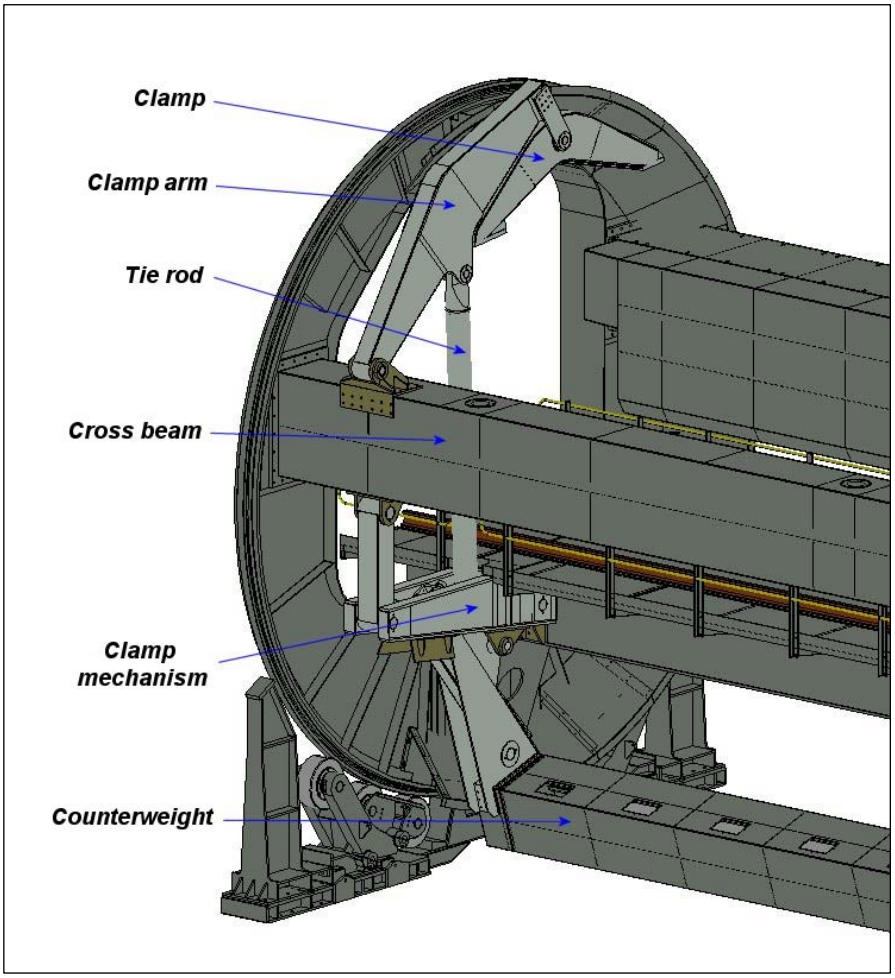

Figure 1.10: Clamp mechanism for one clamp

CHAPTER 2

LITERATURE REVIEW

The focus of this literature review is to familiarise the reader with some of the factors that could influence the accuracy of the results obtained from an analysis of this nature. Furthermore, any tools, methods or applications used in the analysis i.e. the software, functions or equipment used, were described in some detail. More detail is, however provided in the study to provide the necessary background information.

2.1 Factors influencing analysis accuracies

The accuracy of the results obtained from a structural analysis depends largely on the accuracy and applicability of the models and methods used for the analysis. Error associated with an analysis can be categorised in two main groups i.e. idealisation errors and discretisation errors. Errors that occur during the problem formulation, boundary condition specification, geometry construction, material specification or load case assumption all can be classified as idealisation errors. Discretisation errors may occur while imposing the boundary conditions or when selecting the appropriate mesh or mathematical model for the analysis. Many of these errors, however, occur due to “operator error” and could therefore be eliminated by applying the appropriate techniques (Lepi, 1998: 152).

The reliability of any subsequent analysis to be performed thus greatly depends on the accuracy of the original analysis, i.e. Mercer, Melton and Draper highlight four user decisions that may influence the accuracy of a fatigue analysis done from results obtained from a finite element analysis. These are:

i) The way in which the loading information is processed
ii) The material’s fatigue data
iii) The finite element mesh
iv) The fatigue analysis algorithm used for the analysis

The focus of this dissertation is the evaluation of the fatigue life of an original and modified structure and therefore all the above-mentioned factors have a direct influence on the accuracy of the analysis. Each of these factors and their possible influences on the results has therefore been investigated in this literature study and has furthermore been allowed for in the analysis. Furthermore, a suitable algorithm for the fatigue life calculations for the specific application was evolved and evaluated in more detail.

2.1.1 Load information processing

The rotational operation of the Tippler necessitates the use of changing boundary conditions for every interval rotated. This is brought about by the change of the weight of coal in the wagon, the shift in the centre of gravity of the structure and the change in position of some of the structural components, i.e. the clamps, clamp arms and counterweight.

Although each of these factors can be reproduced by means of boundary condition changes or assembly layout changes, the accuracy of this method still needs to be verified, as this will directly influence the accuracy of the results obtained from the analysis. This verification was done by means of strain gauge measurements taken on the Tippler structure while performing consecutive tip cycles. The stress values obtained from the strain gauge readings were compared to the stress values obtained from the FEA for the same tip positions.

The accuracy of the strain gauge readings therefore determines the accuracy of the verification. For this reason, the factors influencing the strain gauge application's accuracy had to be considered. Furthermore, the shape of the stress signal obtained form the strain gauge readings will also be used to evaluate the fatigue life of the original and modified Tippler structure. For this reason, the stress data recorded should provide an accurate representation of the actual stress history at the positions where the strain gauges were applied.

a) Strain gauge arrangement selection

Strain gauges are used to measure local mechanical strain in components by converting a change in electrical resistance to a change in strain by means of a Wheatstone bridge arrangement. The corresponding stress can then be calculated from the following equation:

$$\sigma = \varepsilon \times E$$

Where: σ = stress [Pa]
ε = strain [unitless]
E = Young's modulus [Pa]

Strain gauges can be applied in different arrangements, i.e. quarter bridge, half bridge or full bridge, depending on the strain gauge selected and the gauge connection to the Wheatstone bridge. Each application has its own benefits and compensates for different factors including temperature,

bending or torsional effects. Some of the typical non-torsional strain gauge application methods can be seen in Figure 2.1.

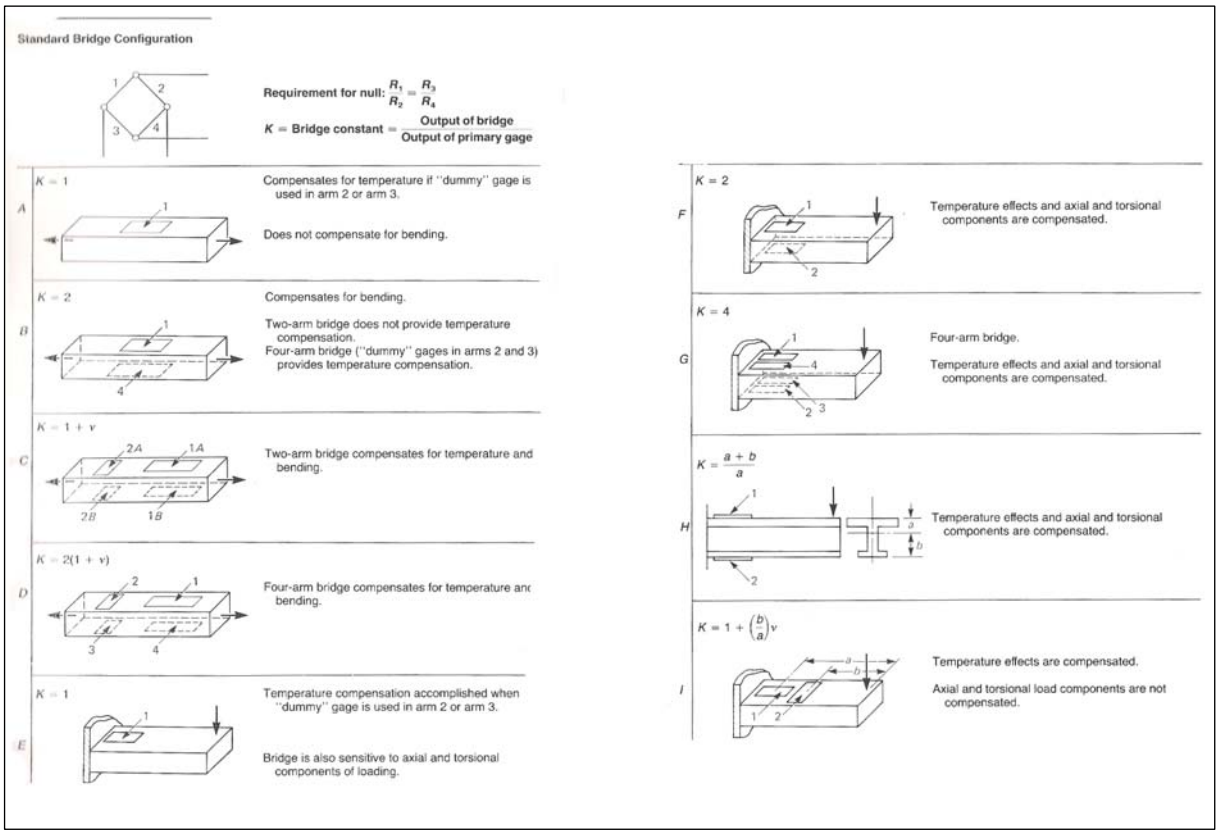

Figure 2.1: Typical non-torsional strain gauge applications

Source: Adapted from MECHANICAL MEASUREMENTS, Fifth Edition, Bechwith et al. 1993

For the Tippler application, a half-bridge arrangement shown as option C in Figure 2.1 was used. Only gauges 1A and 2A were applied. This arrangement compensates for temperature variations but not for bending. Temperature compensation is necessary as water sprayed onto the structure for dust-suppression purposes might have caused temperature fluctuations at the strain gauge positions. From an analysis of the strain gauge positions it was concluded that local bending would not affect the stress readings. Figure 2.2 shows the strain gauge as connected to the bridge amplifier.

An advantage of using a half-bridge arrangement compared to the quarter-bridge or full-bridge arrangements is that while only one 90-degree rosette strain gauge is required as in the case of a single strain gauge, the arrangement still compensates for the temperature as done by a full-bridge arrangement.

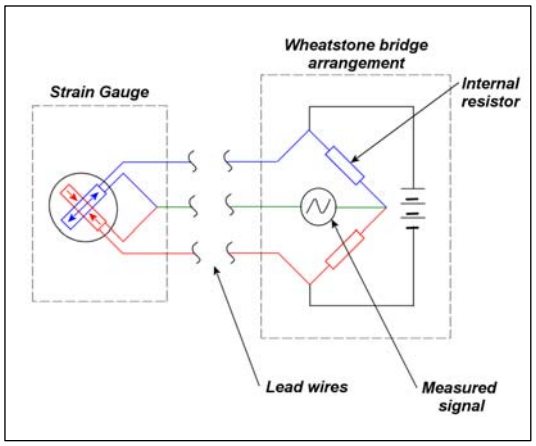

Figure 2.2: Half-bridge strain gauge arrangement

b) Sample frequency

When a strain signal is recorded the possibility exists that the waveform may not be accurately recorded because of too low a sampling frequency. By obtaining the wrong waveform from the sampled data the accuracy of the fatigue analysis can be severely compromised as the peaks and valleys needed for the load history would not be accurately represented.

The frequency at which a signal can be accurately sampled is determined by the Nyquist frequency (Bechwith et al. 1993: 147),

$$f_{Nyq} = \frac{fs}{2}$$

Where: f_{Nyq} = Nyquist frequency
f_s = sample frequency

From this equation the sample frequency can be calculated if the frequency of the measured strain signal is known. The sample frequency should therefore be at least more than two times faster than the frequency of the signal being sampled to avoid aliasing or undersampling. Mercer et al. (2003:2), however, mention that the industry standard for assuring accurately sampled strain data is at least 10 points/cycle or a sampling frequency of ten times the frequency of the measured signal. Note that if spikes occur in the data, care should be taken to sample at a high enough frequency to accurately present the peak, but more importantly to accurately measure the maximum value of the peak.

c) Load history preparation

As the strain gauge data obtained was also to be used to determine the stress history for the position where the cracks developed on the Tippler structure, the accuracy of the signal was of great importance. A poor quality or truncated signal used for fatigue life calculation can provide fatigue-lives that are up to 9 times longer than those calculated using a full signal (Mercer, 2003: 2).

Where cycle omission or gating is applied to the data, caution should be shown as the removal of small peaks may have a significant effect on the fatigue life calculation accuracy. A sensitivity analysis is therefore suggested to verify the effect of cycle removal on the calculated fatigue life.

Mercer et al. (2003: 3) further note that the length of the load history could also have an effect on the accuracy of the calculations and should be considered during the analysis. Shorter histories with a certain number of dominant peaks would provide different life estimates as a longer history with the same amount of dominant peaks.

2.1.2 Material data accuracy

The accuracy of material properties forms an extremely important component of a fatigue life prediction. Should the material properties not accurately represent the actual material used for the component or structure, the fatigue life calculation results would have no relevance. These properties not only include yield strength, tensile strength and endurance limit, but also the influence that other effects, for example corrosion or temperature, may have on these properties. Furthermore, where welding is used to join material in a structure or component, several discontinuities or complex metallurgical areas may be generated in the welds or heat affected zones. The material in these areas cannot easily be related to material test specimens consisting of non-welded materials. For this reason, fatigue data is generated from tests on welded members as the welds may contain material porosity, slag inclusions, small cracks or the welding process may have developed small undercuts that could lead to crack formation. All these defects are viewed as possible crack initiation spots from which cracks would grow if the material were subjected to fluctuating stresses. More detail on component S-N curves will be provided later in the literature.

Ellyin (1997: 22) notes that the following factors would have an influence on the fatigue life of a material:

i) The microstructure of the material
ii) The processing history of the material
iii) The load spectrum experienced by the material
iv) The environment in which the material operates
v) The geometry of the component

Each of these factors can effect the accuracy of the results obtained from the fatigue life calculations and was therefore evaluated and incorporated in the material specification used for this analysis. Where necessary the material properties used for the analysis were adjusted to the proposed values as indicated in the literature.

a) The effect of the microstructure on the material endurance limit

The first factor that could influence the material's endurance limits as listed by Ellyin (1997: 2) is the materials microstructure or grain size and texture. Materials with a fine microstructure generally have a higher endurance limit than the same material with a larger grain size. Furthermore, impurities or precipitates in the structure of the material or cold work that deform the grains of the material increase the endurance limit of a material by increasing the number of dislocations in the material (Dowling, 1999: 385). Ellyin (1997: 23) further notes that cyclic loading in a material may lead to phase transformation in the material which in turn could lead to endurance limit changes

Figure 2.3 shows the effect that the microstructure (phase) of a materials has on the endurance ratio of the material. The endurance ratio is defined as the ratio of the fatigue endurance limit to the tensile strength of the material (S'n/Su – for this dissertation S'_e/S_{ut}).

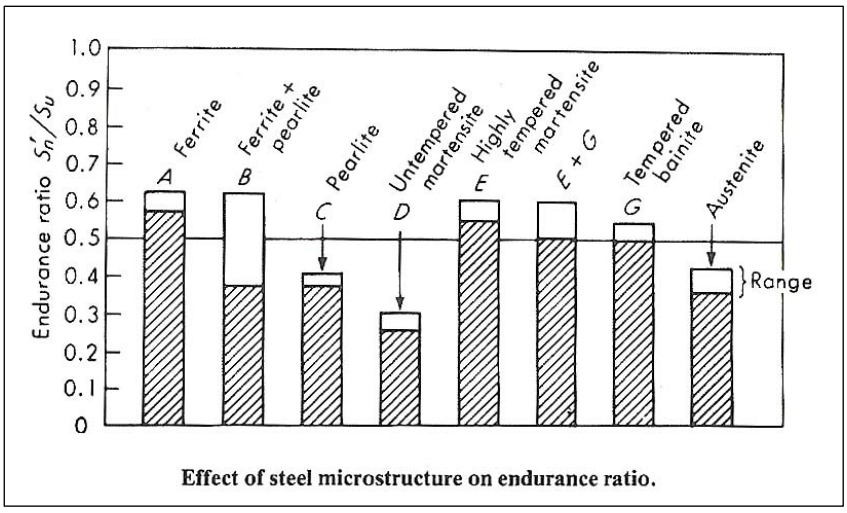

Figure 2.3: Effect of microstructure on endurance ratio
Source: Atlas of Fatigue Curves, Boyer, 2003: 31

Figure 2.3 indicates that a material with a ferritic structure would have the best endurance ratio and a material with an untempered martensitic structure the worst. This is caused by the value of the ultimate tensile strength in the equation, i.e. a material with a higher ultimate tensile strength will have a lower endurance ratio than a material with the same endurance limit, but with a higher tensile strength. More brittle materials as seen in the case of untempered martensite are therefore more susceptible to fatigue failures. The size of a component, i.e. the diameter of a shaft or the thickness of the plates the component is constructed, from also has an influence on the endurance limit of the component as shown in Figure 2.4. A test specimen of diameter 7.62 mm was used to determine the fatigue life of the material. The specimen diameter was then changed to various diameters and the fatigue life of the specimens plotted relative to a 7.62 mm specimen, which represents a size factor of one.

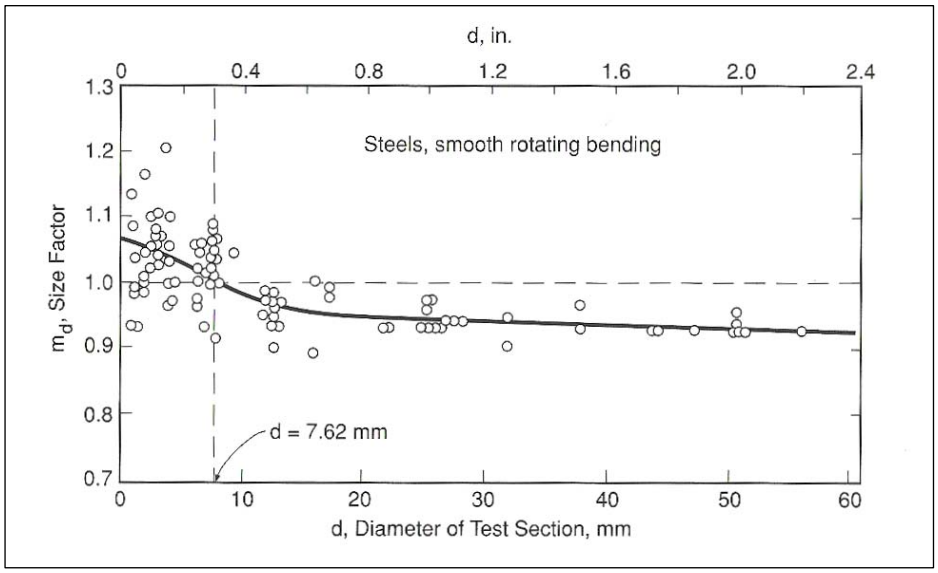

Figure 2.4: Effect of size on the fatigue limit of smoothly polished specimens of steel tested in rotational bending

Source: MECHANICAL BEHAVIOUR OF MATERIALS, Dowling, 1999: 443, (Heywood, 1962)

Thicker components have less homogeneous material matrixes throughout the component, increasing the possibility of material defects or imperfections and reducing the endurance limit. The size factor used in endurance limit calculations highlights this increase in material defects for larger material sections. This factor is normally included in the material yield strength specification, i.e. the thicker the material the lower the yield strength quoted by the suppliers would be. If not included in the material specification the value can be calculated from the following formula:

$$k_b = 1 \qquad d \leq 8\,mm$$

$$or$$

$$k_b = 1.189\,d^{-0.097} \qquad 8 < d < 250\,mm$$

(Shigley, 1986: 246)

Note however that these formulae are only valid for rotational bending of a round component and not for axial loading. Shigley (1986: 247) notes that there is no apparent size effect for specimens loaded in an axial direction. Other authors however list size effects for axial load cases, i.e. a value of 0.7 to 0.9 quoted by Juvinall (Dowling, 1999: 446).

b) Effect of the material- processing techniques on the endurance limit

The endurance limit of a material can be altered by means of different processing techniques. As described above cold forming would increase the number of dislocations in a material and increase the endurance limit. Processing techniques such as rolling, extrusion or forging orientate the grain structure of the material, increasing the fatigue limit if the material is loaded in the direction of the grain-structure orientation. The endurance limit of the material may, however be reduced if the loading is perpendicular to the grain-structure orientation.

Compressive residual stresses generated on a material's surface during processing are beneficial to the endurance limit of the material. Shot-peening is often used to create a compressive stress by locally deforming the component's surface, increasing the endurance limit of the component. Tensile residual stresses lower the endurance limit of a material and can be reduced by heat-treating the material after machining or processing. The heat treatment process should, however, be controlled as it may be detrimental to the material endurance limit due to surface decarburisation (Ellying, 1997: 23; Dowling, 1999: 385).

Another factor that directly influences the fatigue life of a component is the choice of a machining technique used during the manufacturing of the component. Figure 2.5 shows the endurance limit correction factor plotted against the ultimate tensile strength of the material. Note the reduction in the correction factor with the increase in tensile strength. However, for a mirror polished surface, i.e. no surface imperfections the correction factor is equal to one for all tensile strengths. It is therefore necessary to ensure a quality surface finish on components that would experience cyclic loading.

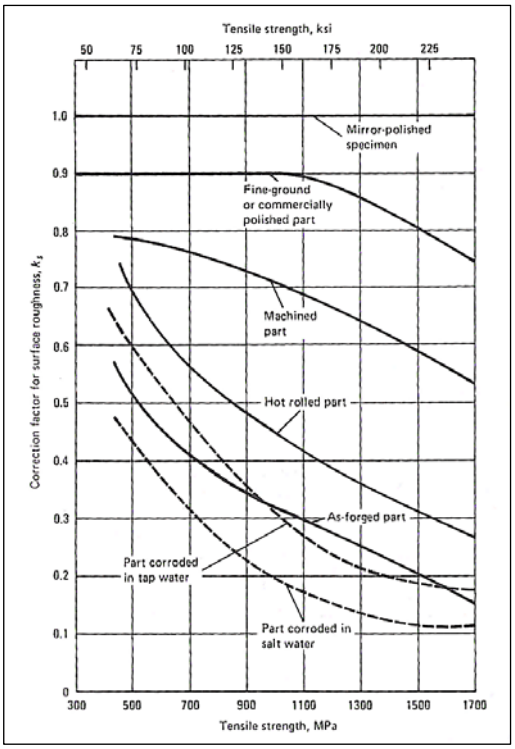

Figure 2.5: Correction factor for surface roughness (k_s – also k_a)
Source: Atlas of Fatigue Curves, Boyer, 2003: 33

c) The effect of the environment on the material endurance limit

Corrosive environments cause degradation of the material surface by means of pitting and surface roughness. These degradation marks act as stress raisers and are generally the sites of crack formation. Furthermore, a cyclic loading experienced by the component or structure would continuously break the protective oxide layer, exposing the uncorroded material to the corrosive environment. This action would enhance crack growth once a crack has formed (Ellying, 1997: 24). Assakkaf and Ayyub notes that for applications near or in sea water where high corrosion levels are expected, a reduction of up to 50% in the endurance limit of the material may be expected.

Furthermore, in corrosive environments a higher ultimate tensile strength relates to a lower endurance limit correction factor for a material as shown in Figure 2.4. This is further demonstrated in Figure 2.6 which illustrates that under corrosive conditions a material has no infinite fatigue life and would eventually develop cracks if not corrode away completely. In the case of the Tippler structure under investigation in this dissertation, the Tippler is situated in a port where salt spray in the air cause high levels of corrosion. Furthermore, the water sprayed for dust suppression mixed with the coal dust from the

offloading coal wagons, forms a corrosive paste that attaches to the structure and accelerates corrosion.

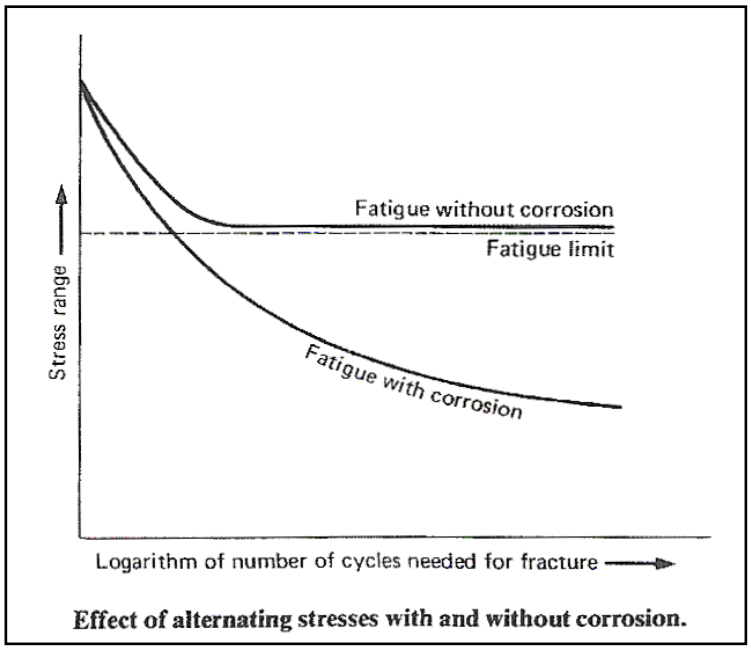

Figure 2.6: Effect of corrosion on a material's endurance limit
Source: Atlas of Fatigue Curves, Boyer, 2003: 37

d) The effect of load spectrum on the material endurance limit

The stress history, stress levels, stress type (tension, compression, torsion) and the rate at which theses factors change will influence the fatigue life of a component (Ellying, 1997: 22). The author further mentions that a tensile mean stress would reduce the fatigue life of a component, while a compressive mean stress would increase the fatigue life for the same amplitude cyclic loading.

Figure 2.7 lists some of the endurance limit reducing factors for different load conditions and different authors. Note that torsional loads would reduce the endurance limit of the material by the largest margin. Further note that a value of 1.0 is quoted as a size effects (k_d) modifier for a component smaller than 10.0 mm in diameter for all load conditions (see paragraph 2.1.2. a).

Parameter	Applicability	Juvinall (1991)	Shigley (1989)
Bending fatigue limit factor: m_e	Steels, $\sigma_u \leq 1400$ MPa	0.5	0.5
	Higher strength steels	≤ 0.5	$\sigma_{erb} = 700$ MPa
	Cast irons; Al alloys if $\sigma_u \leq 325$ MPa	0.4	—
	Higher strength Al	$\sigma_{erb} = 130$ MPa	—
	Magnesium alloys	0.35	—
Load type factor: m_l	Bending	1.0	1.0
	Axial	1.0	0.92[1]
	Torsion	0.58	0.58
Size (stress gradient) factor: m_d	Bending or torsion[2]		
	$d < 10$ mm	1.0	$(d/7.62 \text{ mm})^{-0.1133}$
	$d = 10$ to 50 mm	0.9	$(d/7.62 \text{ mm})^{-0.1133}$
	$d = 50$ to 100 mm	0.8	0.6 to 0.75
	$d = 100$ to 150 mm	0.7	0.6 to 0.75
	Axial	0.7 to 0.9[3]	1.0
Surface finish factor: m_s	Polished	1.0	1.0
	Ground[4]	See Fig. 10.14	$1.58\sigma_u^{-0.085}$
	Machined[4]	See Fig. 10.14	$4.51\sigma_u^{-0.265}$
Life for fatigue limit point: N_e, cycles	Steels, cast irons	10^6	10^6
	Aluminum alloys	5×10^8	—
	Magnesium alloys	10^8	—
Constants for point at $N_f = 10^3$:	Bending or torsion	$m' = 0.9$ $k'_f = k_f$	$m' = 0.9$ $k'_f = 1$
m', k'_f	Axial, small eccentricity	$m' = 0.75$ $k'_f = k_f$	$m' = 0.9$ $k'_f = 1$

Notes: [1]If $\sigma_u > 1520$ MPa, use $m_t = 1.0$. [2]For Shigley, for reversed (nonrotating) bending, replace d with $d_e = 0.37d$ for round sections, and with $0.81\sqrt{wt}$ for rectangular sections, where w is beam depth and t is thickness. [3] Use for $d < 50$ mm only, and use the higher value if the eccentricity is small. [4] For Shigley, enter equations with σ_u in MPa.

Figure 2.7: Endurance limit reducing factors

Source: Mechanical behaviour of materials, Dowling, 1999: 446

e) The effect of geometry on a components fatigue life

Geometric features such as holes, fillets, notches or corners act as stress raisers or stress concentrations, where most fatigue cracks initiate. Weld inclusions or undercuts have the same effect, but is less quantifiable than machined geometry. Notch sensitivity charts as shown in Figure 2.8 indicate a material's sensitivity to different notch radii.

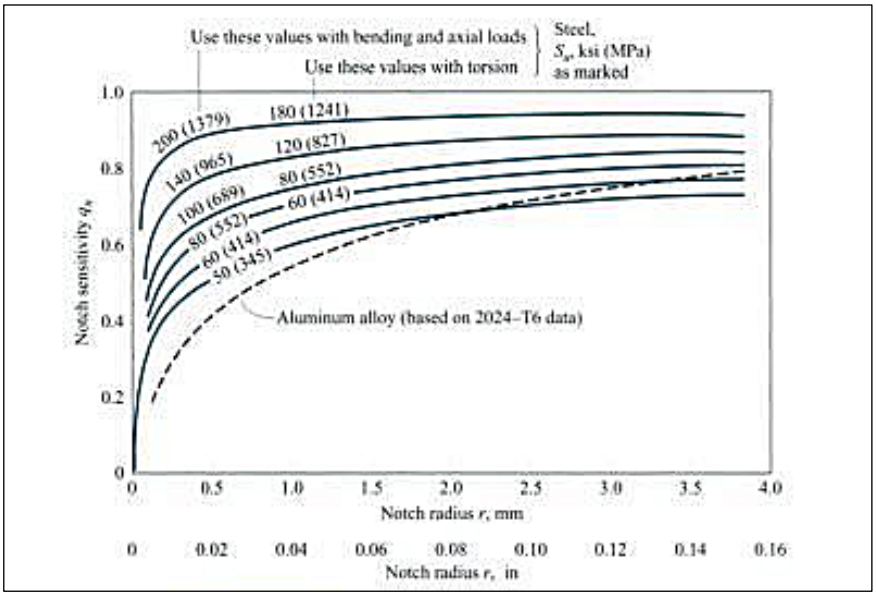

Figure 2.8: Notch sensitivity chart for steels and aluminium

Source: Fundamentals of machine elements, Bernard et al. 2005: 283

From these charts a designer can estimate the effect of the notch on the endurance limit of the material under investigation from the following formulae:

$$K_f = 1 + (K_t - 1)q_c$$

Where : K_f = fatigue strength-reduction factor
K_t = Elastic stress-concentration factor
q_c = notch sensitivity factor

The endurance limit modification factor or shape factor k_e is then calculated from:

$$k_e = \frac{1}{K_f}$$ (Shigley, 1986: 253)

f) Other factors that influence the endurance limit of a material

Another effect that will influence the endurance limit of a material for the conditions as experienced by the Tippler structure is the applied surface coatings. Figure 2.9 shows the effect that different surface coatings have on the endurance limit of a material at 10^7 stress cycles for different environmental conditions. From this data is furthermore clear that salt spray in the

environment have a notable effect on the fatigue life of a material even when coated.

Corrosion Fatigue on Coated 0·5% Carbon Steel

Coating	Fatigue strength at 10^7 cycles, MN/m^2	
	Air	Salt spray
None	253	62
Enamel	265	172
Galvanized	228	255
Sherardized	228	234
Zinc-plated	248	228
Cadmium-plated	234	212
Cadmium and enamel	244	207
Cadmium and oil	244	207
Phosphate-treated	273	200

Figure 2.9: Endurance limit for 0.5% carbon steel for different coatings

Source: Mechanics of solids and strength of materials, Warnock and Benham, 1976, Table 22.2

Another factor that may influence the endurance limit of a material that are not discussed in detail in this dissertation, is temperature effects. This factor has been noted, but is not seen as having an influential effect on the fatigue life of the Tippler structure. Furthermore, a reliability factor of 99% was incorporated into all calculations.

To calculate the modified endurance limit, which quantifies the material properties, the endurance limit modification factors are multiplied with the unmodified endurance limit. The reduced endurance limit value then accurately describes the material for analysis purposes, taking into account all the factors that may influence the fatigue life of the said material. Note however that this method is only valid for unwelded components. When a component or structure is welded together welding defects act as crack initiators, eliminating the crack initiation phase as predicted from the above theory.

2.1.3 Finite element model accuracy

The third effect mentioned by Mercer et al. (2003: 4) that could have an effect on the accuracy of fatigue life calculation based on a finite element analysis is the model used for the analysis. The accuracy of the finite element model, mesh quality, material data specified and boundary conditions all determine the accuracy of the results, therefore these factors are evaluated in more detail to highlight areas that need attention to ensure an accurate model for further analysis.

a) Finite element model construction and mesh selection

Two modelling methods are used in the majority of cases to construct finite element models (FEM), i.e. surface or shell modelling (2D element) and solid modelling (3D element). Each of the methods has its own application advantages. When a structure or model is constructed from surfaces with no thickness, where the surface represents the mid plane of a thicker component, the term surface modelling is used. For a model constructed as a volume, accurately representing the component, as it will be constructed, the term solid modelling is used. More feature details are normally included in solid models, i.e. fillets, chamfers or where needed weld details. These details are not easily represented in surface models. Finite element models should be constructed in such a way as to accurately represent the features of the component under investigation, but simultaneously eliminating all features that would complicate the meshing process without adding to the analysis accuracy.

Adams and Askenazi (1999: 141) indicate that surface modelling is appropriate when the wall thickness of the component is small relative to the overall size or surface area of the system. They further mention a ratio of 10:1 for surface area to material thickness as a guideline for the applicability of shell elements. (1999: 145) This ratio holds true in the case of the Tippler structure analysed in this study. Where shell elements are used to mesh surface models they are applied directly to the surface model surfaces. The mathematical representation of the element used takes into account the thickness of the material used. One advantage of using surface models and shell elements is that accurate results are obtainable from fewer elements; thereby significantly reducing solving times. A further advantage of using surface models is in the fact that shell elements may be significantly more accurate than solid elements where structural bending occurs.

A mesh consisting of quadrilateral elements is usually more accurate than a mesh of similar density constructed from triangular elements (Adams & Askenazi, 1999:

141). Triangular elements are regularly used when meshing difficult geometry or transition areas.

Solid models are volume-meshed by means of solid elements. Typical solid elements used in analysis packages include tetrahedral and cubic elements. Solid element meshes can provide the user with a very accurate representation of the stress patterns in parts with complex geometry. However, when structural bending is suspected the appropriate number of elements should be used through the thickness of the component to accurately characterise the bending stress.

Whenever possible, second order or isoparametric elements should be used in FEA models as fewer elements are necessary to accurately predict complex strain distributions in components. These elements also allow the user to accurately approximate curved boundaries in complex models with fewer elements.

b) Mesh quality evaluation

The mesh quality used for the model could have a significant effect on the results obtained from the model. Adams and Askenazi (1999: 271) note that local mesh effects generally have little effect on the global behaviour of a model. Therefore, they maintain that interest of speed coarse elements should be used far from the areas of interest. The user should, however, consider the effect this assumption may have on the results obtained from the analysis.

Before stress results are analysed, the accuracy of these results at area of interest should be evaluated. On this point Mercer et al. (2003:4) note that a good criterion for determining the suitability of a mesh for fatigue calculations is comparing the averaged and un-averaged nodal stresses results of the FEA model. The difference between the stress values should not be more than 15% (Mercer et al, 2003: 4). A further method to evaluate the quality of a mesh, is to refine the mesh in the area of interest, and re-solving the model. The convergence of the stress at the re-meshed position is compared to the stress obtained from the coarser mesh of the previous model. Once the stress results converged within an acceptable limit, the model is ready for further analysis. Figure 2.10 shows a typical convergence plot for a finite element model.

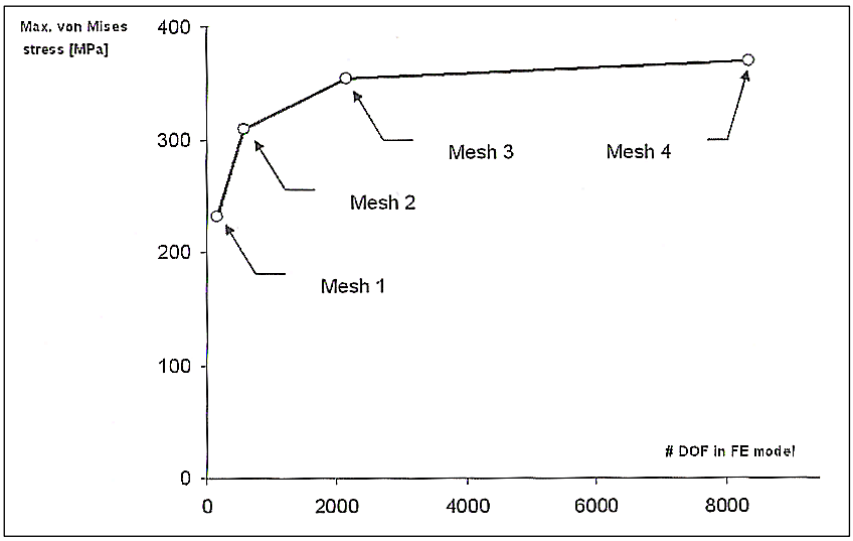

Figure 2.10: Convergence of the maximum Von Mises stress for a FEA model

Source: Finite Element Analysis for Design Engineers, Kurowski, 2004: 28

The effect singularities, distorted or stretched elements have on the results obtained at the area of interest should be evaluated and if necessary, the mesh should be modified to reduce these effects. Degenerated or bad shaped elements are generally too stiff and would therefore affect the accuracy of the displacement matrix created. The strains and stresses subsequently calculated from the displacement matrix would therefore be inaccurate. If identified that these occurrences have no effect on the evaluated area, they can be ignored as fictitious or as known inaccuracies (Adams & Askenazi, 1999: 272).

If all the criteria as described above have been met, the accuracy of the FEA results would be appropriate to guarantee the accuracy of the fatigue life estimation.

2.1.4 The fatigue-analysis algorithm used

The last factor noted that may have an effect on the accuracy of fatigue life results obtained from finite element results is the fatigue-analysis algorithm used for the analysis. One example is the use of principal stresses for the calculation of fatigue life for ductile metals that render unsafe fatigue life estimates. Mercer et al. (2003: 5) notes that principal stresses should only be used for the fatigue life prediction of brittle metals i.e. cast irons and some very high strength steels.

Care should be taken when selecting a fatigue algorithm for an analysis. The algorithm selected should be able to utilise the available data. For example, when using the Von Mises equivalent strain algorithm to evaluate measured signals, the

stress data should always be positive as Von Mises stresses and strains are always positive. Applications such as rain flow counting cannot be applied directly to the results obtained from the analysis.

A further complication is the construction used for the structure or the components under investigation. For a component constructed from a single piece of un-welded material a different fatigue approach would be used, than for a component consisting of different pieces of material joined by welding.

a) Fatigue life algorithm selection

At present there are three main approaches to design against fatigue failures. The three approaches are the stress-based approach, the strain-based approach and lastly, the fracture-mechanics approach (Dowling, 1999: 358). In the stress-based approach, the nominal stress that can be endured is calculated by determining the mean stress in the component and then adjusting this mean stress by allowing for stress raisers such as grooves or holes. In the strain-based approach, possible localised yielding that may occur in the stress raisers during cyclic loading is analysed in detail. The fracture-mechanics approach investigates the effect of progressing cracks in a material. Figure 2.11 indicates how the different approaches are applied during the life cycle of a structure or component.

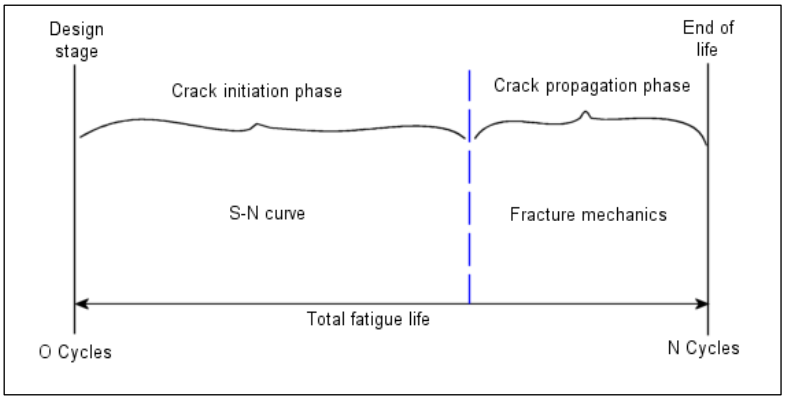

Figure 2.11: Fatigue life approaches as applied during component life
Adapted from: Reality-Based Design for Fatigue of Marine Structures, Assakkaf and Ayyub.

The stress-based and strain-based approaches are mainly used during the design and crack initiation phase of the structure's or component's life. During these phases, the designer or operator is interested in determining where cracks are most likely to develop. The identified positions may be designed during the design phase and monitored during the crack initiation phase. Once a crack is detected, the fracture-mechanics approach can be utilised to

calculate the remaining operational life of the structure or component. The fracture mechanics approach is furthermore used where welds are present in a structure, as possible welding defects would act as crack initiation points, and therefore eliminate the crack initiation phase as described. However, in the Tippler structure's case the influence of corrosion on the crack growth speed complicates the fracture-mechanics approach, as an accurate predicted life would not be possible (paragraph 2.1.2 c). The early detection of fatigue cracks is also complicated due to irregular inspection cycles and the inaccessibility of the crack positions. These complications therefore necessitate an infinite life design for the Tippler structure, i.e. no further crack growth, even from existing welding defects, or crack initiation from unwelded areas, which would eliminate the need for detail inspections.

A further distinguishing factor that should be accounted for is the nature of the fatigue loading experienced by the component. Shigley (1986: 231) limits low cycle fatigue to 10^3 cycles. The high-cycle fatigue region is indicated above 10^3 cycles to infinity as shown in Figure 2.10.

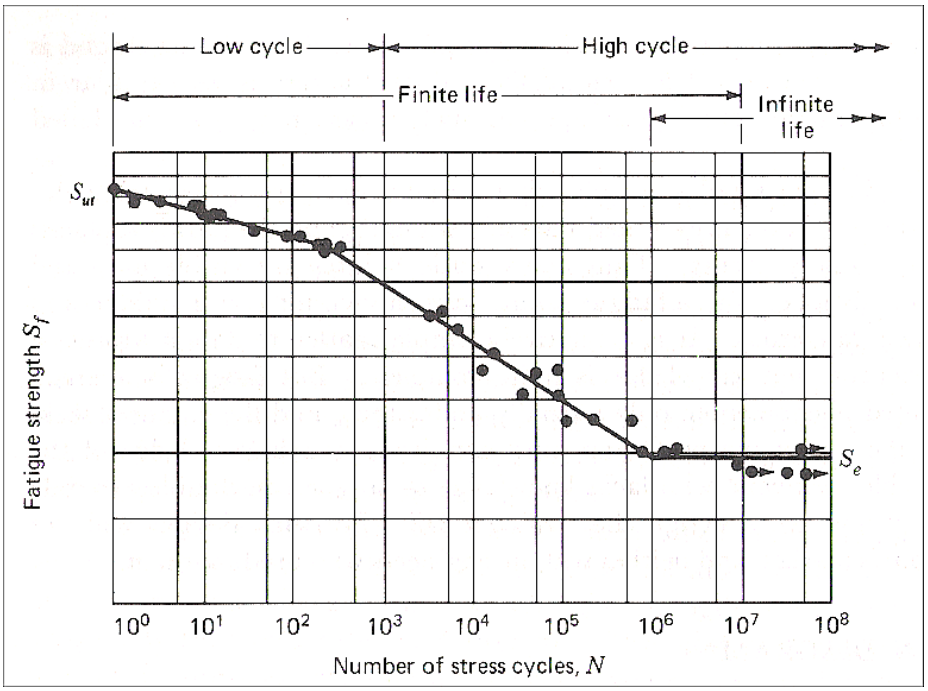

Figure 2.12: S-N diagram plotted from the results of completely reversed axial fatigue tests.
Adapted from: Mechanical engineering design, Shigley, 1968: 230

The figure further indicates that a component's finite life ends at approximately 10^7 cycles. However, the infinite life classification starts at 10^6 cycles. The boundary between finite and infinite life is not clearly defined but lies between 10^6 and 10^7 cycles. Further, note the data point scatter along the curve. This

scatter is caused by multiple factors that influence the fatigue life of a test sample i.e. sample, preparation methods, heat treatment, surface finish quality, even environmental effects.

As indicated previously, the Tippler structure performed on average approximately 294 tip cycles per day for a ten-year period before the fatigue cracks were discovered. This relates to approximately 1.07 million tips, which indicates high-cycle fatigue. The structural life further falls into the transition zone between finite and infinite life. Ellying (1997: 82) notes that the stress-based fatigue life approach is most applicable for the high cycle fatigue range where strains are essentially elastic. The stress life approach as originally developed by Wöhler specifies an endurance limit, which characterises the stress amplitude bellow which a material is expected to have an infinite fatigue life. An operational critical structure, in this case the Tippler structure, would qualify to be designed with an infinite life. Bannantine et al. (1990: 234) further note that the stress-life approach is more appropriate for application in designs for long lives and constant amplitude loading. They however caution the user that the stress-life approach does not distinguish between crack initiation and propagation. The stress-life approach would therefore be suitable to specify allowable stress levels in the structure as the structural changes incorporated in the Tippler structure allows for an infinite life.

The allowable stress amplitudes and cycles at which a structure or component can operate without the danger of structural damage due to fatigue cracking are plotted on an S-N curve as indicated in Figure 2.12. Note that after 10^6 or the infinite life point the allowable stress is indicated as constant. This implies that if a component or structure's stress cycles is kept below the indicated stress, no fatigue damage will occur. The transition or "knee" at 10^6 cycles, however, only holds true for some materials as indicated in Figure 2.13.

The endurance limit as indicated on an S-N curve is, however, not an accurate representation of the material's actual properties under operational conditions. Material properties, environmental effects and manufacturing methods as indicated in paragraph 2.1.2 all contribute to lowering the fatigue endurance limit as indicated in an unmodified S-N curve. Factors such as corrosion can cause the endurance limit to disappear (Figure 2.6).

The S-N curve can be constructed form material properties if not available from literature. Two methods to construct the S-N curve from material data are illustrated by Bannantine et al. (1990: 4), i.e. graphical representation or from a power relationship.

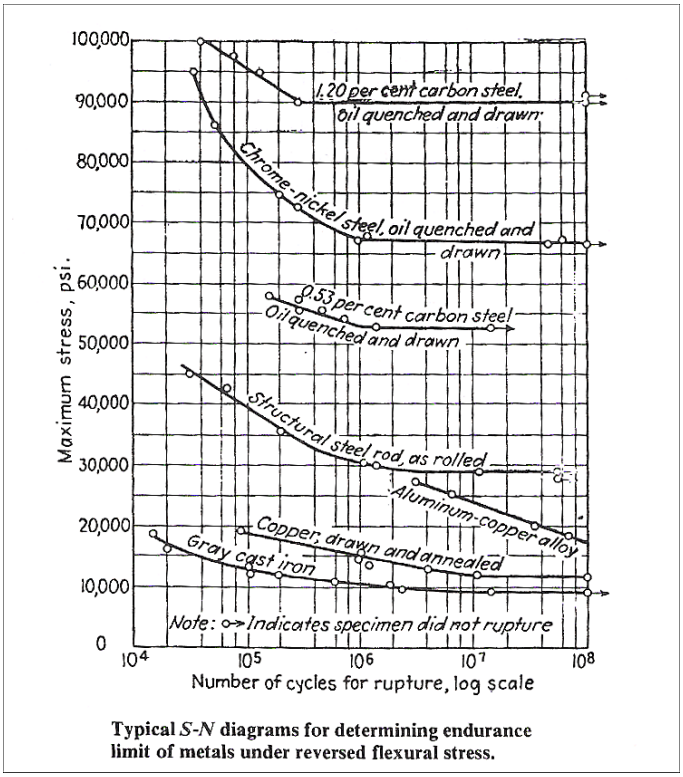

Figure 2.13: S-N diagrams comparing the endurance limit for seven alloys
Source: Atlas of Fatigue Curves, Boyer, 2003: 30

The method selected for this study is the power relationship method. The S-N curve constructed from this method would be appropriate to evaluate the unwelded or virgin material in the structure. The equations used for the construction are indicated below:

$$S = 10^{C} N^{b}$$ (Bannantine et al., 1990: 4)

Where :

$$b = -\frac{1}{3}\log_{10}\frac{S_{1000}}{S'_e} \quad \text{(for } 10^3 < N < 10^6\text{)}$$

$$C = \log_{10}\frac{(S_{1000})^2}{S'_e}$$

From this equation, the sloped S-N curve can be constructed between 10^3 and 10^6 cycles. The curve is further constructed as horizontal line for and cycles beyond 10^6. The values for S_{1000} (position where S-N curve crosses the stress axis at 10^3) and S'_e (unadjusted endurance limit) are calculated from the ultimate tensile strength of the

material under investigation. The following table provides approximation values for S_{1000} and S'_e for different authors.

Table 2.1: Endurance limits as quoted by different authors

	Endurance Limits		
	S_{1000}	**S'_e (10^6)**	**S'_e (10^8)**
Bannantine et al 1990: 5	≈ 0.9 S_{ut}	≈ 0.5 S_{ut}	-
Shigley 1986: 241	≈ 0.65 S_{ut}	≈ 0.4 S_{ut}	-
Ellyin 1997: 82	-	≈ 0.5 S_{ut}	≈ 0.33 S_{ut}

Shigley however cautions that the value quoted represents the minimum endurance limit and should only be used if no other material data is available. Furthermore, Ellyin also warns that these values should only be used if no additional material data is available.

The S-N diagram constructed from the data above would therefore provide the allowable cycle stress for an unwelded component under perfect conditions, and is not applicable for design or analysis purposes. The endurance limit still has to be adjusted for material properties as indicated in paragraph 2.1.2. The adjustment is done by multiplying the S-N data with the appropriate material constants, i.e.

$$S_e = k_a k_b k_c k_d k_e k_f \cdot S'_e \qquad \text{(Blake, 1985: 323)}$$

Where:

S_e = adjusted endurance limit of the component
S'_e = unadjusted endurance limit of the component
k_a = surface finish factor
k_b = size factor
k_c = reliability factor
k_d = temperature factor
k_e = shape factor
k_f = miscellaneous effects (environment, surface treatment, residual stresses, etc.)

The adjusted endurance limit can now be used for fatigue life evaluation as it allows for most factors that would influence a material's fatigue life during operation.

As previously mentioned the constructed S-N curve would only be valid for unwelded components to estimate the number of cycles at which a crack would initiate. Once a crack developed, the linear-elastic fracture mechanics approach should be used to estimate how long it would take a crack of a certain size to grow to a certain length when subjected to a cyclic loading. This is done by estimating a stress intensity factor that characterizes the severity of the crack in the component. Thus, for a given material and a set of loading conditions, the crack growth rate da/dN can be described with the following relationship where C and m are both material parameters and ΔK represents the stress intensity range.

$$\frac{da}{dN} = C(\Delta K)^m \qquad \text{(Dowling,1999: 492)}$$

This equation is known as the Paris equation, which characterize the resistance of a material to fatigue crack growth under a certain conditions. The rate of crack growth depends primarily on the size of the crack and the stress cycle experienced by the cracked area (Kneen, 2004: 2). Kneen further notes that when a crack is first detected it is usually 5mm long and that this can be at anything from 20% to 95% of total life. It is further noted that corrosive environments would increase fatigue damage and lower the materials endurance limit. Dowling notes that a crack can grow even under a constant load if exposed to a hostile chemical environment as would be experienced by the Tippler structure. This phenomenon is known as environmental crack growth. (Dowling, 1999: 488).

However, for this application an infinite structural life is required. For this reason, crack-initiation or growth is interpreted as a failure, as corrosion and unscheduled inspection periods would leave the possibility of undetected cracks or uncontrollable crack growth. By using component S-N curves (discussed in par 2.3), based on experimental data obtained form welded components, a stress range can be determined that would allow for an infinite structural life even with welding defects present. This would however only hold true if the weld could be adequately protected against corrosion.

With the adjusted endurance limit or an endurance limit obtained from the component S-N curve known, the cumulative fatigue damage for a component can be calculated from the Palmgren-Miner cycle ratio summation theory or Miner's rule. This method is used in estimating the fatigue life of a component when not only the stress amplitude varies but also the mean stress value. The formula is as follow:

$$\sum_{i=1}^{m} \frac{n_i}{N_{fi}} = 1$$

where :

n_i = number of cycles applied at the *i*th loading level
N_{fi} = number of cycles to failure at that load level

From this summation, the total damage caused by the cycle analysed is calculated. The number of cycles to crack initiation or crack growth can then be calculated by dividing one by the total damage for one cycle.

Due to the comparative nature of this study (the modified Tippler structure is compared to the original Tippler structure with a known fatigue life), the Palmgren-Miner rule can be applied in a relative form as suggested by Dowling (1999, 473):

$$\sum_{i=1}^{m} \frac{n_i}{N_{fi}} = D$$

Where D differs form unity. The fatigue life of approximately 10 years, of the original structure will be set equal to D, and the life of the modified structure will then be scaled relative to the value D to give an indication of the fatigue life gained by the modifications as applied to the structure.

2.2 Fatigue in welded structures

Steel structures consist of virgin material i.e. material, which has not been further processed from its delivered state that is joined together by bolt or welded joints. Therefore, to evaluate the fatigue life of a steel structure by means of the stress based approach, the fatigue life of the virgin material and the welded material has to be evaluated in the high stress areas. This evaluation would be conducted by means of stress life or S-N curves for both the welded and un-welded material, however, the mechanism of fatigue is totally different. For virgin material, the crack initiation phase as described earlier is taken into account, while for the welded material the crack initiation phase is ignored, as it is assumed that the weld contains defects from which the crack can grow i.e. the defect act as a crack initiator.

Any weld is a potential crack due to weld defects, material changes or notches that may form during the welding process. Das (1997:53) list the following defects and effects that may develop during the welding process:

Table 2.2: Weld defects and their effect on fatigue properties

Source: Metallurgy of failure analysis, Das, 1997: 53

Defect	Effect
Incomplete/inadequate fusion	Reduces the weld joint strength and fatigue strength
Underbead cracks, hot or cold cracks	Affects fatigue strength and act as a point of stress concentration
Undercut	Reduces the weld thickness and strength properties. Also acts as a severe notch for development of a fatigue crack
Non-homogeneous microstructure	Weakens the weld metal strength properties, develops cracks (in the case of formation of martensite in the heat affected zone) and reduces fatigue strength property.
Weld decay	Develop inter-granular/stress corrosion cracking particularly in austenitic stainless steel

All the listed defects have a direct influence on the fatigue life of the welded component. In the case of the Tippler structure, the nature of the defects that may have existed in the welds is unknown. Figure 2.14 shows the influence of weld defects on the fatigue life of a component.

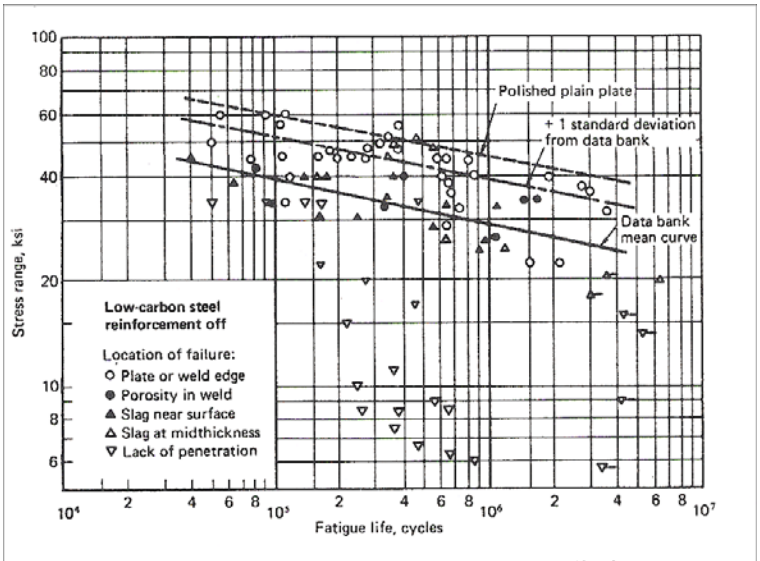

S-N curves showing effect of various weld defects on fatigue life of a low-carbon steel weldment, presented as a comparison with fatigue life of the plate.

Figure 2.14: Effect of weld defects on fatigue life of steel

Source: Atlas of Fatigue Curves, Boyer, 2003: 54

At present fatigue designs are based on S-N curves that evaluate the nominal stress at the area of interest. The data may however not always accurately represent the geometry or properties of the material at the area of interest, as these curves are constructed form un-welded or notch free material. Component S-N curves are constructed from test samples with a limited number of configurations. For this reason in the case of complex weld geometry, “hot spot stresses” are calculated by extrapolating local stress values to the actual weld position. These calculated stress values are then related to a single S-N curve to estimate the allowable stress amplitudes. Also, mean stress and stress amplitude values are generally used for crack initiation (unwelded) calculations while stress range and stress ratio values are used for crack growth (welded or cracked) calculations.

Dowling (1999: 460) notes that S-N curves do not vary for different structural steels where welding is concerned as the tensile residual stress near a weld remains near yield for the material after welding, if not treated.

2.3 Welding codes and component S-N curves

To provide the designer with guidelines and the user with assurance, welding codes based on laboratory evaluations of welded components is available. These codes must cover a wide range of eventualities and, considering all the factors that can negatively influence the integrity of a weld, border on the safe side.

From the test specimens of similar construction, a mean life S-N curve is derived. The data is statistically evaluated to determine a lower confidence limit i.e. the 5 percentile or mean minus two standard deviations curve, which could safely be used in a design (Keene,2004: 3). These curves would provide a probability of survival of 97.6% (Det Norske Veritas, 2005: 12) or 95% as quoted by the IIW code (Hobbacher, 2004: 91). The S-N curves have an endurance limit known as the Constant Amplitude Fatigue Limit (CAFL) below which fatigue cracks, if existing, would not grow (Keene,2004: 3). From the S-N curves for different constructions FAT classes are awarded to each curve or construction. These classes are based on the geometrical arrangement of the joint, the direction of the fluctuating stress relative to the joint and the method of fabrication and inspection of the detail (Det Norske Veritas, 2005: 12). In the case of the IIW code the FAT class represents the position where the CAFL curve intersects the 2 million cycle position as indicated in figure 2.15.

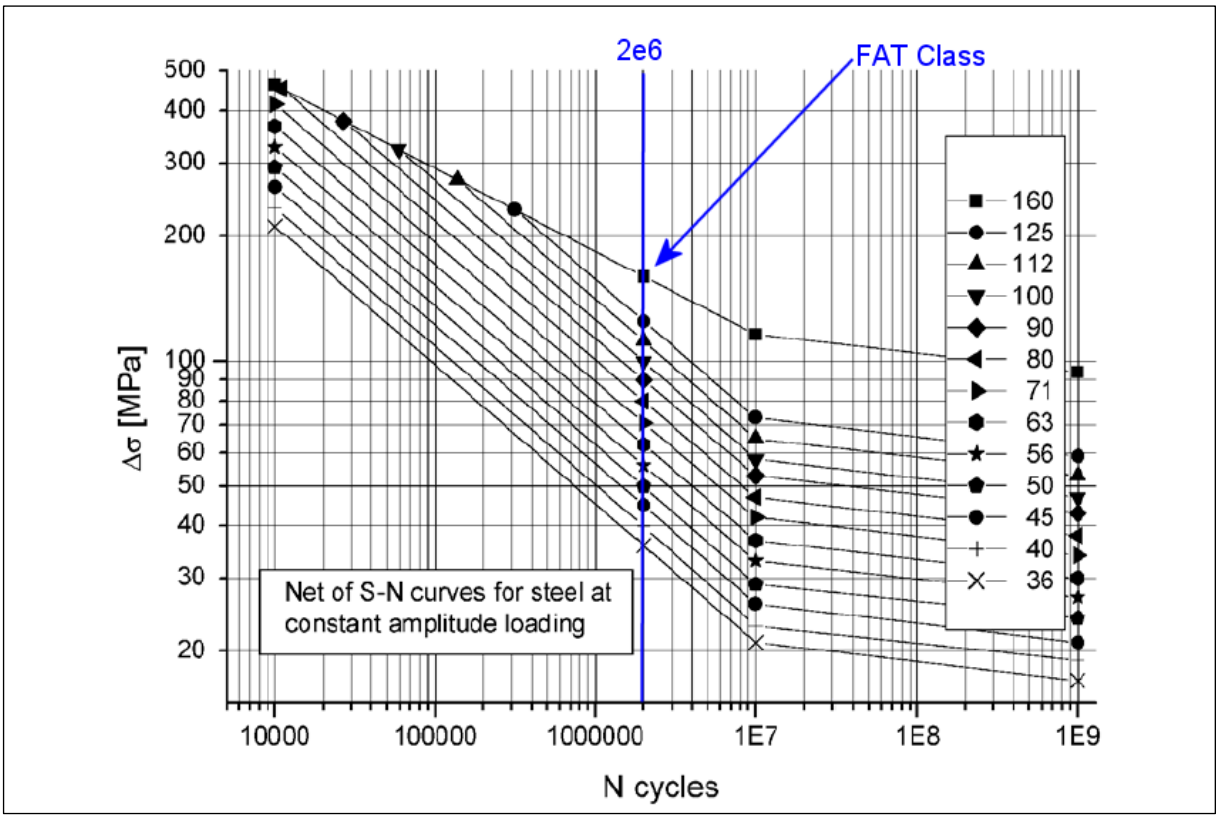

Figure 2.15: FAT classes for IIW welding code.

Source: Recommendations for fatigue design of welded joints and components (Hobbacher, 2004: 45)

A further adjustment of the S-N curve can be made to allow for the thickness of the different plates welded together. This effect is however reduced when the plate welded to the tick plate is less than 25 mm thick, as in the case of the Tippler structure. The FAT classes are furthermore independent of the grade of steel used for the welded construction. For design purposes each part of the welded construction is evaluated according to the S-N curves.

A line is however drawn for general welding codes. If a weld is exposed to corrosion the code predictions in general do not apply as seen in the IIW code witch states that "The recommendations are not applicable to low cycle fatigue, where $\Delta\sigma_{nom}$ >1.5 × fy, max σ_{nom} > fy , for corrosive conditions or for elevated temperature operation in the creep range" (Hobbacher, 2004:8). The BS 7608:1993 welding codes stipulates that when a weld is exposed to corrosion from sea water the basic S-N curve should be reduced by a factor 2 on life for all weld classes (BS7608:1993, 32).

For the structure under investigation, this presents a dilemma, as corrosion from salt spray is definitely present. For this reason a component S-N curve was selected for the evaluation and then adjusted to allow for corrosion and other factors, until a S-N curve was available that closely represented the fatigue life as experienced by the

structure. This curve was then used to evaluate the fatigue life of the modified Tippler platform structure.

2.4 Conclusion

To obtain accurate fatigue life estimations from finite element data the user should ensure that the loading data obtained is accurate, the finite element models used is accurate, that the material specification and data used for the analysis allows for all possible endurance limiting factors and lastly that the fatigue life calculation algorithm is suitable for the application. Only once all these influences have been quantified, an estimation of the reliability of the structure is possible.

CHAPTER 3

STRAIN GAUGE MEASUREMENTS

The main purpose of the strain gauge measurements was to obtain stress history data for known positions on the Tippler structure. This data was used to verify the accuracy of the FEA model of the Tippler structure that was constructed and as input data for the calculation of the fatigue life for the original and modified Tippler structure. A detail analysis was however done on the data obtained to identify any additional factors that could have an influence on the fatigue life of the structure but cannot be easily simulated by means of a FEA. Some of these factors include internal residual stresses, forces generated by misalignment between structural components or friction in connections and pins. Note that the stress results obtained from the strain gauges do not include mean stresses in the structure caused by gravitational acceleration as the strain gauges were applied and their outputs set to zero while the structure was subjected to gravitational acceleration.

3.1 Description of the strain gauge equipment used

The rotation of the Tippler structure during operation makes it very difficult to do strain gauge measurements with conventional wiring methods, as the wires tend to get damaged. It was therefore decided to make use of wireless strain gauge amplifiers. The equipment was specifically developed for this and similar projects and consists of a battery-powered bridge amplifier with on-board memory. The amplifier is set up and controlled through a wireless connection and the readings are stored on board. The sampled data can be downloaded via the wireless connection or through an RS485 connection. The system also has the capability to provide a real-time display of the stresses for setting up and verification purposes while the machine is in operation. Figure 3.1 shows the bridge amplifier used in a similar application. Figure 3.2 shows an amplifier and battery mounted on the ingo outgo ring of the Tippler structure. The applied strain gauge can be seen in the background. The amplifiers were laced in plastic bags to protect them from the water spayed for dust suppression during the tip cycle.

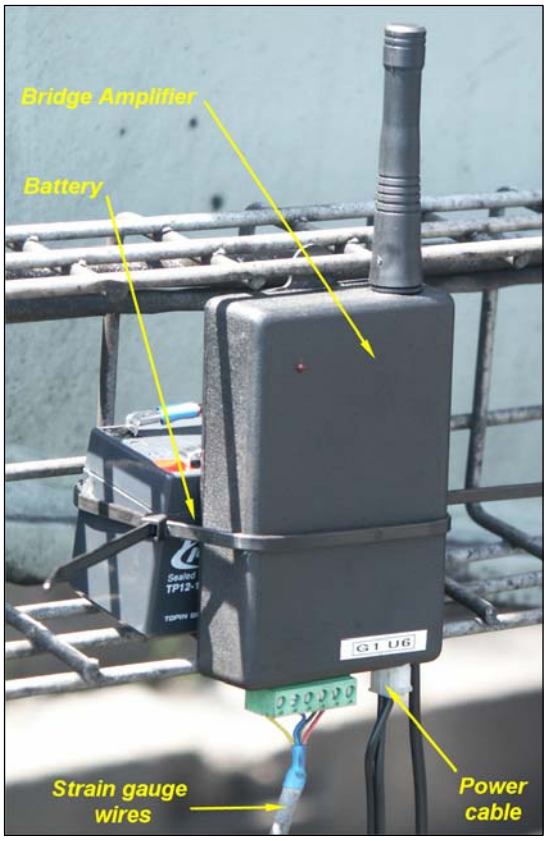

Figure 3.1: Wireless bridge amplifier

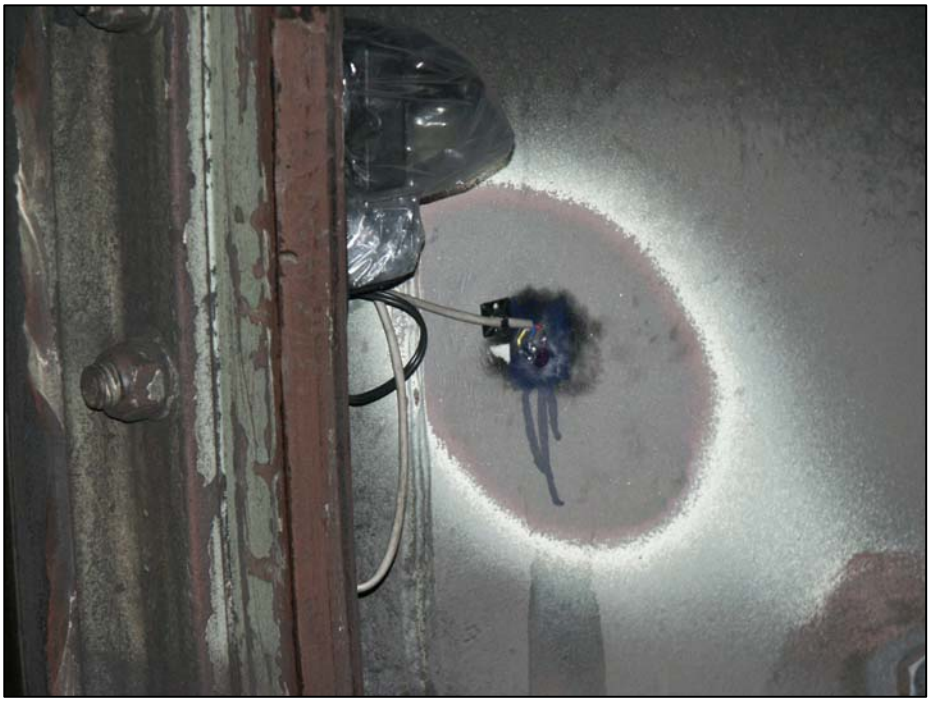

Figure 3.2: Wireless bridge amplifier mounted on the ingo-outgo ring

3.2 Strain gauge positions

The decision as to where to apply the strain gauges had to be made before any finite element results were available. It was therefore decided to apply the strain gauges at positions on the structure where there are no stress concentrations that could complicate check calculations. The strain gauge measurements were not aimed at determining the stress at a specific position, but to determine the general stress in a structural member when the Tippler is rotated to a certain position. As mentioned before, the main focus of this investigation is on the ingo cage. Most of the strain gauges were therefore applied to this cage with some applied to the ingo side support roller assemblies of the outgo cage to investigate the possibility of side forces on this cage. The measured stresses were to be compared to the stress values for the corresponding locations and Tippler positions, obtained from the finite element results. The following positions were selected:

a) On bottom plate of platform structure:

Two strain gauges were applied to the bottom plate of the platform as indicated in Figure 3.3. The purpose of these strain gauges was to determine the stresses at the selected positions under no loading and the increase in these stresses when the full wagons are pushed onto the platform. The stress induced when a locomotive passes over the platform could also be investigated.

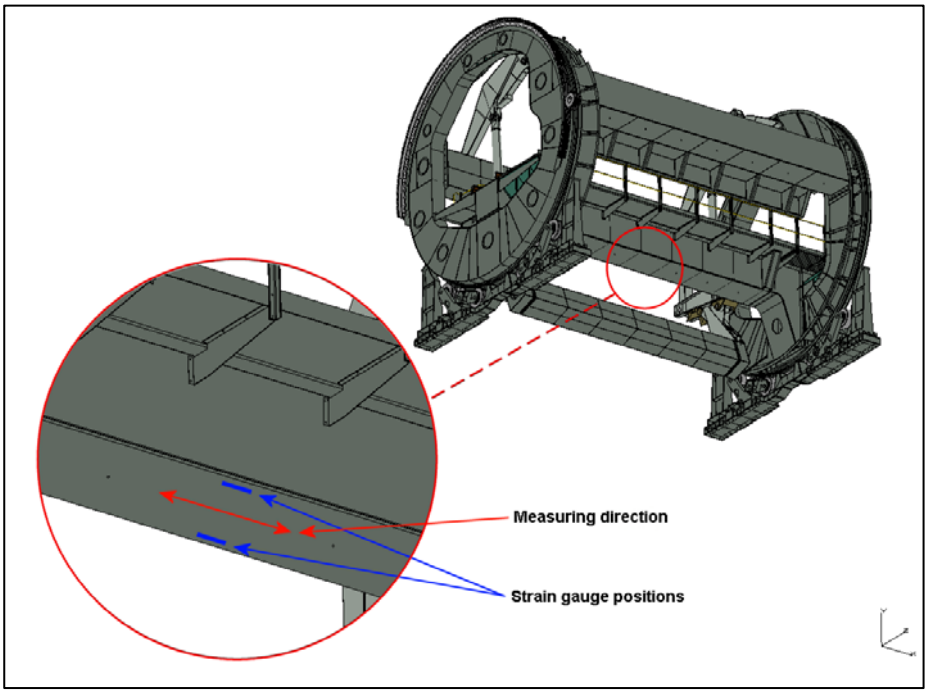

Figure 3.3: Strain gauge positions on bottom plate of platform

Using the standard strength of material theory, the stress increase was calculated to determine the magnitude of the stresses that would be measured by the strain gauges when a full wagon is located on the platform. This calculation was done for a section through the platform as indicated in Figure 3.4.

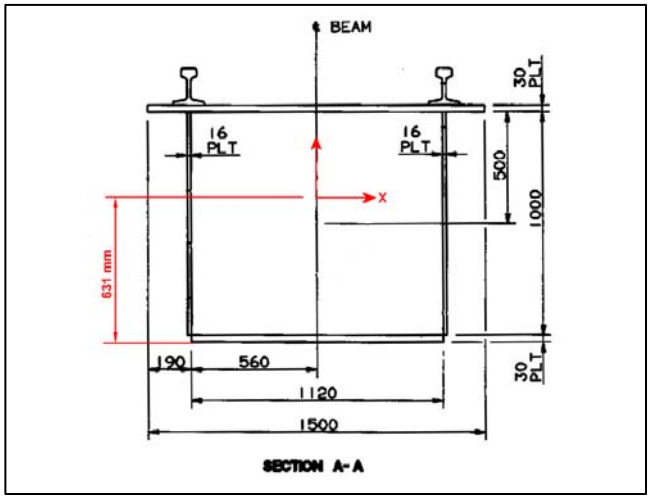

Figure 3.4: Section through platform beam

Source: Extracted from original structural drawing as provided by RBCT

The section as shown was sketched with the I-DEAS software and the section properties calculated. The values obtained were as follows:

Moment of inertia:	Ixx = 2.67917e10 mm^4
Distance to strain gauge position:	y = 631 mm

For the calculation, the beam was pivoted at one end and placed on rollers at the other end as shown in Figure 3.5. This approach does not represent the actual constraint caused by the two end rings, but provides a fair representation of the actual boundary conditions. It thus provides a close estimate of the stress values that should be measured by means of the strain gauges.

From this information the stress increase at the strain gauge position, when a fully laden wagon is rolled on, was calculated as:

$$\sigma = \frac{M \times y}{Ixx}$$

$$\sigma = \frac{660.095e6Nmm \times 631mm}{2.67917e10mm^4}$$

$$\sigma = 15.54MPa$$

Thus, when a fully loaded wagon is positioned on the platform, the stress increase measured by the strain gauge should be in the region of 15.5 MPa.

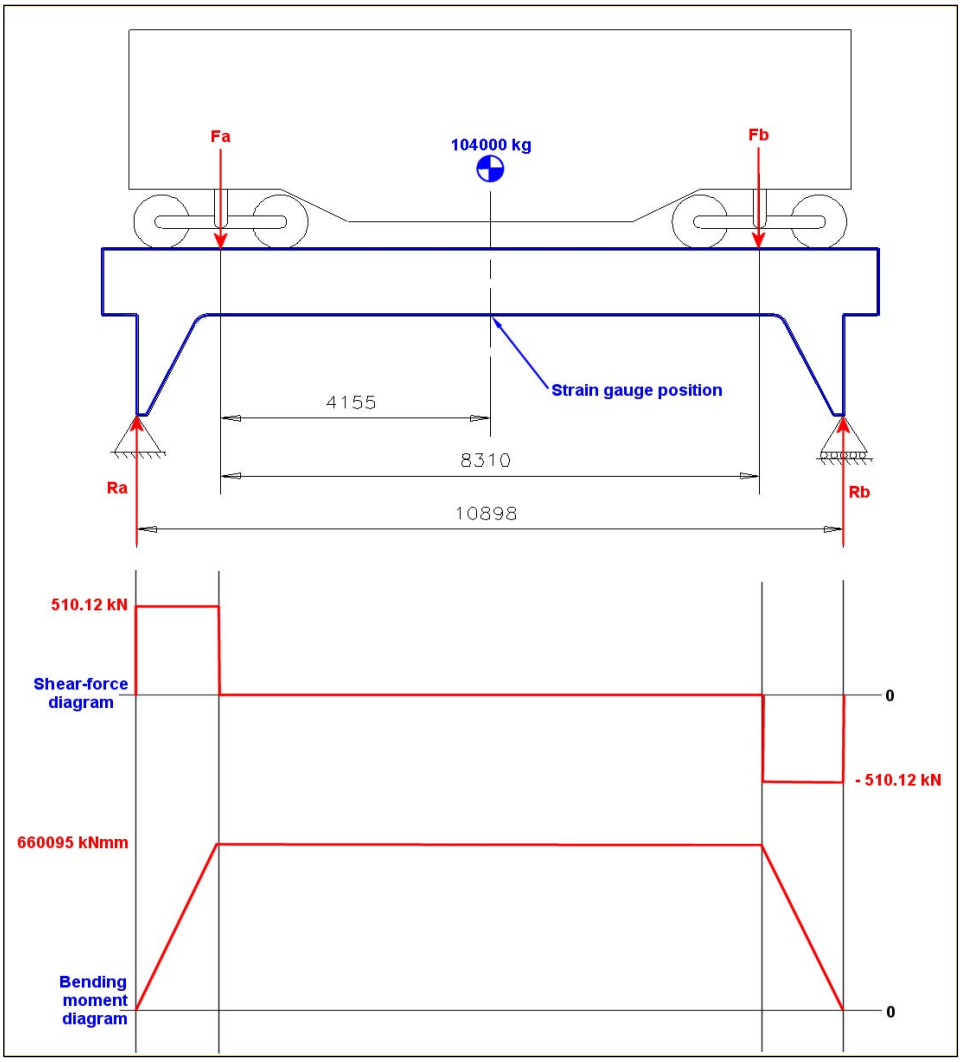

Figure 3.5: Shear-force and bending moment diagram for Tippler platform

b) On top of the cross beam

The third strain gauge was applied to the top of the cross beam between the two clamp-mounting positions. The stress measurement would indicate the magnitude of bending caused by the force acting on the clamps. The position of the strain gauge is shown in Figure 3.6.

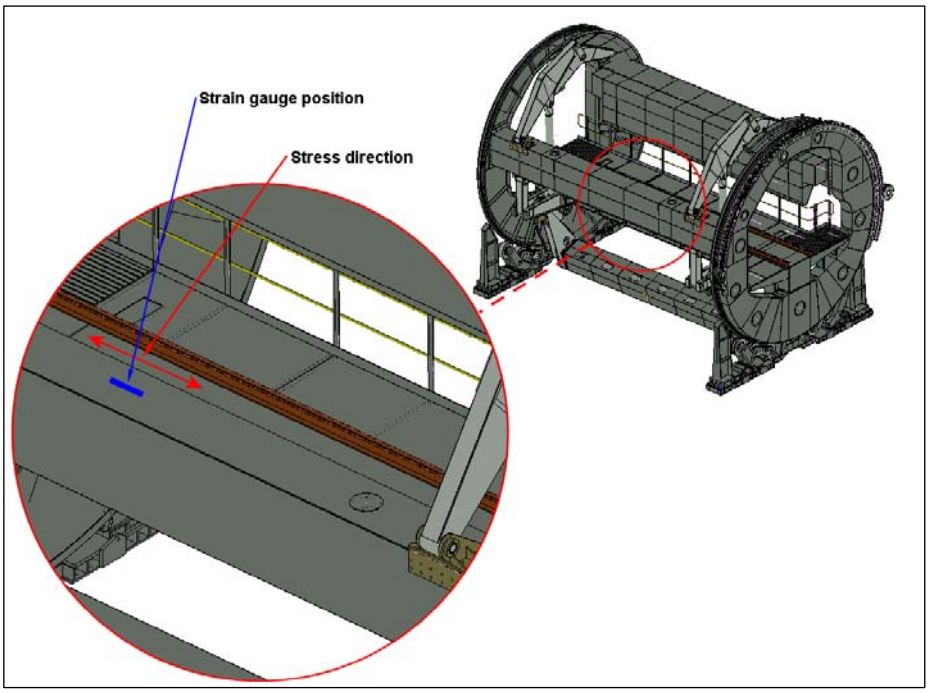

Figure 3.6: Strain gauge position on top of the cross beam

c) On clamp arm

The fourth and fifth strain gauges were applied to the two clamp arms of the ingo cage. Both strain gauges were applied in the same position on the two clamps. The strain gauge position is shown in Figure 3.7.

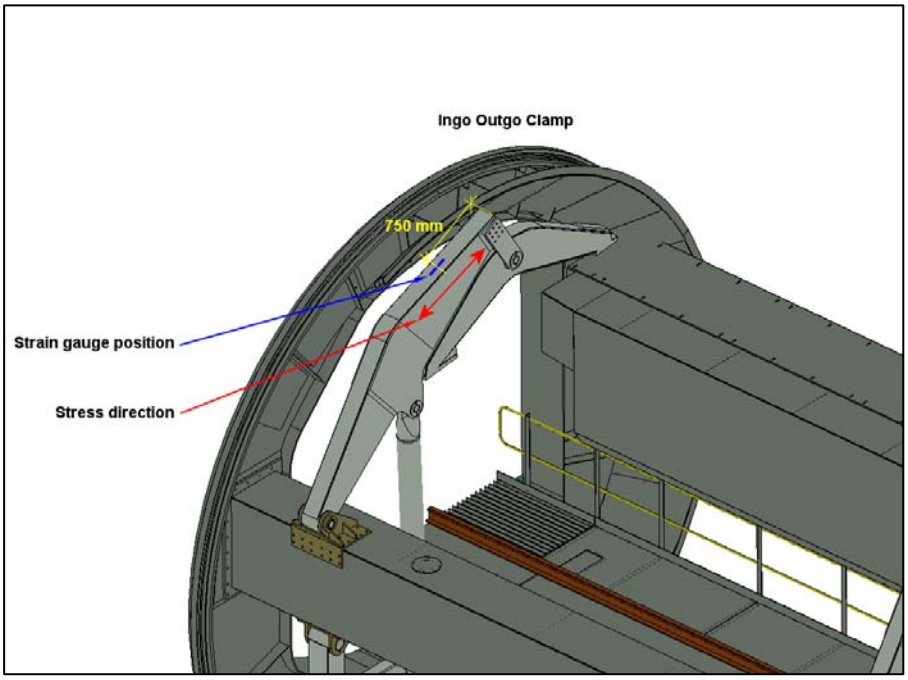

Figure 3.7: Strain gauge position on ingo outgo arm

These stress measurements would indicate the force in the clamps when the clamps are applied.

d) On ingo outgo end ring

The sixth strain gauge (also shown in Figure 3.2) was applied to the ingo outgo end ring. The strain gauge position is shown in Figure 3.8. The stress measurement would highlight any difference in wheel loading when the Tippler cage is rotating.

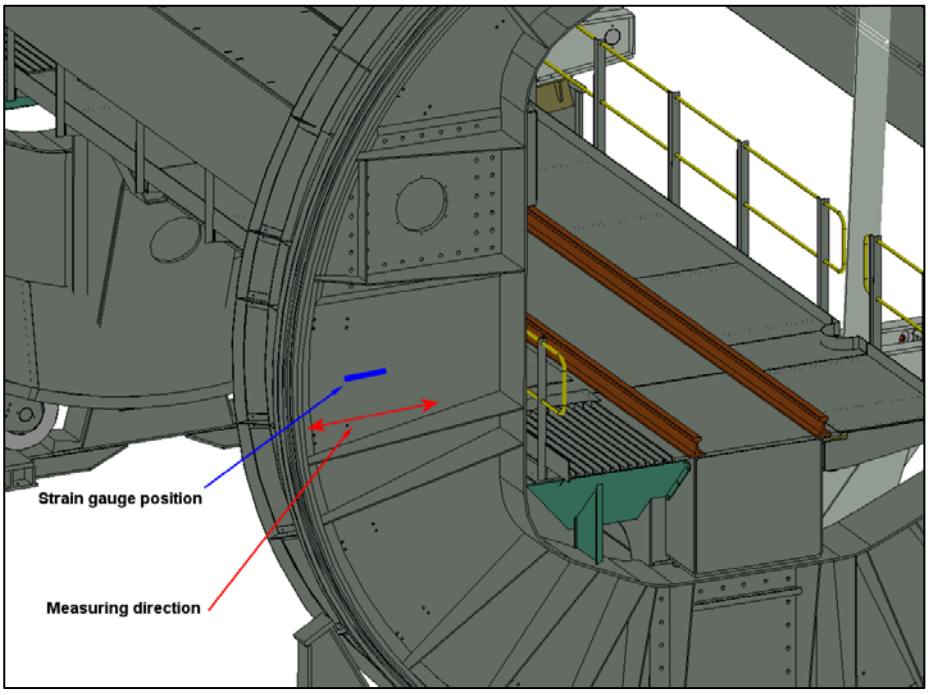

Figure 3.8: Strain gauge on ingo outgo end ring

e) On support roller structures

The last twelve strain gauges were applied to the support roller assemblies as shown in Figure 3.9. The strain gauges were applied in the same positions on the primary compensating beams of all four support roller structures of the ingo cage and the ingo side support rollers of the outgo cage. The purpose of these measurements was to determine if any bending takes place in the structures while the Tippler cage rotates. Bending in these structures would indicate crabbing forces on the cage or external forces acting on the tipper structure.

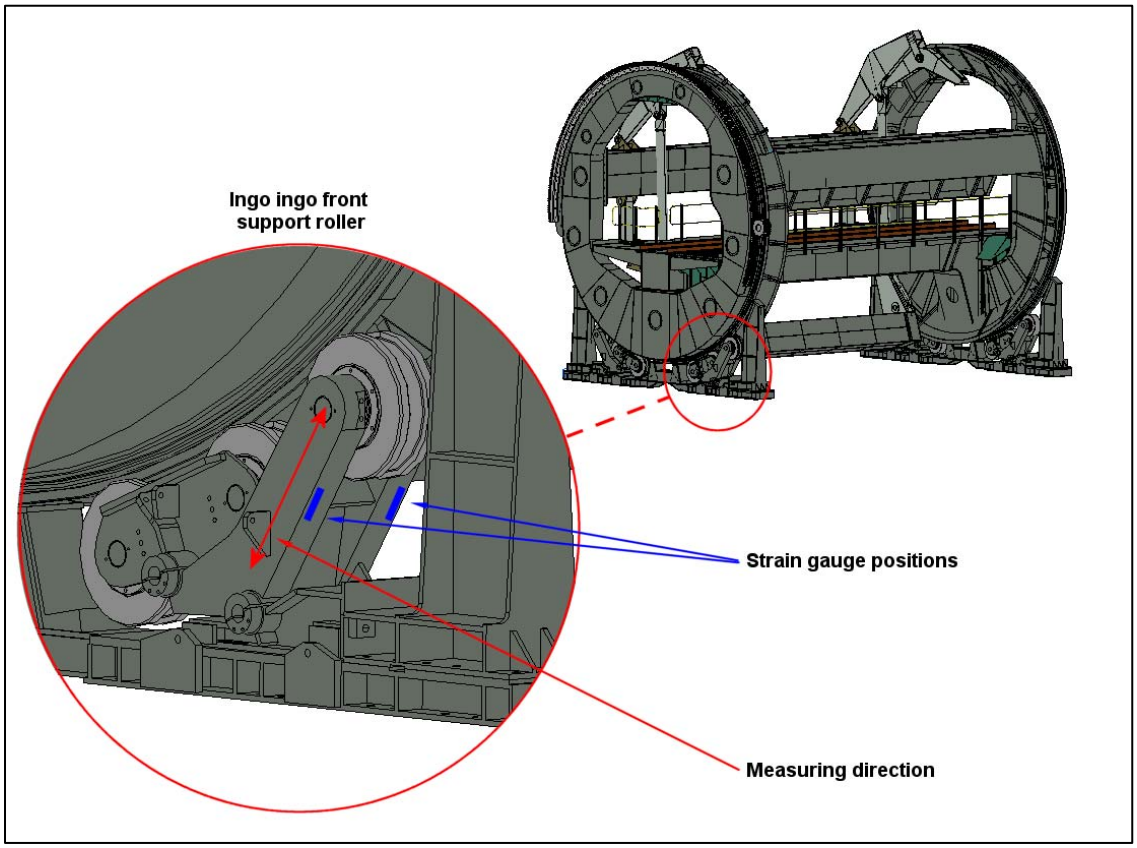

Figure 3.9: Strain gauge positions on the primary compensating beam of the ingo cage ingo side front support roller

3.3 Strain gauge installation and set up procedure

For the application, a half-bridge strain gauge arrangement was used. This arrangement compensates for temperature changes that may influence the strain gauge readings during operation. In this application, the water sprayed in the air to reduce coal dust during the tip cycle may have caused temperature fluctuations that could influence the readings. Note that local bending on the strain-gauged plates was ruled out because of the section size of the structure where the strain gauges were applied. The properties of the strain gauges used are as follow:

Table 3.1: Strain gauge properties

Gauge type and arrangement	Kwoya KFG 90° Rosette – applied in a half bridge arrangement
Gauge type	Steel
Gauge resistance	120 Ω with 5 mm grid length
Gauge factor	2.12

Figure 3.10 shows a strain gauge in the half-bridge arrangement for a similar application on one of RBCT's stacker reclaimers. The strain gauge is covered with a

non-conductive coating to protect it against moisture and coal dust. Note the corrosion already forming on the unprotected metal.

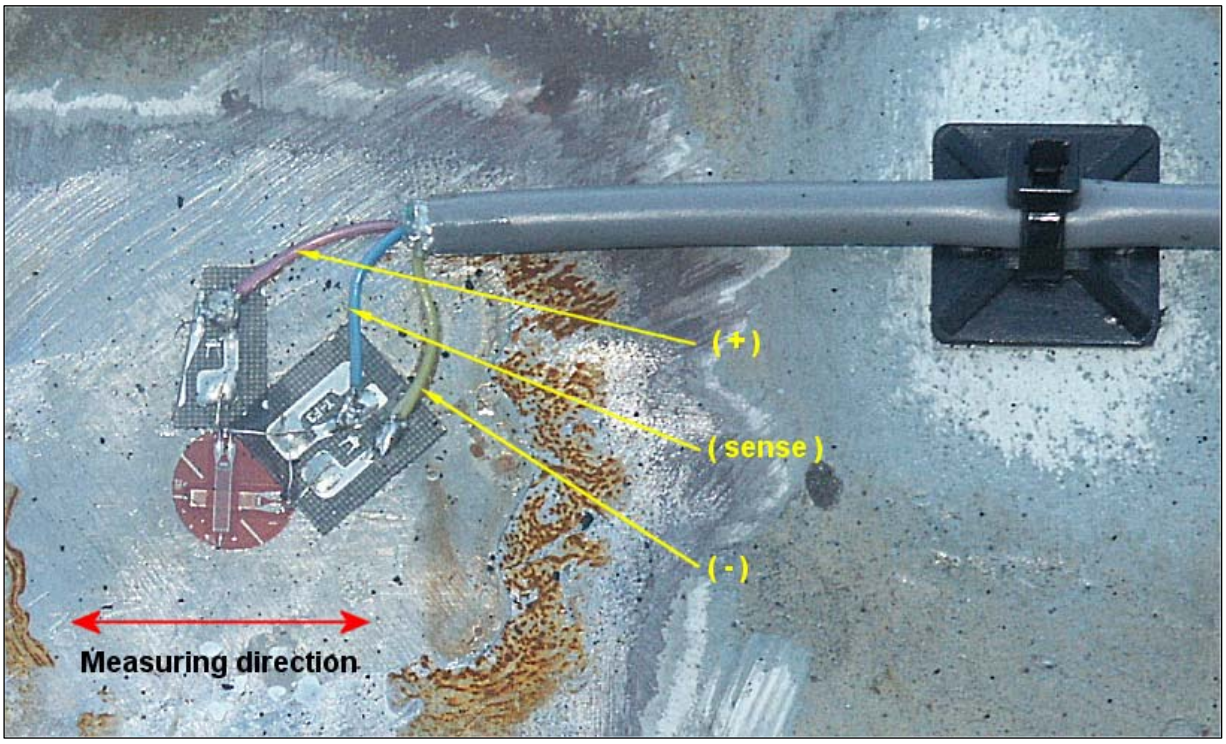

Figure 3.10: Half-bridge strain gauge application

After installation, the strain gauge outputs were set to zero when there were no wagons on the platform. The stress measurements therefore do not include the stress in the structure caused by gravity or other static internal or external forces. A test recording was made to evaluate the stress amplitude and the sampling frequency. During this recording, a locomotive passed over the platform and the muscle arm positioned the wagons on the platforms. The first few tipping cycles were also recorded. The convention used for the stress readings was positive for tensile and negative for compression stresses.

Figure 3.11 shows the stresses recorded when the locomotive passed over the platform and the muscle arm positioned the wagons on the platforms. A maximum stress of 26 MPa was measured when the locomotive passed over the platform. Note the slight difference in the stress values measured on the front and the back strain gauges on the platform. This can be contributed to a local stress effects on the strain gauge or uneven bending of the Tippler platform.

While the muscle arm pushed the full wagons onto the platform, a stress value of 40 MPa was measured. With the wagon in position, the stress measured was in the region of 14 MPa, which corresponds well with the 15.5 MPa stress calculated

earlier. This correlation indicates that the results obtained from the strain gauges are representative and can therefore be used for further analyses.

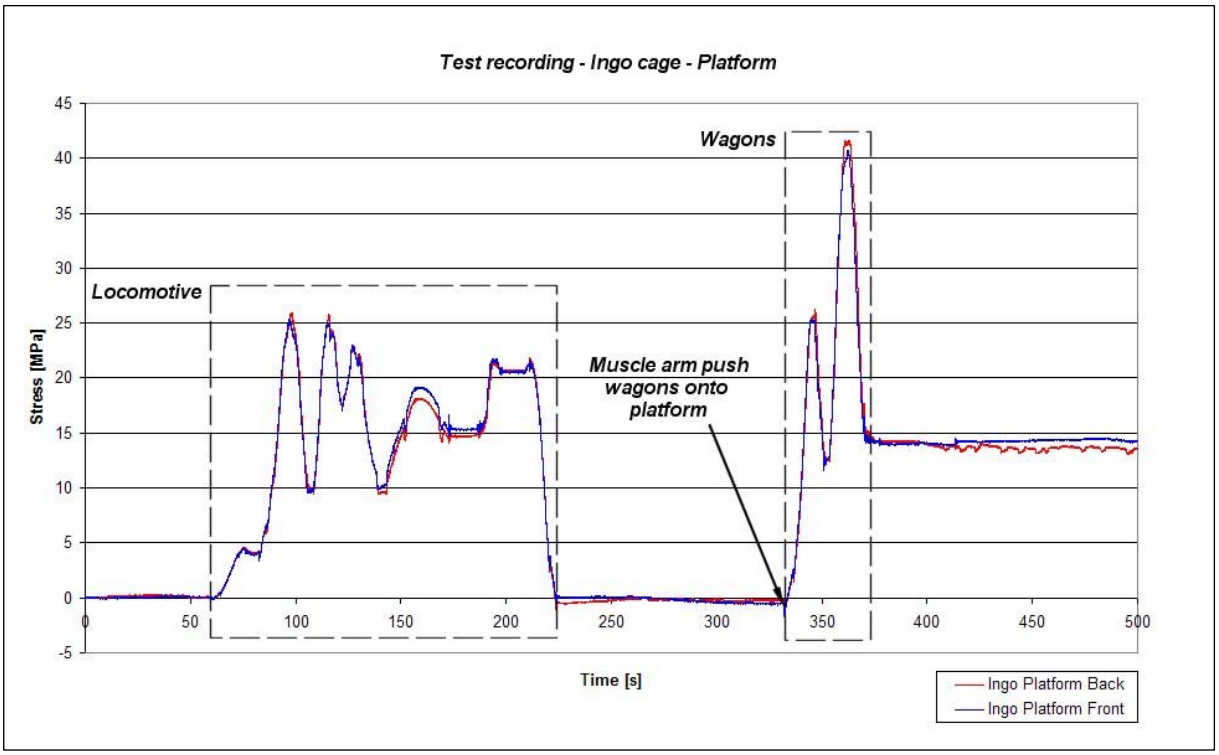

Figure 3.11: Platform stresses recorded during test recording

As no stress fluctuation frequency data was available for the Tippler structure, the industry standard of sampling at ten times the operating frequency could not be used to select a suitable sampling frequency (Mercer et al., 2003: 2). It was therefore decided to first sample at 50 Hertz (Hz) and then evaluates the data before selecting the final sampling frequency.

Stress measurements at three strain gauge positions sampled at 50 Hz are shown in Figure 3.12. The load cycle and tip cycle can clearly be distinguished. At the beginning of the tip cycle, a period with definite stress fluctuations is clearly visible. The sampling frequency would have the biggest influence on the accuracy of the data during this period. The data for this period is shown in Figure 3.13. The plotted data shows that enough measurement points were taken, i.e. no peaks were lost due to too low a sampling frequency. The sample frequency of 50 Hz therefore provides a close representation of the actual trace. The sampling frequency was kept at 50 Hz for the rest of the measurements.

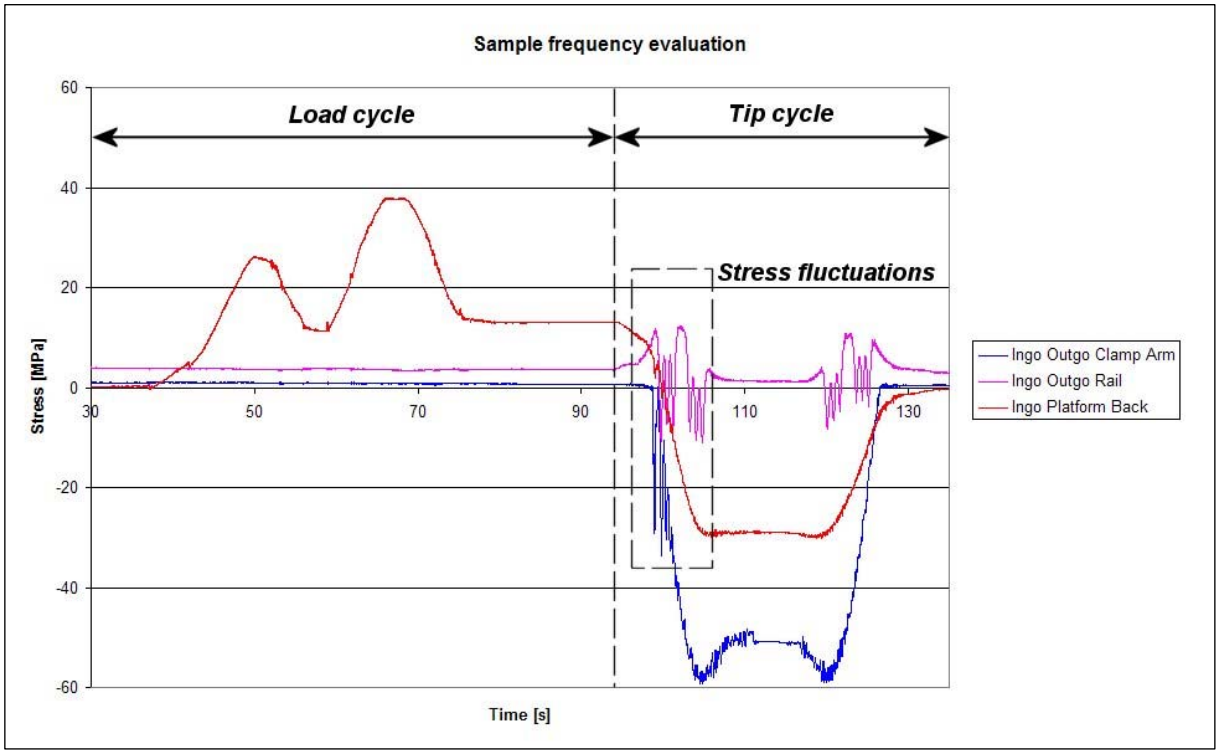

Figure 3.12: Stress measurements for a complete load and tip cycle

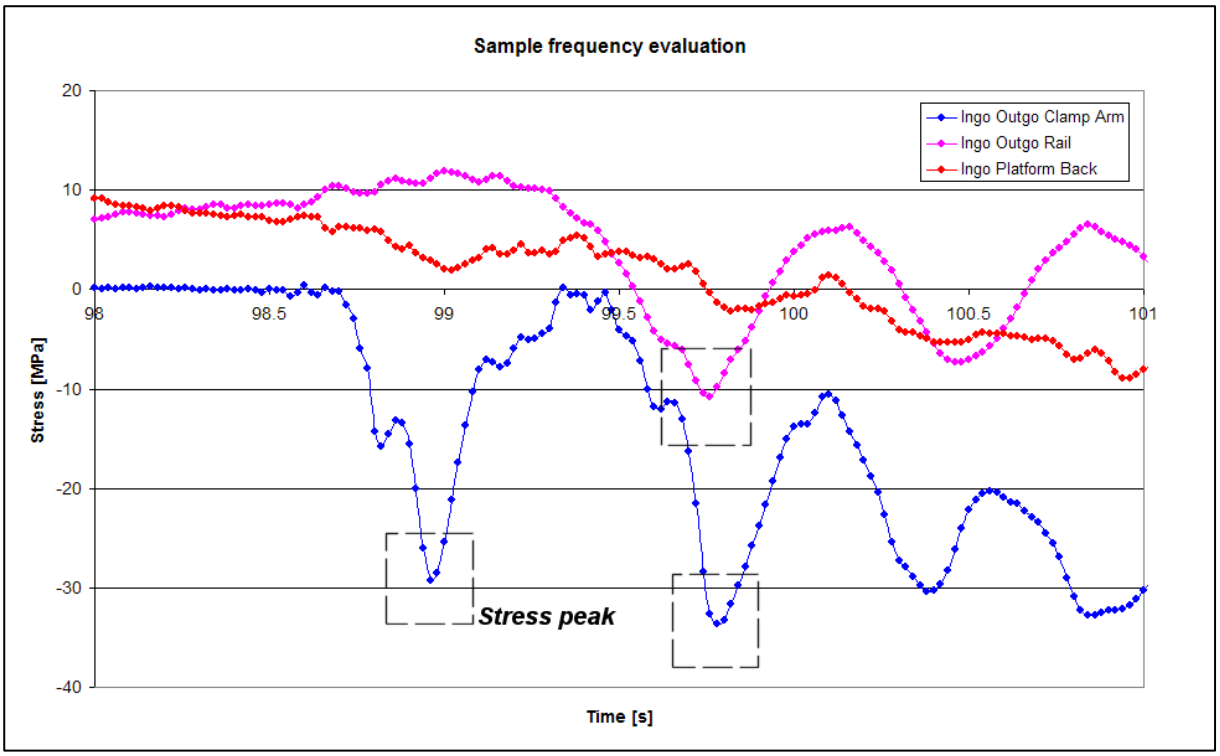

Figure 3.13: Close-up of demarcated stress data shown in Figure 3.12

3.4 Strain gauge measurement results

With the equipment installed and calibrated, the strain gauge outputs were again set to zero and a one-hour recording was made of the tipping process. The data obtained from the strain gauge measurements was processed and analysed for mean and maximum stress amplitudes and for any trends in the data during the tip process.

Note: Some of the data channels did not record during the process. This was, however, only discovered after the train cycle was completed. Because of operational limitations the recordings could not be repeated for another train. Enough data was, however obtained to complete the investigation.

As cracks previously occurred on the platform beam, the data from the strain gauges, installed on the beam and shown in Figure 3.14, was analysed in detail to identify any high-stress occurrences that would influence the fatigue life of the structure. The data clearly highlights a drift in the mean stress of the structure between 500 sec and 2 200 sec and high-stress peaks at approximately 1 400 sec, 1 600 sec, and 2 050 sec.

A detailed explanation of the measured data is shown in Figure 3.14. Each event discussed below is highlighted in the figure by the event number:

a) At 0 sec (sec), the strain gauge outputs were set to zero and the recording started for the duration of one hour. Data for the first 25 tip cycles was extracted from the measured data.

b) At approximately 110 sec, the locomotive passes over the platform after it positioned the wagons in front of the muscle arm of the train positioner. A stress of approximately 26 MPa was measured on the platform while the locomotive passed over the strain gauges. This corresponds well with the measurement for a similar event obtained during the set-up process. Note the slight separation between the two readings after the locomotive passed over the platform. This separation is due to unequal bending in the cage, caused by the single constraint against rotation at the pinion gear on ingo side end ring. The structure deforms and does not return to the original position due to internal stresses and friction between the structural components.

c) At approximately 360 sec the muscle arm positions the first wagons in the Tippler cages. The stress increase on the platform is approximately 14 MPa which corresponds with the value calculated earlier.

d) At 530 sec, the first two wagons are tipped. Directly after the tip cycle the separation between the two stress values is approximately 17.5 MPa as shown in Figure 3.15. The offset is caused by the internal stress levels that changed during the single tip cycle, i.e. while the cage rotated the end rings repositioned themselves on the support rollers, changing the boundary conditions and with it the internal structural stress values. This internal stress change would occur with every tip cycle, caused by the ever-changing boundary conditions. The stress levels would, however, all fall within a certain envelope, confined by two extreme boundary conditions.

e) At 580 sec the first continuous tip cycle is started and the second pair of wagons is loaded and tipped. The measurements for this cycle are also shown in Figure 4.15. From the data the total load and tip cycle duration was confirmed as approximately 110 sec with the tip cycle duration, i.e. when the cage rotates, calculated at approximately 40 sec.

f) At approximately 1 950 sec, the drift in the mean stress fades away and the mean stress remains constant for the remainder of the recorded tip cycles.

g) At approximately 2 150 sec, there is a short break in the tip process. The process, however, restarts approximately 200 sec later. The cause of this delay is not known.

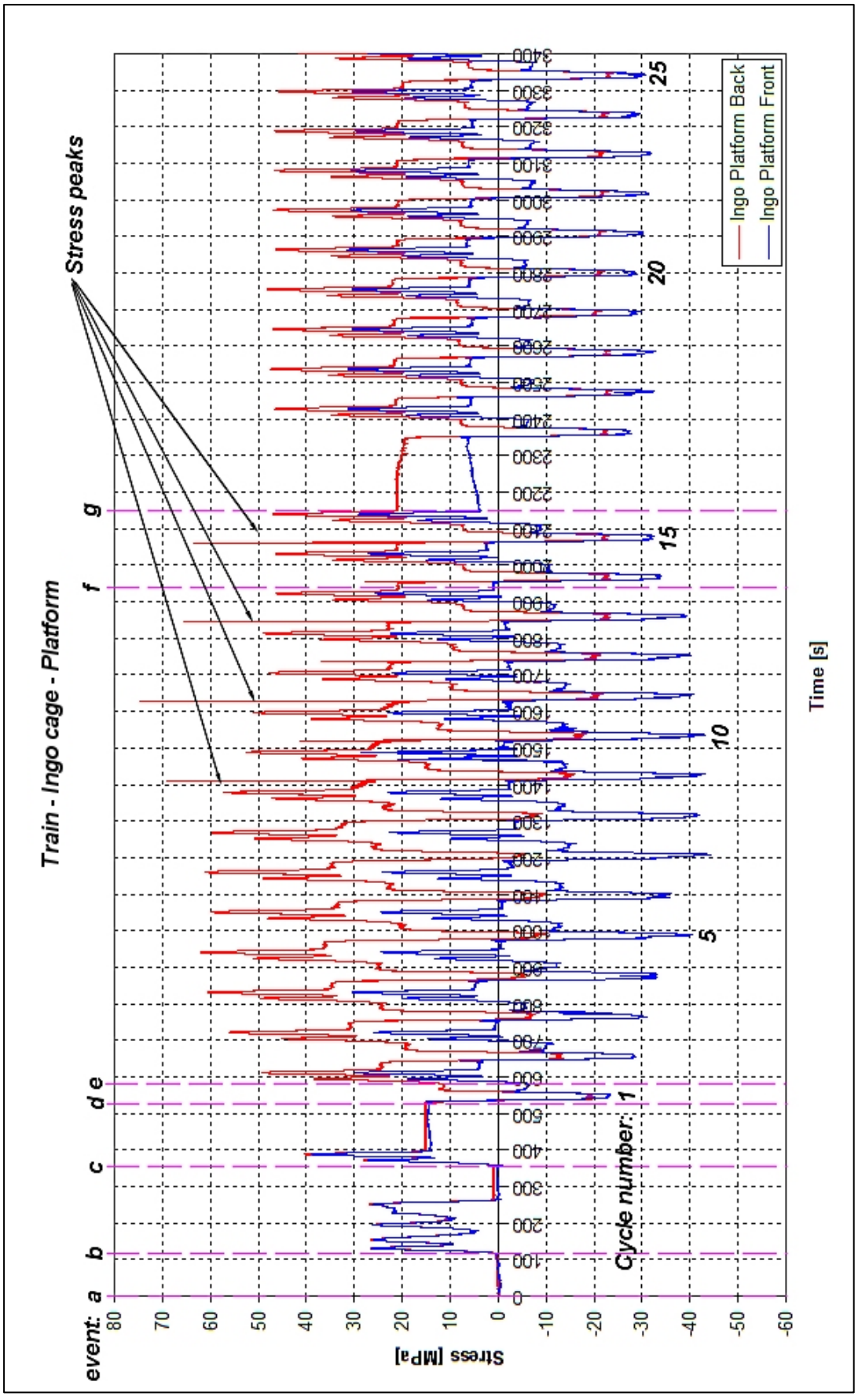

Figure 3.14: Platform stresses for first 25 tip cycles

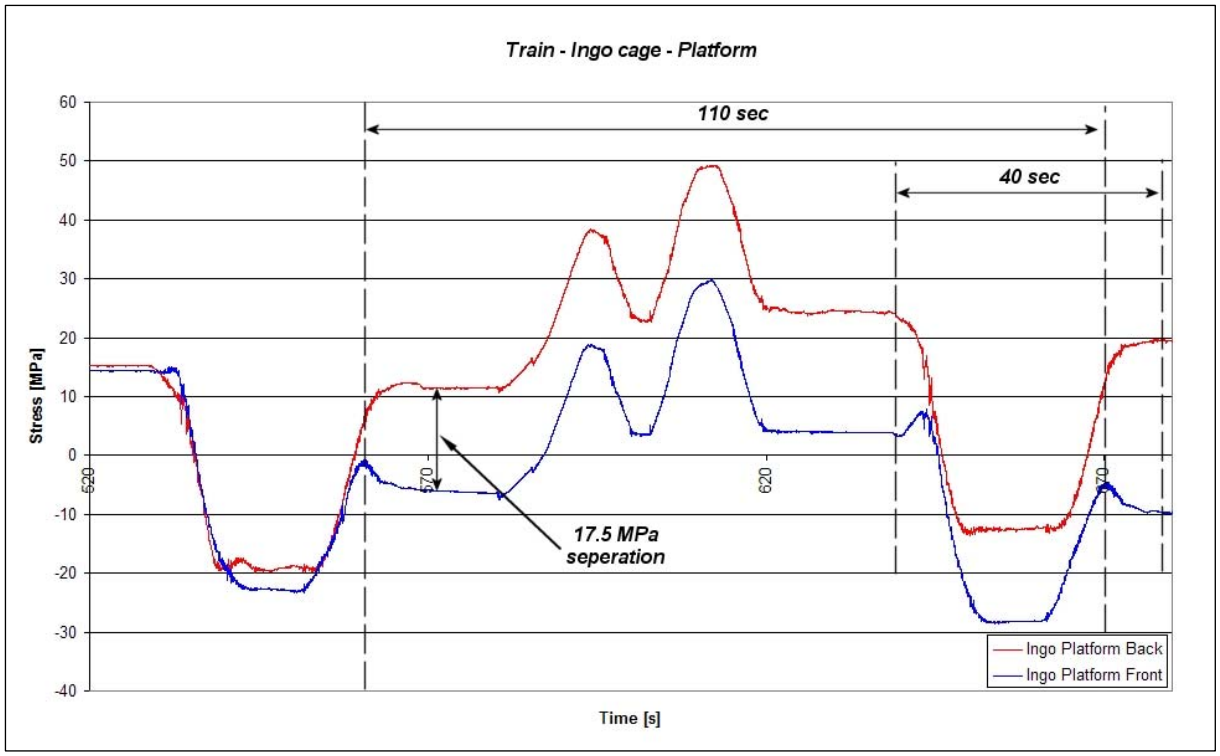

Figure 3.15: Measured stress on ingo platform for first two tip cycles

The main occurrences to be highlighted from the above data are:

a. A variation in the measured platform stress during consecutive tip cycles.
b. The occurrence of high stress peaks at the beginning of some of the tip cycles.
c. A drift in the mean stress that was present during the first 13 tip cycles but evened out during the last tip cycles measured.

To identify a possible cause for these occurrences the stress data obtained from all the strain gauges applied to the structure was analysed in more detail.

3.5 Strain gauge data evaluation

The stress data obtained from all the strain gauges was analysed for any possible trends, shocks, offsets or variations that could generate internal stresses in the structure contributing to the occurrences as listed in paragraph 3.4. For each occurrence possible causes were listed and the data analysed for any notions that could support the causes listed.

a) Variation in stress on platform during tip cycle

In order to compare the actual measured stress values for the front and rear strain gauges for the first loaded tip cycle, the offset caused by the internal stresses was removed by setting both readings to zero at a set interval before the load cycle starts. Figure 3.16 shows a stress comparison between the two stress measurements. The data indicates that during the loading cycle the stress values on the front and rear of the platform stay close together, however, during the tip cycle a definite stress develops between the stress readings obtained from the front and rear strain gauges. This supports the data obtained previously (paragraph 3.3 d). To obtain an estimation of the stress variation envelope, the stress values for the 5^{th}, 10^{th}, 15^{th}, 20^{th} and $25^{th\ tip}$ cycles were plotted on one graph as shown in Figure 3.17. For each cycle, the data was offset to a zero point to highlight the stress distribution at the end of the tip cycle.

The result shown in Figure 3.17 indicates a stress variation between the tip cycles of approximately 12.6 to 12.8 MPa. Further note that during the 15^{th} tip cycle a vibration is visible in the front strain gauge reading that is not visible in any of the other data sets. A further observation is the slight ramp-up speed variation between different tip cycles. This is visible in the spread of data at approximately 15 sec. The spread in the stress values during the loading cycle further highlights the structural bending caused by the single constraint at the pinion gear (paragraph 3.3 a).

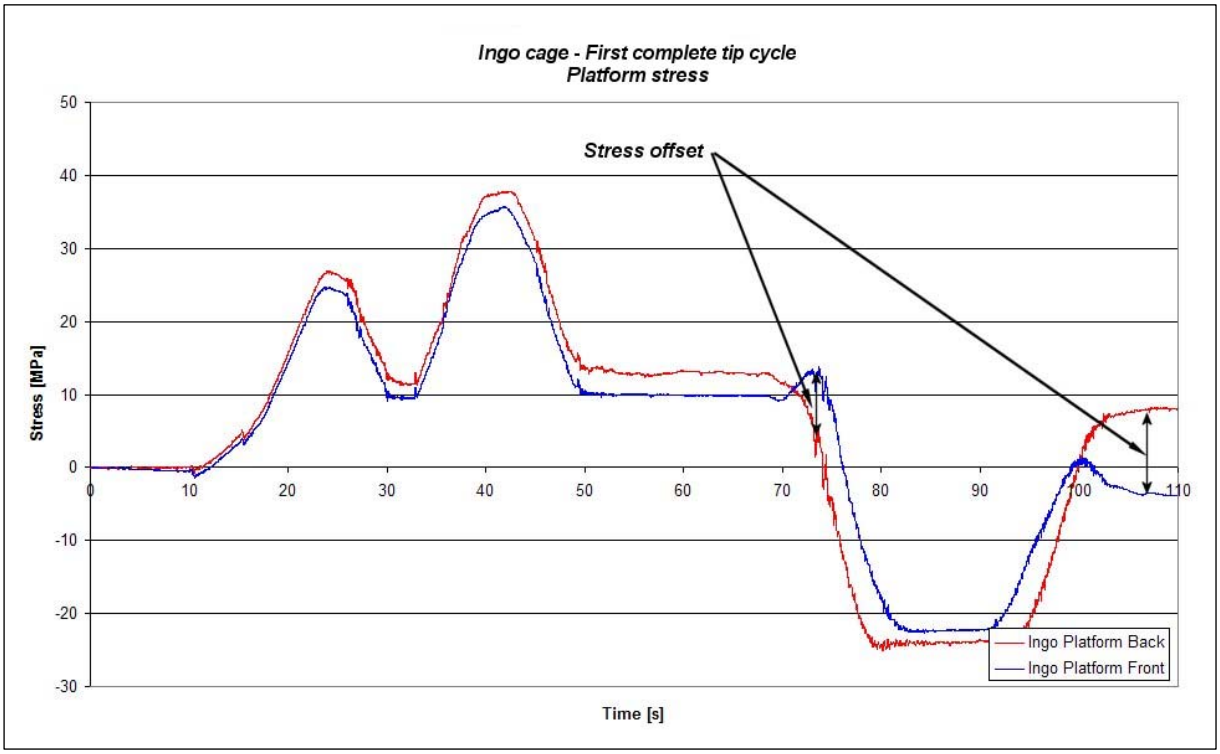

Figure 3.16: Measured stress for first loaded tip cycle – internal stress effects removed

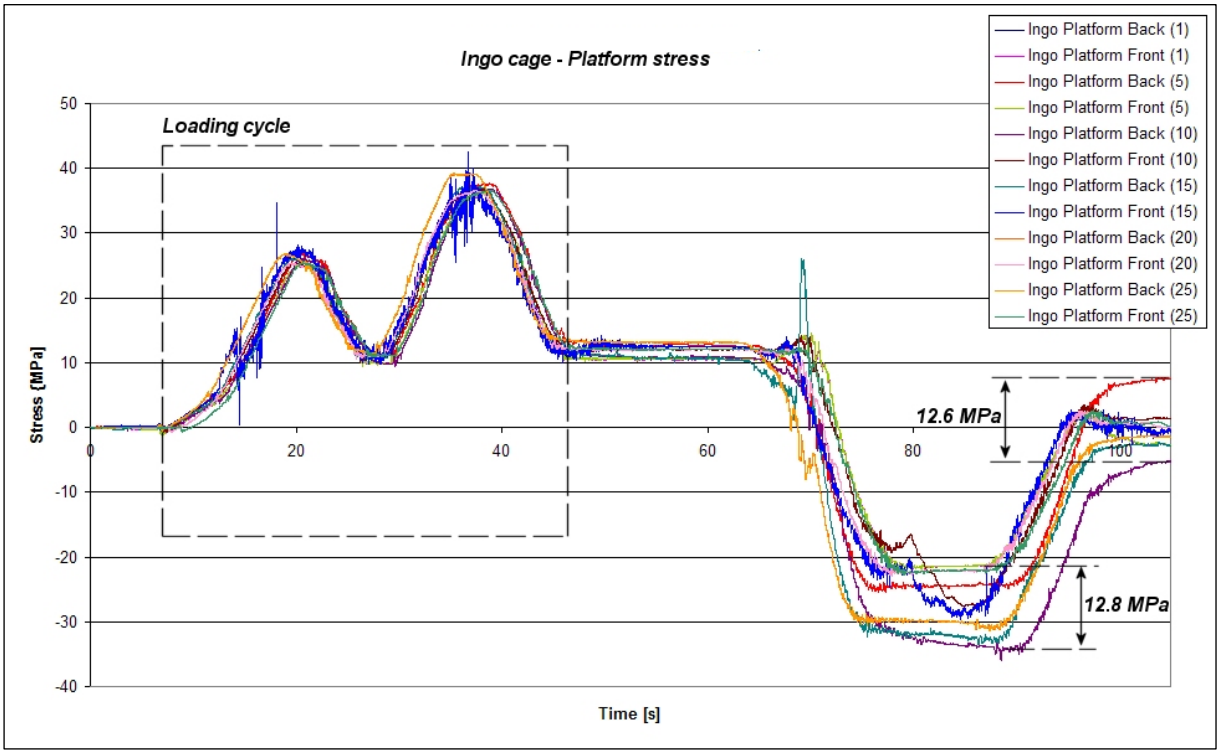

Figure 3.17: Stress variation envelope for different tip cycles

b) Stress peaks at beginning of tip cycle

At the beginning of the 8th, 11th, 13th and 15th tip cycles four high stress peaks, as shown in Figure 3.18, are visible in the back strain gauge readings. These peaks occur approximately 71 sec into the complete tip cycle or 7 sec after the Tippler started to rotate.

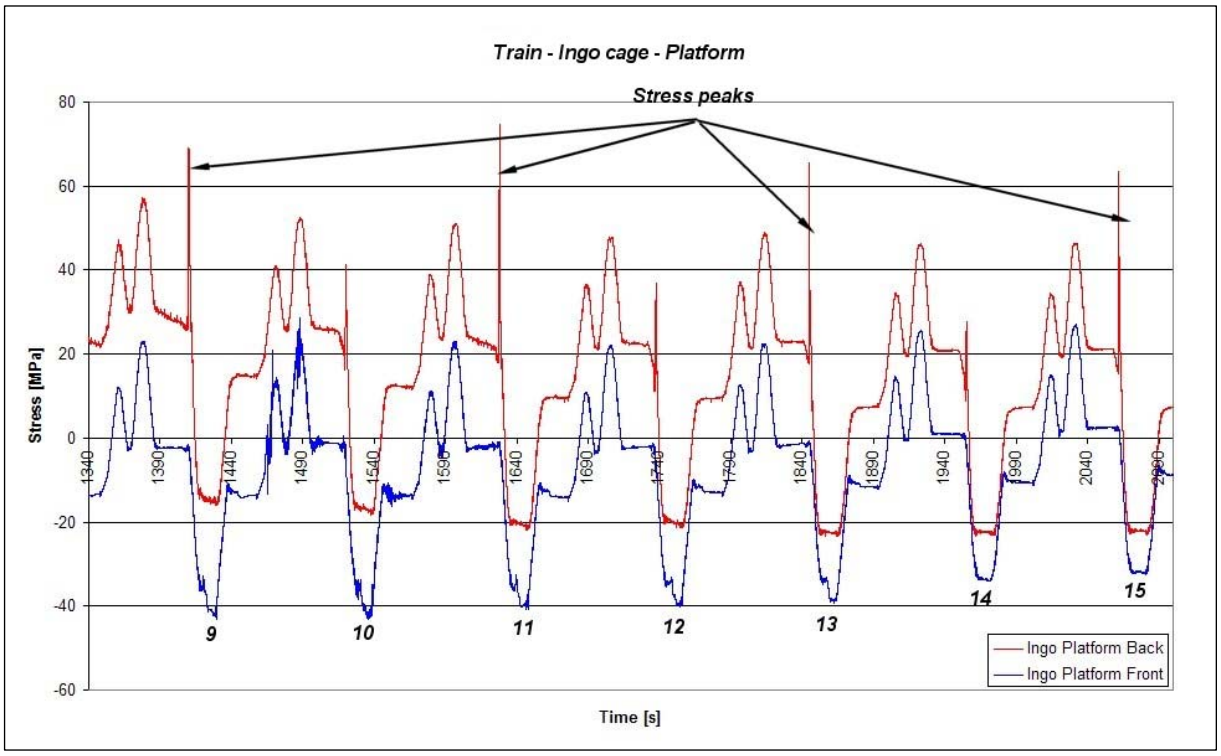

Figure 3.18: High stress peaks at beginning of tip cycle

To identify a possible cause for the peaks the measured stress data for four tip cycles was compared on the same graph. Two data sets (tip cycle 1 and tip cycle 20) had no visible stress peaks present while for the other two data sets (tip cycle 11 and tip cycle 13) the stress peaks were present. The purpose of the comparison was to highlight any stress variations that occur during the tip cycles, that may exist between the “with-peak” and “without-peak” and similarly compare the two “with-peak” and “without-peak” data sets with each other. This comparison was done for all the measured positions for the tip cycles listed above. Figure 3.19 shows the stress readings obtained from the back strain gauge on the Tippler platform. The peaks occur at almost exactly the same time interval during the tip cycle. The slight offset between the data sets is caused by the different ramp-up speeds for the two tip cycles. For the two “without-peak” data sets, a small vibration is visible in the data during the first part of the tip cycle. Furthermore, the spread between the two stress values is larger for the “without-peak” data pair than for the “with-peak” stress values.

The minimum stress value measured when the Tippler is in the upside down position is lower for the data sets where the stress peak occurred than that of the data where no stress peak is present. This may be an indication of some internal stress relieve that takes place, generating the stress peak as seen.

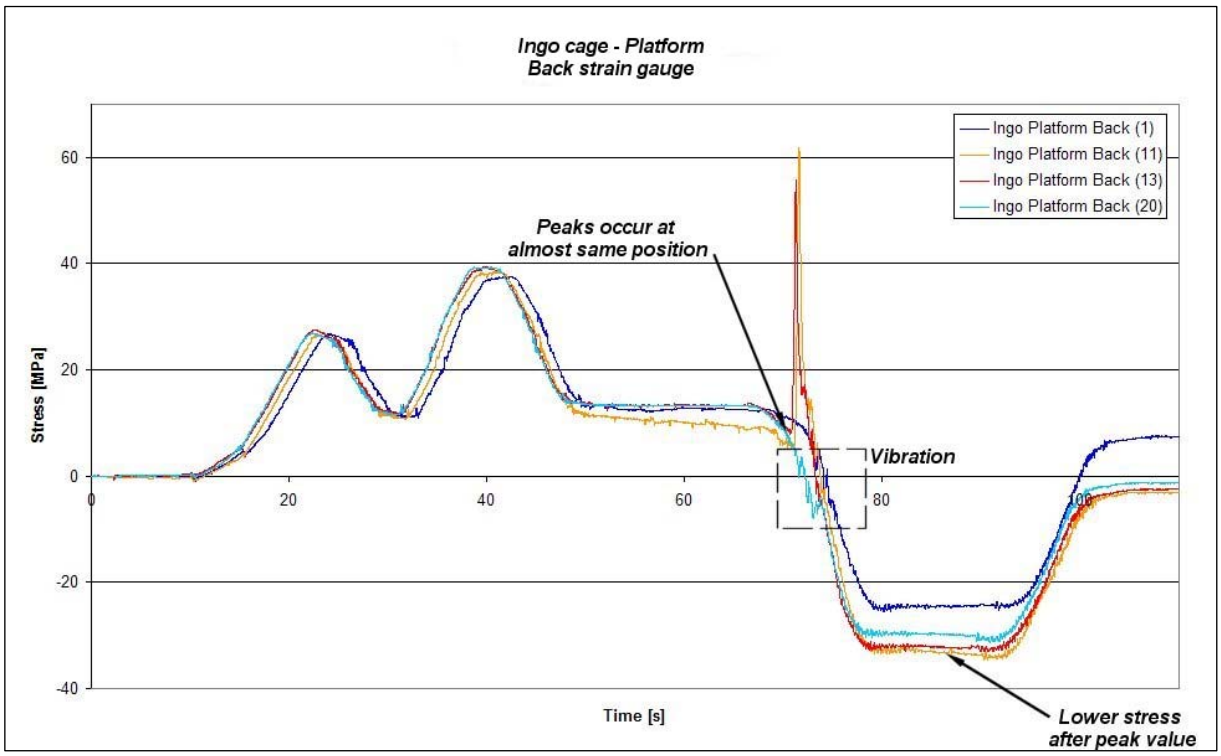

Figure 3.19: Stress data comparison for back strain gauge on platform structure

Figure 3.20 shows the “with-peak” and “without-peak” data for the strain gauge applied to the front of the platform structure. A definite stress difference exists between the two pairs of data when the Tippler is in the upside-down position. The small stress increase at the beginning of the tip cycle is present only in the data of the first tip cycle, but does occur in some of the other stress data not included in this comparison. Note that the stress values for the “with-peak” and “without-peak” data pairs stay closely paired together throughout the tip cycle. The variance between the data pairs is also less that the variance visible in the back strain gauge data (Figure 3.19).

Figure 3.21 shows the stress data obtained from the strain gauge applied to the cross beam of the ingo cage. No visible stress differences exist between the two data pairs. A vibration is, however, visible in all the data sets when the clamps are applied, the Tippler starts with the return cycle and the clamps released from the wagon. These vibrations are caused by the operation of the clamp gear attached to the cross beam.

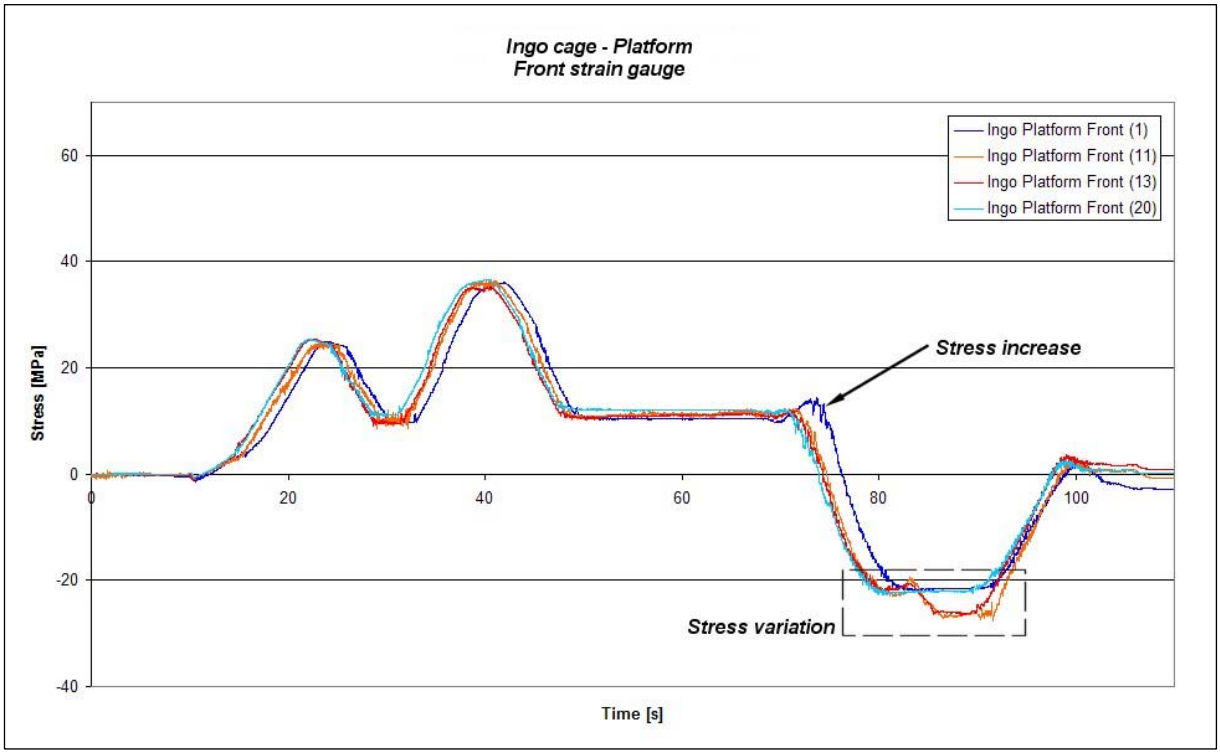

Figure 3.20: Stress data comparison for front strain gauge on platform structure

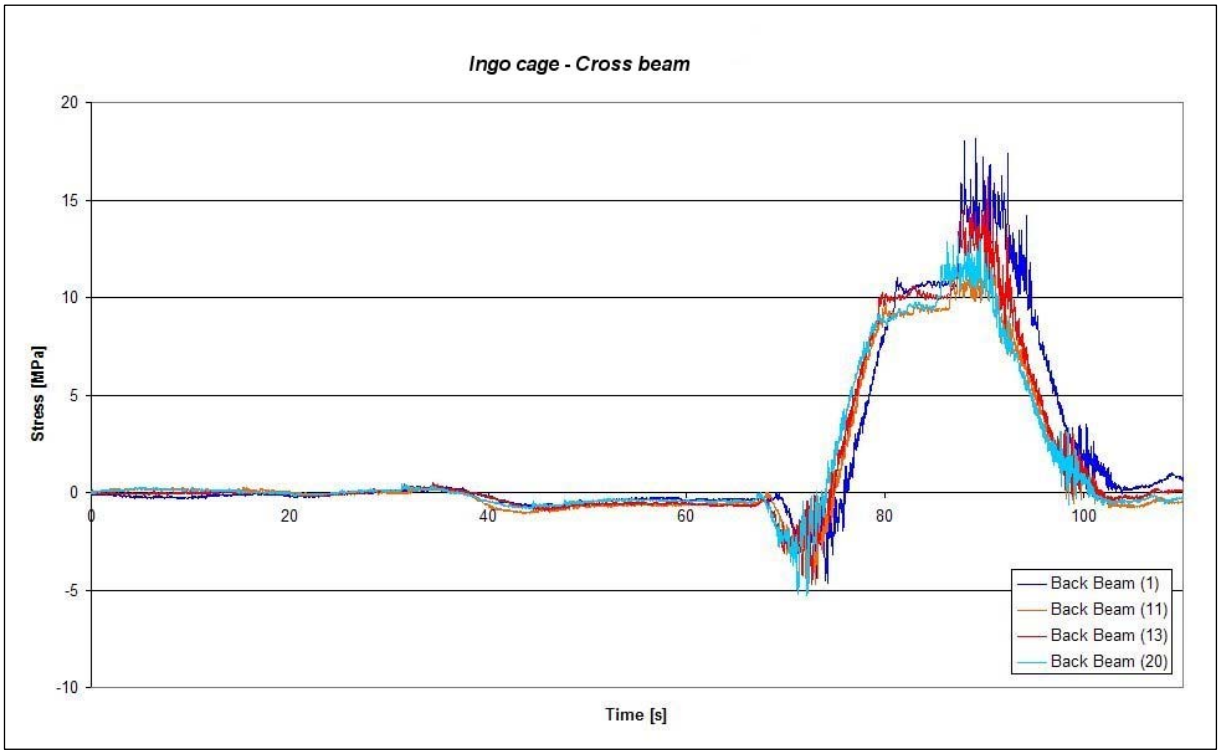

Figure 3.21: Stress data comparison for strain gauge on cross beam

Figure 3.22 shows the stress comparison for the strain gauge mounted on the clamp arm of the ingo cage outgo side. No visible stress difference can be seen between the data pairs. Note the stress vibration at the beginning of the clamp cycle caused by the clamp arm's contact with the wagon's edge. The same data could not be obtained for the ingo side clamp arm as the amplifier only recorded noise after the 9th tip cycle. It was later determined that the strain gauge cable was damaged by falling coal during the tip cycle.

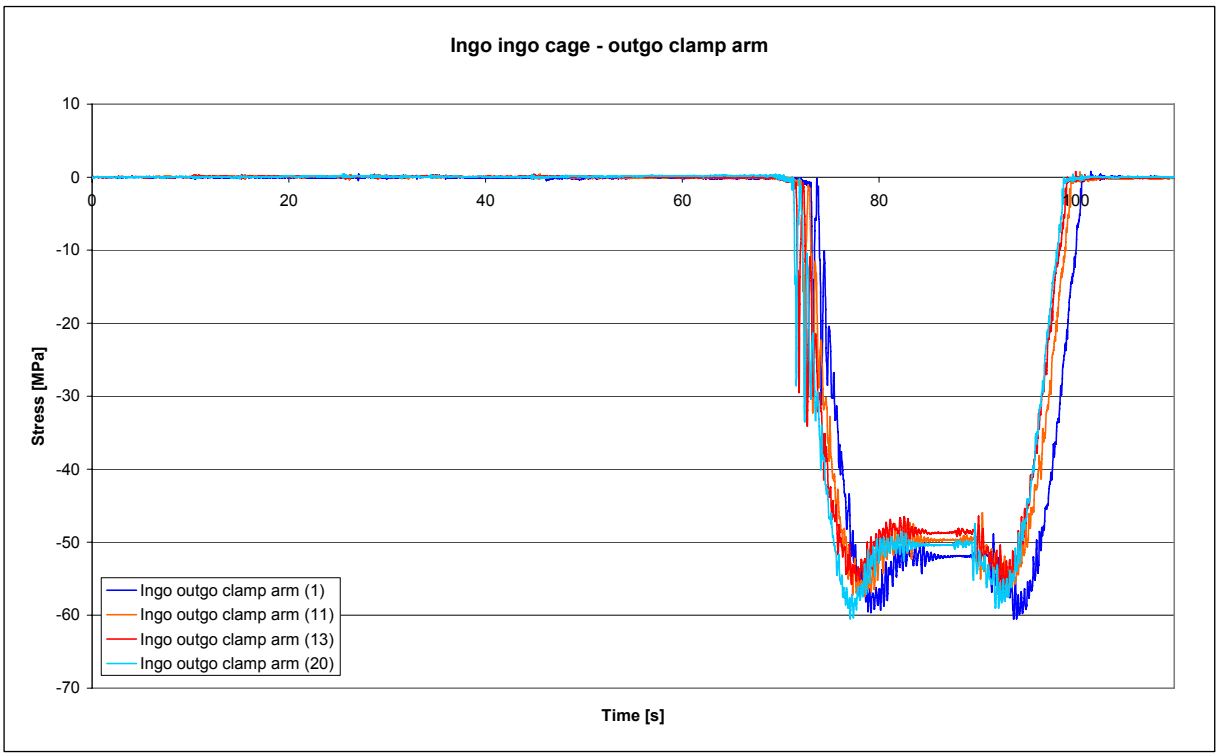

Figure 3.22: Stress data comparison for strain gauge on outgo side clamp arm

Figures 3.23 and 3.24 show the stress comparisons for the strain gauges mounted on the ingo side back support roller assembly, i.e. one strain gauge on each side of the support roller assembly. No indication of any occurrence that could lead to the stress peaks was found in these data sets. The data, however, shows the presence of a large vibration during the tip cycle. These vibrations are, however, only present when the Tippler rotates. The cause of these vibrations can be relayed to the condition of the rails mounted on the two end rings. Figure 3.25 shows a photo taken of the outgo rail of the ingo cage. The unevenness of the rail caused by wear, combined with the absence of any damping between the support rollers and the rail and the stiffness of the support roller structure, all contribute to these vibrations. These vibrations are not visible in the rest of the strain gauge readings due to the structural damping that takes place in the massive cage structure.

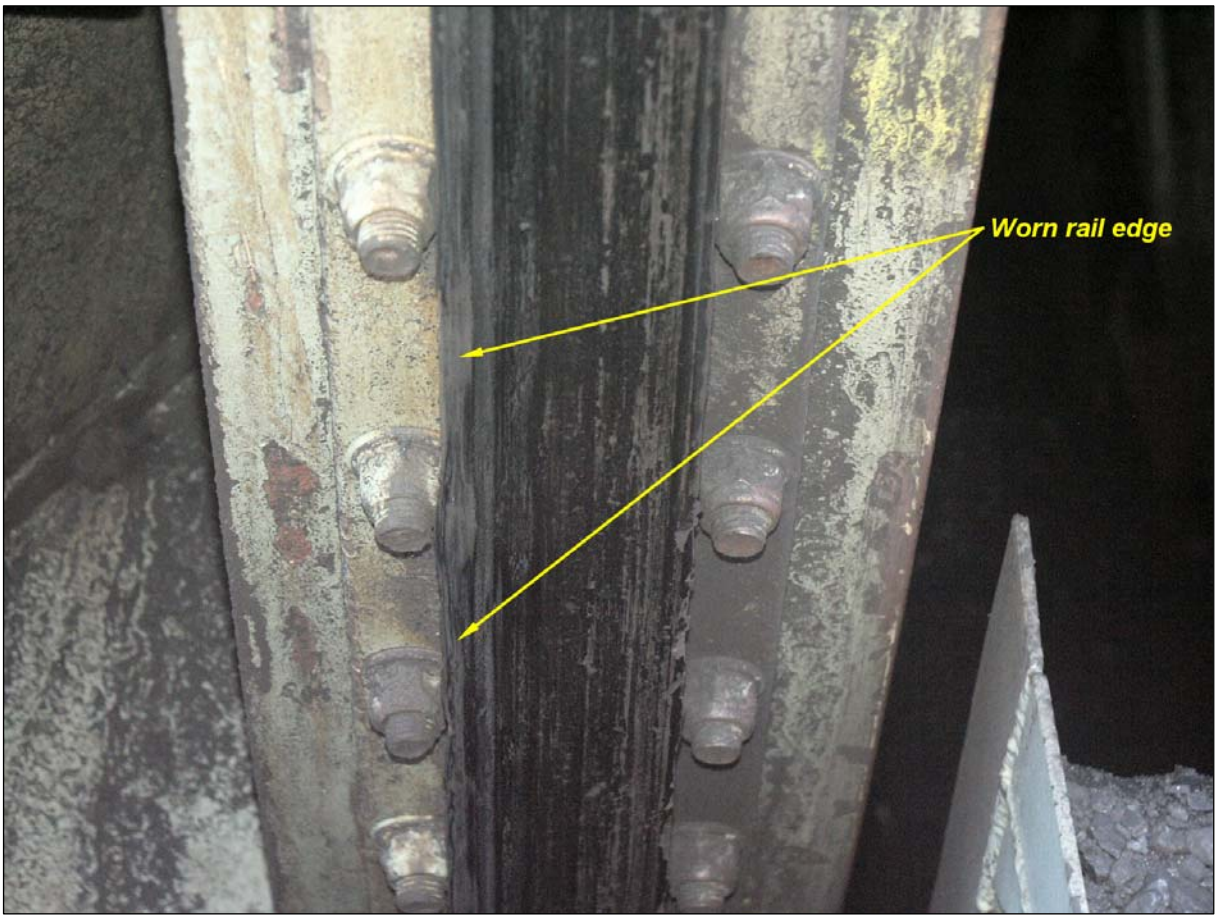

Figure 3.25: Wear on the outgo rail of ingo cage

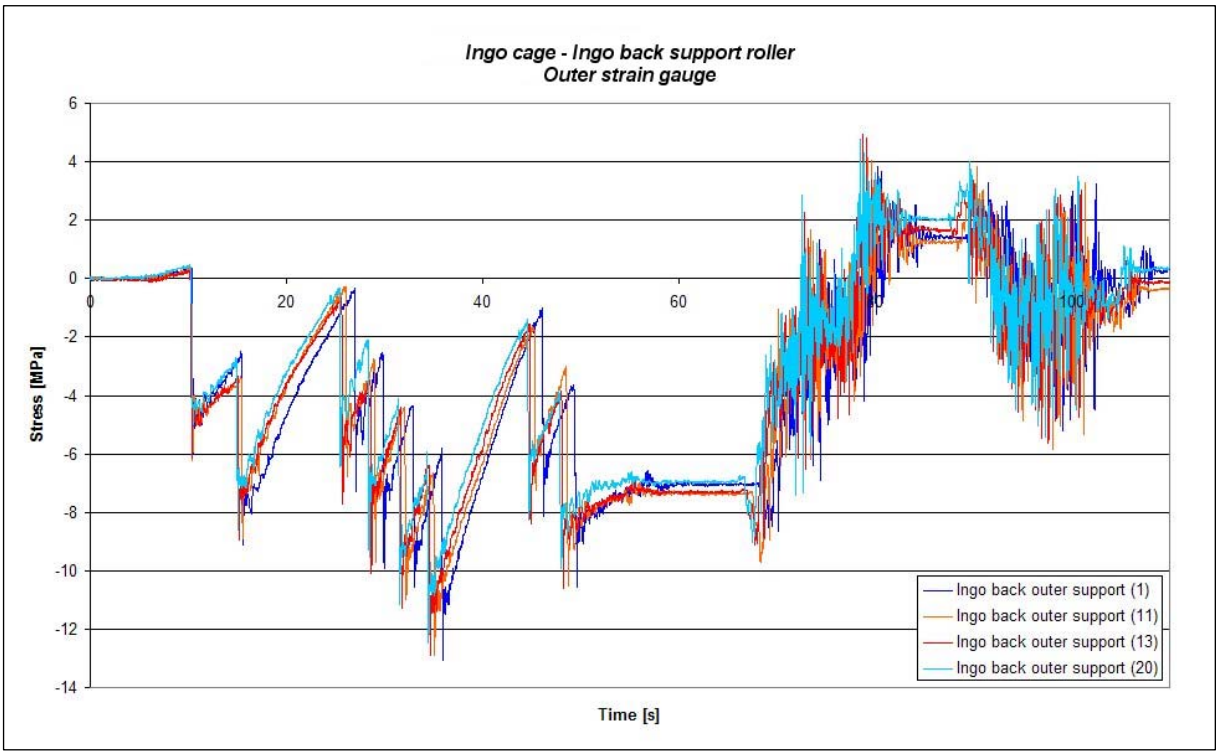

Figure 3.26: Stress comparison for inner strain gauge data on ingo side back support roller assembly

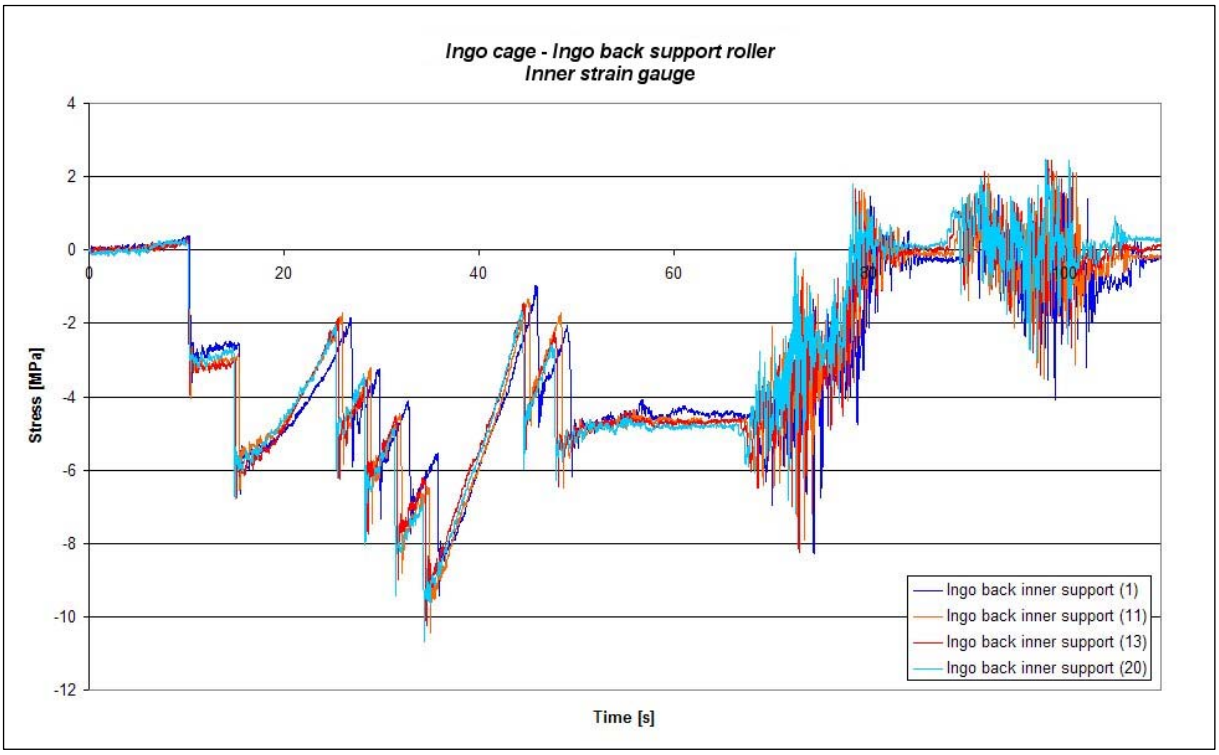

Figure 3.27: Stress comparison for outer strain gauge data on ingo side back support roller assembly

c) Drift in the mean stress that occurred at the beginning of the train offload cycle

The variation in the mean stress visible during the first 13 tip cycles (Figure 3.14), can only be caused by forces generated within the structure while the cage is rotating. A first indication of such forces is the variance in the stresses measured on the platform structure at the end of each tip cycle (Figure 3.17). As discussed, these forces are generated by changes in the cage's boundary conditions due to possible crabbing forces or the presence of external forces acting on the cage. Crabbing describes the sideways movement that would be experienced by the cage if the four roller support assemblies were not aligned. This misalignment between the roller assemblies would have the same effect on the cage as would be experienced by a vehicle with misaligned wheels. The side force generated by this misalignment would bend the support roller assemblies and generate internal stresses in the structure. The internal stress level in the cage after each tip cycle would be dependent on the amount of sideslip that occurred between the rail and the rollers for the given tip cycle. More slip would translate to less internal stress and vice versa. This slip on the rail would further contribute to the wear on the rail as shown in Figure 3.25.

To quantify the bending that occurs in the support roller assemblies the stress values obtained from the inside and outside of the primary compensating beam were plotted on one graph as shown in Figure 3.28. Data could not be obtained for all the strain gauges applied to all the support roller assemblies, but the data available did provide a clear indication of the side forces involved.

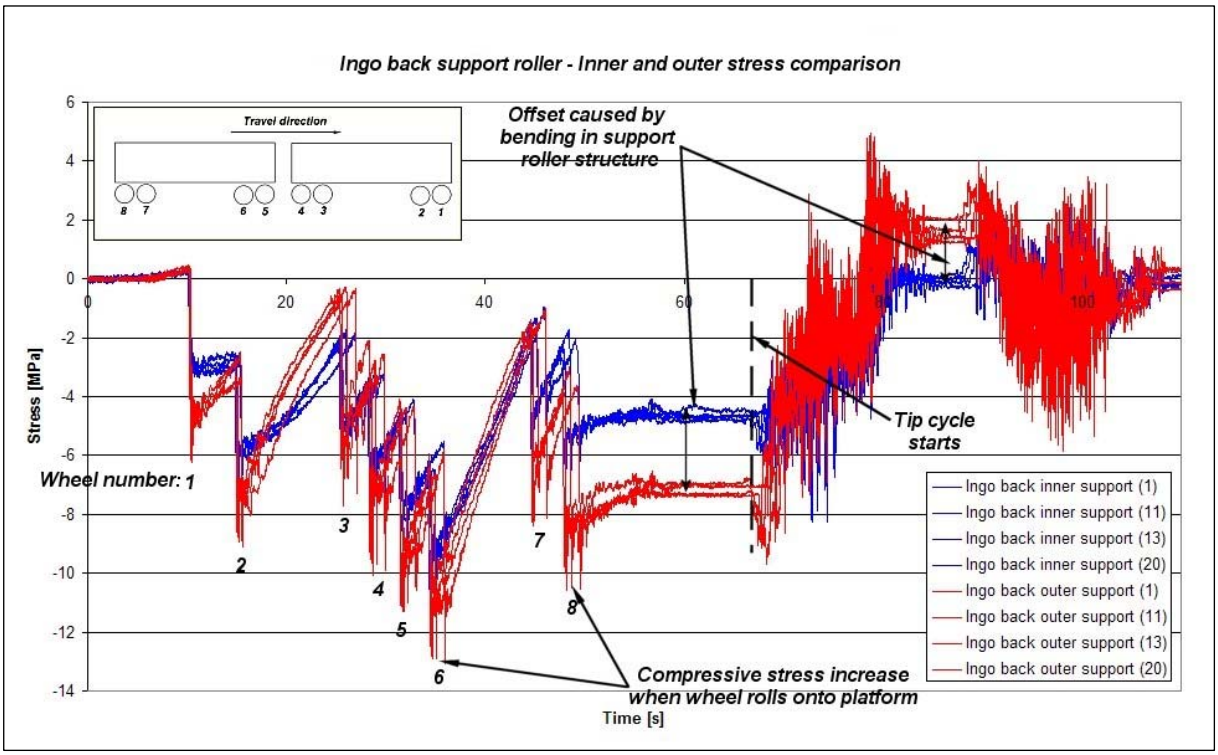

Figure 3.28: Inner and outer stress comparison for ingo back support roller

By comparing the two data sets, an outward bending of the primary compensating beam was identified. The first indication of structural bending is when the first wheel-pair passes onto the platform at approximately 10 sec. The separation in the stress values visible when the first wheel passes onto the platform indicates that bending takes place. The fact that the outer strain gauge stress reading is more negative than the stress reading obtained from the inner strain gauge, indicates that the bending is in an outwards direction i.e., the outer strain gauge is compressed more than the average stress while the tension caused by the bending “reduces” the stress measured by the inner strain gauge. This phenomenon is repeated each time the next wagon wheel-pair passes onto the Tippler platform and is repeated in all four tip cycles.

When the wheel-pair rolls further onto the platform the direction of bending changes, reducing the offset between the stress values. At the end of the loading cycle a resultant force exists that pulls the support roller assembly in an outward direction. Immediately after the tip cycle starts and the cage begins to rotate, the resultant force changes direction, swapping the two stress readings around. The magnitude of this force is, however, less as indicated by the small separation between the readings. When the Tippler is in the upside-down position the roller support assembly is bent in the opposite direction, i.e. inwards.

The vibration obscures the real trends in the data, but at the end of the tip cycle the offset between the stress values for the two strain gauges is much less. The

reason for the reduced offset between the stress readings is twofold: the reduced weight of the wagon causes less bending of the platform and some slip has taken place between the rail and the flangeless roller on the outgo side support roller assemblies. The combination of these two effects would reduce the internal stress levels in the structure.

To further evaluate the existence of resultant internal forces working in on the structure, the outer strain gauge data of an ingo and outgo side support roller assemblies was compared for the four tip cycles under investigation. If the two support roller assemblies are pulled together both stress readings would become less, i.e. more positive or if pushed apart the stress readings would increase, i.e. become more negative. The measured data for the four tip cycles is shown in Figure 3.29.

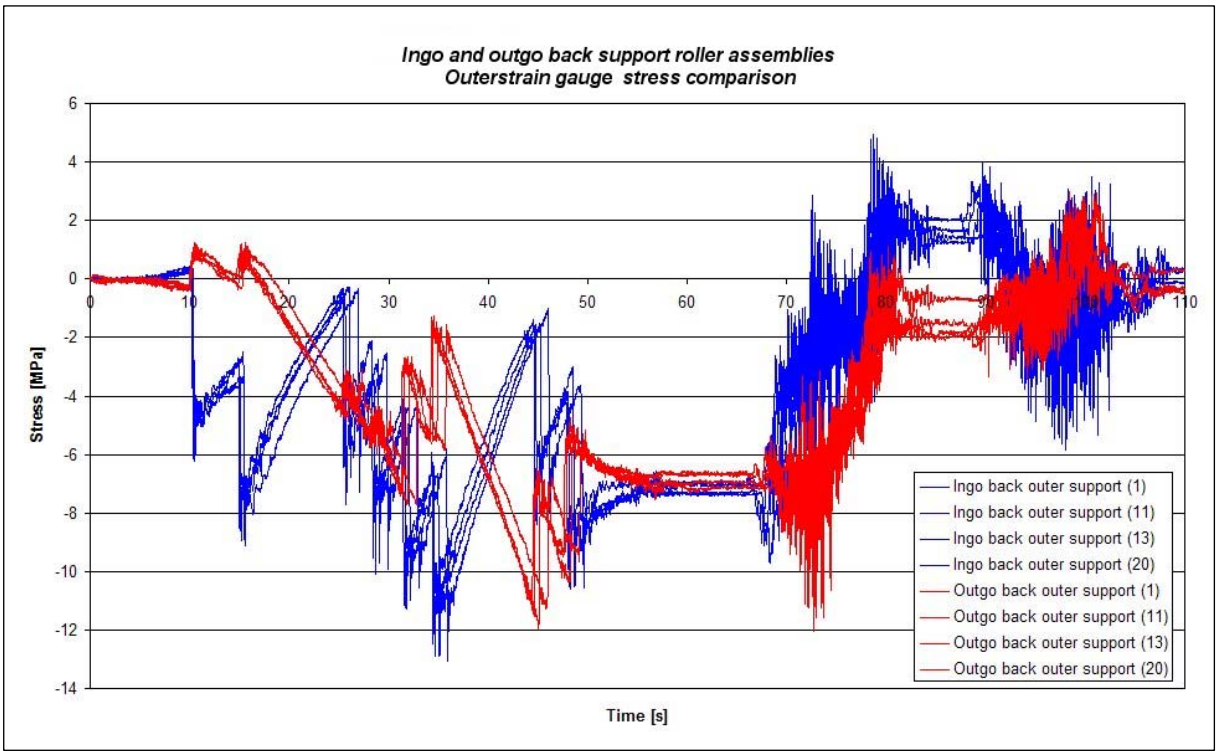

Figure 3.29: Stress data comparison for outside strain gauges on back support roller assemblies

The data indicates that both support roller assemblies are pulled towards the ingo side of the Tippler when the first wagon passes onto the platform. The stress measured by the outside strain gauge on the ingo support assembly becomes more compressive indicating bending towards the outside. This is supported by the data in Figure 3.28 that indicates the outward bending. The stress measured on the outside strain gauge of the outgo side support assembly becomes positive indicating a tension stress, confirming that the support roller is bending over towards the ingo side of the Tippler. However, when both wagons are in position

the stresses measured at both strain gauges are almost equal, indicating force equilibrium between the support roller assemblies.

Once the tip cycle starts, a separation is again visible between the stress readings of the two support rollers. This confirms the presence of a resultant side force that pulls the cage towards the outgo side of the Tippler assembly, as the ingo side strain gauge goes into tension and the outgo side strain gauge goes more into compression. This is supported by the data in Figure 3.28 that indicates that the support roller assembly bends toward the outgo side of the Tippler. Once the tip cycle is completed, the stress readings in both strain gauges are again almost equal, indicating a reduced resultant force on the support structures.

The last stress data comparison for the support roller assemblies is for the ingo side support roller assemblies of the outgo cage. Data was obtained for both the inside and outside strain gauges of the front and back support roller assemblies and is shown in Figure 3.30. The stress values obtained from the inner strain gauges are indicated in blue and those obtained from the outside strain gauges are indicated in orange.

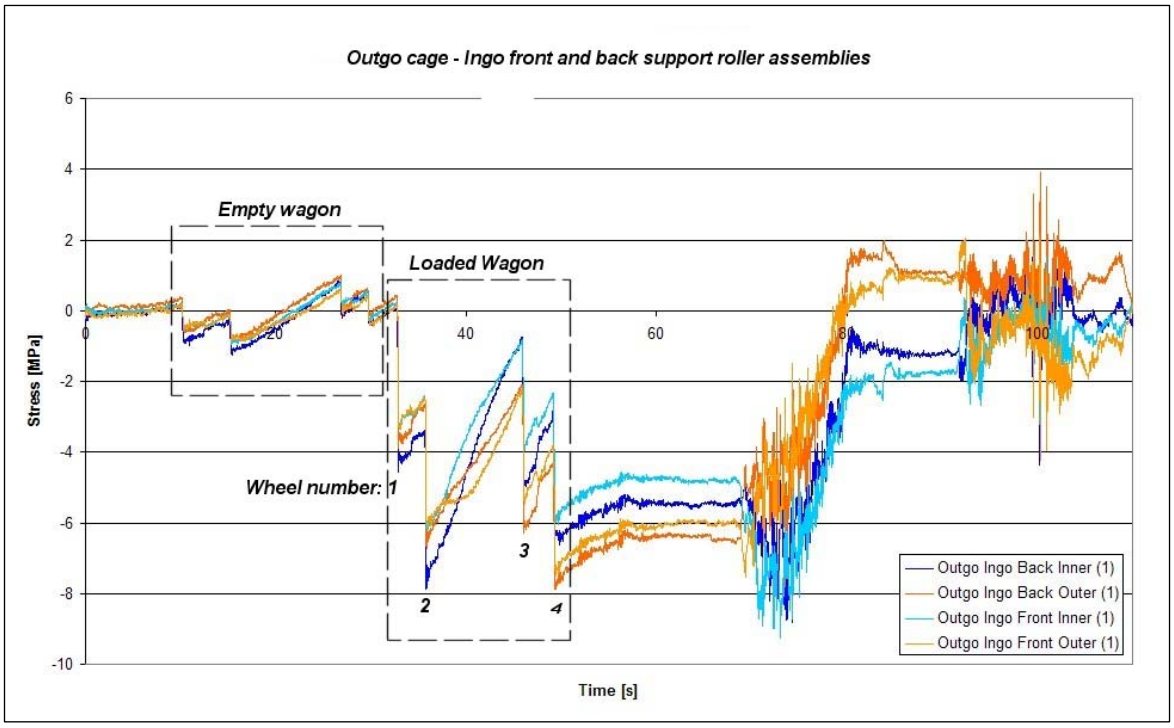

Figure 3.30: Stress data comparison for ingo support roller assemblies of outgo cage

The first part of the graph shows the stress values measured while the empty wagon is pushed from the ingo cage platform onto the platform of the outgo cage.

The stress offsets between the inside and outside strain gauge readings are smaller than that measured on the ingo cage ingo side support roller assembly as

shown in Figure 3.28. This difference in the readings is mainly due to the difference in construction of the two end rings supported by these assemblies. The ingo side end ring of the ingo cage is stiffer due to the box-like construction, while the ingo side end ring of the outgo side cage is less stiff, due to its web-plate construction. During the tip cycle the stress readings of the inside and outside strain gauges again swap as seen in Figure 3.28.

The last stress data set analysed was obtained from the strain gauge mounted on the outgo side end ring of the ingo cage as indicated in Figure 3.8. The twelve peaks shown in the Figure are generated when a roller pass over the strain gauge position. The data further indicates that the end ring is bent inwards during the first and last part of the tip cycle and outwards midway into the tip cycle when the cage is in the upside-down position. These readings confirm the bending seen on the support roller assemblies as seen in Figure 3.29. The data further suggests that "crabbing" takes place during the tip cycle.

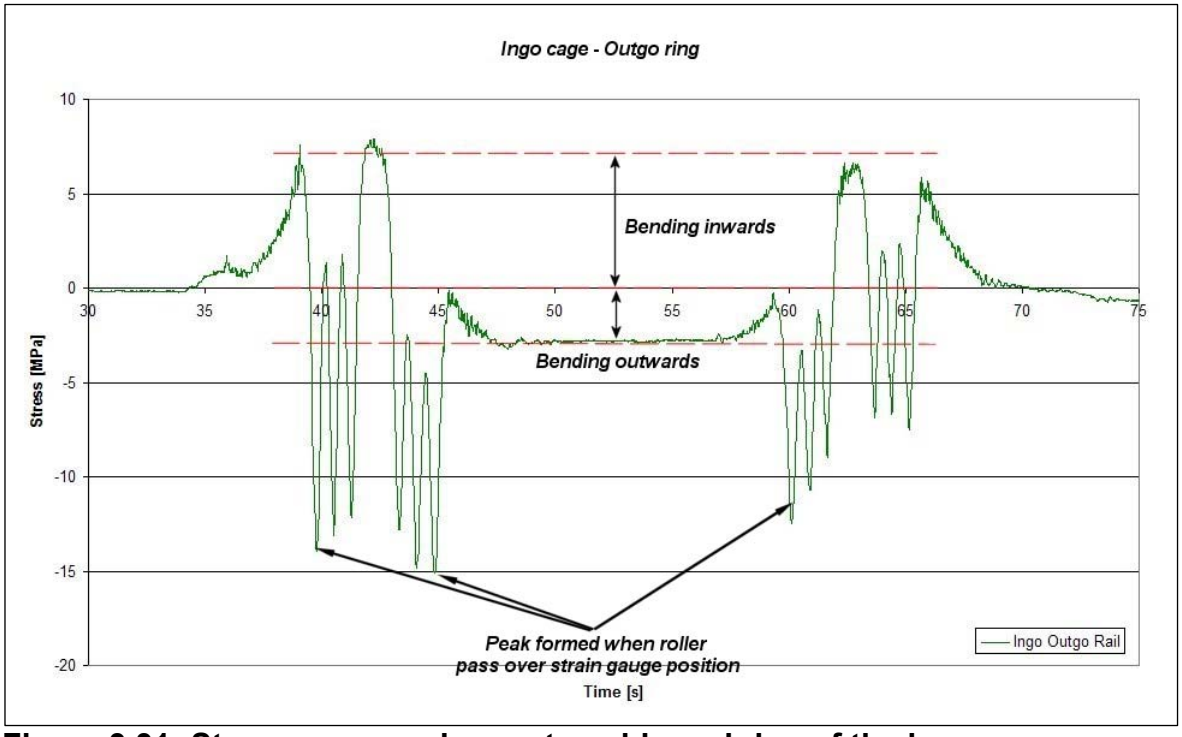

Figure 3.31: Stress measured on outgo side end ring of the ingo cage

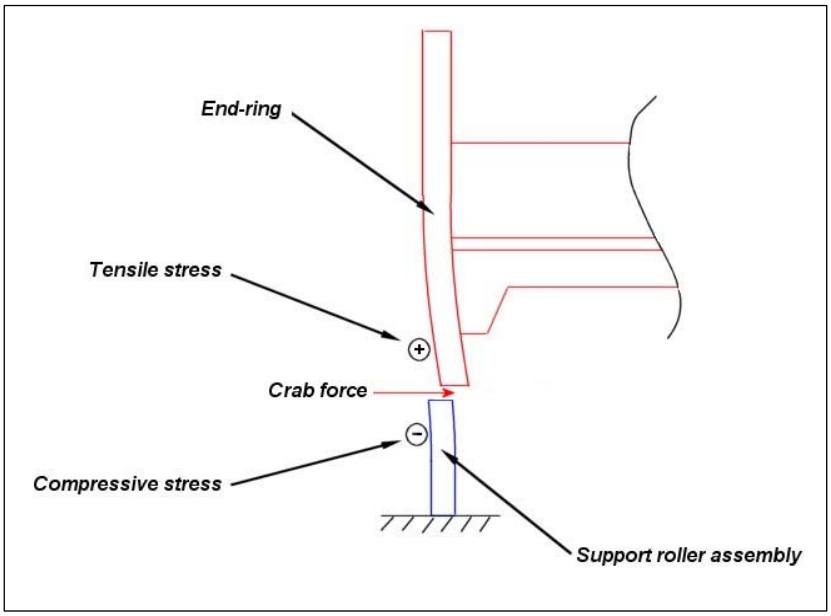

Figure 3.32: Bending in structure due to crab forces

3.6 Conclusion

The analysis of the stress data obtained from the strain gauges mounted to the platform structure of the ingo cage, highlights three occurrences that may have contributed to the formation of the cracks in the platform corners. These occurrences are as follows:

a) A random shift in the stress measured on the ingo cage platform during consecutive tip cycles as shown in Figure 3.17.
b) High stress peaks that occur at the beginning of some of the tip cycles as shown in Figures 3.14 and 3.18.
c) A drift in the average measured stress on the platform structure for the first 13 tip cycles as shown in Figure 3.14.

To find a possible explanation for these occurrences, the stress data obtained from the other strain gauges installed on the Tippler structure were examined in detail. Possible explanations for these occurrences was evaluated. The only explanation found from the data is the existence of continuously varying internal forces generated by crabbing and bending of the Tippler cage while rotating. The change in magnitude of these forces, caused by ever changing boundary conditions, generates the different stress levels in the structure as measured by the strain gauges. No clear effects indicating overload conditions could be identified from the results.

CHAPTER 4

FINITE ELEMENT ANALYSIS

The aim of the finite element analysis conducted was to obtain representative stress levels for the positions where the fatigue cracks developed on the Tippler structure. The stress concentration created by the structure's design would complicate strain gauge measurements, as the main stress direction is not known for the corner arrangement. For this reason, it was decided to create a finite element model of the structure and to verify the accuracy of the model by means of strain gauge measurements. Once the model has been verified, the stress levels at the corner positions and any other areas of interest would be available for further analysis. This chapter describes the process used and results obtained from the finite element analysis.

4.1 Finite element analysis process

The rotational operation of the Tippler complicates the construction of a mathematical or finite element model (FEM) that could describe the complete tipping cycle accurately. The strain gauge data obtained indicates continuously changing stress levels, i.e. the boundary conditions of the structure change with each rotational increment. To simulate these conditions accurately as necessitated for the fatigue life calculations the tip cycle would need to be divided into an infinitely large amount of increments and the model would need to be solved for each small increment. This would, however, require a large amount of solving capacity that would make an investigation of this type very expensive.

For these reasons, it was decided to break down the FEA into two steps. For the first step the tipping cycle was divided into only seventeen intervals and analysed for each interval by means of a linear static analysis. The stress data obtained from these analyses was compared to the stress data obtained from the strain gauge analysis to estimate the accuracy of the finite element model and the boundary conditions used. The mesh used in the first part of the analysis i.e. to verify the model accuracies, was coarser and therefore required less solving time. The mesh was, however, refined at the positions of interest to ensure that the stresses obtained from the FEA results at the strain gauge positions were accurate.

Once the models were verified the stress values at the positions where the cracks developed were recorded for al seventeen tip intervals. These stress values were plotted to identify the tip intervals where the highest stress levels occur, i.e. the most fatigue damage would be experienced.

For the second step, the models of the original structure was re-meshed with a finer mesh and the modified Tippler structure was meshed with a similar size mesh, in the positions simulating the tip positions where the most fatigue damage would be incurred at the crack positions. This was done to ensure the accuracy of the stress values obtained from the analysis. These models were re-solved for the same boundary conditions as applied previously. The results obtained from the second iteration analysis were used for the fatigue life calculations and comparison.

The linear static analysis method was used for the analysis on the tipper structure as this method is simpler, faster to complete, and the software used is readily available and less costly. For a linear analysis to hold true, the material properties, geometry and boundary conditions should be linear throughout the analysis. For the material properties, this means that the stress levels should be of such nature that no yielding takes place during the analysis. Furthermore, no geometric stiffening should take place during the analysis and the boundary conditions should not change from the original application to the final deformed shape. The loads applied should furthermore remain constant in magnitude, direction and distribution (Adams & Askenazi, 1999: 104).

The method used in which the Tippler's tip action is broken down into seventeen intervals and where each interval is dealt with as a linear static analysis with its own set of static boundary conditions therefore meets the criteria of a linear static analysis.

The complete finite element analysis process followed is indicated in Figure 4.1.

4.2 Finite element model preparation

The solid model as constructed from the drawings provided by RBCT was used as template to construct the finite element models for the ingo cage assembly. As previously mentioned, the similarity of the two cages only necessitated the detail analysis of one cage, in this case the ingo cage (paragraph 1.3). From the template, a surface or shell model of the main structural components was constructed. The primary compensating beam in the support roller assembly was constructed as a solid component to be able to obtain accurate comparative stress readings for the positions where the strain gauges were applied.

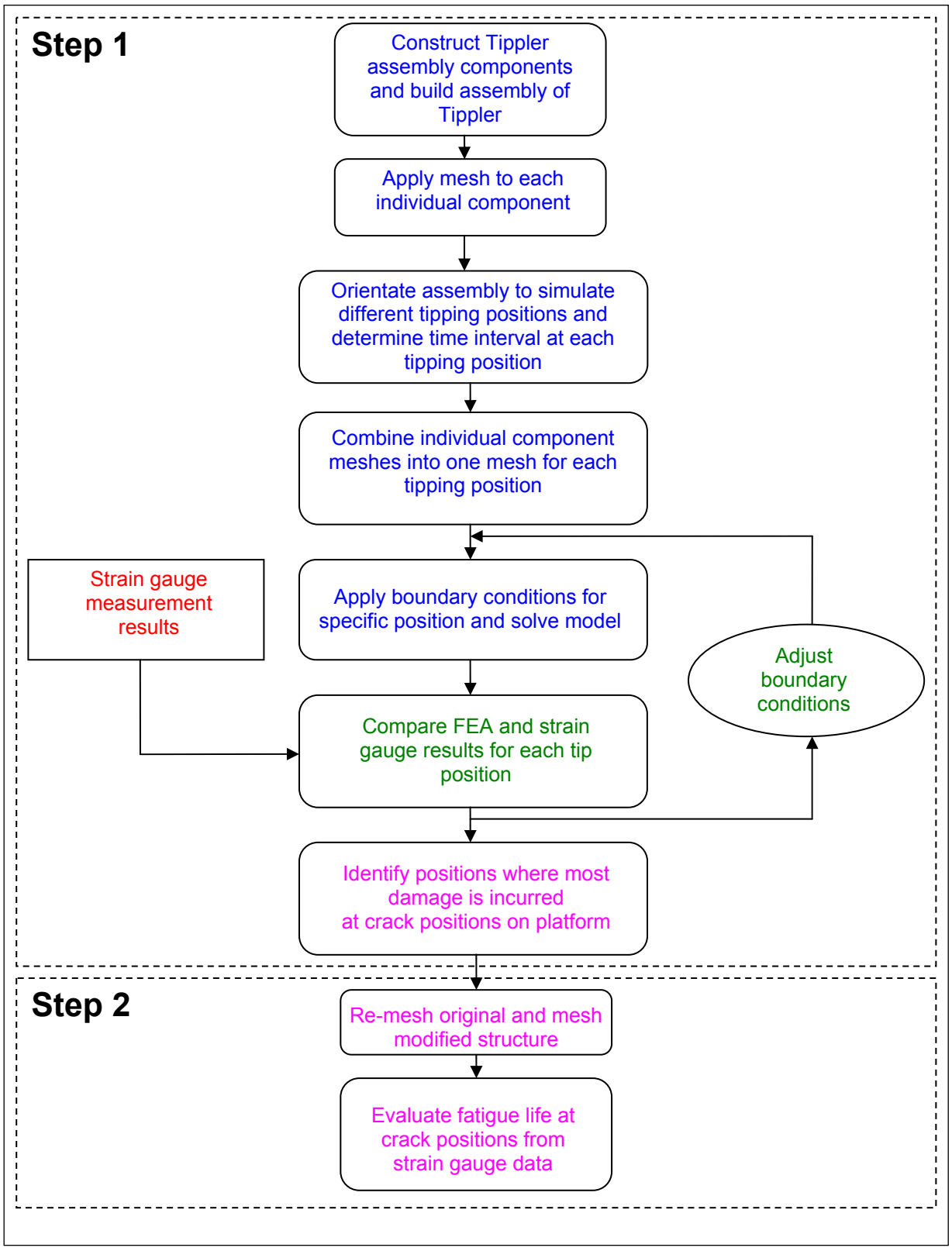

Figure 4.1: Analysis process used in investigation

The size and complexity of the model necessitated the following assumptions to reduce the complexity of the model constructed:

a) All welds used on the structure are full penetration and no weld defects exist in any of the welds.
b) Where two plates are bolted together, the bolt connection is viewed as preloaded with adequate friction between the plates to counter any relative movement. The two plates are therefore constructed as one plate with a thickness equal to the combined thickness of the two plates.
c) No misalignment exists between any of the Tippler components that could induce internal forces on the structure.
d) The support roller assemblies for each cage are perfectly aligned and the assemblies of the two cages are perfectly aligned.
e) All material thicknesses indicated on the drawings are correct and possible material thickness reduction caused by corrosion was ignored.
f) All rotational connections (pins and shafts) are frictionless.

The main advantage of building a model of the complete cage assembly lies in the accurate weight distribution and stiffness representation that the model provides. Each of these factors could influence the stress results obtained at the crack position during the rotation simulation. The difference in model stiffness created by simulating the bolted connections as a single plate of representing thickness would not influence the stress results as these connections are situated far from the area of interest.

The model of the ingo cage is shown in Figure 4.2. Note the different colours used on the model surfaces. Each colour represents the plate thickness used in the structural component. Where two plates are bolted together the plate thickness represents the combined thickness. Where possible all short surfaces, broken edges and scarred surfaces were removed from the models to reduce the possibility of generating badly shaped elements during the meshing process.

Figure 4.3 shows the solid model constructed of the primary compensating beam. The position where the strain gauges was applied is also indicated on the model. No weld detail was simulated in the model. Other components that was modeled as solids is the tie rods and the rollers. The tie rods were, however, replaced with beam elements in the second iteration analysis.

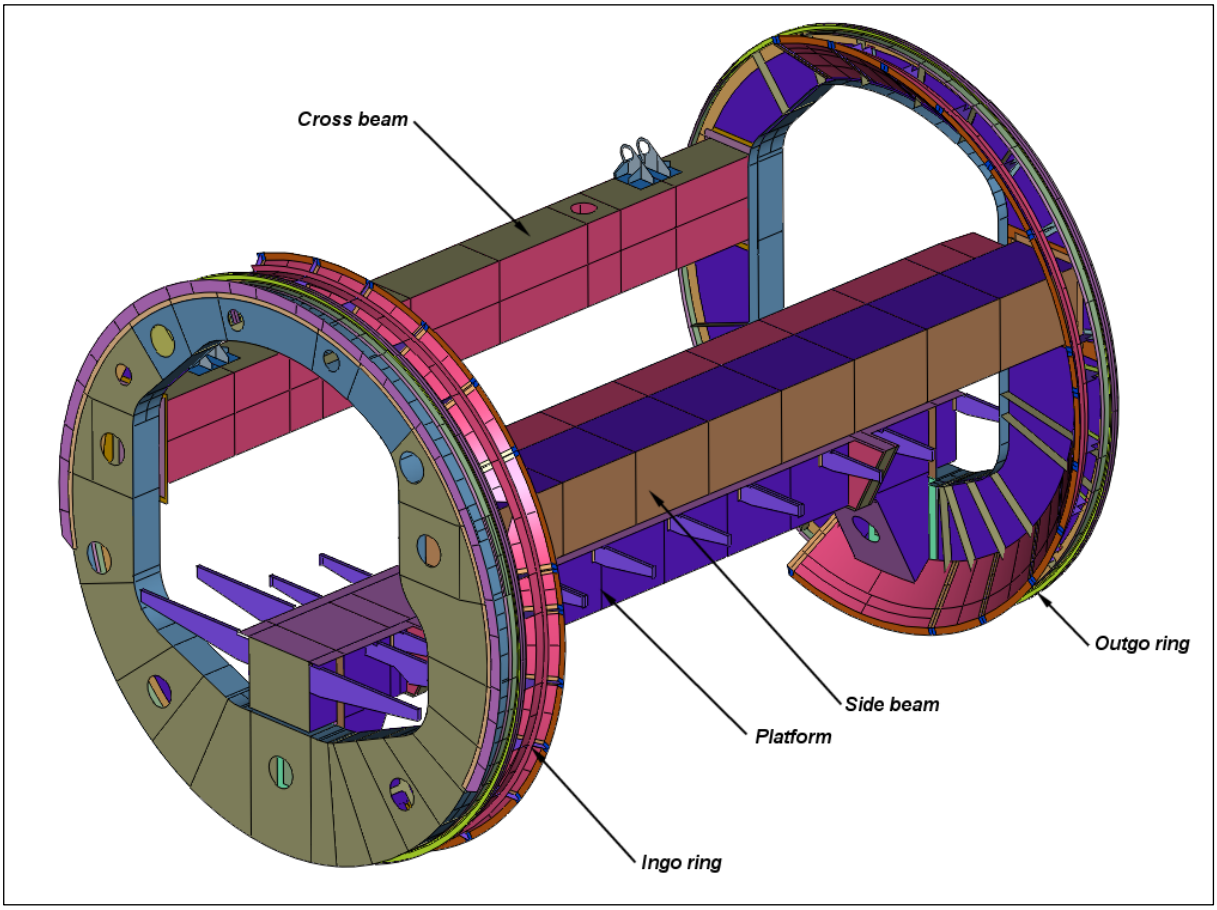

Figure 4.2: Surface model constructed of the ingo cage assembly

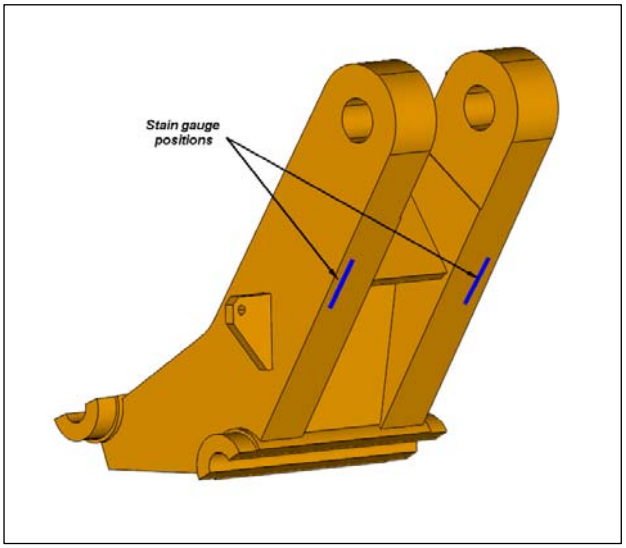

Figure 4.3: Solid model constructed of the primary compensating beam

The surface and solid models were combined into an assembly that could be manipulated to simulate the different tipping intervals that were used in the finite element model construction. Figure 4.4 shows a model of the complete assembly with the cage rotated in the 160-degree position.

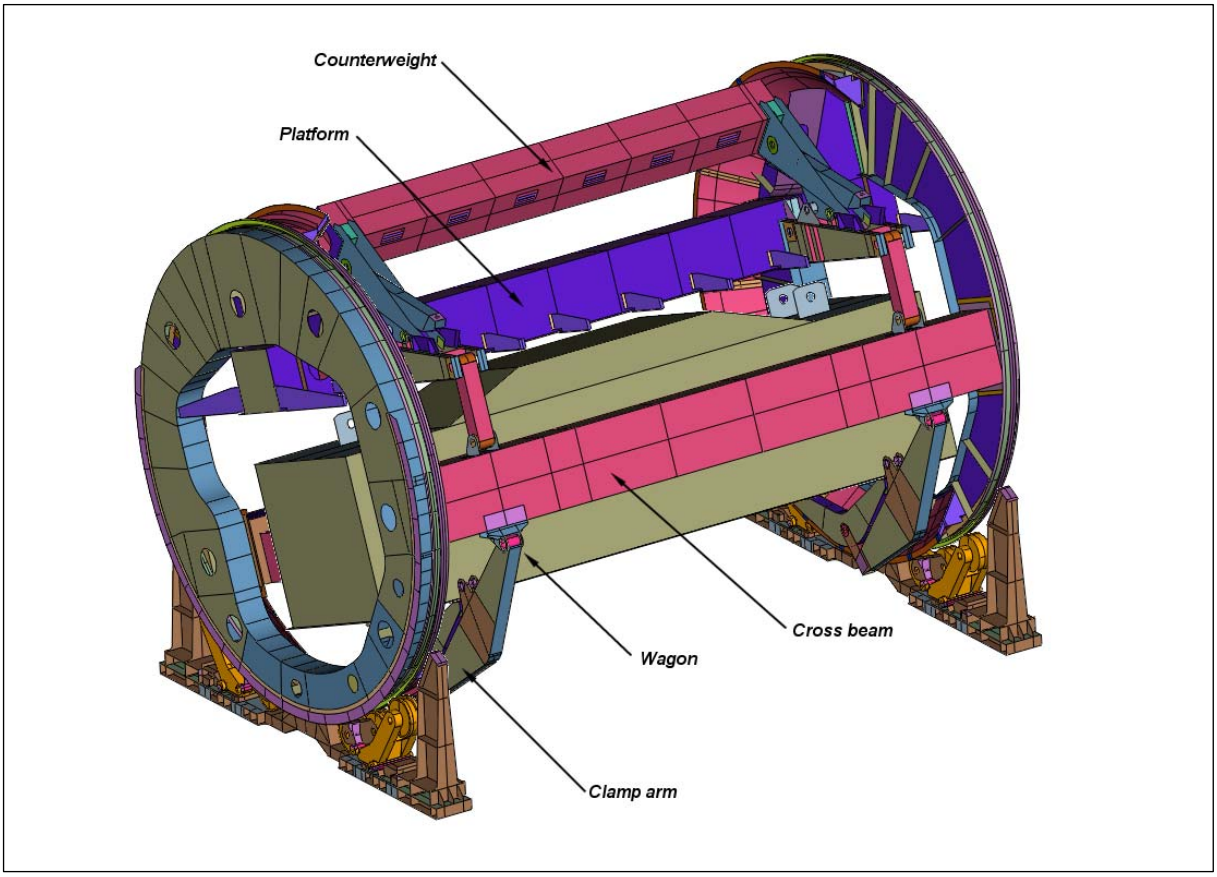

Figure 4.4: Tippler assembly model rotated in the 160-degree position

4.3 Finite element mesh preparation

To reduce finite element model construction time, the I-DEAS mesh from assembly function was used. This function allows the user to mesh all assembly components separately and then combine all the separate meshes into one assembly mesh that represents the assembly orientation used. This process sped up the process of generating meshes for all the tipping positions investigated.

4.3.1 Individual component mesh selection

As mentioned, the construction of the different Tippler components necessitated the use of solid and surface models to accurately model the Tippler structure. This furthermore necessitated the use of shell and solid elements to mesh the different components. These meshes in turn were imported into an assembly mesh and therefore needed to be compatible. Based on an evaluation of some of the curved surface edges in the model, the decision was made to use second-order elements as it have the advantage of providing more accurate results on curved geometries

(Adams & Askenazi, 1999: 141). Fewer elements could therefore be used and accurate results would still be obtained from a smaller model size.

For step 1 of the analysis process i.e. to verify the model accuracy, a second-order or parabolic quadrilateral thin shell mesh was used with an average element length of 150 millimetre (mm). Where needed the element length was reduced and triangular elements were used. Again, note the different colours of mesh representing the different element thicknesses. The refined mesh used in step 2 of the analysis consisted of elements with a maximum length of 75 mm with the areas of interest meshed with an element length of 40 mm.

The mesh applied to the ingo cage assembly for the first iteration is shown in Figure 4.5.

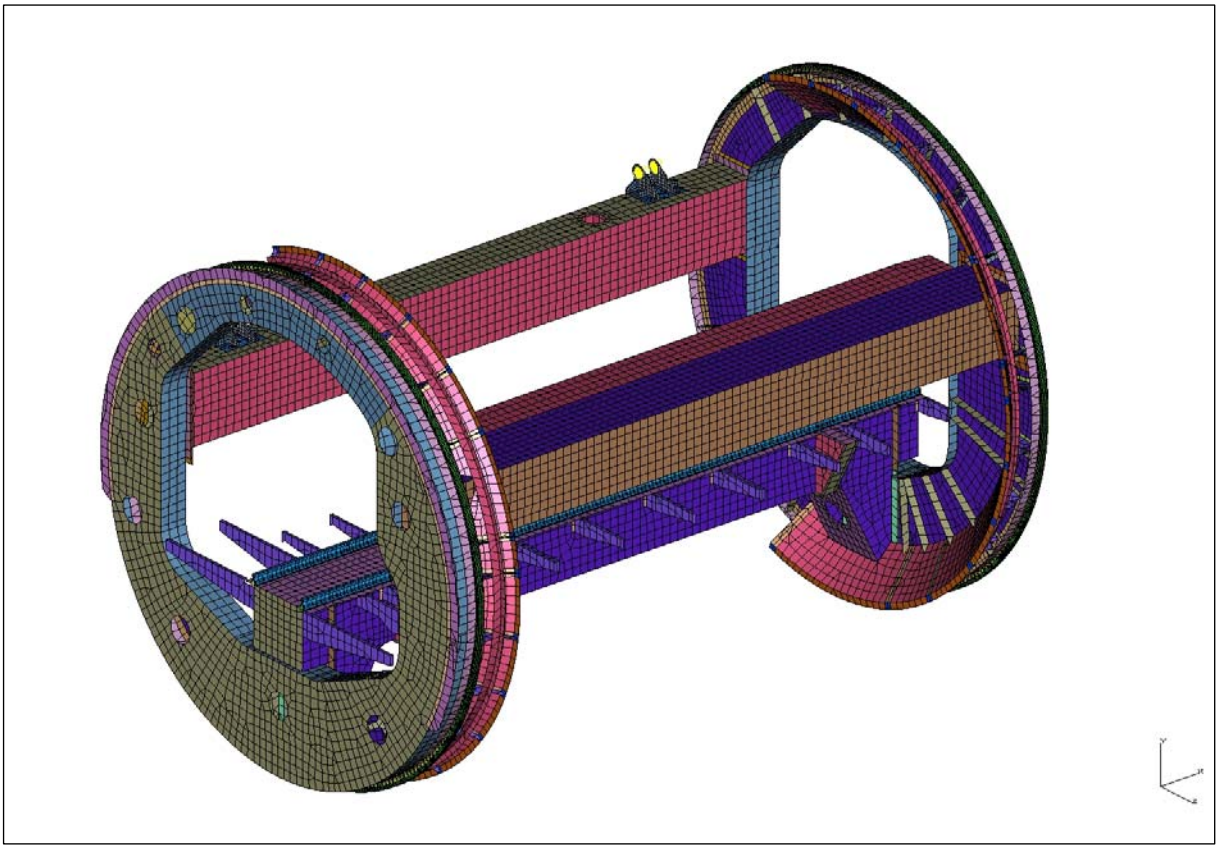

Figure 4.5: 150 mm mesh applied to ingo cage assembly

For the solid model components, a second-order tetrahedral element with an element length of 40 mm was used. The rollers were map-meshed with second-order solid parabolic bricks. This was done to accurately represent the roller / rail interface and to allow for the roller weight on the support roller structures. The mesh applied to the support roller assembly is shown in Figure 4.6

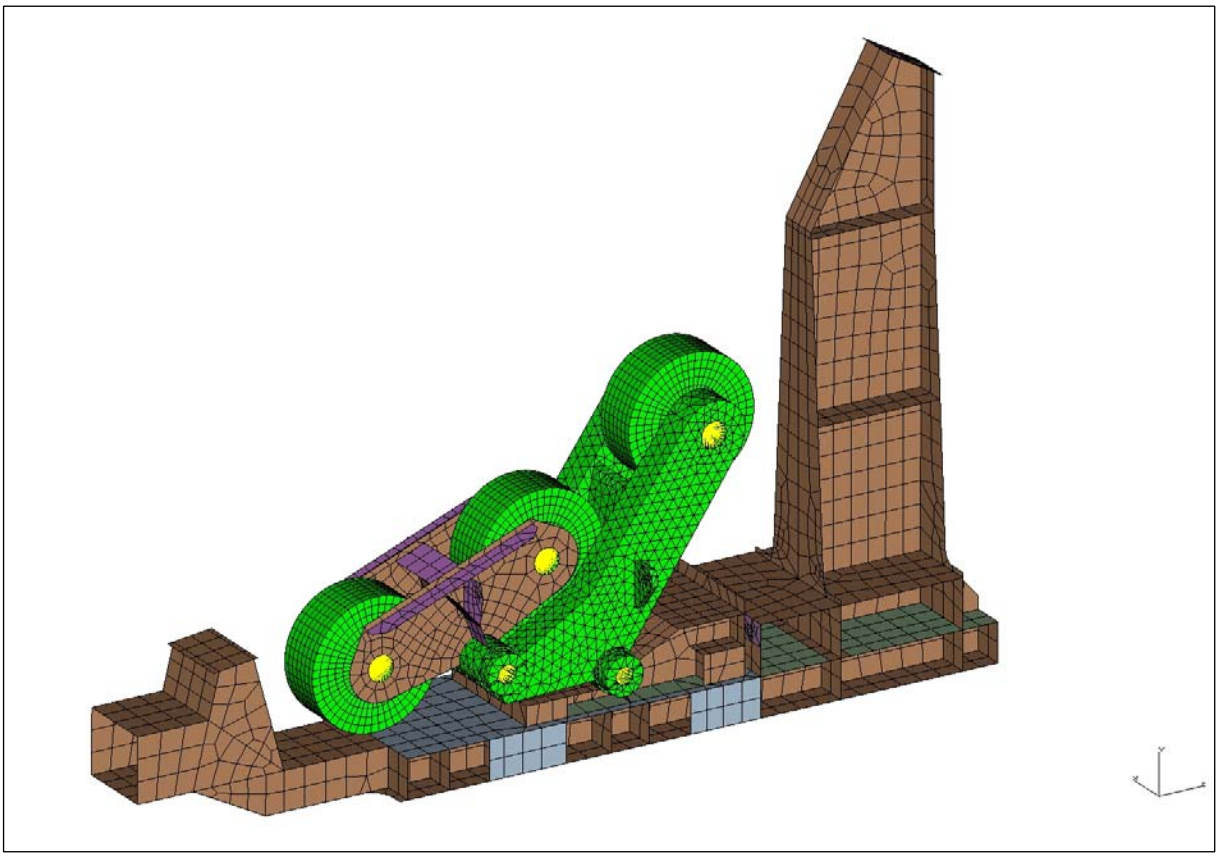

Figure 4.6: Mesh applied to support roller assembly

To simulate the rail section mounted to the platform structure, beam elements with the same cross-sectional profile as the rail indicated on the structural drawings were used. The rail was tied to the platform structure by means of rigid elements to simulate the rail / platform interface. No relative movement is possible between the rail and the platform.

All pins, shafts and damping springs were simulated by means of ridged elements to reduce model set-up times. This assumption was made as the effect of shaft-or pin-bending or the stress levels obtained in these components would have no influential effect on the stress levels calculated in the platform corners.

4.3.2 Assembly mesh generation

The individual meshes constructed as described above were combined into an assembly meshes for each 10-degree tip interval. Figure 4.7 shows the assembly meshes for the ingo cage rotated in the 60-degree position. In total 17 assembly meshes were constructed for the ingo cage assembly. The wagon used for the analysis was modelled as surface model and meshed with thin shell elements. The element thicknesses selected for the wagon do not represent the actual construction of the wagon structure, but provides an accurate estimation of the

wagon with its centre of gravity at a height of 933 mm above the rail as indicated in the wagon specification (Appendix A). Additional stiffness was added to the wagon structure by means of ridged elements that do not contribute to the weight of the wagon. The main functions of the wagon model are to simulate the weight of the empty wagon, to provide the force transfer points from the wagon to the Tippler structure and to provide clamping areas for the clamps on the wagons.

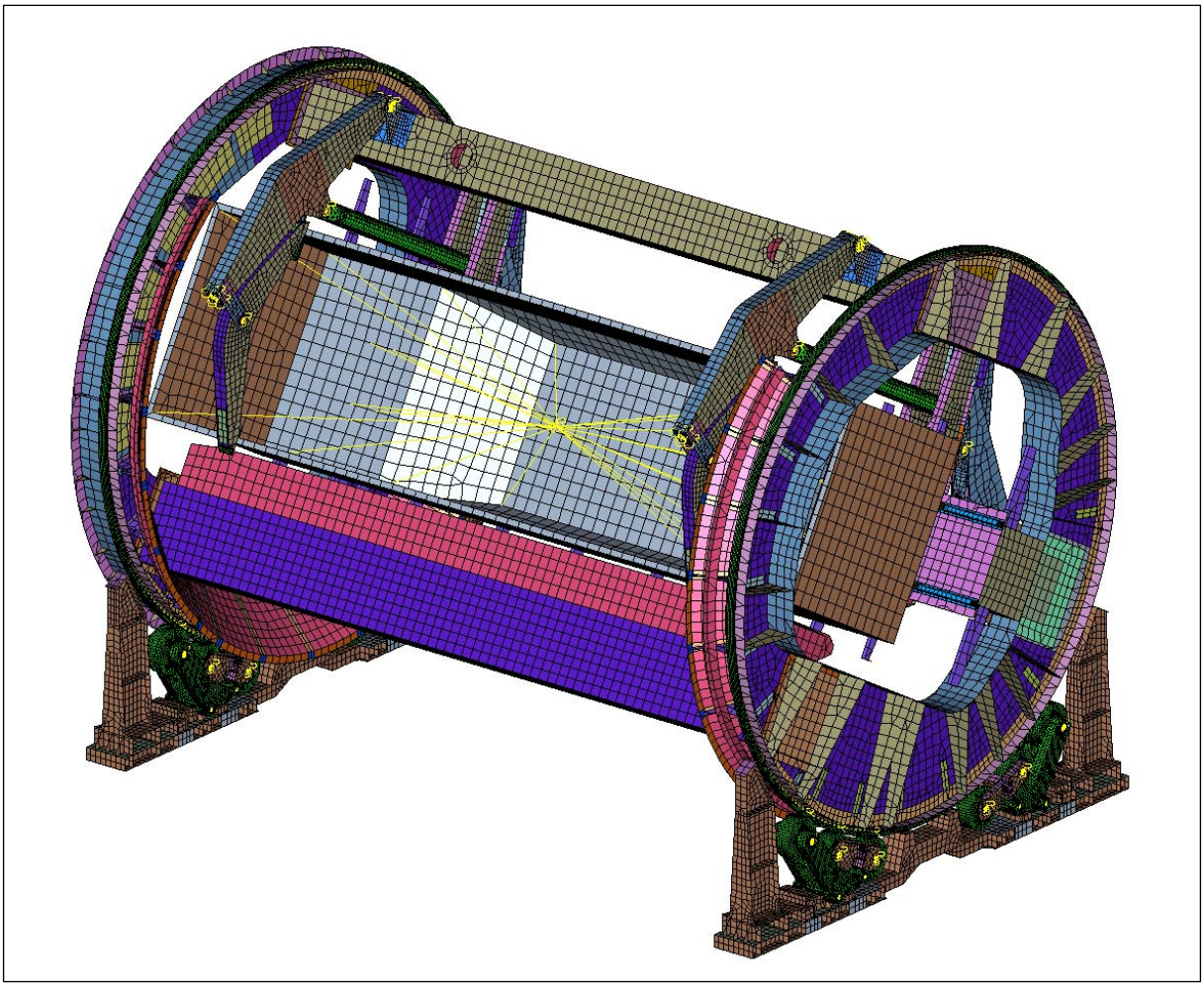

Figure 4.7: Assembly mesh constructed for ingo cage in the 60-degree position

All access-hole covers in the structure were left open as the bolt connections on these covers are normally not preloaded and the cover is sealed with water-resistant putty which is applied between the cover and the structure. The covers would therefore not provide any structural stiffness to the Tippler structure. Furthermore, no hand railing, walkway structures or piping on the structure was allowed for. The structural weight contribution of these components is negligible.

4.4 Boundary conditions

The boundary conditions applied to the finite element model describe the boundaries in which the model will be solved. Boundary conditions can be defined in terms of displacements and/or forces (Kurowski, 2004: 5). The accuracy with which these conditions are applied would determine the accuracy of the results.

4.4.1 Displacement boundary conditions

To accurately simulate component interfaces in the models, the boundary conditions applied should be able to transfer all translations and rotations needed from the one component to the other and vice versa. This is made possible by using coupled degrees of freedom, which is a set of nodes that are linked in specific directions and rotations. No frictional forces can however be simulated by these connections.

All pinned connections were simulated by means of coupled degrees of freedom. Where the connection pins are not able to transfer moments the rotational constraints around the pin centrelines were disabled allowing the components to rotate freely about these centrelines.

The support roller shafts were constrained by means of ridged elements and were not allowed to rotate around their centrelines. This would have no effect on the results, as the rollers are free to slide on the rail interface in their directions allowed for. The rails are however, not allowed to slide in the horizontal direction on the grooved rollers but can slide on the non-grooved rollers. Any sliding on the non-grooved rollers would simulate play that exists in the support roller assemblies of the tipper structure. It would furthermore simulate relative slip that occurs between the rail and the rollers during the rotational motion of the cage when the static friction coefficient is overcome.

For the rail/roller interface, a coupled degree of freedom was applied that simulates the perpendicular reaction force that would be generated by the rollers on the rail. The applied coupled degrees of freedom are shown in Figure 4.8. The cage is free to rotate around its own centreline to allow for twisting during the analysis.

The wagon wheel interface on the platform rail was also simulated with coupled degrees of freedom. This method only transfers the vertical load to the rail and the side force generated by the wheel flange on the rail when the cage is rotating. The constraints would not affect the bending pattern of the platform structure. The

constraints used on the wagon assembly are shown in Figure 4.9. Note, however, that these constraints change when the cage rotates. From an inspection of the wear plate on the side beam during the strain gauge installation process, it was clear that the wagons lean against the plates during the tip cycle. This would suggest that the wheels on the back rail of the platform would reduce their reaction force on the rail or even lift from the rail when the wagon leans against the wear plate.

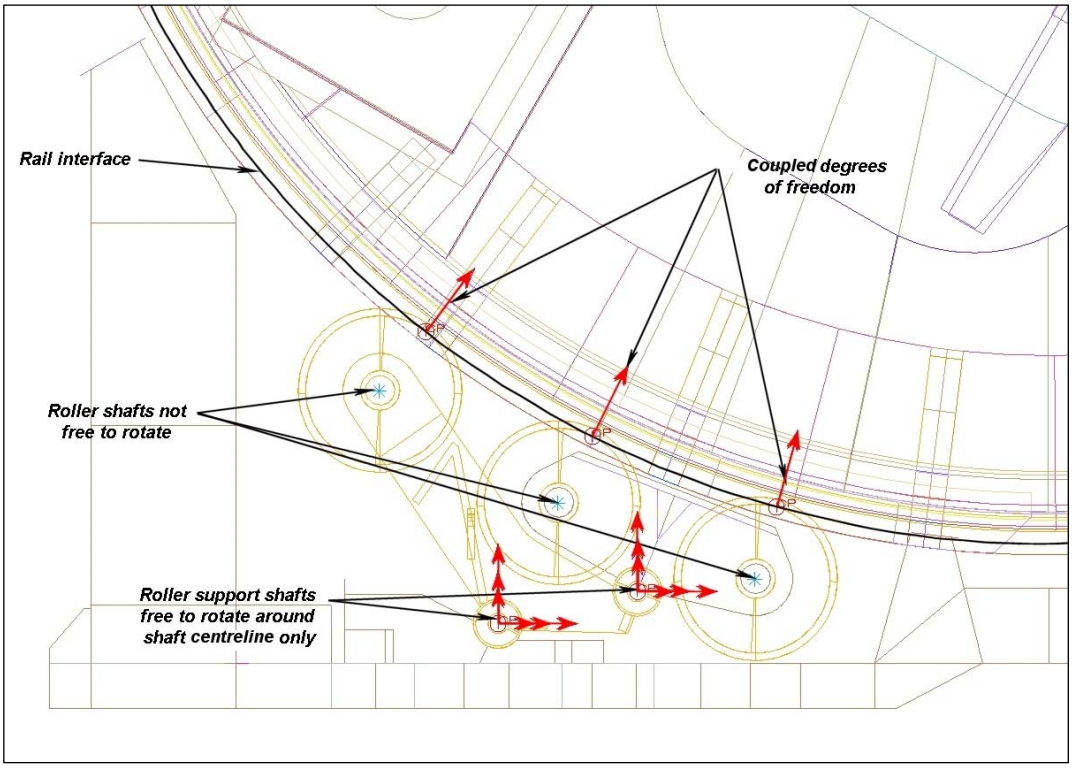

Figure 4.8: Coupled degrees of freedom applied at the roller assembly interfaces

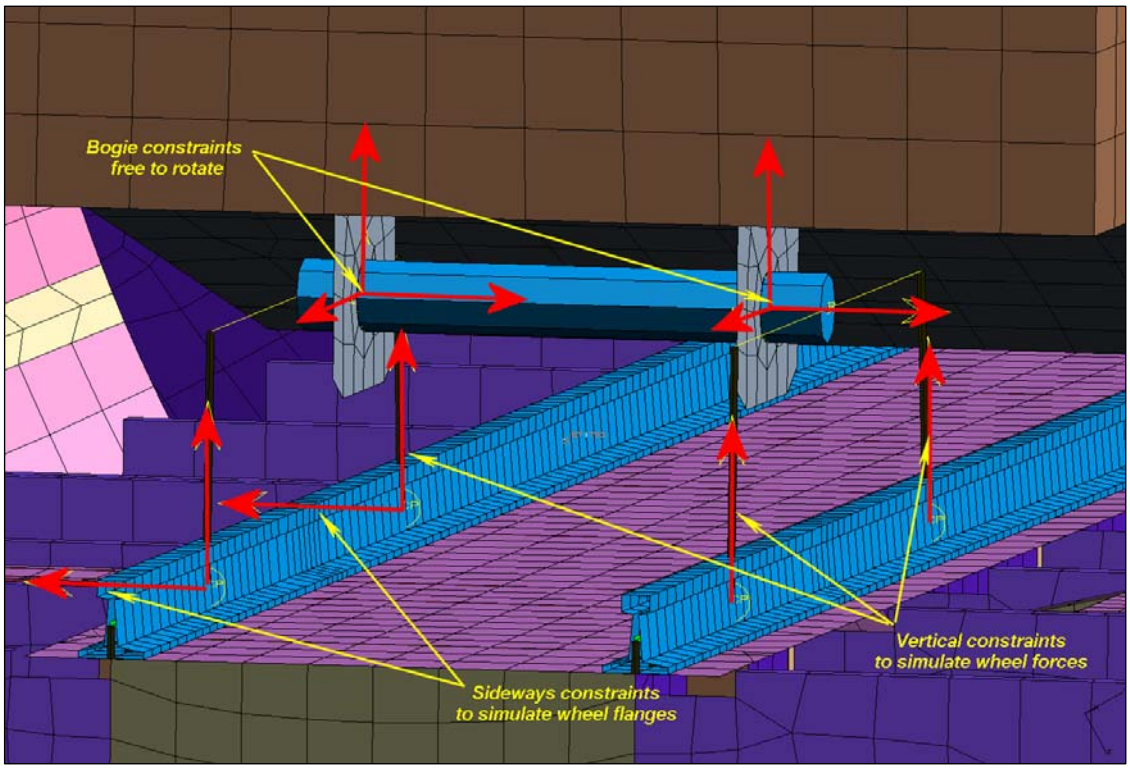

Figure 4.9: Constraints applied at the wagon-wheel/platform-rail interface

The exact angle (θ) at which the wagon starts to lean over was calculated from the available data for the CCL – 5 wagons (Appendix A). Note that for coal transport various wagon designations are used, however, all the wagons are of the same construction with the same centre of gravity (CG) positions.

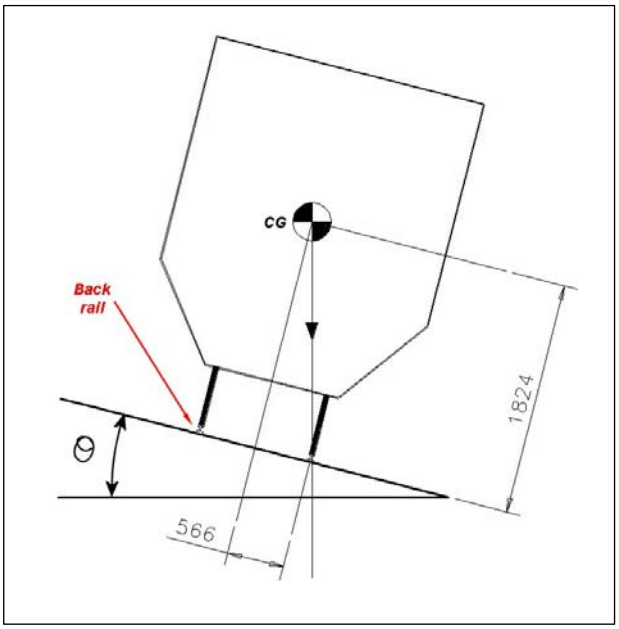

Figure 4.10: Fall-over position of loaded wagon

$$\theta = bg \tan\left(\frac{566}{1824}\right)$$
$$\theta = 17.23°$$

The wagons would therefore start to lean over at 17.23°. To simulate this situation the coupled degrees of freedom was removed between the rail and the wagon and applied between the wagon and the side-beam wear plates for all positions after the 20-degree rotation interval.

The support roller assembly bases were constrained in all directions on the surface interfacing with the concrete foundation. Furthermore, the cage was constrained against rotation at the pinion/ring gear interface on the ingo side end ring

4.4.2 Force boundary conditions

The main forces contributing to the stress in the Tippler structure are the gravitational force and the forces introduced to the structure by means of the wagon and coal load. A gravitational acceleration value of 9.81 m/s^2 was used for analysis.

To simulate the reduction in the weight of coal in the wagon during the tip cycle a constant load curve was assumed as shown in Figure 4.14. This approach was selected to eliminate the complexity of estimating the weight of coal in the wagon at each tip angle simulated. From video material taken of the tip cycle and the angle of repose of coal of between 30 and 40 degrees (Conveyor knowledge and information technology) it was estimated that the first coal would start dumping at a tip angle of between 30 and 40 degrees. The lower value of 30 degrees was selected for analysis purposes to allow for all possible angles of repose. The weight of coal in the wagon was reduced by 6 000 kg for each 10-degree interval rotated up to the 160-degree interval. For the return cycle the wagon was simulated as empty.

The weight of the coal as obtained from the graph was applied as a point load at the CG position of the wagon. Although this boundary condition could influence the structural stresses for certain tip intervals, applying this condition to all the tip intervals the error introduced is constant for all tip intervals. The data was therefore still valid for evaluating stress trends in the structure during the tip cycle.

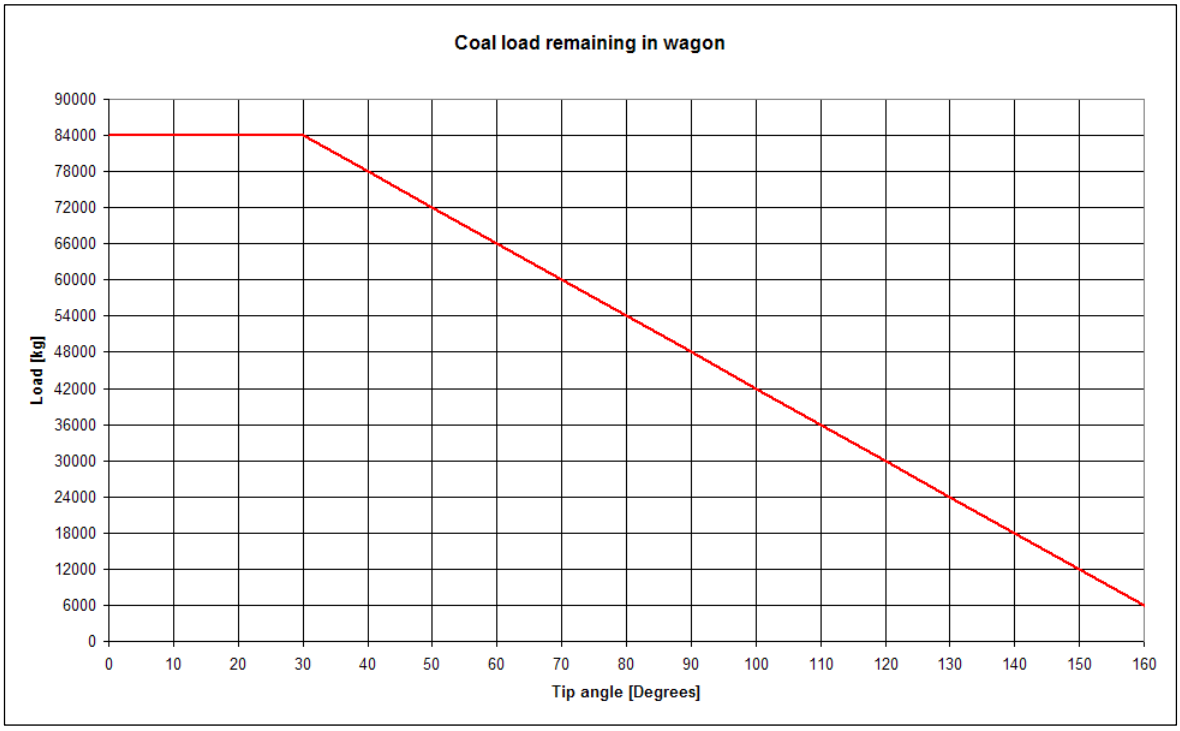

Figure 4.11: Coal weight in wagon for different tip angles

The seventeen FEA models simulating the different tip intervals were solved, each model solution taking approximately 40 minutes on a Windows-based workstation.

An additional analysis was also done on the ingo cage with no wagon positioned on the platform. The results of this analysis were used to determine the mean stress in the structure caused by gravity alone. The strain gauge data obtained earlier does not take into account the stress in the structure caused by gravity and can therefore not be compared to the FEA results directly.

4.5 FEA model verification

The finite element model constructed needs to be verified before the results obtained can be used for analysis purposes. This verification can be done by means of a theory of strength calculation or with data obtained from measurements. For this analysis, data obtained from strain gauge measurements was used for the verification process. This section of the dissertation describes the verification process used to verify the accuracy of the finite element model.

4.5.1 Tip interval time estimations

As previously described, an FEM was constructed and solved for each 10-degree interval of the tipping cycle. To verify the accuracy of the models, stress data obtained from the strain gauge readings was available. The FEA results for a specific tip interval should, however, be compared to the strain gauge data for the exact same time step when the Tippler cage rotates through the set angle used in the FEA. To be able to perform this comparison the time steps at the different tip angles had to be determined. Further, note that the cage will pass each interval angle twice during the tip cycle, the first time with a loaded wagon and the second time with an empty wagon.

From the strain gauge results, the total tip cycle time was determined as approximately 40 sec. This Figure was verified by means of short video clips recorded on the day the strain gauge analysis was done. RBCT confirmed that the ramp-up and ramp-down intervals for the Tippler cage were set at 3 sec. No further cycle detail were however available. Figure 4.12 shows the speed / time graph for the cage calculated for a 160 degree tip angle to be completed in 17 sec with the 3-sec ramp-up and ramp-down intervals included. The area under graph represents the 160-degrees rotated. From this graph the time intervals at each 10-degree tip angle were calculated from the slope of the graph and the area underneath the graph.

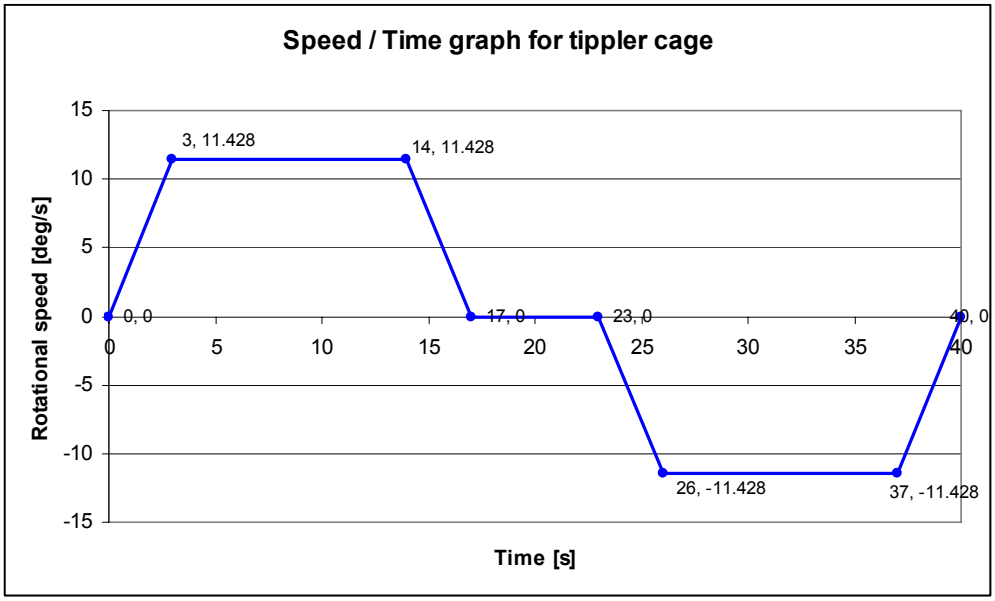

Figure 4.12: Rotational speed / Time graph for the Tippler cage

Figure 4.13 shows the time interval for every tip interval of 10 degrees. These time intervals would be used as reference to compare the stress values from the strain gauge data to the stress values obtained from the FEA results angles.

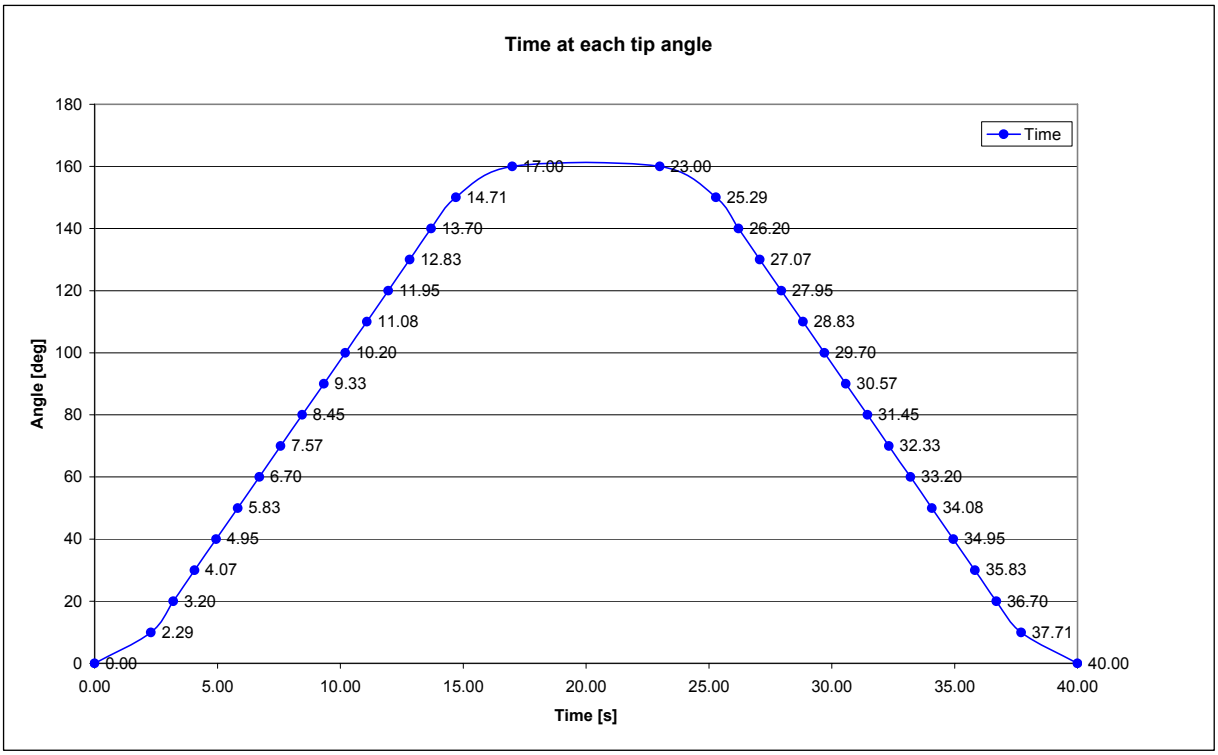

Figure 4.13: Tip angle / Time graph for Tippler cage

4.5.2 Model verification

Two data verifications were done to verify the accuracy of the FEA method used. For the first verification, the Tippler results for an empty and loaded cage were compared. For the second verification, the strain gauge data and FEA data for the different tip intervals were compared. From these results, the accuracy of the FEA method was determined.

A comparison was also done between the averaged and unaveraged node stresses at the strain gauge positions and the positions where the platform structure developed cracks. The difference between the two values should be less than 15% for a good quality mesh (Mercer et al., 2003: 4).

a) Loaded and unloaded Tippler structure

The stress results obtained from the finite element models of the empty and loaded cages were compared to the strain gauge results obtained for the same

load cases and with the values obtained from the calculations done earlier (paragraph 3.1). The comparison data is shown in Table 4.2. The data for the used comparison is shown in Figures 14.14 to 14.18.

Table 4.2: Comparative stress values for Tippler platform

	FEA result		Measured value		Calculated value	
Position	**Front**	**Back**	**Front**	**Back**	**Front**	**Back**
Full wagon being loaded onto platform	14.89 MPa	14.97 MPa	14.00 MPa	14.30 MPa	15.54 MPa	15.54 MPa
Full wagon replacing empty wagon	10.05 MPa	10.95 MPa	11.2 MPa	12.4 MPa		

The largest stress difference between the measured and FEA results is 11.7%. This is for the back strain gauge where the full wagon replaces the empty wagon on the platform.

Figures 4.14 to 4.16 show the stress results obtained from the FEA for three load cases, i.e.:

I. The Tippler cage empty with only gravitational forces applied
II. An empty wagon positioned on the platform
III. A loaded wagon positioned on the platform

To compare the stress values with the calculated and measured stress levels the Case I stress was deducted from the Case III stress to simulate a full wagon being loaded onto the platform and the Case II stress was deducted from the Case III stress to simulate the difference in stress for an empty and loaded wagon on the platform. Note for all three Figures the stress scale was kept the same.

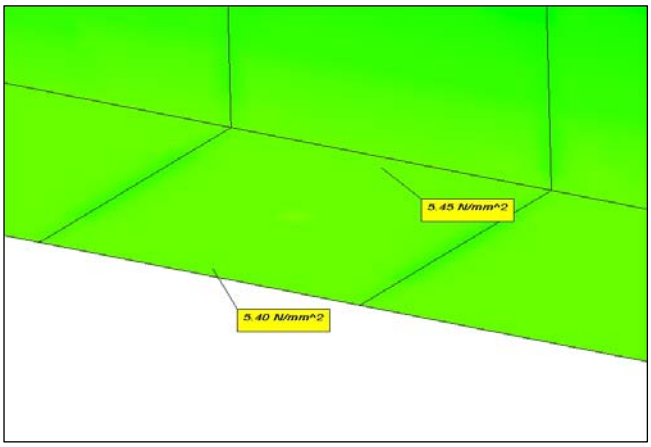

Figure 4.14: Platform stress – Case I (Cage empty)

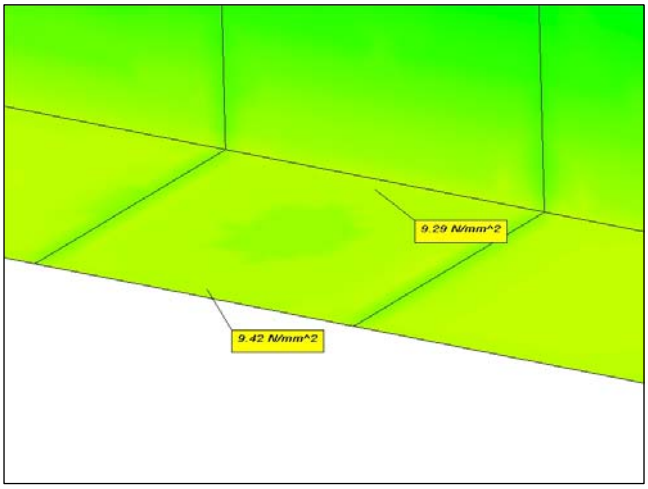

Figure 4.15: Platform stress – Case II (Empty wagon)

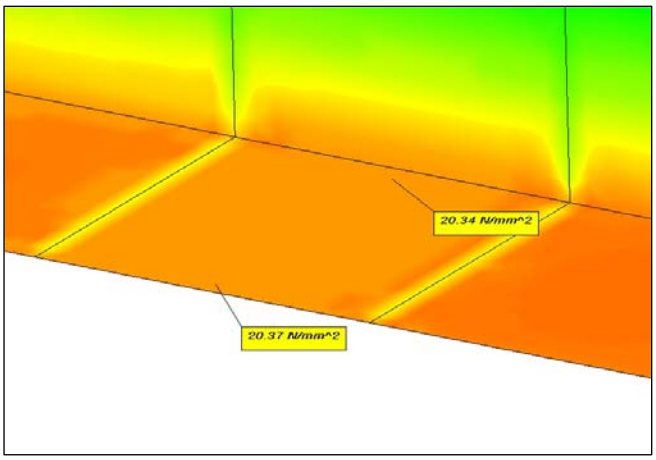

Figure 4.16: Platform stress – Case III (Full wagon)

The results used for the strain gauge comparison can be seen in Figures 4.17 and 4.18. The stress values used for the comparison and shown in Figure 4.17 were calculated from the average stress values for the data used for the stress peak comparison as shown in Figure 3.17.

The data for the comparison between the FEA model and the measured stress differs by 11.7% at most. This indicates the model is representative of the actual conditions when the Tippler is loaded with wagons.

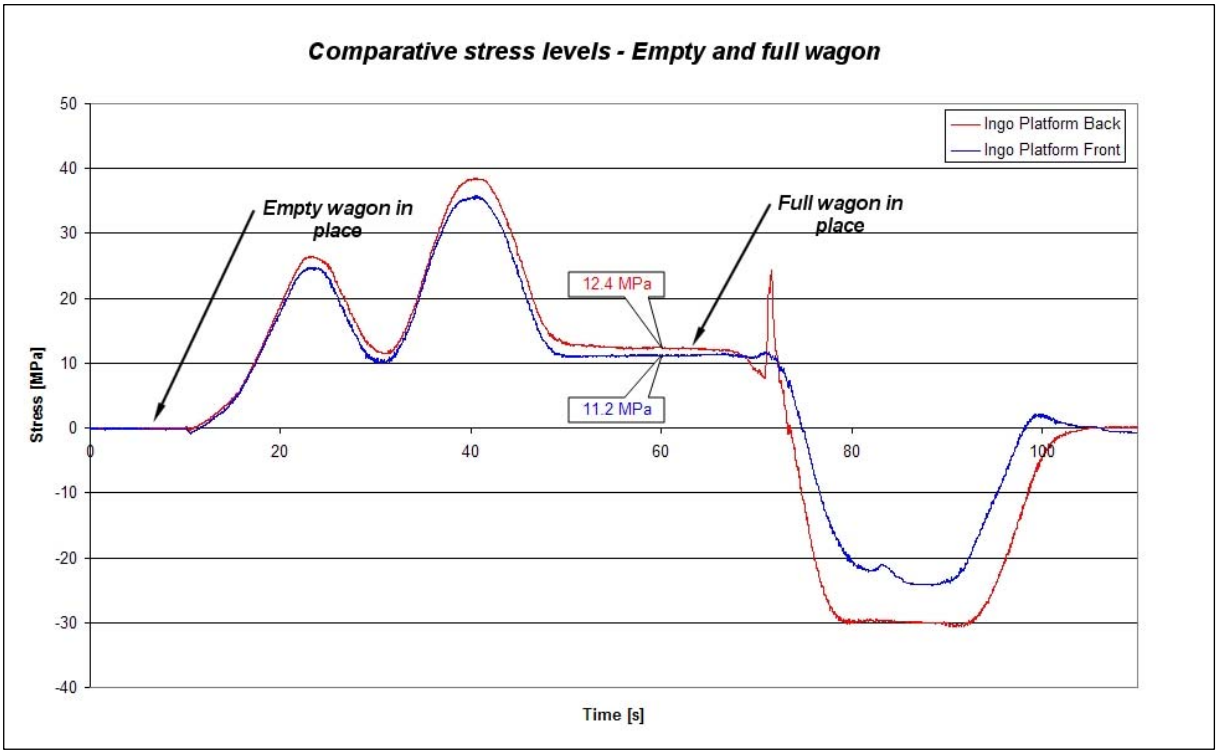

Figure 4.17: Average measured stress for empty and full wagon on platform structure

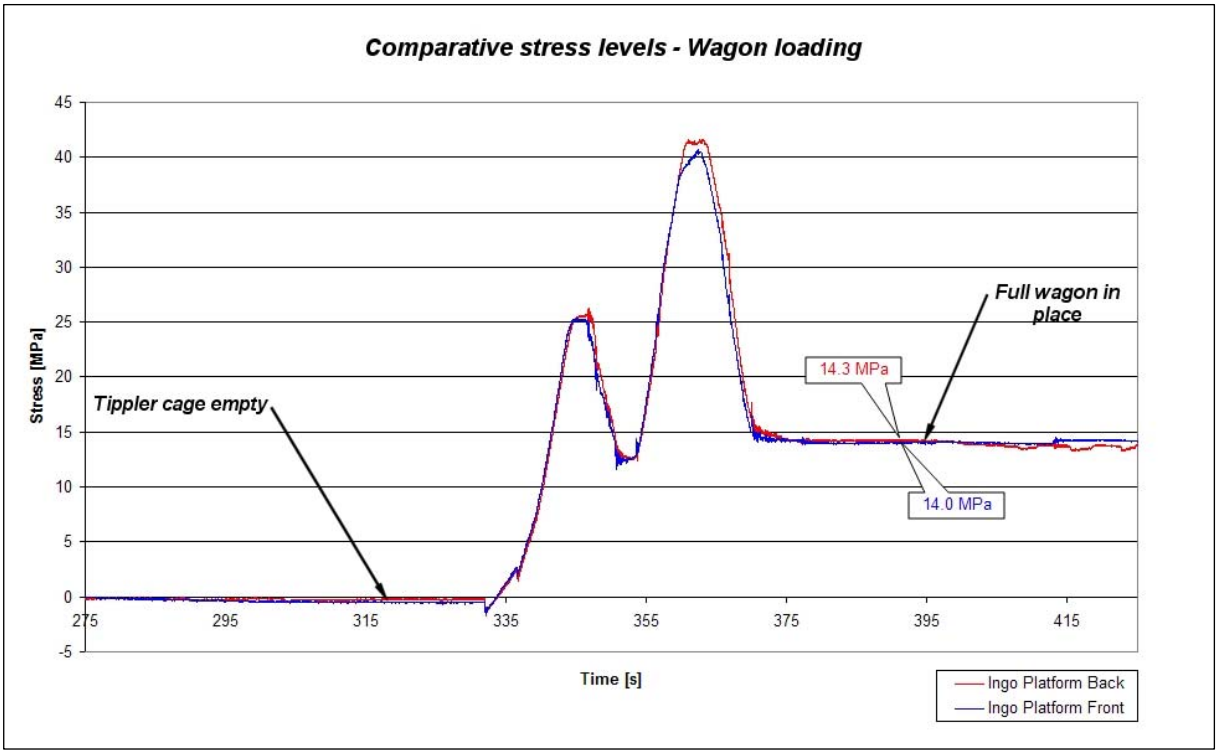

Figure 4.18: Measured stress for wagon loaded onto platform structure

b) Stress comparison for full tip cycle

The stress values obtained from finite element models for the positions where the strain gauges were applied were compared to the stress values obtained from the strain gauge readings. The comparison was done per time interval as calculated earlier. A stress plot for each tip interval of the Von Mises stress in the complete structure can be seen in Appendix B.

For the stress value comparison the average stress value was calculated from the data used in the strain gauge evaluation. The original data can be seen in Figures 13.17 to 13.22. The first two sets of data as shown in Figures 4.19 and 4.20 show the stress comparison for the two strain gages applied to the platform structure. The deviation between the stress values at the maximum stress values is approximately 11.0% for the front strain gauge and 5.0% for the back strain gauge. The data for the strain gauge on the cross beam is indicated in Figure 4.20. There is a slight deviation in the stress pattern between the two data sets. This is caused by a difference in the time of contact between the clamps and wagon, in the FEA model and the actual occurrence. The maximum deviation at the highest stress for the cross beam is approximately 9.4%. The last comparison is between the stress values obtained from the strain gauge readings on the clamp arm and the FEA results obtained for the similar position. The results shown in Figure 4.22 and have maximum difference in value of approximately 8.8%

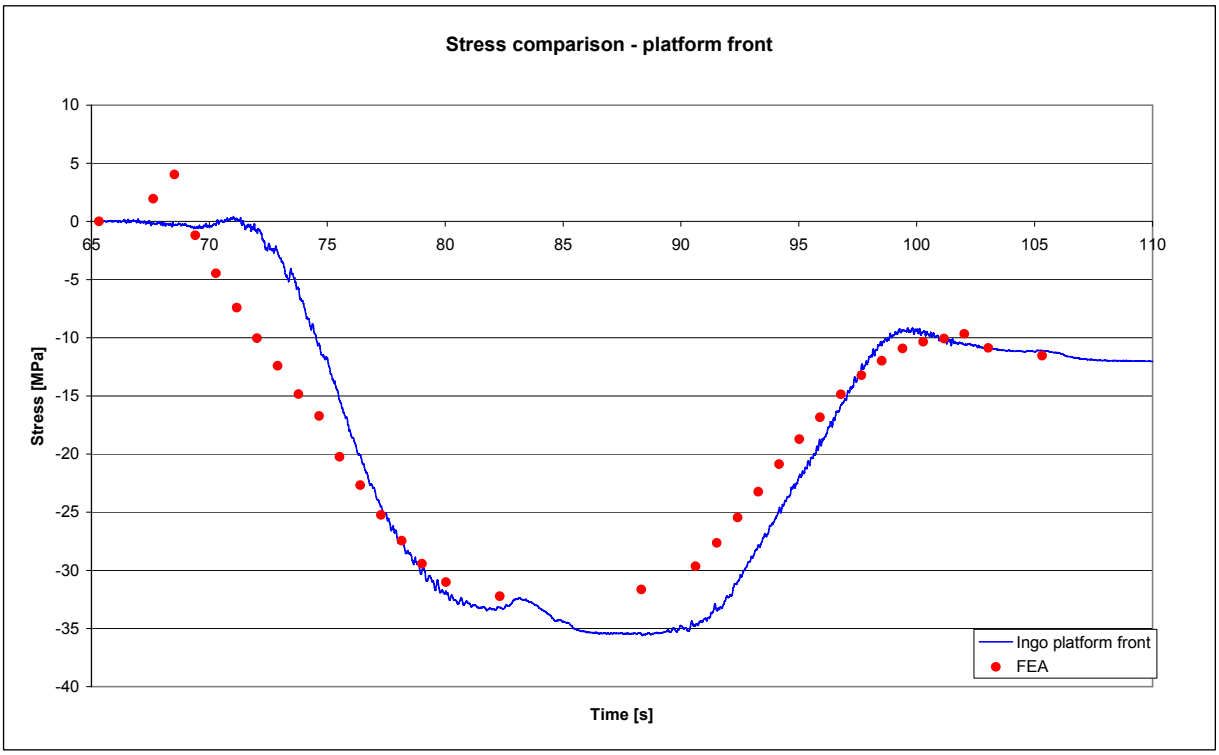

Figure 4.19: Stress comparison for the front strain gauge on the platform structure

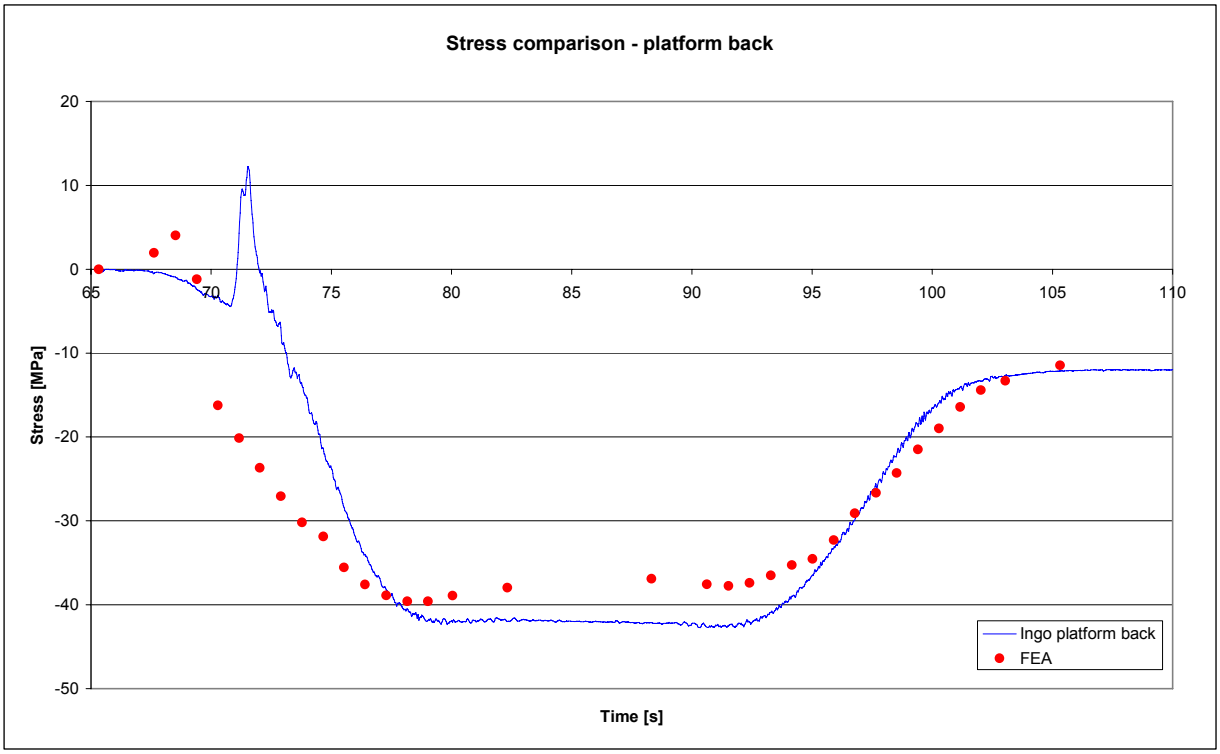

Figure 4.20: Stress comparison for the back strain gauge on the platform structure

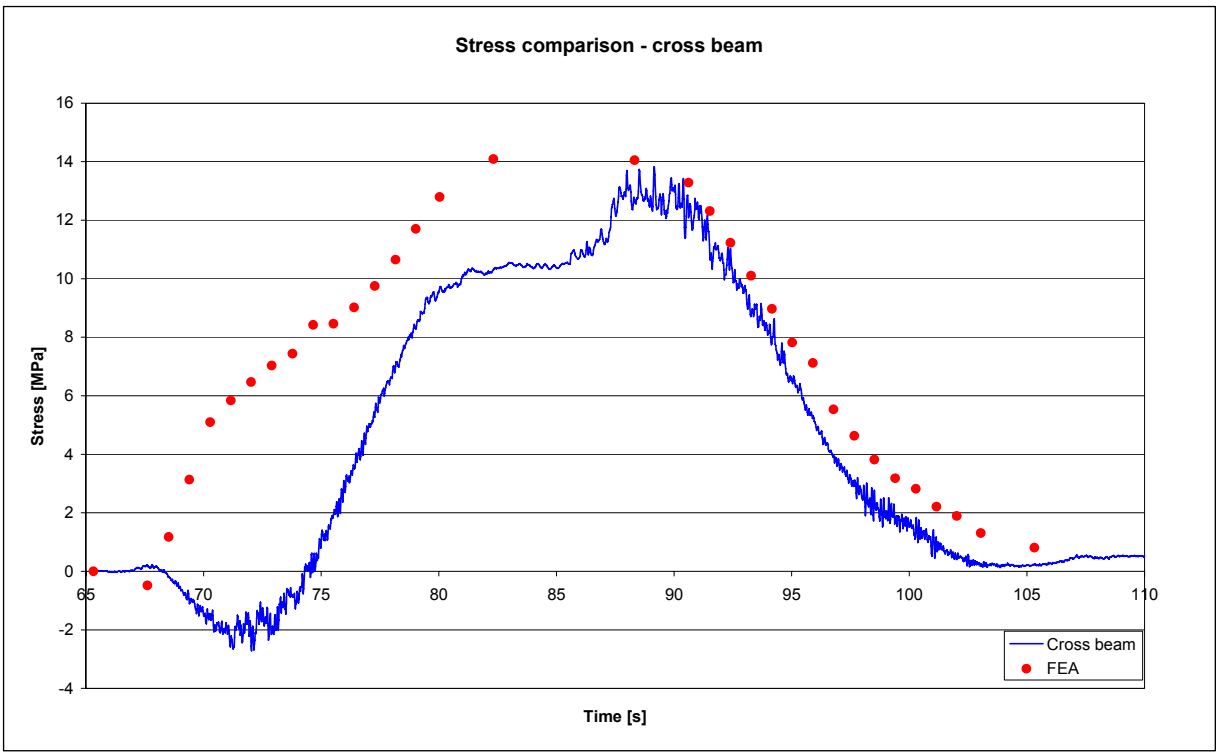

Figure 4.21: Stress comparison for the strain gauge on the cross beam

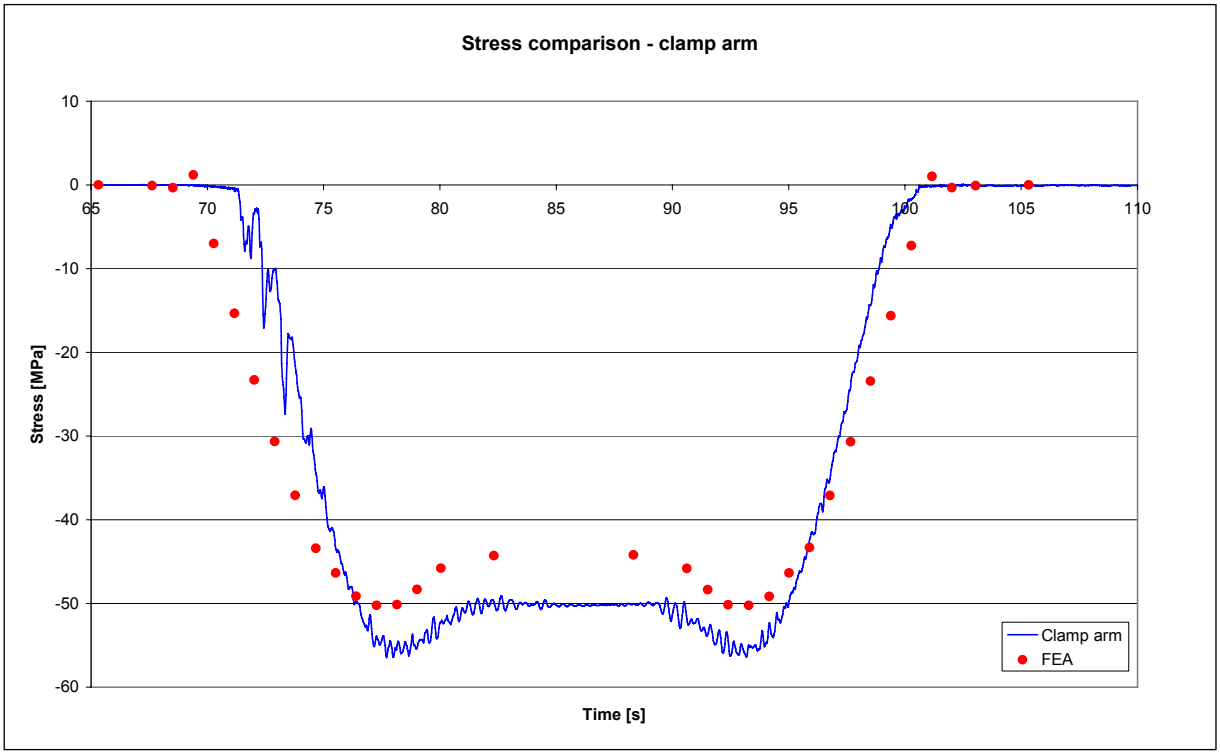

Figure 4.22: Stress comparison for the strain gauge on the clamp arm

The difference between the measured and FEA results can be contributed to effects such as differences in the boundary conditions applied, ramp-up and ramp-down speeds of the Tippler structure, weight distributions or other effects not simulated in the FEA model. The largest difference in the measured and FEA data is seen for the cross beam data. This may be caused by the fact that the spring assembly in the clamp arm mechanism was simulated by means of a ridged element. The deviation is however, only seen in the shape of the signal and not the maximum stress levels obtained. The data therefore indicates that the method applied to simulate the tip cycle by means of multiple linear static FEAs does provide an accurate representation of the actual stresses obtained during the tip cycle.

c) Mesh quality evaluation

To determine the quality of the mesh applied to the structure, a comparison was made between the averaged and unaveraged stress at the node point where the strain gauge comparison readings were obtained from. The same was done for the position where the cracks developed on the structure. This difference should be less than 15% for reliable fatigue results (Mercer et al., 2003: 4).

The comparison at the strain gauge positions was made with the Von Mises stress values as indicated in Figure 4.23. The difference between the averaged

and unaveraged stress values at the strain gauge positions is 0% for the complete tip cycle, indicating a directional stress and a sufficiently fine mesh.

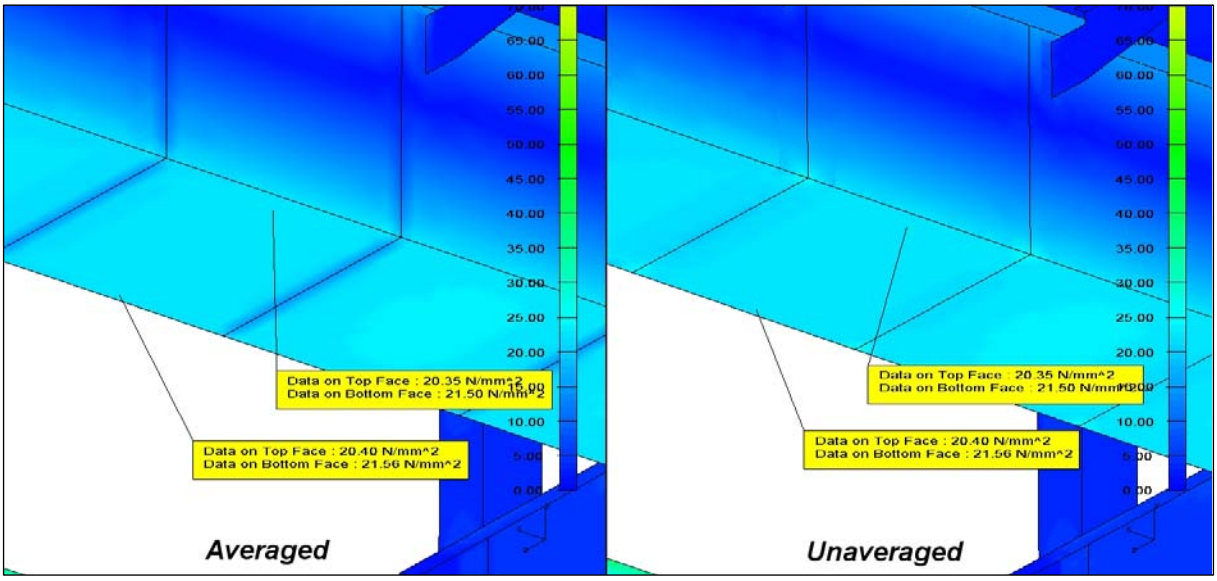

Figure 4.23: Averaged and unaveraged stress comparison for platform

Due to the stress changes in the front and back corners of the outgo side of the ingo cage, it was found that in some cases when the averaged and unaveraged Von Mises stress values are compared, the difference between the averaged and unaveraged stress values may be less than 15% while the same test for one or more of the directional stresses or shear stress values may deliver a result of much higher percentages.

It was further found that the comparison is sensitive to stress magnitude, i.e. a small difference between the averaged and unaveraged stresses at low stress values delivers a different result than the same difference for a high stress value. The method as proposed by Mercer et al. (2003: 4) should therefore be used with care when quantifying mesh quality.

For this study, the method as proposed above was utilised to evaluate the mesh accuracy, as it provides a fast indication of the model accuracy. It was, however, applied to all the stress directions separately, and the mesh was refined at the areas of interest until the difference between the averaged and unaveraged stresses was acceptable. The final percentage deviation for the two main stress directions and the shear stress was less than 6%.

The FEA model results compare well with the strain gauge readings obtained from the Tippler structure. The maximum error between the readings and the model is approximately 11.0% at the front strain gauge position on the platform structure. The

deviation between the averaged and unaveraged stress values obtained from the models in the platform corner is 6%.

From the verification results, it is therefore clear that the constructed FEA simulation of the tipping cycle provides an accurate estimation of the stress values obtained in the original Tippler structure during a tip cycle. The stress values obtained from the FEA can therefore be used to calculate the fatigue life of the original and modified structures.

CHAPTER 5

FATIGUE LIFE ESTIMATION

In order to evaluate the increase in fatigue life for the modified Tippler structure the fatigue life calculated for the modified structure was compared to the life calculated for the original structure. For both the original and the modified Tippler structures, the presence of welds in the high stress areas, which is further influenced by the corrosive environment, complicates the selection of an appropriate fatigue life algorithm. For this reason it was decided to modify a component S-N curve, which closely represents the weld construction, to obtain a "representative" S-N curve that provided a fatigue life (period after which cracks would start to grow from the weld detail) that closely represents the 10 year life of the original structure. This S-N curve would then be used to evaluate the fatigue life of the modified Tippler structure as a similar weld detail was used in the modified structure.

This comparison gave a good estimation of the life expected from the modified structure compared to the original structure. The material properties, mesh size, and S-N curve used and method of calculation were kept the same for both evaluations.

Furthermore, a material S-N curve was constructed for the unwelded material used in the Tippler's construction. This curve was created to obtain an estimate of the allowable stress levels in the unwelded portions of the structure.

5.1 Component S-N curve selection for welded material

From the weld detail available as indicated in figure 5.1, an appropriate weld class was selected from the IIW welding code. To ensure the accuracy of the class selection, the selection was furthermore compared to a class selected from the BS 7608:1993 code.

Figure 5.1 describes a double fillet weld i.e. a fillet weld on the outside of the structure corner with a similar weld on the inside of the corner. The weld can almost be described as a full-penetrated K-butt weld. The weld is loaded as indicated in figure 5.2. (Refer to figure 5.7 for the load direction)

The weld detail available can be described as a combination of the two details as shown in figure 5.3. The detail would therefore represents a FAT class of 125 as indicated. If the class is selected according to the BS 7608:1993 code, the class selected is a class C detail as shown in figure 5.4. Figure 5.5 shows the component S-N curve for the 125 FAT class weld. Note the fatigue limit of 125 MPa at 2 million

cycles. Figure 5.6 shown the component S-N curve for a FAT class C weld, obtained from the BS code. The fatigue limit at 2 million cycles is also approximately 125 MPa.

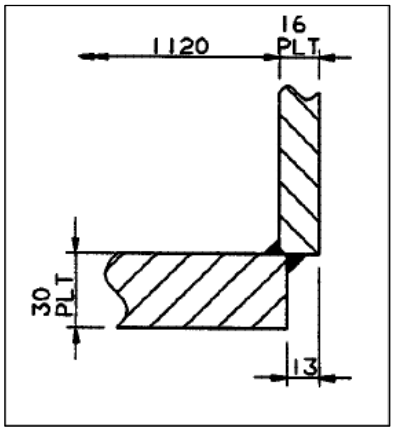

Figure 5.1: Weld detail at the platform corner

Source: Extracted and modified from original structural drawing as supplied by RBCT

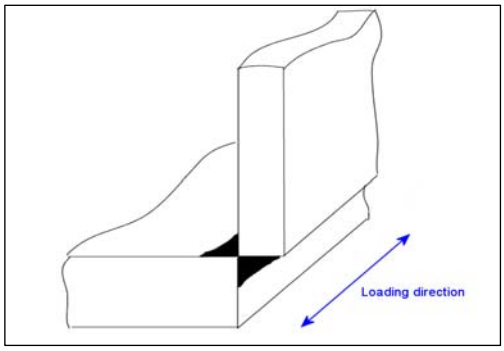

Figure 5.2: Load direction for the weld detail

No.	Structural Detail	Description (St.= steel; Al.= aluminium)	FAT St.	FAT Al.	Requirements and Remarks
311	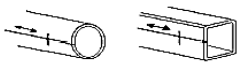	Automatic longitudinal seam welds without stop/start positions in hollow sections with stop/start positions	125 90	50 36	
312	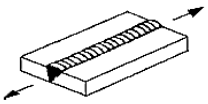	Longitudinal butt weld, both sides ground flush parallel to load direction, 100% NDT	125	50	
313	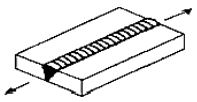	Longitudinal butt weld, without stop/start positions, NDT with stop/start positions	125 90	50 36	
321	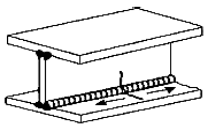	Continuous automatic longitudinal fully penetrated K-butt weld without stop/start positions (based on stress range in flange) NDT	125	50	No start-Stop position is permitted except when the repair is performed by a specialist and inspection is carried out to verify the proper execution of the weld. A very good fit between flange and web plates is essential.

Figure 5.3: Weld class according to the IIW code

Source: Recommendations for fatigue design of welded joints and components, (Hobbacher, 2004: 452)

4.2	C	Accidental stop/starts are not uncommon in automatic processes. Repair to the standard of a C classification should be the subject of specialist advice and inspection and as a result, the use of this type is not recommended.
4.3	D	For situation at the ends of flange cover plates see joint type 5.4. Backing strips, if used, need to be continuous and either not attached or attached by continuous fillet welds. If the backing strip is attached by discontinuous fillet welds see type 4.6.

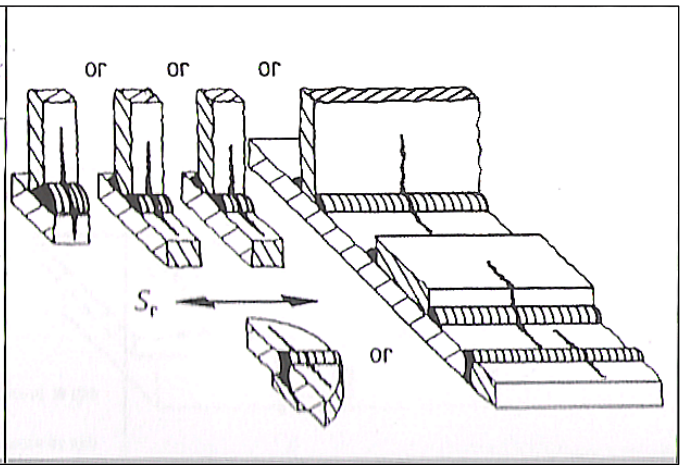

Figure 5.4: Weld class according to the BS code

Source: Fatigue design and assessment of steel structures, BS7608:1993

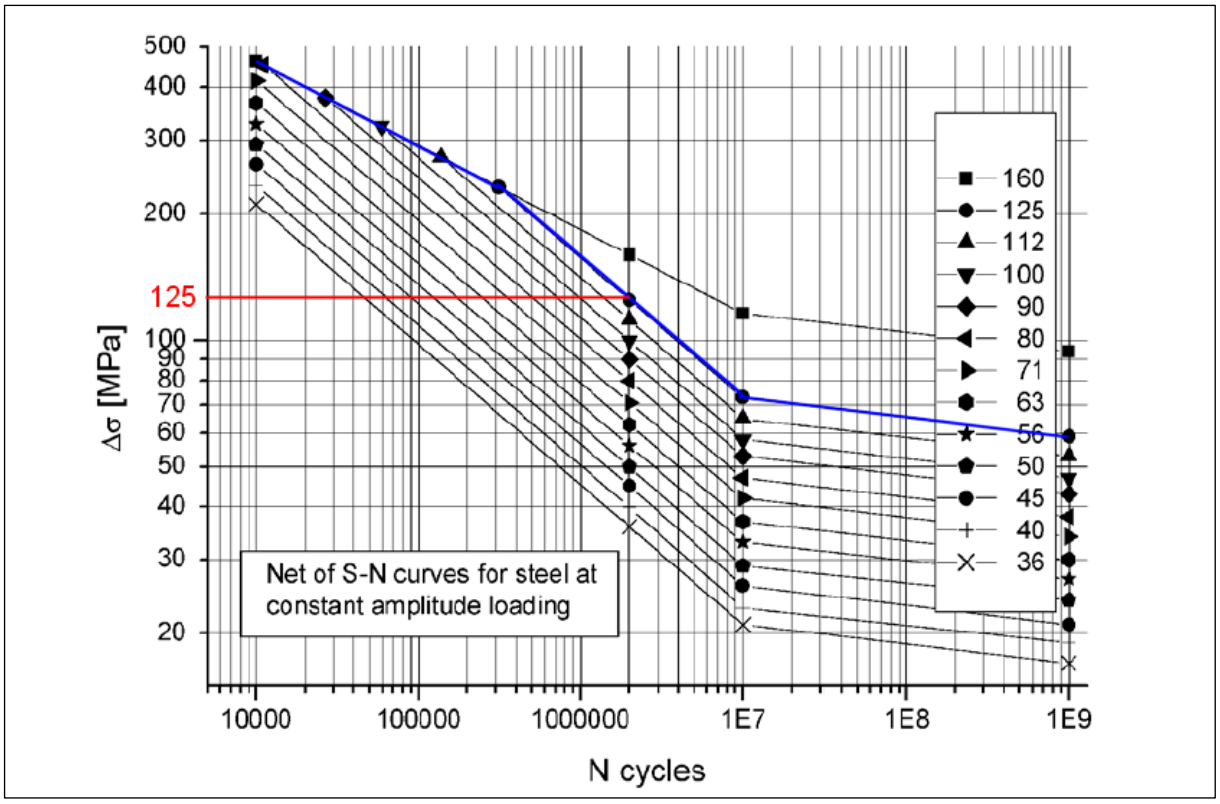

Figure 5.5: Proposed S-N curve for the selected weld construction – IIW code

Source: Recommendations for fatigue design of welded joints and components
(Hobbacher, 2004: 45)

Note that the curve selected is for steel with a constant amplitude loading. This selection was made based on the "shape" of the stress signal used for the analysis as shown in figure 5.17.

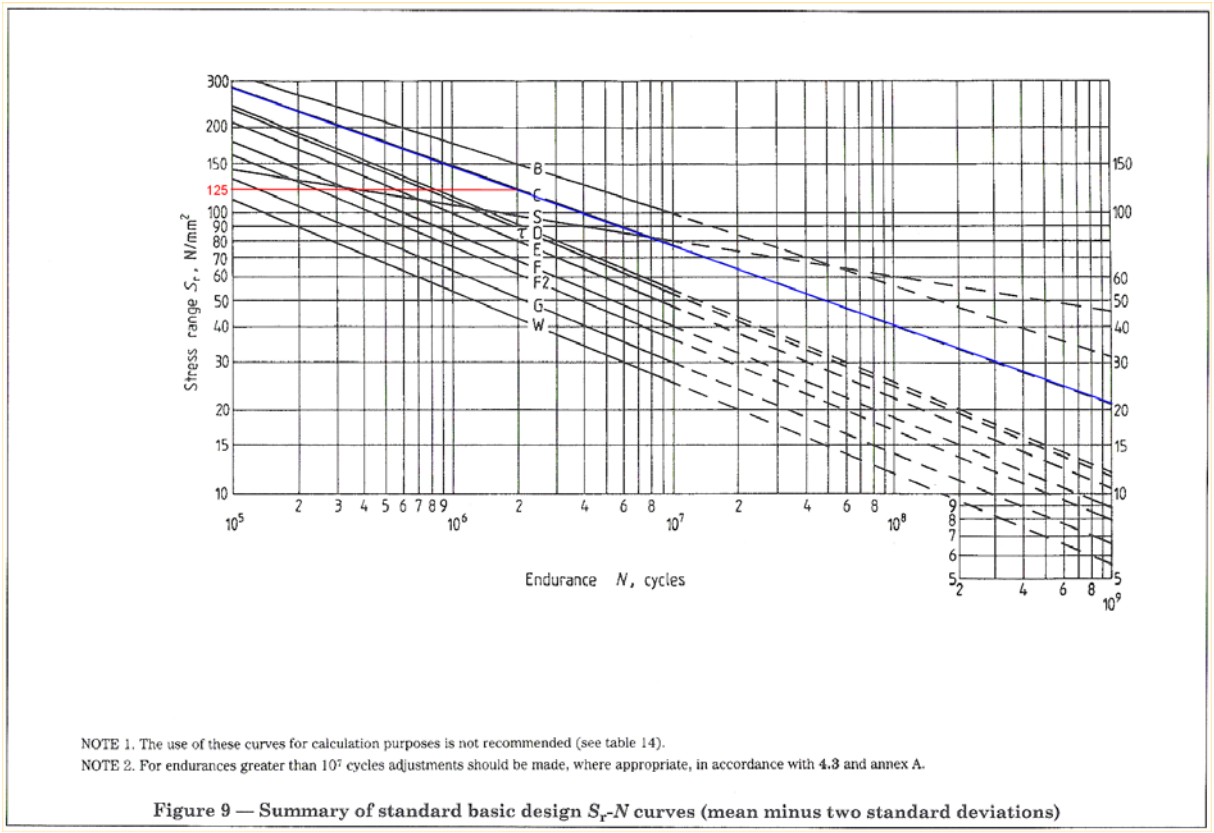

NOTE 1. The use of these curves for calculation purposes is not recommended (see table 14).
NOTE 2. For endurances greater than 10^7 cycles adjustments should be made, where appropriate, in accordance with **4.3** and annex A.

Figure 9 — Summary of standard basic design S_r-N curves (mean minus two standard deviations)

Figure 5.6: Proposed S-N curve for the selected weld construction – BS code.
Source: Fatigue design and assessment of steel structures, BS7608:1993

From the above detail, the component S-N curve for the FAT 125 class weld was selected for the fatigue life analysis. This curve was further adjusted to provide a represent able fatigue life for the structure.

5.2 S-N curve characterisation for unwelded material

The Tippler structure is constructed from BS 4360 Grade 43 A as shown in Figure 5.7.

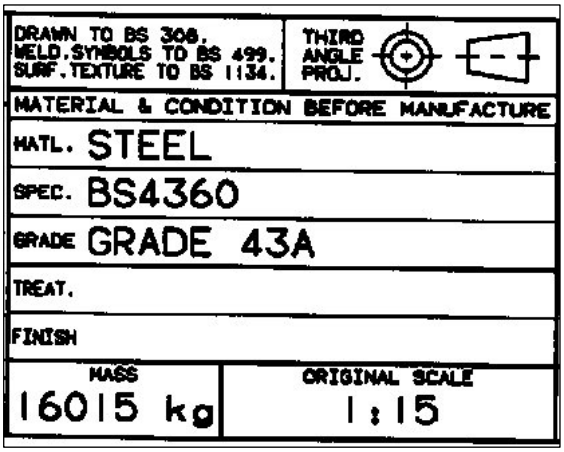

Figure 5.7: Material specification for Tippler structure
Source: Extracted from original Tippler platform drawing

No definite endurance limit values for the material were obtainable from the literature so the endurance limit was calculated from the method as described in paragraph 2.1.4.

The material properties obtained are as follows:

Table 5.1: Material properties for BS 4360 Grade 43A

Source: Material specification sheet – Appendix C

Material Property	Value
Ultimate tensile strength	430 – 580 MPa
Yield strength 16 mm < t < 40 mm	265 MPa

Note the variation in the ultimate tensile strength as listed. For this analysis, the lower value of 430 MPa was used to allow for all possible material qualities. Furthermore, the yield strength of the material was selected for a 16 – 40 mm plate as the construction of the platform corner as shown in Figure 5.1 consists of a 30 mm base plate welded to a 16 mm side plate.

The material properties as noted were used to construct the unmodified S-N curve for the material by using the equations as listed in Bannantine et al. (1990: 4). The endurance limit calculated does not allow for any factors that would reduce the fatigue life of the structure.

$$b = -\frac{1}{3}\log_{10}\frac{S_{1000}}{S'_e} = -\frac{1}{3}\log_{10}\frac{0.9S_{ut}}{0.5S_{ut}} = -\frac{1}{3}\log_{10}\frac{387}{215} = -8.50908e-2$$

$$C = \log_{10}\frac{(S_{1000})^2}{S'_e} = \log_{10}\frac{(0.9S_{ut})^2}{0.5S_{ut}} = \log_{10}\frac{(387)^2}{215} = 2.84298$$

The equation for the construction of the unmodified S-N curve between 10^3 and 10^6 cycles is therefore:

$$S = 10^C N^b$$
$$S = 10^{2.84298} N^{-8.50908e-2} \qquad (5.1)$$

This equation was used to construct the unmodified S-N curve for the material. The endurance limit after 10^6 cycles was kept constant for this S-N curve.

The S-N curve as constructed was now adapted to allow for all effects that would influence the endurance limit for the material for this specific application.

a) Surface finish factor - k_a

The material used for the construction of the platform structure is hot rolled plate as indicated in the material specification attached in Appendix C. A correction factor for surface roughness (k_s - in this case k_a), as indicated in Figure 2.4, of 0.74 was selected for hot rolled plate with a tensile strength of 430 MPa.

$$k_a = 0.74$$

b) Size factor - k_b

The FEA results obtained indicate almost no bending at the crack position, therefore only axial loading is considered. Shigley (1986: 246) notes a size factor value for axial loading of 1.0 while Dowling (1999: 446) notes values between 0.7 and 0.9 for the same load case. Further, note that Boyer (2005: 33) quotes a modifying factor for different load conditions in a component (Figure 2.6). This value relates to the size factor as it also modifies the material properties for different load conditions. For this study, the value quoted by Shigley will be used as some of the size effects are already included in the material specifications as used (Table 5.1).

$$k_b = 1.0$$

c) Reliability factor - k_c

The purpose of this study is to evaluate the fatigue life of the modified Tippler structure. An infinite fatigue life would be the most appropriate in this case as the structure is operated without definite maintenance intervals as previously indicated. For this reason a 99% reliability would be appropriate. This translates to a k_c value of 0.814 (Shigley, 1986: 251)

$$k_c = 0.814$$

d) Temperature factor - k_d

The Tippler is operated at a temperature less than 350 degrees Celsius. For this reason k_c was selected as 1.0 (Shigley, 1986: 253)

$$k_d = 1.0$$

e) Shape factor - k_e

The construction of the Tippler structure does not allow for an easy estimation of a value for the shape factor. For this reason, it was decided to set the value for k_e equal to one. This would have no effect on the results of the evaluation as the stress results obtained from the FEA include the effect of the stress concentration at the platform corner. Furthermore, the modified S-N curve obtained from the calculations was used for the analysis of both the unmodified and modified structure, cancelling the effect of this omission.

$$k_e = 1.0$$

f) Miscellaneous effects - k_f

The presence of corrosion at the position of the cracks indicates that the S-N curve needs to be modified to allow for corrosion. Modifying factors for corrosion are, however, not well quantified and listed. Figure 2.4 indicates that a value of 0.47 for saltwater corrosion and 0.66 for freshwater corrosion can be selected for a material with a tensile strength of 430 MPa. Many authors, including the British Standard (BS 7608:1999: 32), however, list a value of 0.5 for corrosion in seawater for materials with an even lower yield strength. The structure is, however, painted and not operated directly in contact with salt water. The quoted values is therefore very conservative, and would not provide a clear representation of the actual conditions. Warnock and Benham (1976, Table 22.2) provide endurance limits for 0.5% carbon steels with different surface coatings as shown in Figure 2.9. The data indicates that an enamel coated part has a 2.7 times higher endurance limit than an uncoated component.

$$k_f = 1.0$$

Therefore:

$$\begin{aligned} S_e &= k_a k_b k_c k_d k_e k_f \cdot S'_e \\ &= 0.74 \cdot 1.0 \cdot 0.814 \cdot 1.0 \cdot 1.0 \cdot 0.5 \cdot 1.0 S_{ut} \\ &= 129.5 MPa \end{aligned}$$

The modifying factors as selected were used to modify the endurance limit of the S-N curve for the Tippler material as indicated in figure 5.8. The endurance limit for the unwelded material at 10^6 cycles was calculated at 129.5 MPa. Note that at 1000 cycle's values of 0.9Sut as suggested by Shigley (Dowling, 1999: 446) was used for both curves. Furthermore, the stress life approach is not recommended for predicting fatigue life values for less than 1000 cycles. Both axes were constructed using a log scale as shown in Dowling (Dowling, 1999: 445).

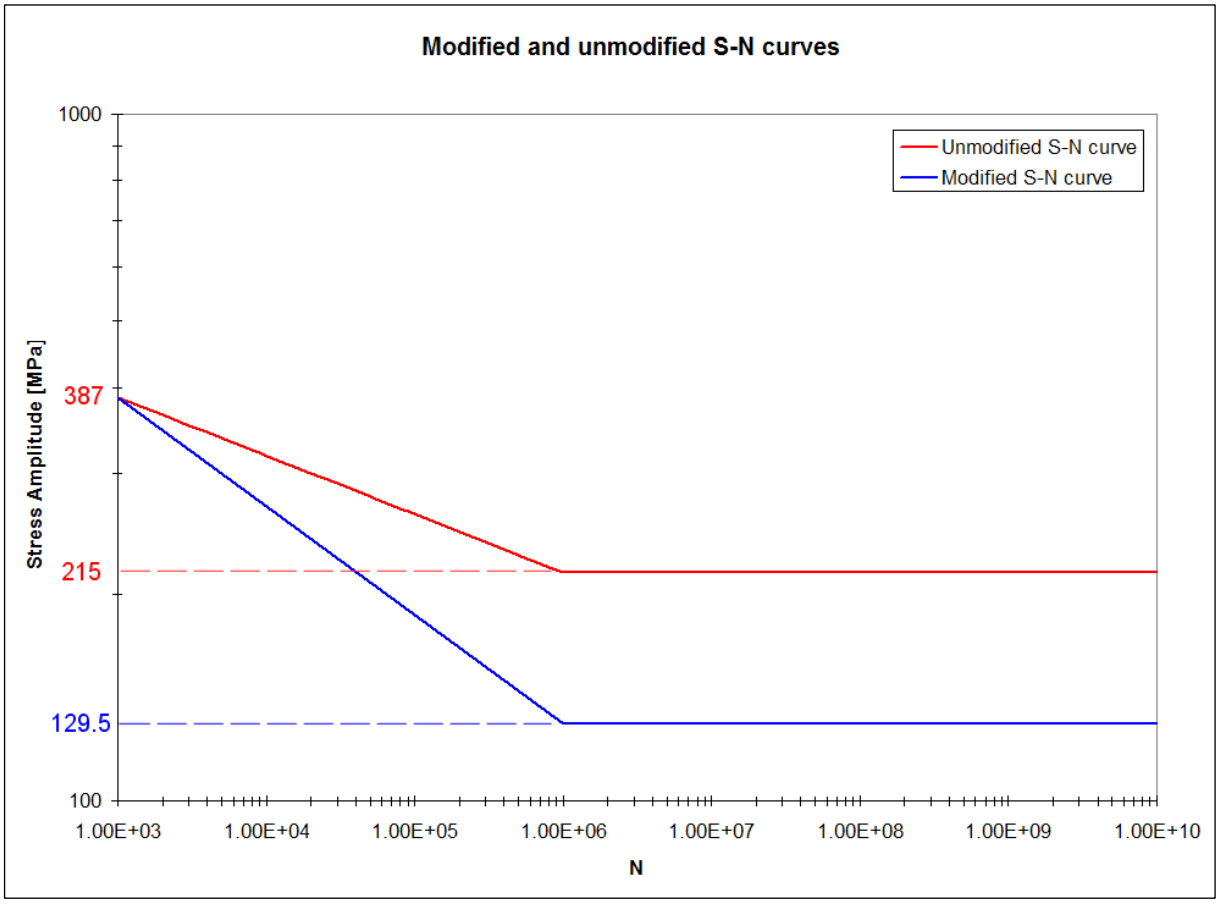

Figure 5.8: Unadjusted and adjusted S-N curves

The data indicates that should the maximum stress amplitudes at the high stress areas in the unwelded material of the structure remains below 129.5 MPa no crack initiation would take place, ensuring an infinite fatigue life for these positions.

The S-N curve as presented above would however be only applicable where no corrosion is present.

5.3 Stress history data

The stress history data as shown in Figure 3.14 was scaled according to a scaling factor calculated from the FEA results to relate the stress at the strain gauge

positions on the platform to the stress in the platform corners. This scaled data was then used to calculate a miscellaneous effect factor, k_f that provides a structural life of approximately 10 years on the original structure in both the front and back corners. Once the representative values of k_f was calculated, S-N curves was constructed that was used to evaluate the re-designed structure's fatigue life. Note that for the final fatigue life comparison the original model and modified FEA model were meshed with a finer mesh at the crack positions to obtain a more accurate representation of the stresses at these positions.

5.3.1 Stress scale factor calculation

In order to determine the stress values at the platform corners while rotating, the stress values obtained from the strain gauge readings had to be correlated to the stress values as determined from the FEA results for the corner positions. To do this scale factors was calculated based on the magnitude of the principal stress in the platform corners.

To be able to calculate the main principal stress in the platform corners a coordinate system was created approximately tangential to the curve formed by the platform base plate in the corner in question as indicated in Figure 5.8. The stress values relative to the coordinate system, i.e. in the x-direction (σ_{xx}), y-direction (σ_{yy}) and the shear stress (τ_{xy}) for each corner were obtained from the FEM for each tip position.

From these values the direction of the main principal stress (θ) relative to the created coordinate system was calculated from the following equation:

$$\tan 2\theta = \frac{2\tau_{xy}}{\sigma_x - \sigma_y} \qquad \text{(Gere \& Timoshenko, 1991: 387)}$$

The results of this calculation can be seen in Figure 5.6.

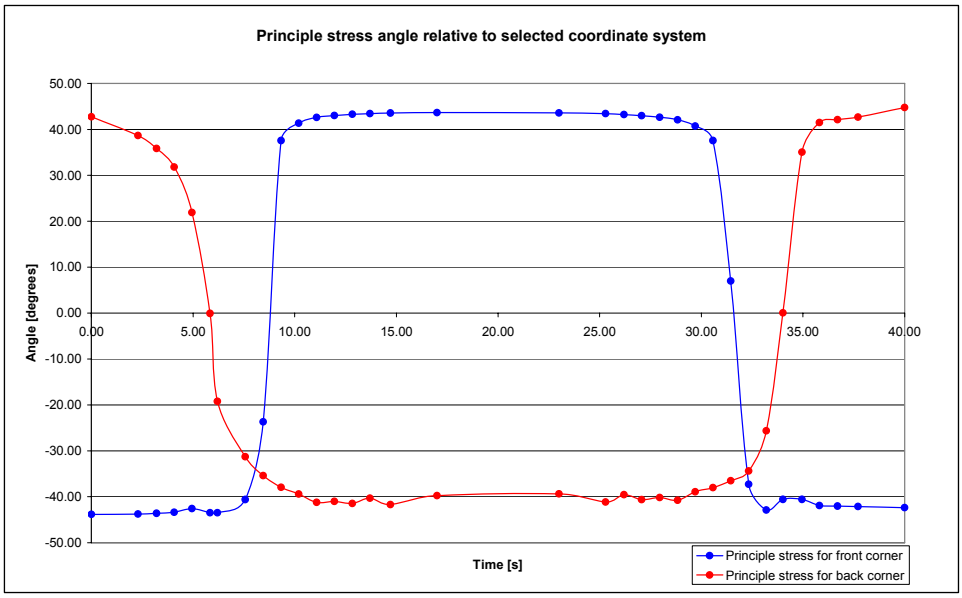

Figure 5.9: Calculated principal stress direction

Note the difference in direction caused by the difference in the element orientation relative to the selected coordinate system. From the plots, it is clear that the main stress direction is at an angle of between 40 and 44 degrees to the coordinate system as selected. The direction of the stress also remains constant for the largest part of the tip cycle and only varies when the stress direction changes from tension to compression and back during the tip cycle. For the purpose of this study, the main stress direction was selected at 42 degrees as shown in Figure 5.7. Note the correlation between the maximum principal stress direction as calculated (σ_1) and the direction of crack growth.

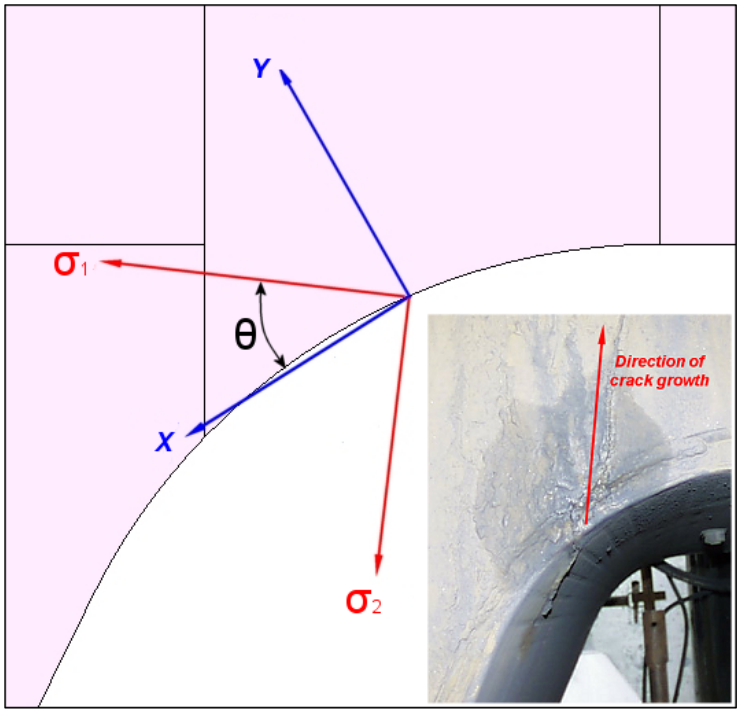

Figure 5.10: Maximum principal stress direction (σ_1)

Note, however, that the calculated principal stresses relate to mid-plane stresses of the elements as a stress perpendicular to the outside surface in this case σ_2 cannot exist on the outside surface of the structure.

From the directional stresses values and the shear stress values as obtained, the principal stress in the 42-degree direction was calculated for every tip position from the following equation:

$$\sigma_1 = \frac{\sigma_x + \sigma_y}{2} + \frac{\sigma_x - \sigma_y}{2}\cos 2\theta + \tau_{xy}\cos 2\theta$$ (Gere & Timoshenko, 1991: 382)

The calculated maximum principal stress (σ_1) as calculated is shown in Figure 5.8. Note that the average stress at the front corner is marginally higher than the average of the back corner.

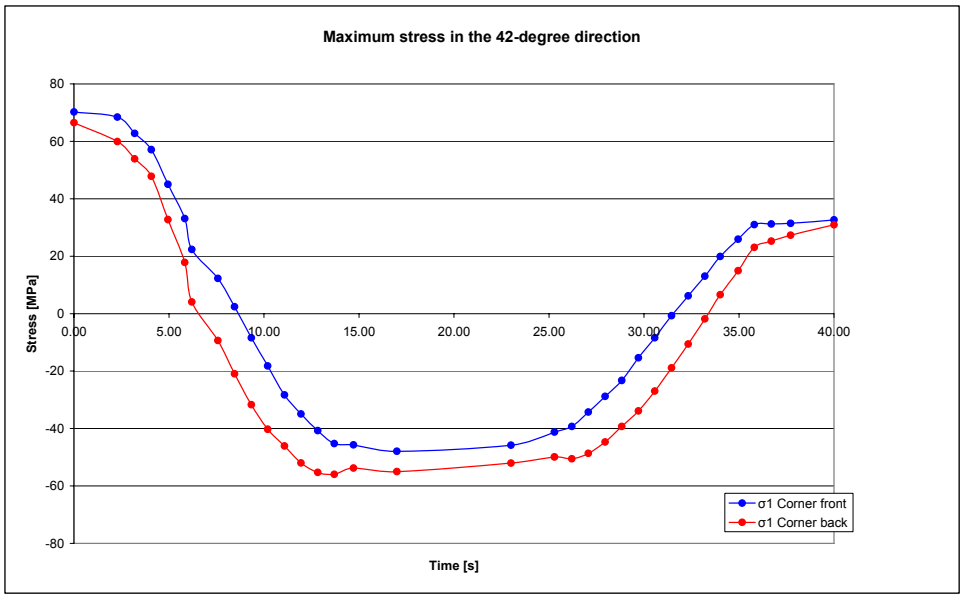

Figure 5.11: Calculated principal stress values for each tip position

The maximum principal stress values calculated from the FEA results at the platform corners were then compared to the stress values obtained from the FEA results at the positions where the strain gauges were applied. A comparison between the stress values is shown in Figure 5.9. Note that the stress values in the platform corners follow the trend of the stresses measured at the strain gauge positions.

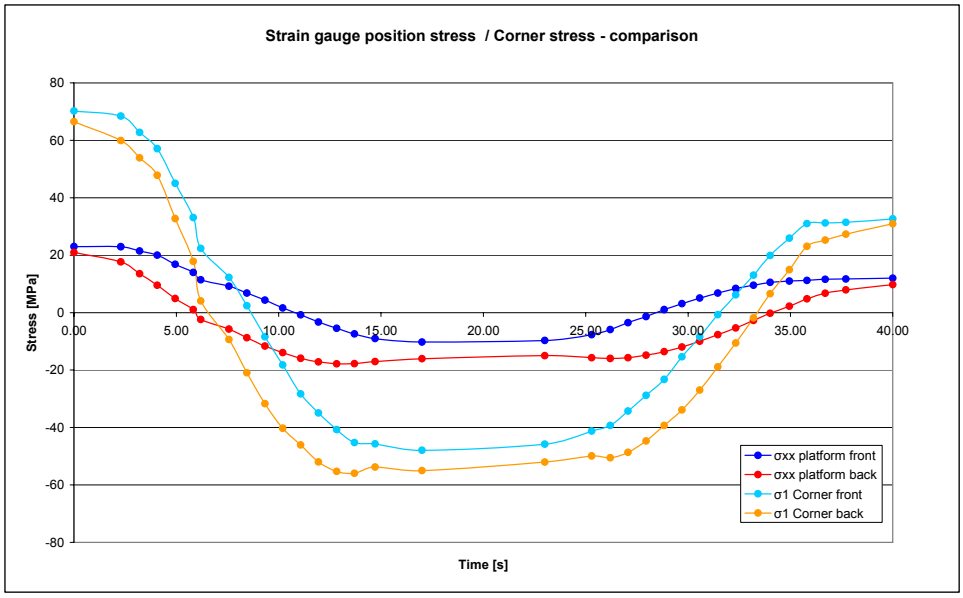

Figure 5.12: Strain gauge position stress / Corner stress comparison (FEA results)

The stress data obtained from the FEA results at the strain gauge positions and the platform corners were used to estimate scaling factors that was used to scale the stress data as obtained from the strain gauge readings. These scaling factors should provide an accurate representation of the actual stresses as experienced in the platform corners.

The following equation was used to scale the strain gauge position stress values:

$$\sigma_{corner} = k_{scale}\sigma_{strain\ gauge} \tag{5.2}$$

To calculate the first iteration value for k_{scale}, the FEA stress values obtained from the FEA model at the strain gauge positions was multiplied by a scale factor calculated from the stress in the corner position divided by the stress at the strain gauge position for the Tippler in the 0-degree position. This was done for both the front and rear strain gauge position data sets. These scaled FEA stress values was then plotted against the FEA stress values obtained from the corner positions. The next step was to adjust the scale factors until the scaled data accurately approximated the minimum and maximum stress values, as experienced by the Tippler structure during the tip cycle. Note that the first value of both data sets (corner and scaled data) were set to zero to make the data comparison easier.

Figures 5.10 and 5.11 shows the scaled strain gauge position FEA stress values, for different scaling factors, plotted with the FEA stress values obtained

from the corner positions. From the figures it was estimated that a scaling factor of approximately 3.55 for the front strain gauge data and 3.20 for the back strain gauge data would provide the best estimation of the corner stress values, should the strain gauge position data be scaled.

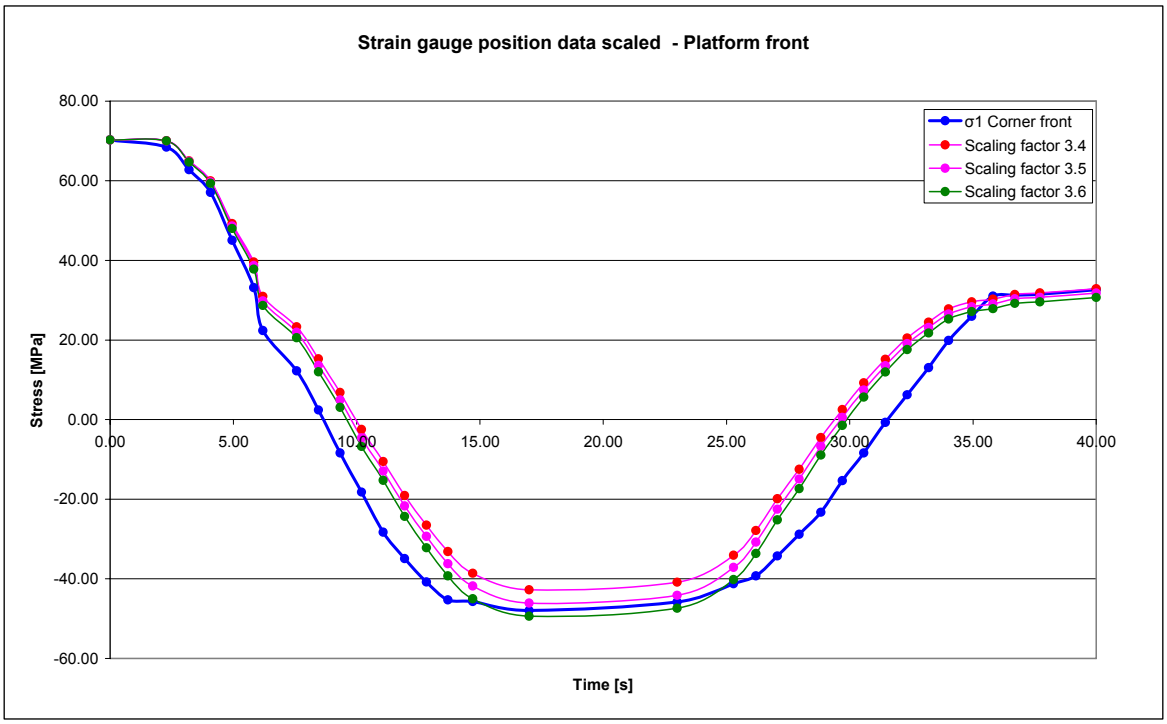

Figure 5.13: Scaled front strain gauge position / Corner stress comparison

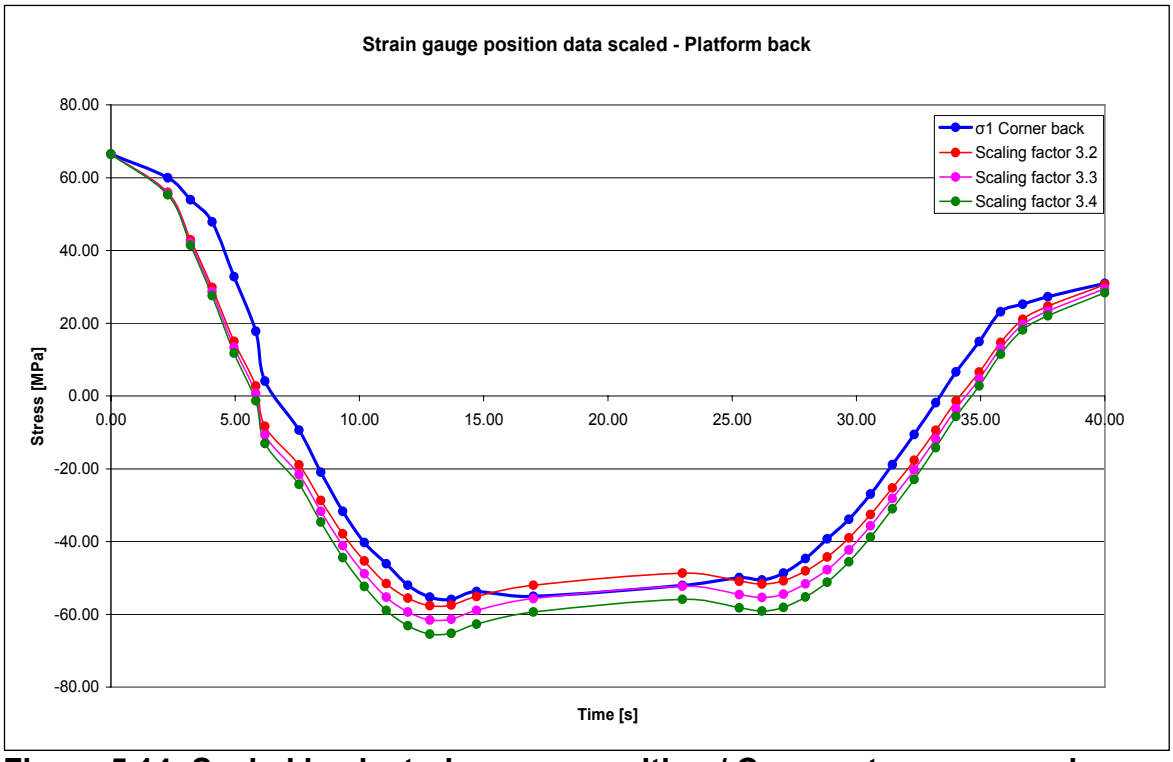

Figure 5.14: Scaled back strain gauge position / Corner stress comparison

The stress values obtained at the strain gauge positions multiplied by the scale factors calculated provide a good estimation of the stress values as obtained from the FEA at the corner positions on the platform where the cracks developed. It is thus clear that the stress at the strain gauge positions can be scaled to obtain the stresses in the platform corners for the complete tipping cycle.

5.3.2 Strain gauge stress data scaling

The strain gauge data obtained from the front and back strain gauge readings was imported into the I-DEAS software package's durability module. Both data sets were then scaled according to the scale factors as calculated in paragraph 5.2.1. The original and scaled data are shown in Figures 5.12 and 5.13.

From the scaled data, a comparative train tip cycle was compiled for 50 wagons as shown in Figure 5.14. It was decided to exclude the stress peak values as seen in the strain gauge data from the comparative data, as it is unclear if these stress peaks would be present in the platform corners, seeming that they are not present at the front strain gauge position.

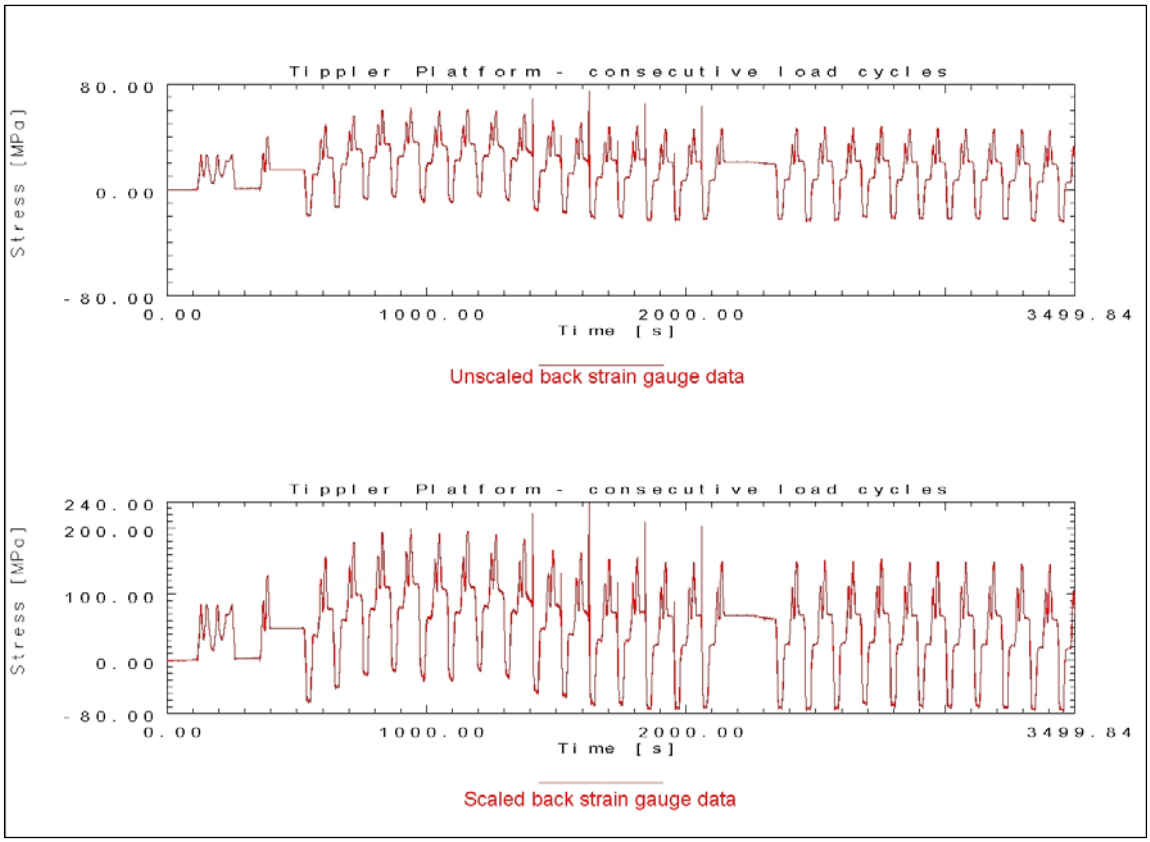

Figure 5.15: Scaled and unscaled back strain gauge data

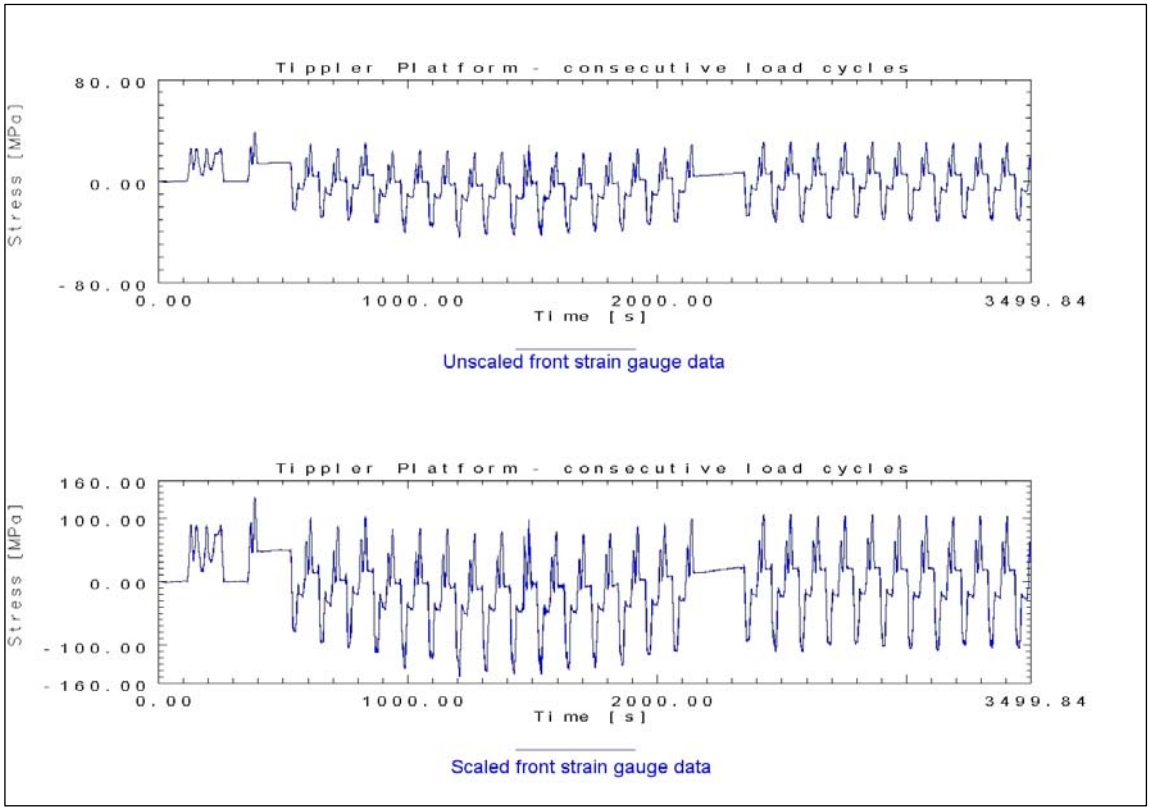

Figure 5.16: Scaled and un-scaled front strain gauge data

Figure 5.14: Scaled and unscaled front strain gauge data

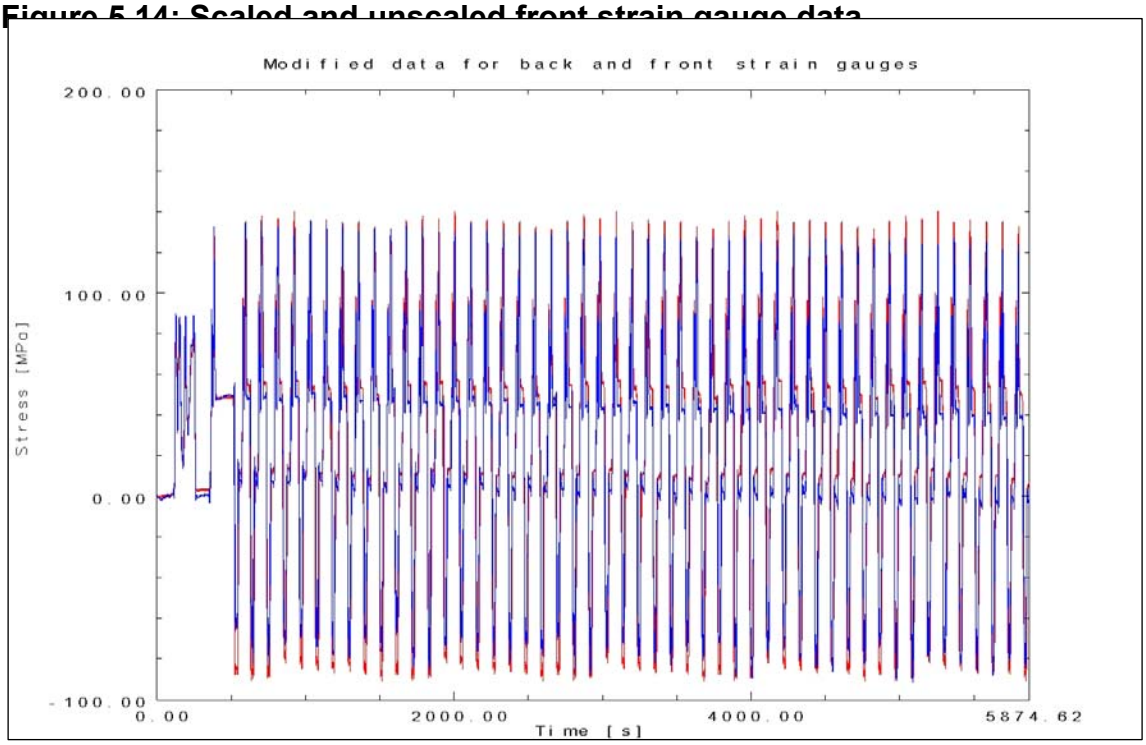

Figure 5.17: Comparative data set for one complete train tip cycle

The stress data as shown in figure 5.17 represents the stress cycle that would be experienced by the Tippler structure during one train cycle of 100 wagons. With the current throughput of 72 million tons per year this cycle would be repeated 2146 times per year. For each individual tip cycle the stress amplitude stays relatively constant and repeatable. For this reason it was decided to use the constant stress S-N curve for the analysis.

5.4 Fatigue life estimation and comparison

For a first estimation, the fatigue life for the cracked area was calculated from the data as shown in figure 5.17 and the S-N curve for a FAT-125 class weld as shown in figure 5.18.

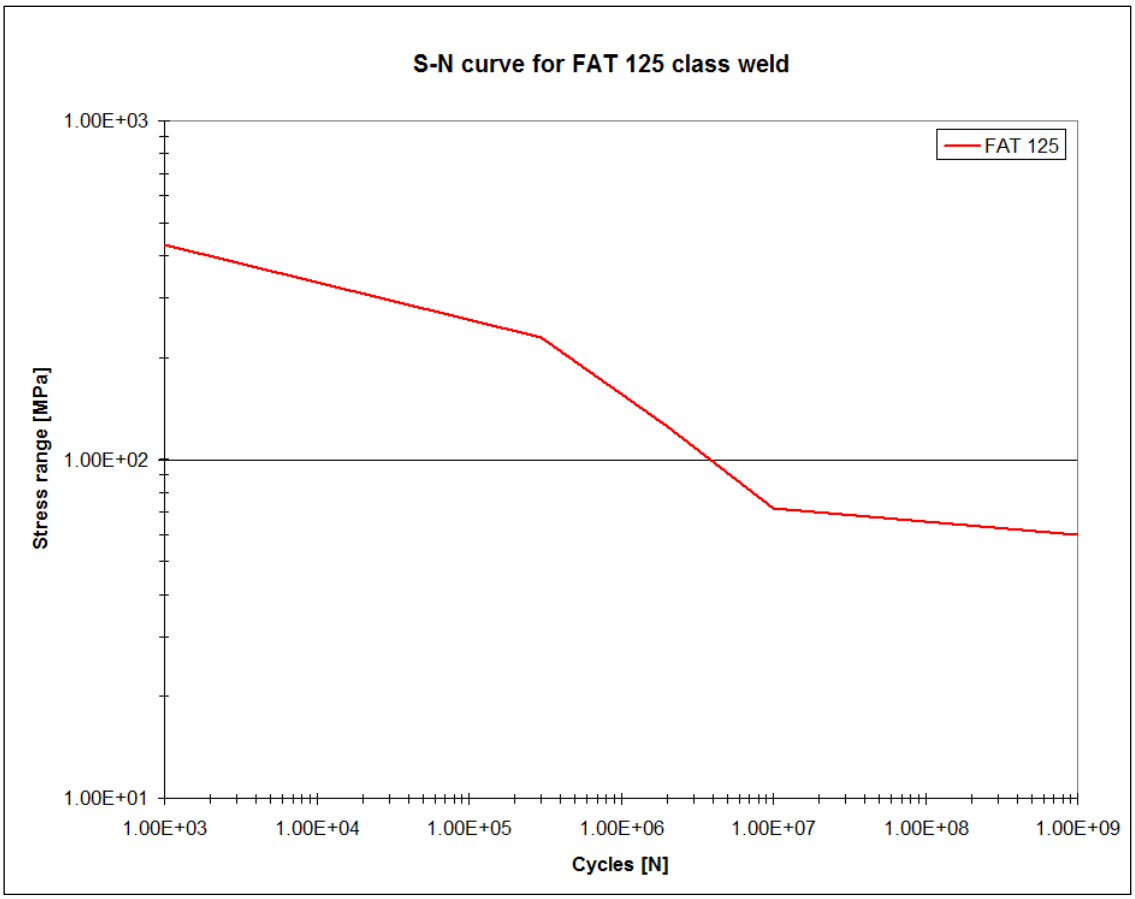

Figure 5.18: Un-adapted component S-N curve for FAT 125 class weld

The calculated fatigue life results for the front and back corner of the structure is listed in table 5.2. Note that for both corners the fatigue life is much shorter than the obtained life of 10 years. This is due to the build-in safety margin for the FAT curves that allows for a 97,6 % chance that no cracks would develop in the welds during the first 3 to 4 years of the structures life, if subjected to the stress levels as shown in figure 5.17. It is not exactly known when the cracks

developed, but it can be safely assumed that the cracks did not develop within the first 3 years of the structure's life. However, once the cracks started to grow from the welds, it is assumed that the crack growth phase was quite short due to the corrosive environment. For this reason, the representative S-N curve was adjusted to allow for a crack-from-weld initiation period close to the 10-year structural life.

Table 5.2: Rain flow data for original structure for un-modified FAT 125 curve

Back corner fatigue					Front corner fatigue				
Range Number	Range Values	Counts	Damage Ratio	Percent Damage	Range Number	Range Values	Counts	Damage Ratio	Percent Damage
1	10	5.53E+04	0.00E+00	0	1	10	5.69E+04	0.00E+00	0
2	20	112	0.00E+00	0	2	20	124	0.00E+00	0
3	30	5	0.00E+00	0	3	30	0	0.00E+00	0
4	40	0	0.00E+00	0	4	40	0	0.00E+00	0
5	50	41	0.00E+00	0	5	50	1	0.00E+00	0
6	60	16	0.00E+00	0	6	60	50	0.00E+00	0
7	70	0	0.00E+00	0	7	70	1	2.03E-09	0
8	80	1	8.97E-08	0.001	8	80	1	1.30E-07	0.001
9	90	1	1.78E-07	0.001	9	90	0	0.00E+00	0
10	100	0	0.00E+00	0	10	100	1	2.39E-07	0.002
11	110	0	0.00E+00	0	11	110	0	0.00E+00	0
12	120	0	0.00E+00	0	12	120	0	0.00E+00	0
13	130	0	0.00E+00	0	13	130	0	0.00E+00	0
14	140	1	6.01E-07	0.004	14	140	1	7.28E-07	0.005
15	150	0	0.00E+00	0	15	150	0	0.00E+00	0
16	160	0	0.00E+00	0	16	160	0	0.00E+00	0
17	170	0	0.00E+00	0	17	170	0	0.00E+00	0
18	180	0	0.00E+00	0	18	180	0	0.00E+00	0
19	190	0	0.00E+00	0	19	190	0	0.00E+00	0
20	200	0	0.00E+00	0	20	200	0	0.00E+00	0
21	210	0	0.00E+00	0	21	210	5	1.22E-05	0.087
22	220	14	4.04E-05	0.27	22	220	24	6.43E-05	0.459
23	230	30	9.13E-05	0.609	23	230	20	6.24E-05	0.446
24	240	5	0.00E+00	0	24	240	0	0.00E+00	0
25	250	0	0.00E+00	0.00	25	250	0	1.40E-45	0
Out of range counts		0.00E+00			Out of range counts		0.00E+00		
Total counts		5.55E+04			Total counts		5.72E+04		
Out of range damage		0.00E+00			Out of range damage		0.00E+00		
Total damage ratio		1.50E-04			Total damage ratio		1.40E-04		
Crack initiation estimate		6.68E+03	Events		Crack initiation estimate		7.15E+03	Events	
		3.1	Years				3.3	Years	

In order to obtain a representative S-N curve that would provide a fatigue life of as mentioned the reliability was decreased by pushing the mean minus two standard deviations FAT curve more towards the mean as originally calculated. This was accomplished by dividing the S-N curve data by 0.868 to obtain a 50% probability of survival or mean curve. The value was obtained from figure 5.19. The fatigue lives obtained for the mean curve was approximately 4.9 years for the back corner and 5.2 years for the front corner of the structure. It was therefore decided to further push the curve up to increase the probability of failure to 99% by dividing the data by a further 0.814, that would represent a mean plus three standard deviations curve. For this curve as shown in figure 5.20, a fatigue life of 9.3 years for the back corner and 9.9 years for the front

corner were obtained. The S-N curve as constructed closely represents the actual life obtained from the fracture and was therefore used for the comparative assessment. Note that the value at 1000 cycles was again held constant as discussed in paragraph 5.2.

Table 7-7 RELIABILITY FACTORS k_e CORRESPONDING TO AN 8 PERCENT STANDARD DEVIATION OF THE ENDURANCE LIMIT

Reliability R	Standardized variable z_r	Reliability factor k_e
0.50	0	1.000
0.90	1.288	0.897
0.95	1.645	0.868
0.99	2.326	0.814
0.999	3.090	0.753
0.999 9	3.719	0.702
0.999 99	4.265	0.659
0.999 999	4.753	0.620
0.999 999 9	5.199	0.584
0.999 999 99	5.612	0.551
0.999 999 999	5.997	0.520

Figure 5.19: Reliability factors for 8% standard deviation

Source:. Mechanical engineering design Shigley, J.E. 1986: 251

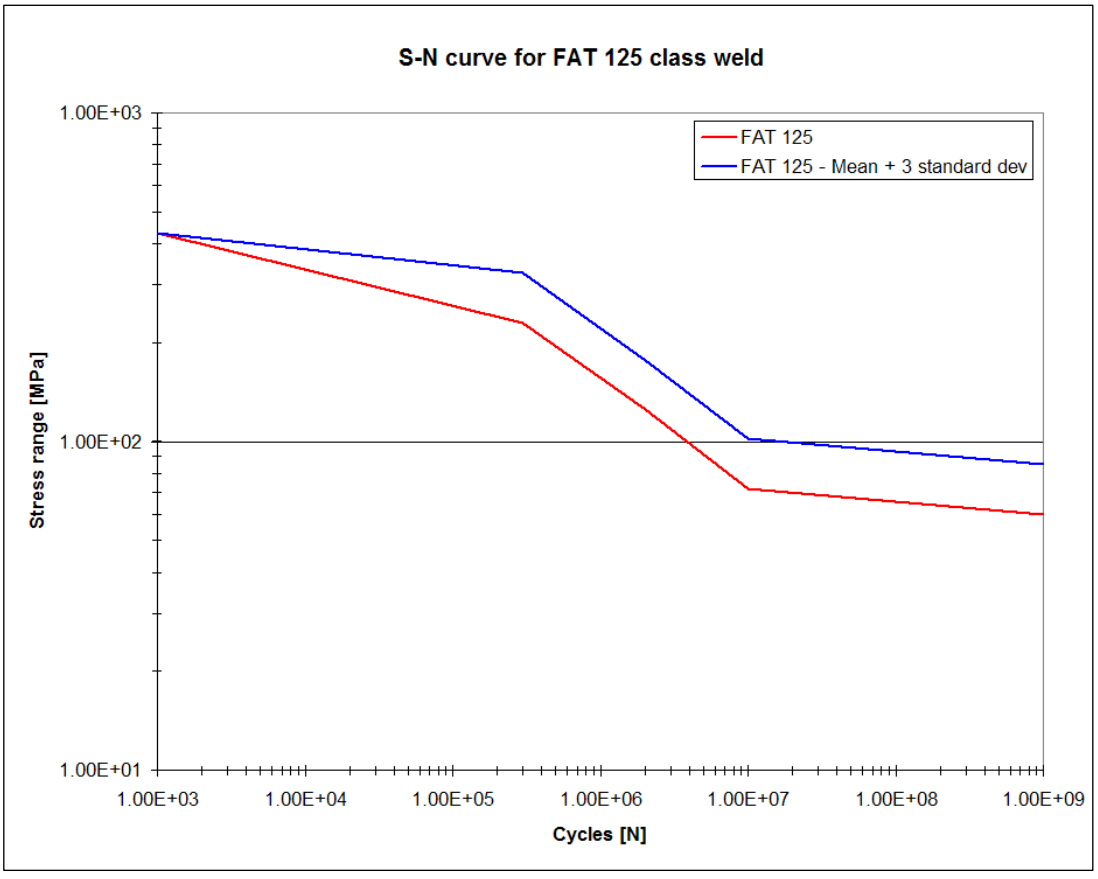

Figure 5.20: Un-adapted component S-N curve for FAT 125 class weld

For the fatigue life comparison the original structure and modified structure were meshed with a finer mesh on the platform structures to obtain a more accurate representation of the scaling factors to be used for the fatigue life comparison.

Detail of the modifications introduced to the Tippler platform is shown in Figure 5.21. Note that the original platform was symmetrical, therefore the different views. These modifications were made to the FEA model used for the analysis as shown in Figure 5.22.

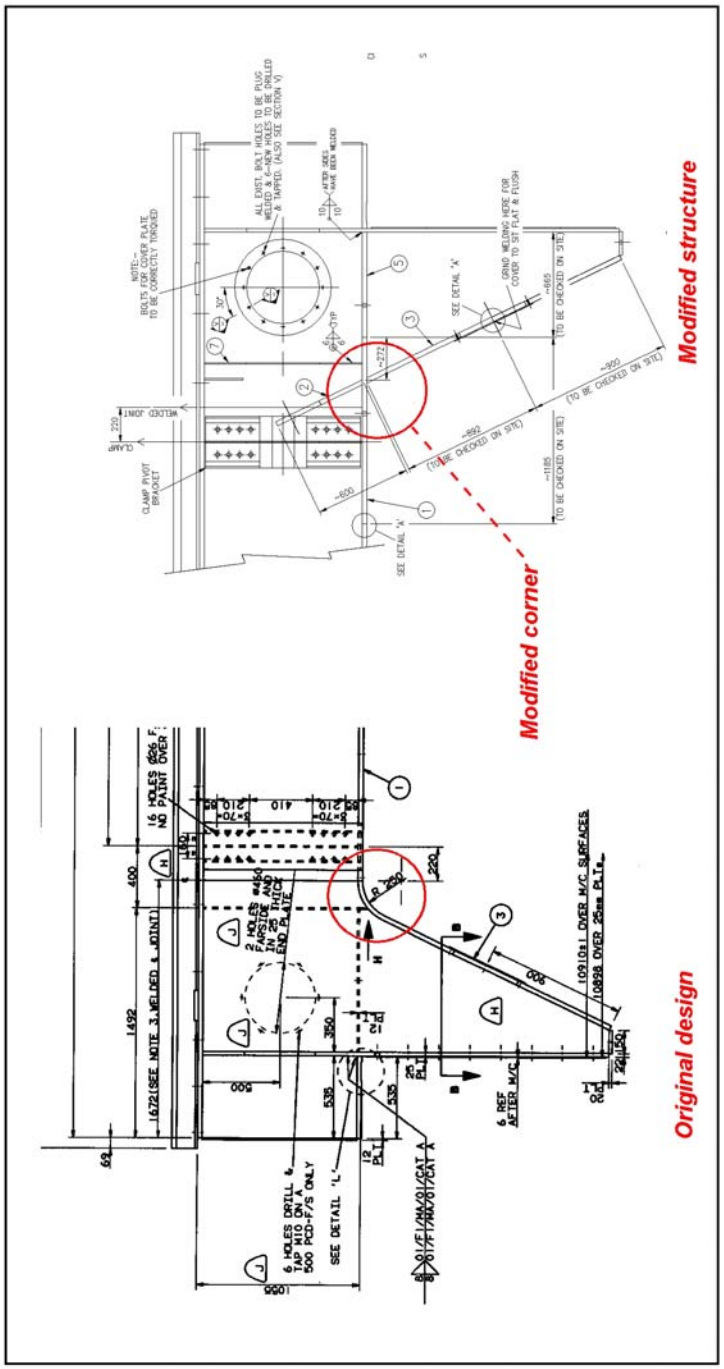

Figure 5.21: Modifications made to Tippler platform structure

Source: Extracted from structural drawings as provided by RBCT

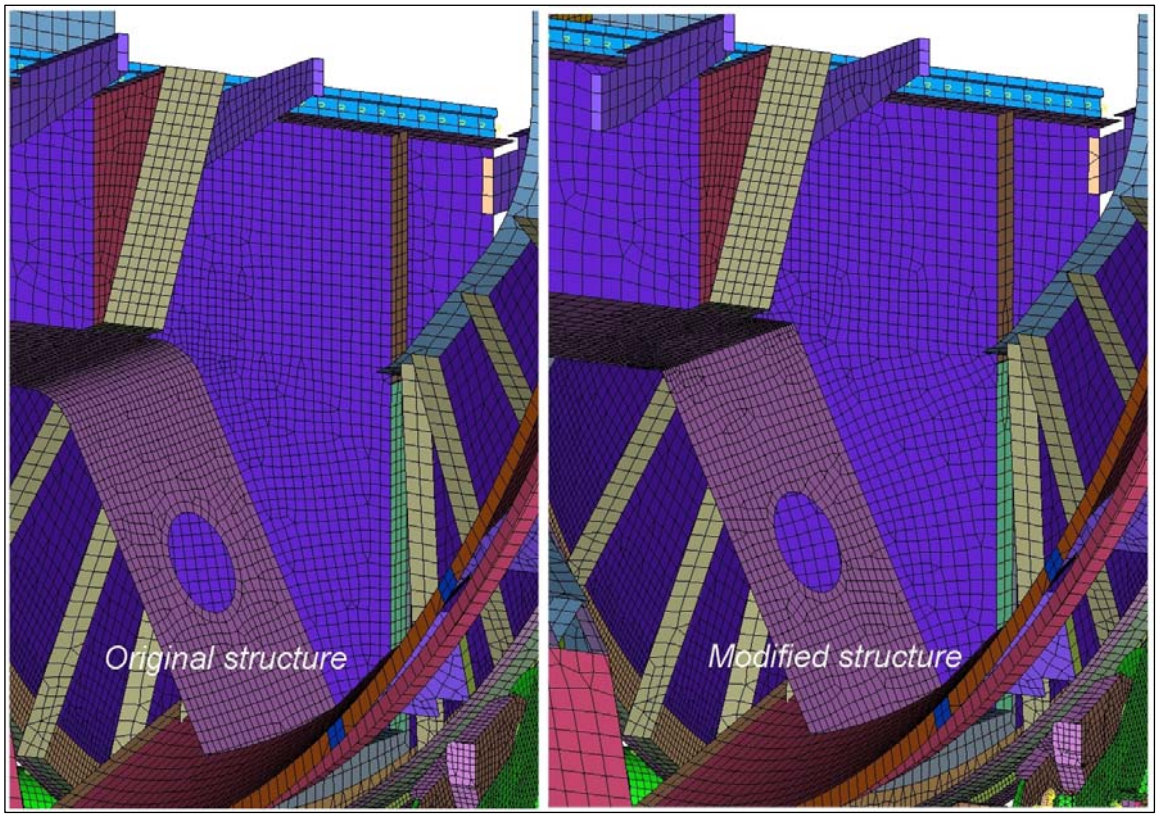

Figure 5.22: FEA models of original and modified structures

By evaluating the stress results shown in Figure 5.9, it was found that the highest stress values in the platform corners are present when the Tippler is in the 0-degree position. These values would be the highest when the link between the two loaded wagons passes over the centre line of the platform, i.e. the two ends of the wagons are positioned close to the centre of the platform, effectively applying a load of 84 t to the centre of the platform. For this load position, a stress of approximately 140 MPa was calculated in the corner of the original Tippler structure.

As the corner geometry of the modified Tippler structure is different, it was necessary to recalculate the scaling factor for the modified structure. To do this it was decided to use three of the load conditions that are possible when the Tippler is in the 0-degree position. These positions are an empty cage under gravitational load, a cage with one empty wagon in place and a cage where a full wagon is in place. The approximate loads on the platform would be 0 kg, 20 250 kg, and 104 000 kg, based on the wagon specification (Appendix A). Boundary conditions simulating these three load cases were applied to both the original and modified FEA models. In both cases the effect of gravity on the system was taken into account in the boundary conditions.

The same coordinate system as previously created was again used for a reference direction to determine the x-direction stress, y-direction stress and shear stress for the three load conditions. Note that the highest stress point on the modified structure

is not directly in the corner of the platform, but slightly in front of it on the platform bottom plate as indicated in Figure 5.23 for the loaded wagon in position.

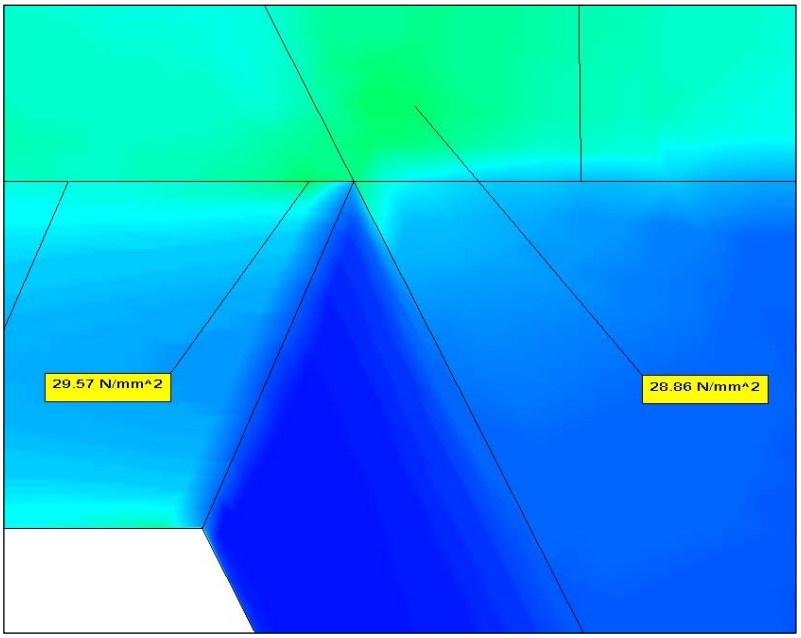

Figure 5.23: Maximum principal stress in platform corner

From these stress values the direction of the principal stresses (θ) was calculated for each load case for the two models. The main principal stress angle was calculated at approximately 39 degrees for the modified structure where the direction of the original structure's maximum principal stresses was at an angle of approximately 42 degrees. This indicates that the stresses in the corners will still follow the same trend during the tip cycle as the principal stress of the two configuration's directions remain very close together. The weld details and stress direction in the high stress area of the modified structure, is the same as for the weld details as indicated in figures 5.1 and 5.2.

The comparison between the calculated principal stresses and the measured platform stresses for the original and modified structures is shown in Figures 5.24 and 5.25. A reduction in the corner stresses is clearly visible for the modified structure. From this data the scaling factors for both the structures were calculated by dividing the maximum principal stress in the corner as calculated from the FEA stresses by the strain gauge position stress also obtained from the FEA for each load cases, and then calculating the average scaling factor from the scale factors of the three separate load cases. The scale factors is listed Table 5.3.

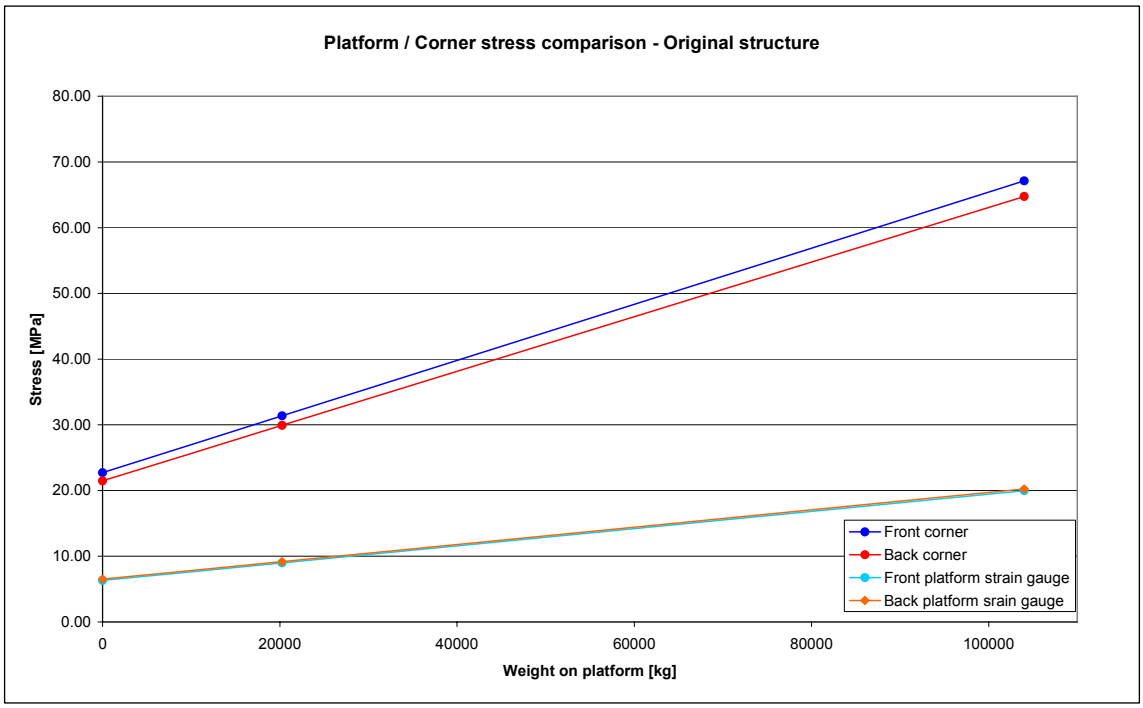

Figure 5.24: Corner and platform stresses for original Tippler structure (FEA results)

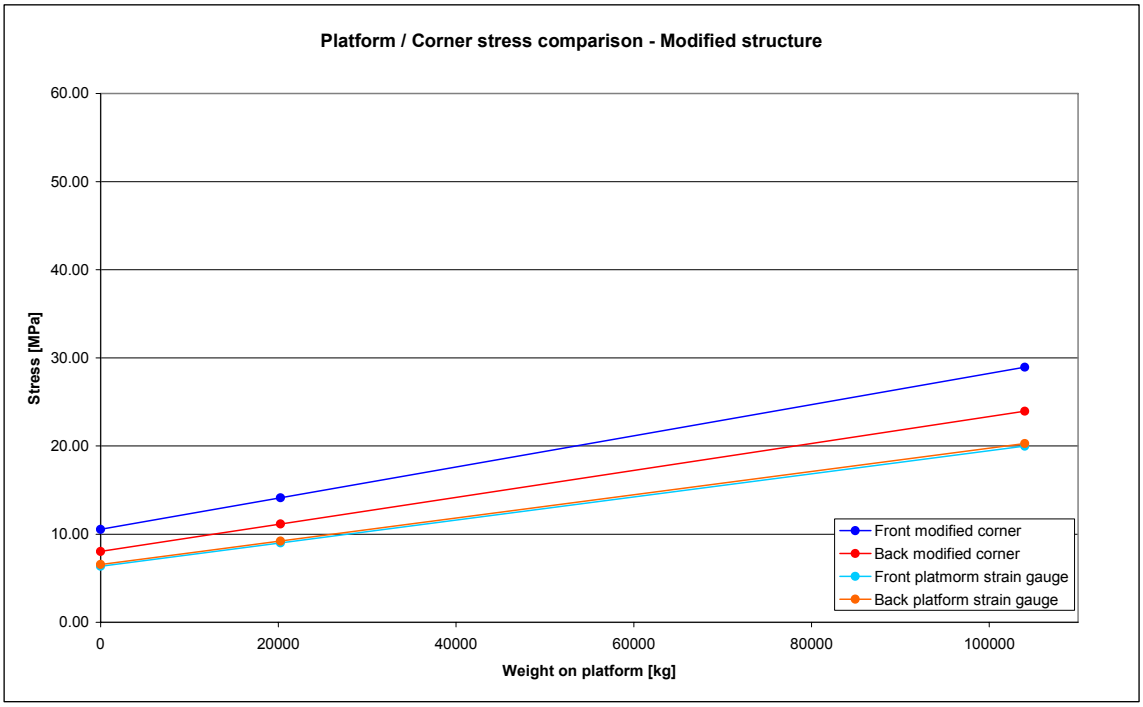

Figure 5.25: Corner and platform stresses for modified Tippler structure (FEA results)

Table 5.3: Calculated scaling factors for original and modified Tippler structures

Structure	Scaling Factor	
	Front corner	Back corner
Original	3.48	3.25
Modified	1.56	1.21

Note the slight change in the scaling factor from the original values as calculated in paragraph 5.2.2 for the original structure. This change is about 2% for the front corner and 1.5% for the rear corner and would have an insignificant effect on the life calculations, especially for comparative purposes. The scaling values were used to generate comparative stress data sets for each of the corners for the modified Tippler structure as shown in Figure 5.26. These data sets were evaluated with the I-DEAS durability module to calculate the fatigue lives of the modified Tippler structure. The same component S-N curve as shown in Figure 5.20 were used for the front and back corners of the modified Tippler structure.

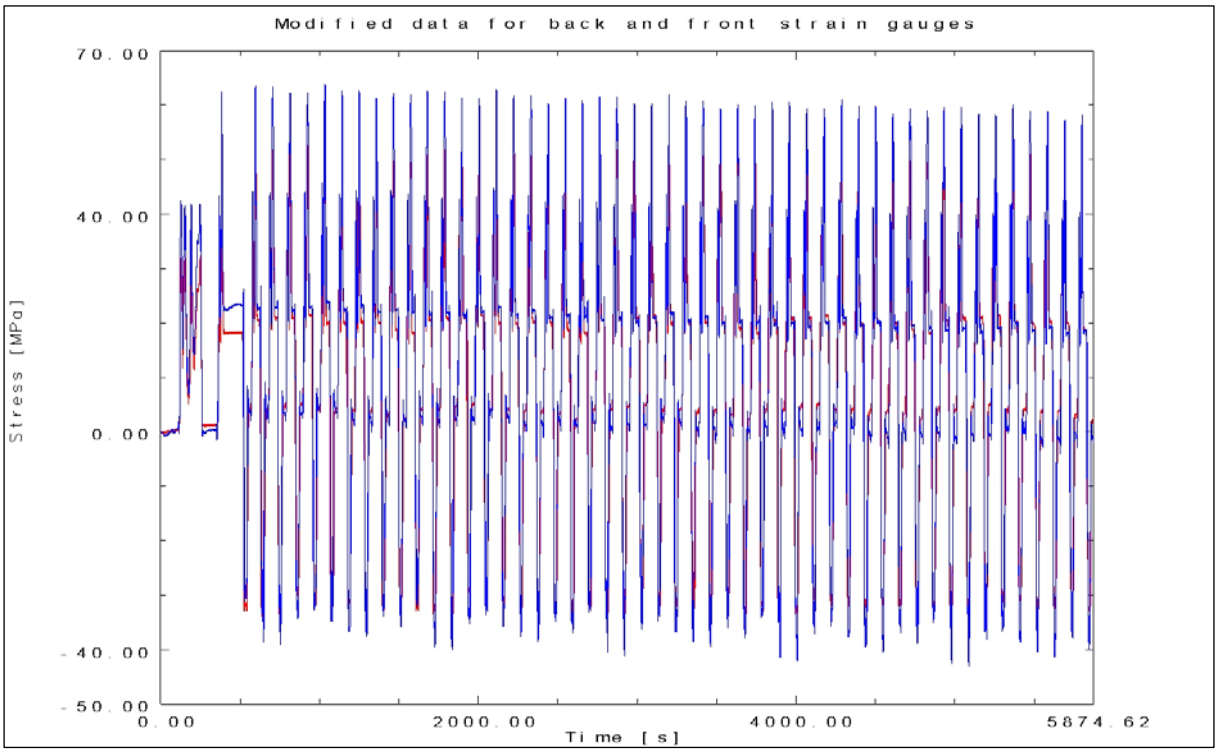

Figure 5.26: Corner stresses for the modified Tippler structure

The comparison results for the original and modified structures are shown in table 5.4. For all practical purposes the modified structure would have an infinite life.

Table 5.4: Rain flow data for modified structure with modified FAT 125 curve

Back corner fatigue					Front corner fatigue				
Range Number	Range Values	Counts	Damage Ratio	Percent Damage	Range Number	Range Values	Counts	Damage Ratio	Percent Damage
1	10	5.54E+04	0.00E+00	0	1	10	5.71E+04	0.00E+00	0
2	20	55	0.00E+00	0	2	20	0	0.00E+00	0
3	30	3	0.00E+00	0	3	30	52	0.00E+00	0
4	40	1	0.00E+00	0	4	40	1	0.00E+00	0
5	50	1	0.00E+00	0	5	50	1	0.00E+00	0
6	60	0	0.00E+00	0	6	60	0	0.00E+00	0
7	70	0	0.00E+00	0	7	70	1	0.00E+00	0
8	80	0	0.00E+00	0	8	80	0	0.00E+00	0
9	90	49	6.56E-09	1	9	90	0	0.00E+00	0
10	100	0	0.00E+00	0	10	100	34	7.99E-07	0.38
11	110	0	0.00E+00	0	11	110	15	1.30E-06	0.62
12	120	0	0.00E+00	0	12	120	0	0.00E+00	0
13	130	0	0.00E+00	0	13	130	0	0.00E+00	0
14	140	0	0.00E+00	0	14	140	0	0.00E+00	0
15	150	0	0.00E+00	0	15	150	0	0.00E+00	0
16	160	0	0.00E+00	0	16	160	0	0.00E+00	0
17	170	0	0.00E+00	0	17	170	0	0.00E+00	0
18	180	0	0.00E+00	0	18	180	0	0.00E+00	0
19	190	0	0.00E+00	0	19	190	0	0.00E+00	0
20	200	0	0.00E+00	0	20	200	0	0.00E+00	0
21	210	0	0.00E+00	0	21	210	0	0.00E+00	0
22	220	0	0.00E+00	0	22	220	0	0.00E+00	0
23	230	0	0.00E+00	0	23	230	0	0.00E+00	0
24	240	0	0.00E+00	0	24	240	0	0.00E+00	0
25	250	0	0.00E+00	0	25	250	0	1.40E-45	0
Out of range counts		0.00E+00			Out of range counts		0.00E+00		
Total counts		5.55E+04			Total counts		5.72E+04		
Out of range damage		0.00E+00			Out of range damage		0.00E+00		
Total damage ratio		6.56E-09			Total damage ratio		2.10E-06		
Crack initiation estimate		1.53E+08	Events		Crack initiation estimate		4.76E+05	Events	
		71062.4	Years				221.8	Years	

Table 5.5: Calculated structure fatigue lives (years)

	Front Corner	Back Corner
Original structure	9.9	9.3
Modified structure	221.8	71062.4

An infinite fatigue life will however only be obtained if the condition of the surface coating or paint used on the Tippler structure is kept intact and corrosion is eliminated. If corrosion sets in the modified structure would have a longer fatigue life than the original structure although it may not be infinite. The presence of peak stresses as measured in the original structure would also have an effect on the fatigue life of the modified structure, but this effect will be much less than on the original structure.

5.5 Conclusion

The fatigue life calculations indicated that the modified structure would have an infinite life compared to the original structure, if the surface protection on the structure can be kept in the same condition as for the original structure. Once corrosion sets in the fatigue life would be reduced but the chances of a catastrophic failure would be much less. The modifications to the structure therefore served the purpose as intended.

CHAPTER 6

DISCUSSION OF RESULTS

A tandem Tippler structure experienced severe structural cracking while in operation at Richards Bay Coal Terminal. Due to the operational critical nature of the structure, the structure had to be repaired and placed back in operation as soon as possible. Structural modifications were implemented to limit future cracking. From the data available at the time it could not be determined with certainty that the structure would have an infinite life after modification.

The purpose of this study was to establish an accurate verifiable method that could be used to evaluate the Tippler life and to use this method to evaluate the structural fatigue life of the modified Tippler structure. This was done by first creating an accurate FEA simulation of the complete tip process and verifying this simulation by means of strain gauge data obtained from the structure. The stress values obtained from the FEA was accurate to within 11.0% of the measured stress data. Furthermore, the strain gauge data obtained was used to identify any spurious load phenomena that could not be simulated by means of an FEA analysis. Furthermore, a literature study was on non-load related effects that would shorten the fatigue life of the structure was done.

The verified model, fatigue related data and known life of the original structure were used to construct an accurate representation of the endurance limit (S-N curve) for the original structure that would have provided it with a 10-year life as obtained. The presence of a weld in the cracked areas necessitated the use of component S-N curves as bases for the construction of the “representative” S-N curve. For this study, a base curve was selected from the IIW code, to represent the corner welding detail as closely as possible. This curve however had 95% probability of survival margin build in, as normally used in the compilation of welding curves. This curve was therefore “pushed” back to the mean value and then further adapted to obtain a the representative S-N curve that provided a fatigue life of approximately 10 years with a probability of failure of approximately 99% at the weld positions. This was done as the original structure did developed cracks at the weld positions in the corners. The purpose this exercise was therefore to create a quantifiable S-N curve, based on actual welding fatigue data and a known fatigue life, to use in the comparison between two different platform structures, under the same environmental and loading conditions.

The comparison between the original and modified structure indicated that the modified structure would have an infinite fatigue life if compared to the original

structure. This would, however, only be true if all factors, i.e. surface protection, load conditions, structural integrity of mechanisms and components remains within the range as experienced by the original structure. It was found that the effect corrosion could have on the fatigue life of a structure of this nature was not easily quantifiable. More work is needed to provide designers and analysts more comprehensive and reliable guidelines.

The study further established that the rotational operation of a Tippler structure or similar structures can be accurately simulated by means of linear static finite element models, where each model represents a position at a certain time interval during the cycle. Furthermore, if strain gauge stress data is available for known positions on the structure under investigation, these data sets can be accurately scaled to obtain stress histories for other positions on the structure. By using this method, structures can be designed or modified to obtain their fatigue lives as required.

REFERENCES

Adams, V. & Askenazi, A. 1999. *Building better products with finite element analysis.* 1st ed. Santa Fe, NM: OnWord Press

Assakkaf, I.A. & Ayyub, B.M. *Reliability-based design for fatigue of marine structures*. Civil Engineering Department, University of Maryland.

Bannantine, J.A., Comer, J.J. & Handrock, J.L. 1990. *Fundamentals of metal fatigue analysis*. , Eaglewood Cliffs, NJ: Prentice-Hall

Bechwith, T.G., Maragoni, R.D. & Lienhard, J.H. 1993. *Mechanical measurements*. 5th ed., USA: Addison-Wesley Publishing Company Inc

Benham, P.P. Warnock, F.V. 1981. *Mechanics of solids and structures*. Marshfield: Pitman Publishing INC.

Blake, A. 1985. Handbook of mechanics materials, and structures., USA: John Wiley & Sons.

Boyer, H.E. 2005. *Atlas of fatigue curves*, American Society for Metals, OH: Metals Park,

British Standard. BS 7608:1993. *Code of practice for fatigue design and assessment of steel structures,* London

Conveyor knowledge and information technology, 2005. Available online: http:/www.ckit.co.za. Last accessed: September 2005.

Das, A.K. 1997. *Metallurgy of failure analysis*., USA: McGraw Hill.

Det Norske Veritas*, Fatigue design of steel structures, Recommended practice*, DNV-RP-C203, August 2005

Deiters, T. & Antal, G. 2001. *I-DEAS Durability training course material.* Presented by ATA Engineering, Inc. San Diego, CA, September 2001.

Dowling, N.E. 1999. *Mechanical Behaviour of Materials, Engineering Methods for Deformation, Fracture and Fatigue*, 2nd ed., Upper saddle river, NJ: Prentice-Hall

Ellyin, F. 1997. *Fatigue damage, crack growth and life prediction***.** London: Chapman and Hall.

Gere J.M. & Timoshenko S.P. 1994. *Mechanics of materials*, 3rd SI edition. Singapore: Chapman & Hall

Hobbacher, A. 2004. *Recommendations for fatigue design of welded joints and components*. IIW document XIII-1965-03 / XV-1127-03., Paris: International Institute of Welding..

Keyser, C.A. 1962. *Basic Engineering Metallurgy*, 2nd ed., Englewood Cliffs, NJ: Prentice—Hall.

Kneem, P. 2004. *Steel construction,* Fatigue design of steel structures, Journal of the Australian steel institute, Volume 38, Number 1,

Kurowski, P.M. 2004. *Finite element analysis for design engineers*. Warrendale, PA: SAE International.

Lepi, S.M. 1998. *Practical guide to finite elements, a solid mechanics approach*. New York: Marcel Dekker.

Mercer, I. Melton, G. & Draper, J. 2003. *The Effect of User Decisions on the Accuracy of Fatigue Analysis from FEA.* Safe Technology Limited. 2003 ABAQUS Users' Conference

Richards Bay Coal Terminal, 2003. *Complete as-build Tippler drawing pack*. Richards Bay Coal Terminal

Richards Bay Coal Terminal. 2005. Available online: http:/www.rbct.co.za. Last accessed: September 2005.

Stephens, R.I., Fatemi, A., Stephens, R.R., & Fuchs, H.O. 2001. *Metal Fatigue in Engineering.* Second Edition. New York: John Wiley & Sons.

Shigley, J.E. 1986. *Mechanical engineering design*. 1st ed. Singapore: McGraw-Hill.

Van Zyl, P.J.A. 2004. *Video clips tip cycle recorded during strain gauge process*, Richards Bay Coal Terminal

Window, A.L. 1992. *Strain gauge technology*. 2nd ed. Essex: Elsevier science publishers LTD.

APPENDIX A

CCL 5 Wagon detail
Spoornet specification sheet

Drawgear Equipment - Trekwerkuitrusting

KK Coupler hydraulic cushioning device
Koppelaar hidroulies kussinginrigting

SSC Centre sill hydraulic cushioning device
Middelbalk hidroulies kussinginrigting

Brake System - Remstelsel

A Dual Power - Automatic
Tweekrag - Outomaties

R Slack Adjuster
Remversteller

Vacuum
Vakuum
Air
Lug
Dual Power - Manually operated
Tweekrag - Handbediening

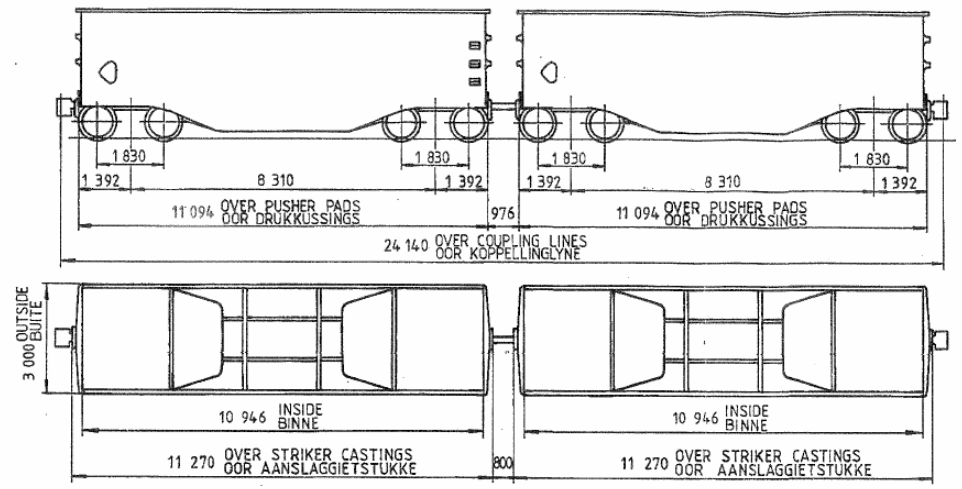

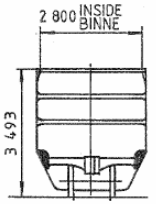

ARROW INDICATES ROTARY COUPLER/DRAWBAR END. OPPOSITE END FITTED WITH NON-ROTARY COUPLER/DRAWBAR
PYL DUI DRAAIKOPPELAAR/-TREKSTANG ENT AAN. TEENOORGESTELDE KANT GEPAS MET NIE-DRAAIENDE KOPPELAAR/-TREKSTANG
FITTED WITH "HOLDING BRAKE"
GEPAS MET "VASHOUREM"

Remarks / Opmerkings :-
SET OF 2 WAGONS WITH SEMI-PERMANENT DRAWBAR
STEL VAN 2 TROKKE MET HALFPERMANENTE TREKSTANG

✱1 4,5:1 BRAKE RATIO, REMVERHOUDING, Ø 915 WHEEL WIEL

✱2 LOADED 84t LEVEL WITH TOP: 1 824 mm
84t GELYK GELAAI TOT BO: 1 824 mm

✱3 TOP: BO: 76,2 m^3, BATH: BAD: 9,46 m^3

✱4 PER WAGON
PER TROK

Vehicle Numbers / Voertuignommers	Placed in Service / In Gebruik Geneem
63 - 515 407 / 63 - 524 198	1982 - 1983
63 - 524 260 / 63 - 533 030	1983 - 1984
63 - 555 077	1992

Converted from / Omskep van	Date / Datum

Drawing Number / Tekeningnommer	CME 175/12-A21		Centre of Gravity (Empty) / Swaartepunt (Leeg)	933 ✱2	Tare (Average) kg / Tarra (Gemiddeld) kg	20 250 ✱4
Bogie Type / Draaisteltipe	HS Mk V ✱1				Load / Vrag kg	84 000 ✱4
Bearing Size / Laergrootte	F				Load (Coal) kg / Vrag (Steenkool) kg	84 000 ✱4
Springs per Bogie Outer / Inner / Vere per Draaistel Buite / Binne	12/8				Floor Area / Vloeroppervlakte m^2	
Brake System / Remstelsel	L/R				Capacity / Inhoudsvermoë m^3	85,66 ✱3
Brake Cylinders / Remsilinders	(V)	(L) 2/7×12	Design Limit - Mass on Rail kg / Ontwerplimiet - Massa op Spoor	104 000 PER WAGON / PER TROK		
Train Pipe / Treinpyp / Brake Pipe / Rempyp	(V)	(L) 32	Originally designed for / Oorspronklik ontwerp vir	COAL / STEENKOOL		
Brake Percentage Empty / Loaded / Rempersentasie Leeg / Met Vrag	(V)	(L) 68,5/13,3	Converted for / Omskep vir			
Drawgear Equipment / Trekwerkuitrusting	AAR M 901 E		Revision / Hersiening			

RRI-5

APPENDIX B

Ingo Cage Tip Cycle
Von Mises Stress

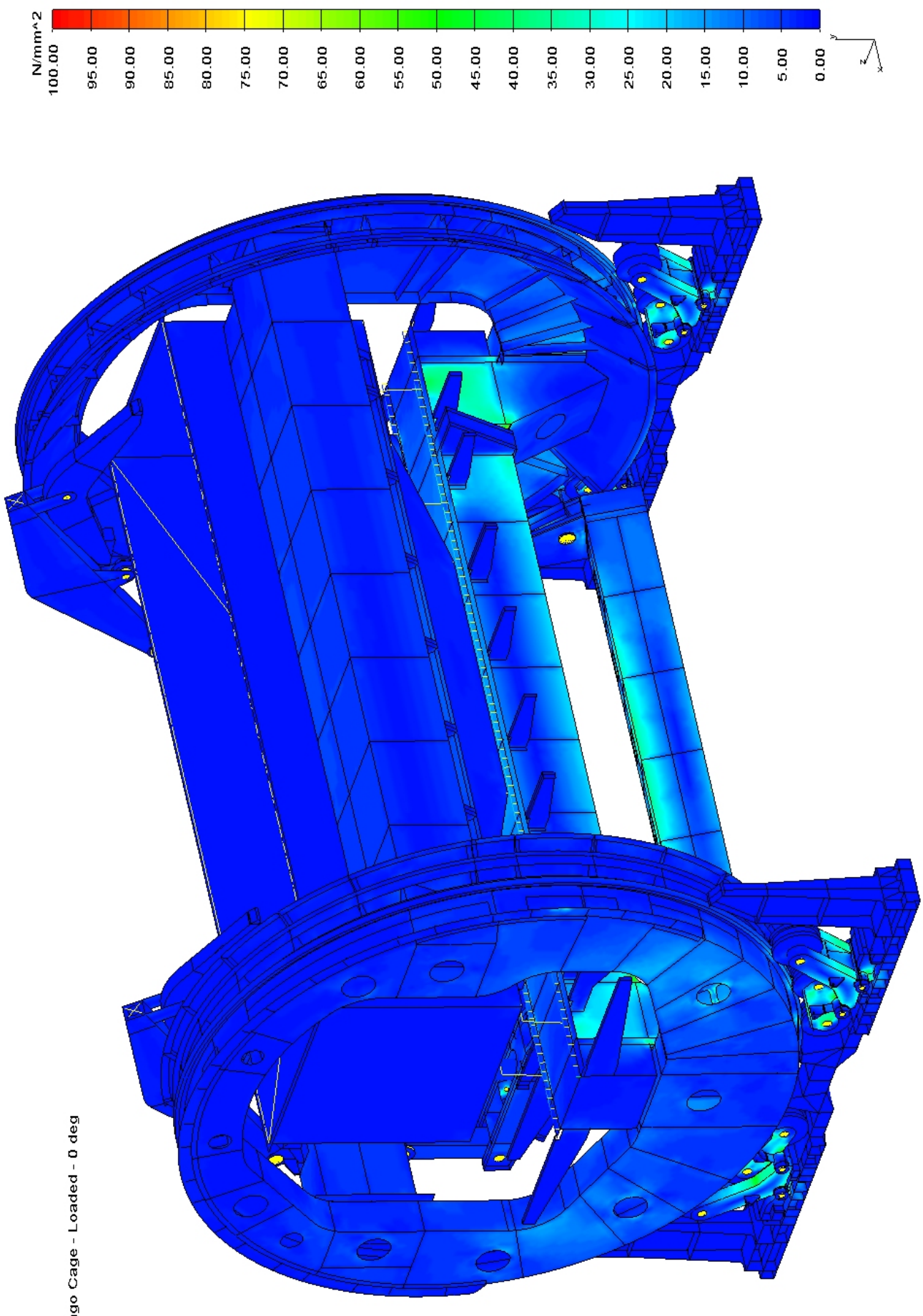
N/mm^2
100.00
95.00
90.00
85.00
80.00
75.00
70.00
65.00
60.00
55.00
50.00
45.00
40.00
35.00
30.00
25.00
20.00
15.00
10.00
5.00
0.00
Ingo Cage - Loaded - 0 deg

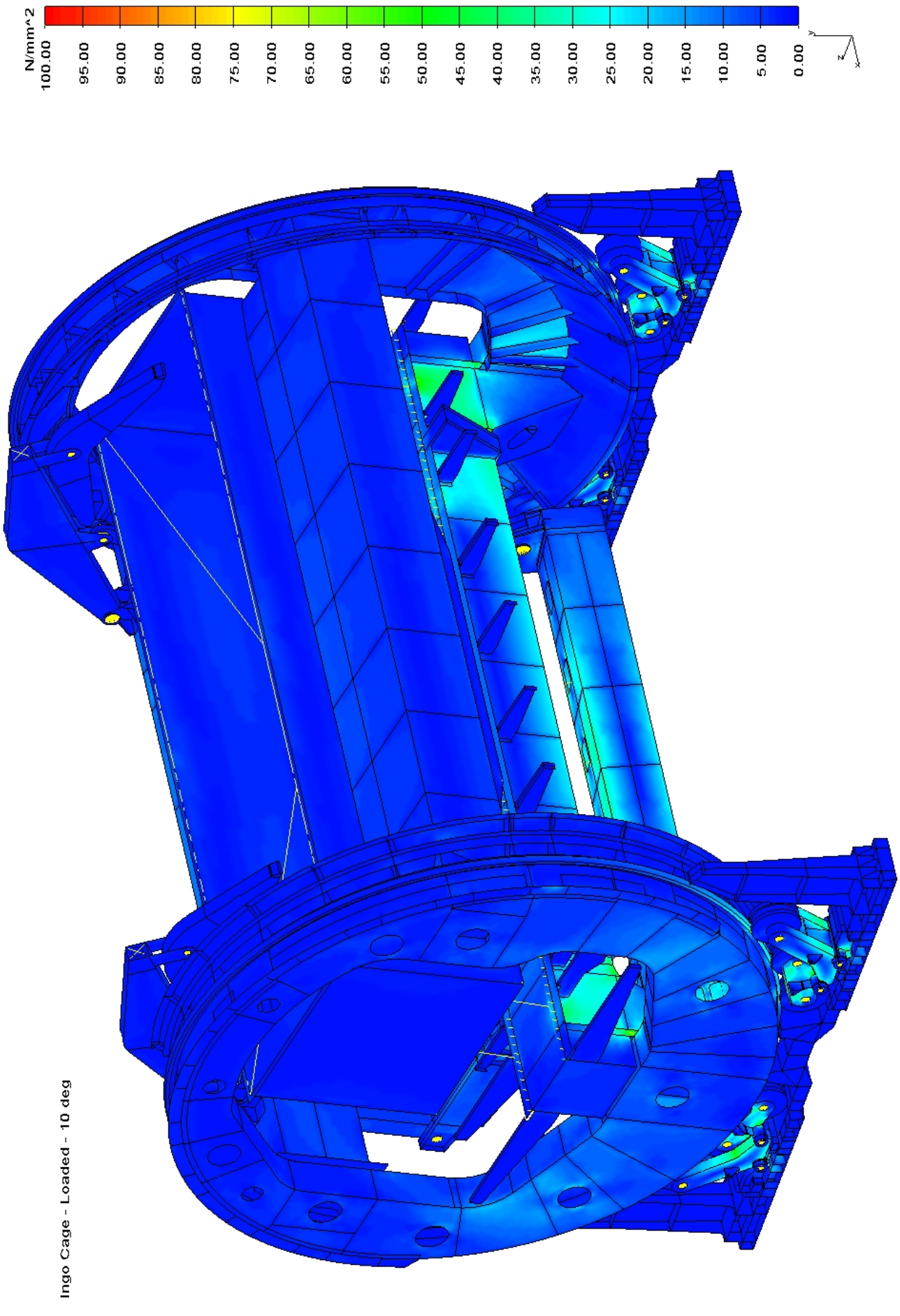
N/mm^2
100.00
95.00
90.00
85.00
80.00
75.00
70.00
65.00
60.00
55.00
50.00
45.00
40.00
35.00
30.00
25.00
20.00
15.00
10.00
5.00
0.00
Ingo Cage - Loaded - 10 deg

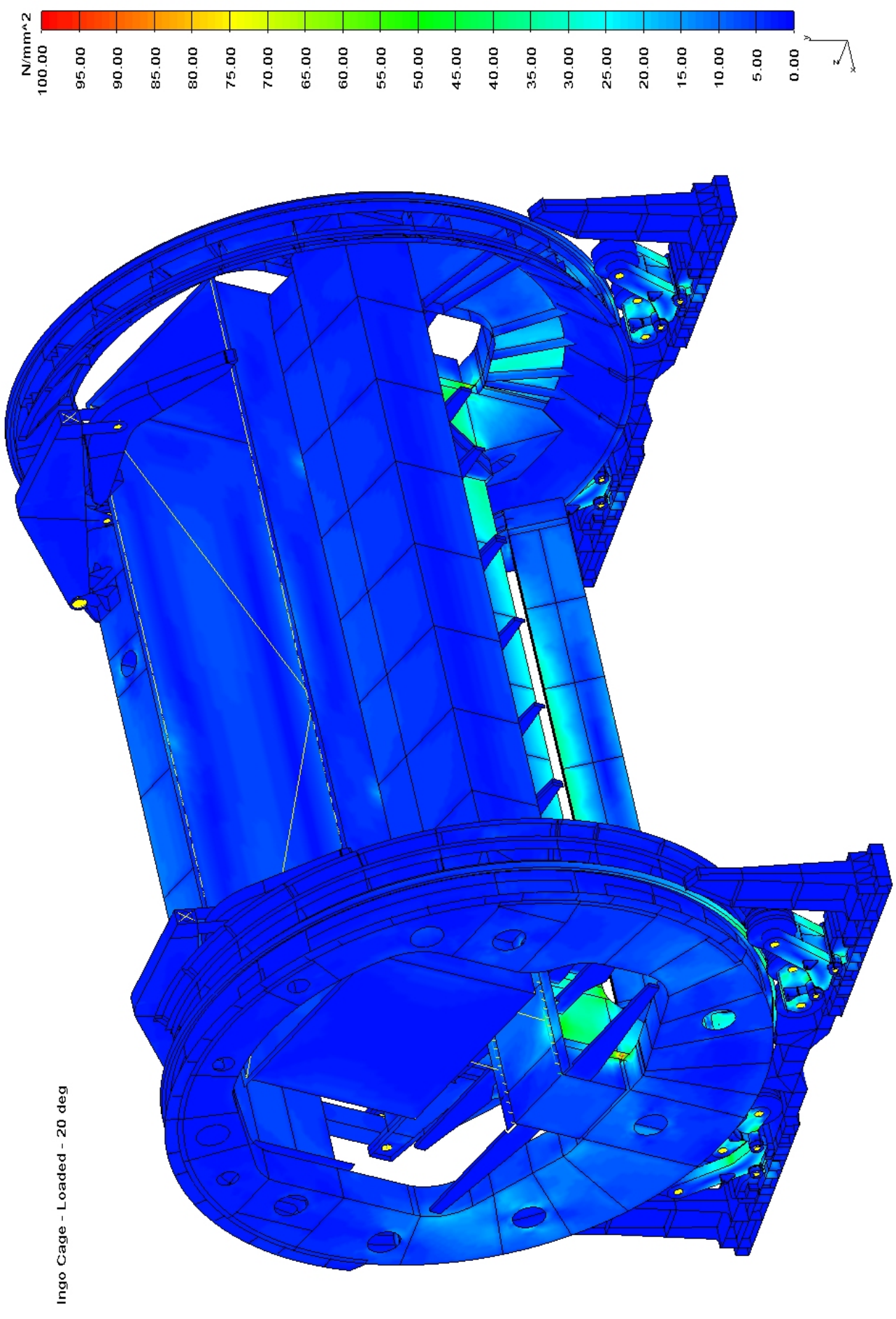
N/mm^2
100.00
95.00
90.00
85.00
80.00
75.00
70.00
65.00
60.00
55.00
50.00
45.00
40.00
35.00
30.00
25.00
20.00
15.00
10.00
5.00
0.00
Ingo Cage - Loaded - 20 deg

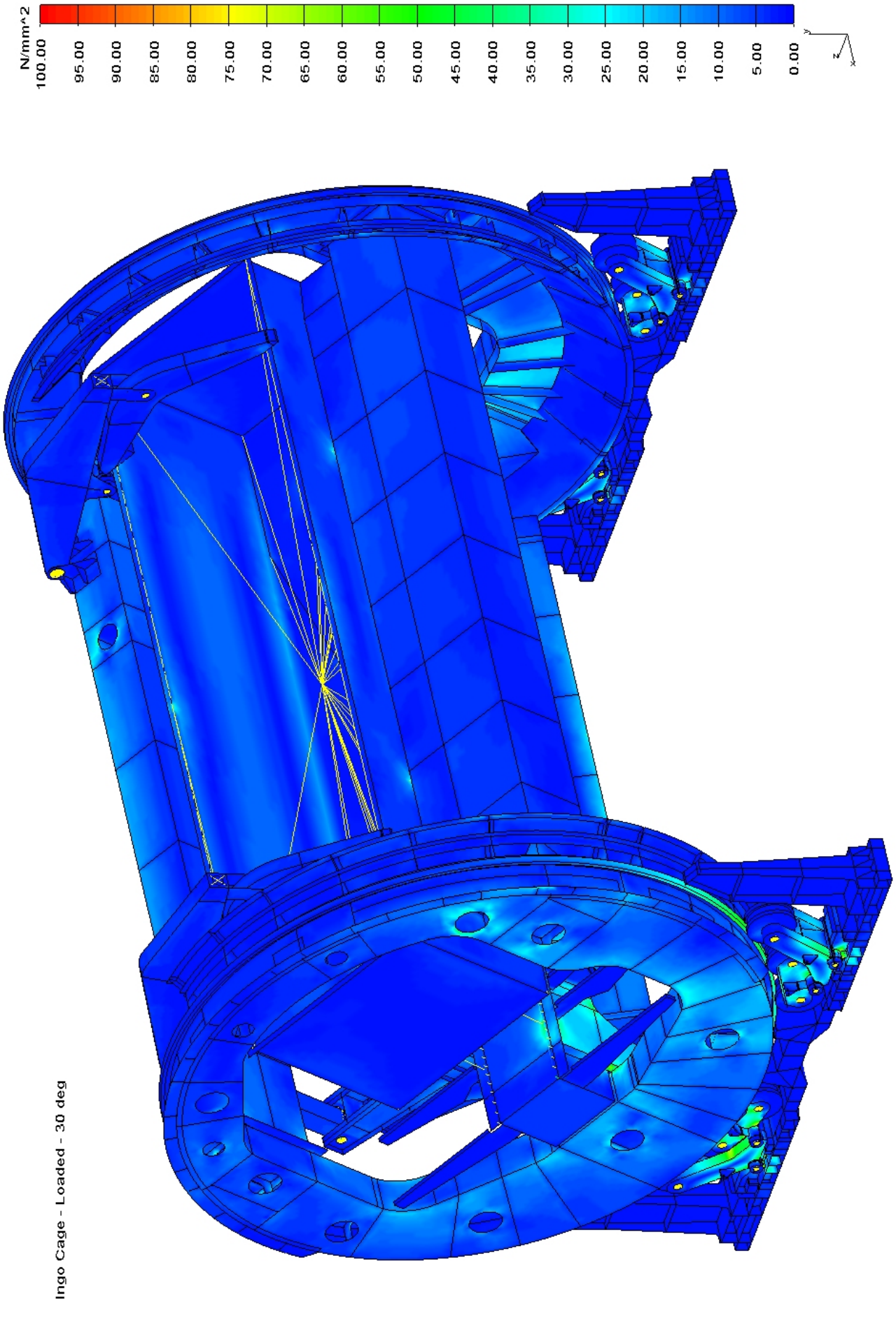
N/mm^2
100.00
95.00
90.00
85.00
80.00
75.00
70.00
65.00
60.00
55.00
50.00
45.00
40.00
35.00
30.00
25.00
20.00
15.00
10.00
5.00
0.00
Ingo Cage - Loaded - 30 deg

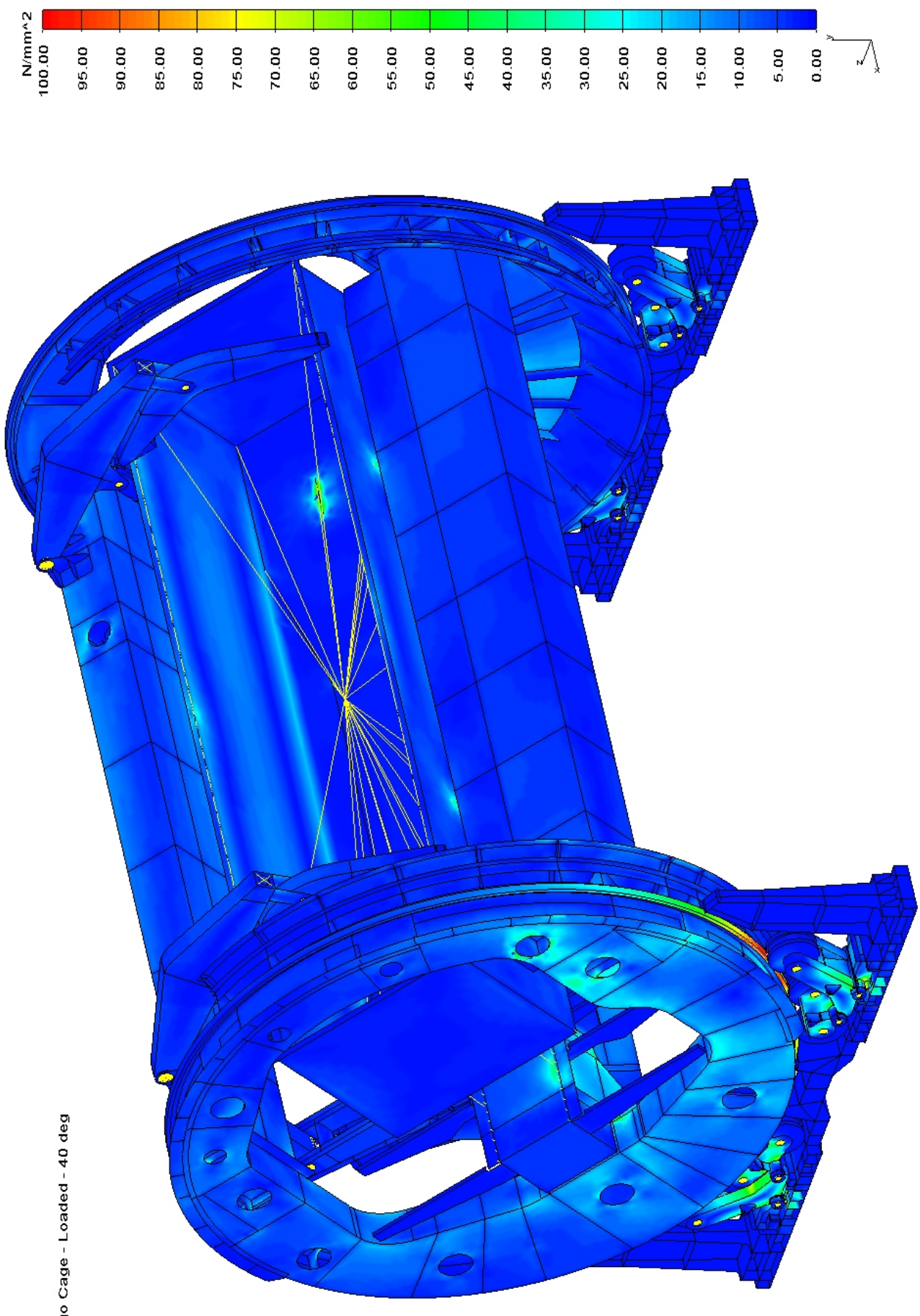
N/mm^2
100.00
95.00
90.00
85.00
80.00
75.00
70.00
65.00
60.00
55.00
50.00
45.00
40.00
35.00
30.00
25.00
20.00
15.00
10.00
5.00
0.00
Ingo Cage - Loaded - 40 deg

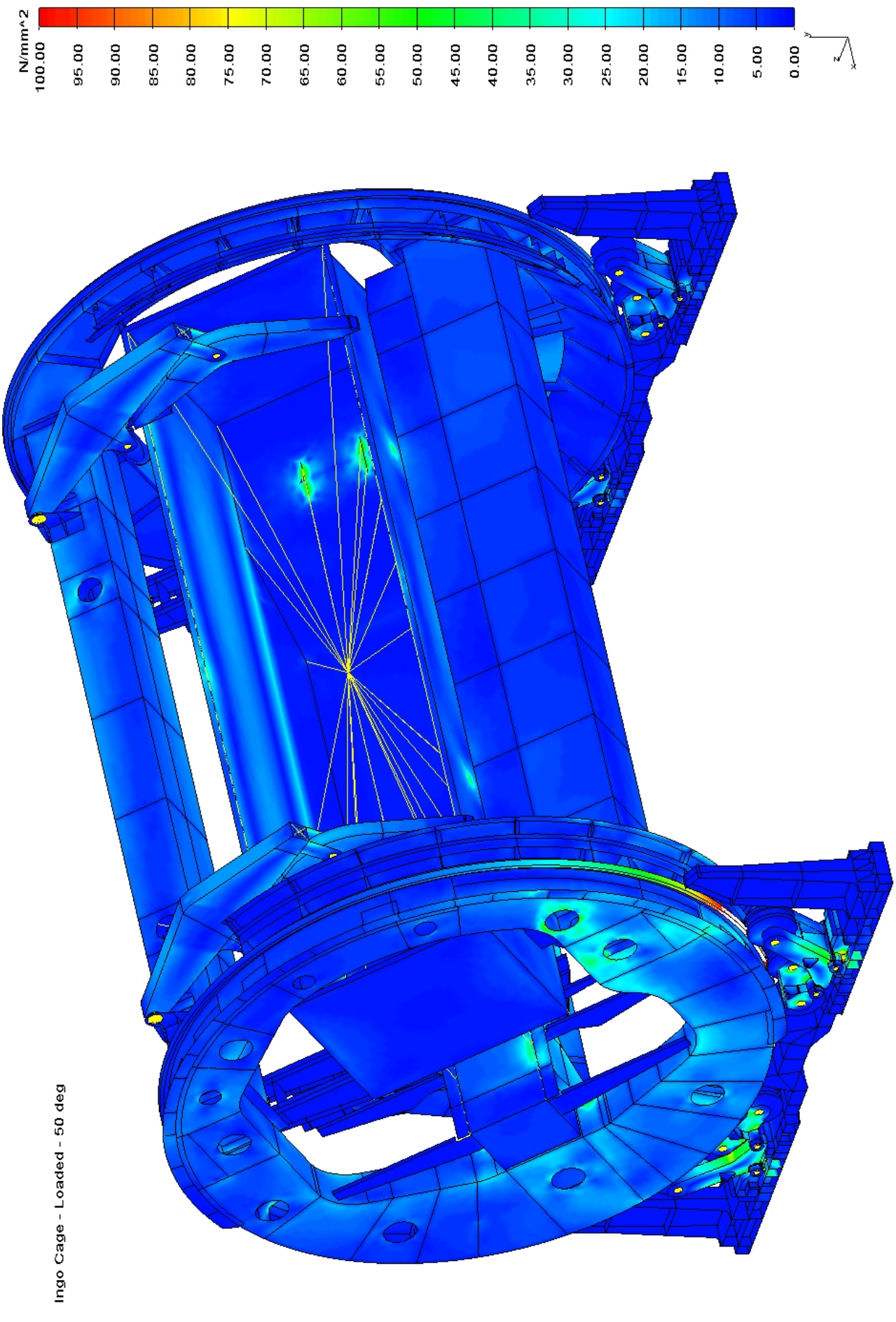
N/mm^2
100.00
95.00
90.00
85.00
80.00
75.00
70.00
65.00
60.00
55.00
50.00
45.00
40.00
35.00
30.00
25.00
20.00
15.00
10.00
5.00
0.00
Ingo Cage - Loaded - 50 deg

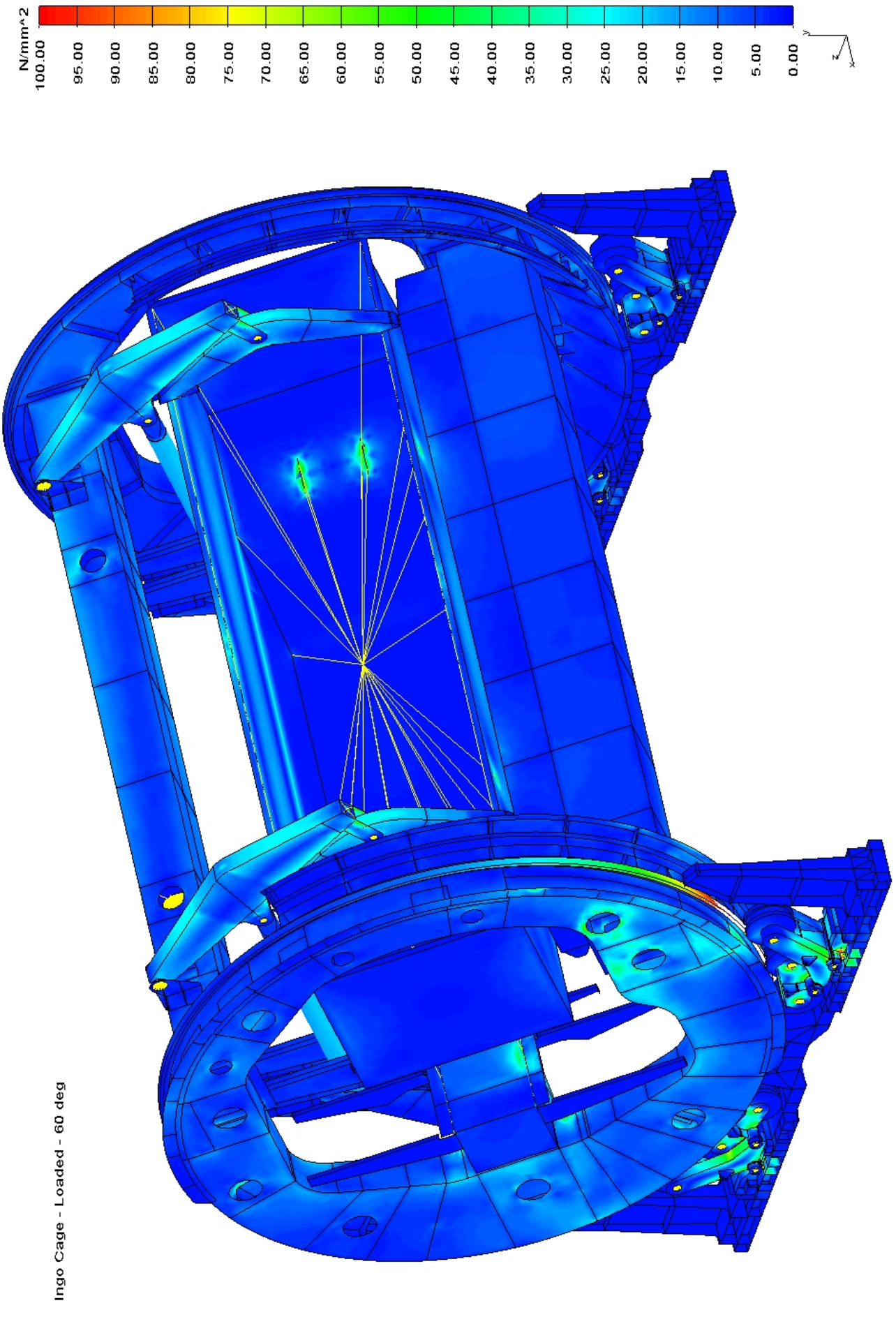
N/mm^2
100.00
95.00
90.00
85.00
80.00
75.00
70.00
65.00
60.00
55.00
50.00
45.00
40.00
35.00
30.00
25.00
20.00
15.00
10.00
5.00
0.00
Ingo Cage - Loaded - 60 deg

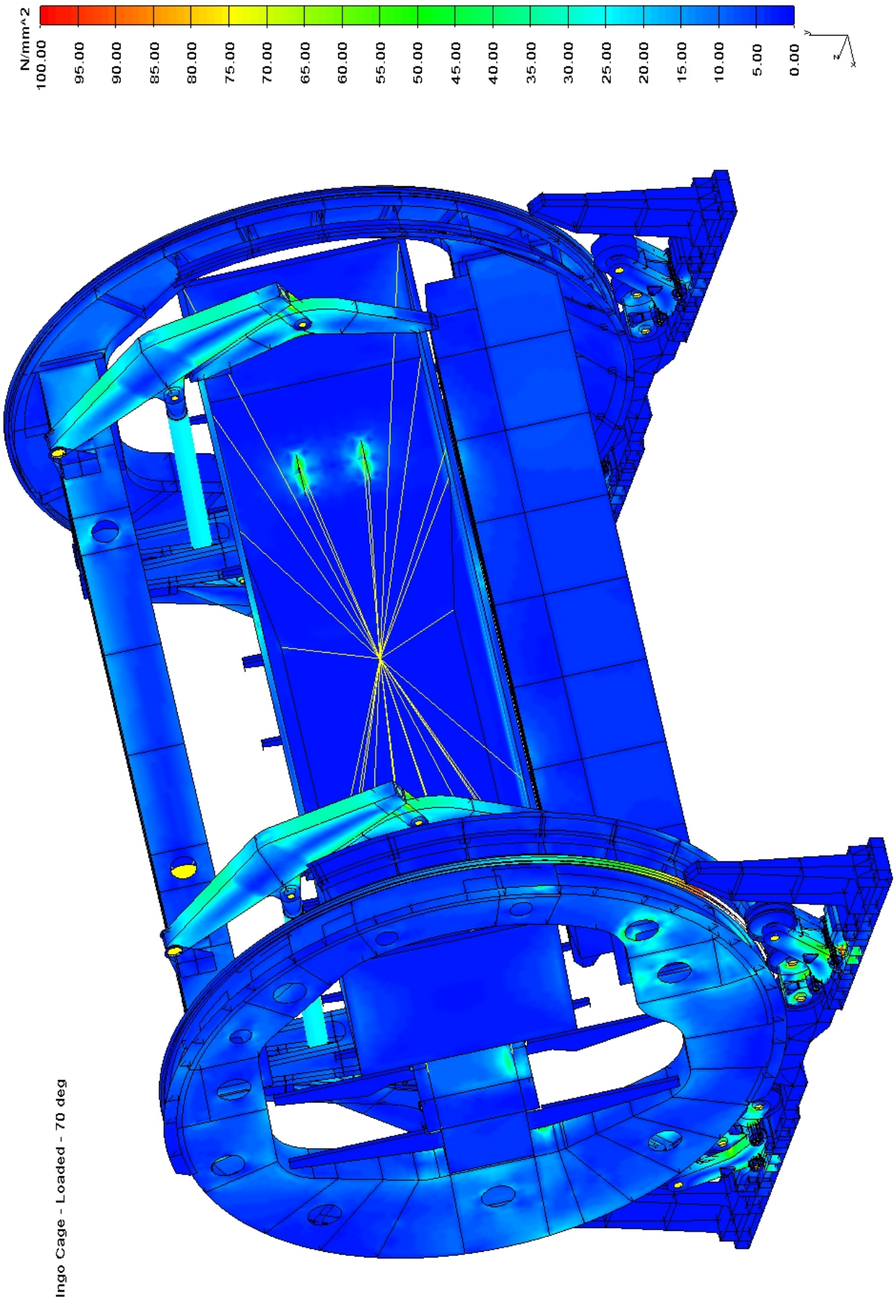
N/mm^2
100.00
95.00
90.00
85.00
80.00
75.00
70.00
65.00
60.00
55.00
50.00
45.00
40.00
35.00
30.00
25.00
20.00
15.00
10.00
5.00
0.00
Ingo Cage - Loaded - 70 deg

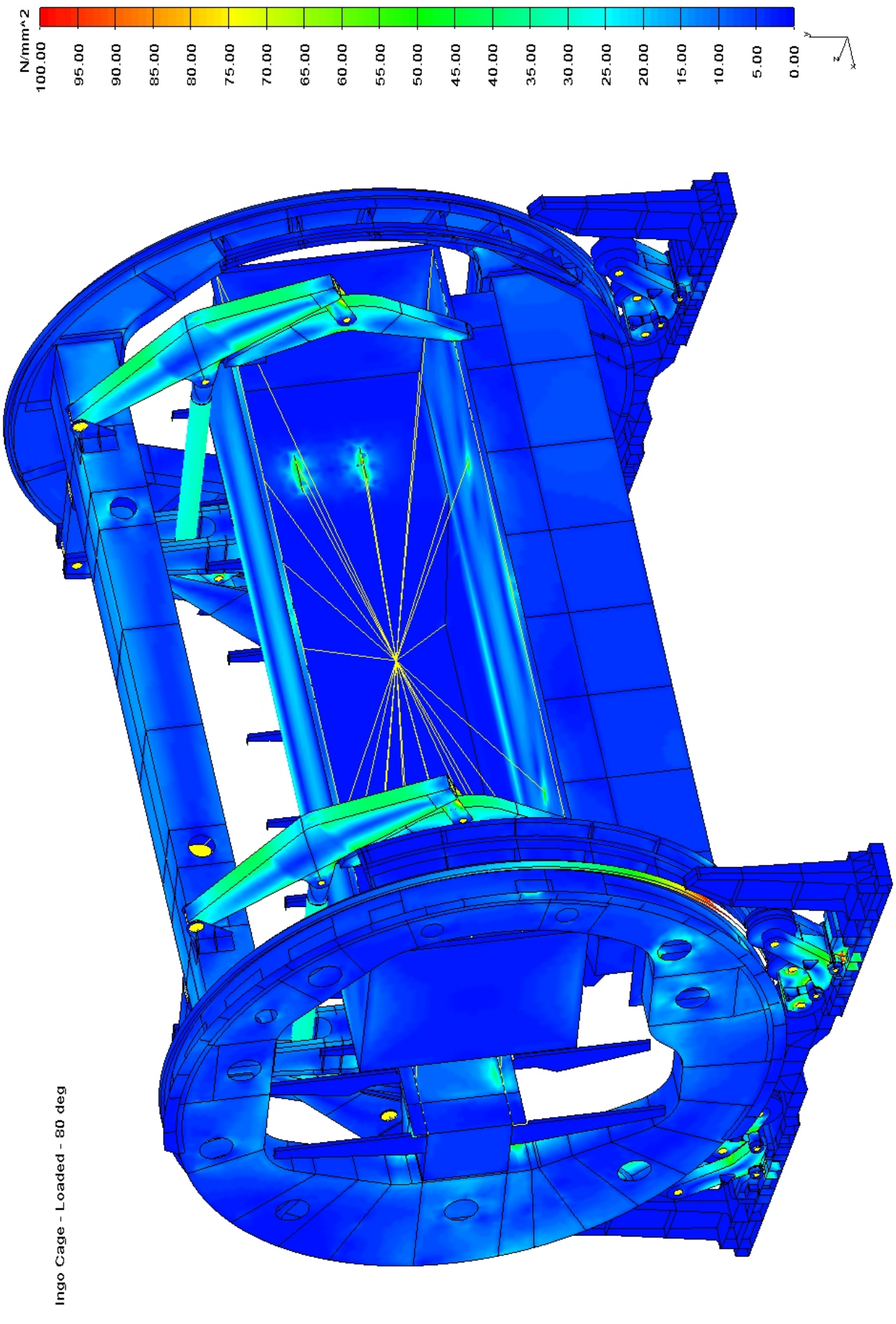
N/mm^2
100.00
95.00
90.00
85.00
80.00
75.00
70.00
65.00
60.00
55.00
50.00
45.00
40.00
35.00
30.00
25.00
20.00
15.00
10.00
5.00
0.00
Ingo Cage - Loaded - 80 deg

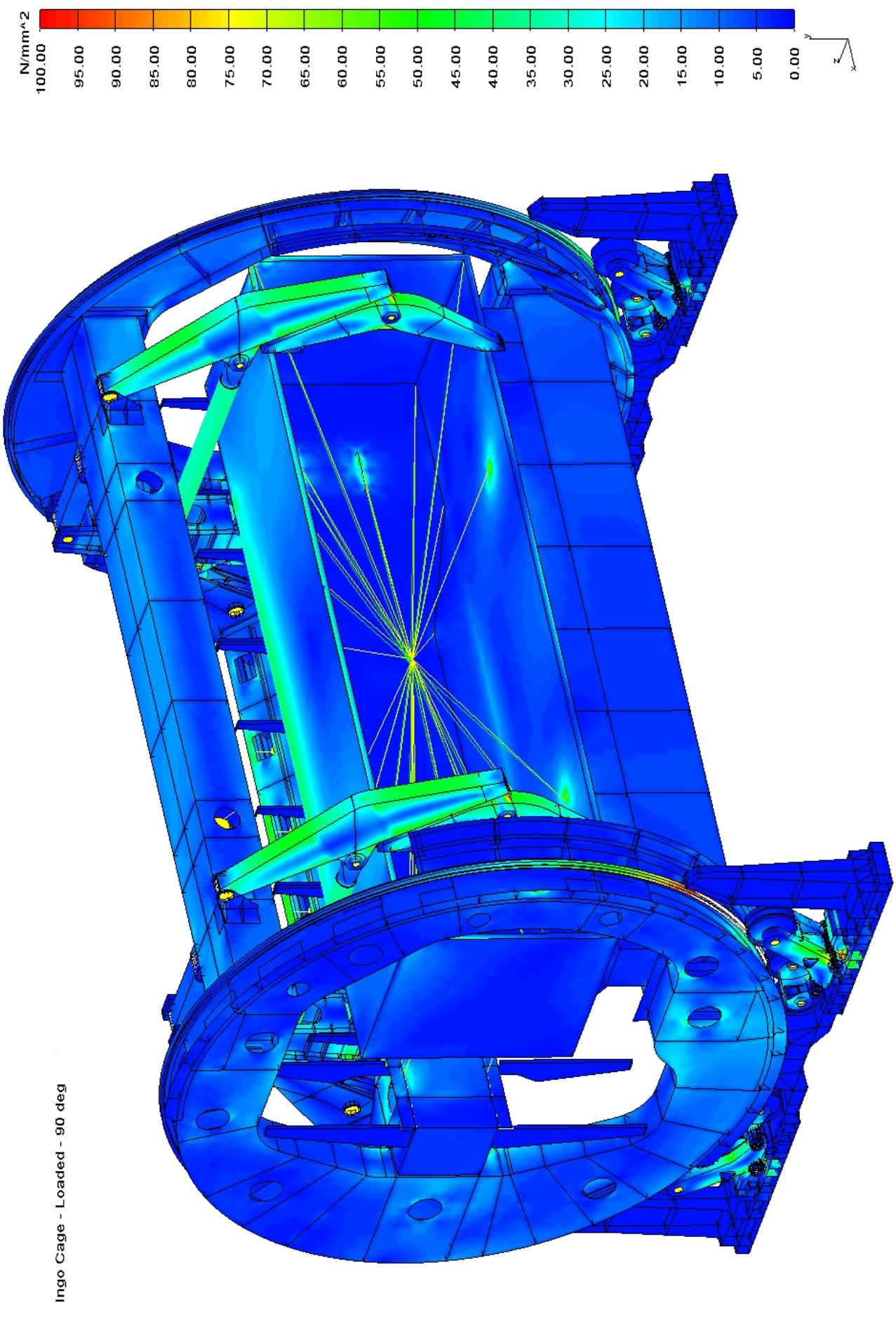
N/mm^2
100.00
95.00
90.00
85.00
80.00
75.00
70.00
65.00
60.00
55.00
50.00
45.00
40.00
35.00
30.00
25.00
20.00
15.00
10.00
5.00
0.00
Ingo Cage - Loaded - 90 deg

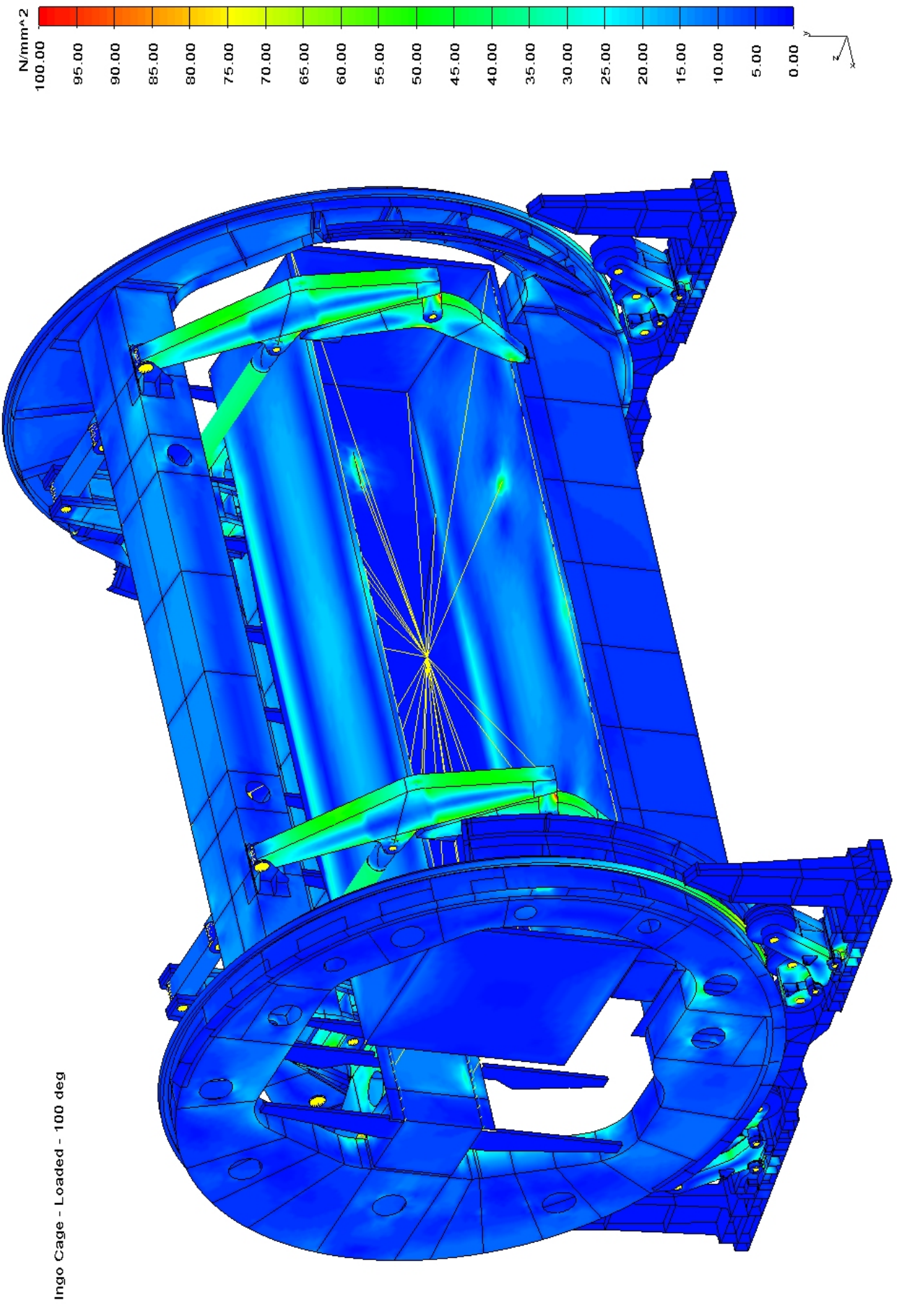
N/mm^2
100.00
95.00
90.00
85.00
80.00
75.00
70.00
65.00
60.00
55.00
50.00
45.00
40.00
35.00
30.00
25.00
20.00
15.00
10.00
5.00
0.00
Ingo Cage - Loaded - 100 deg

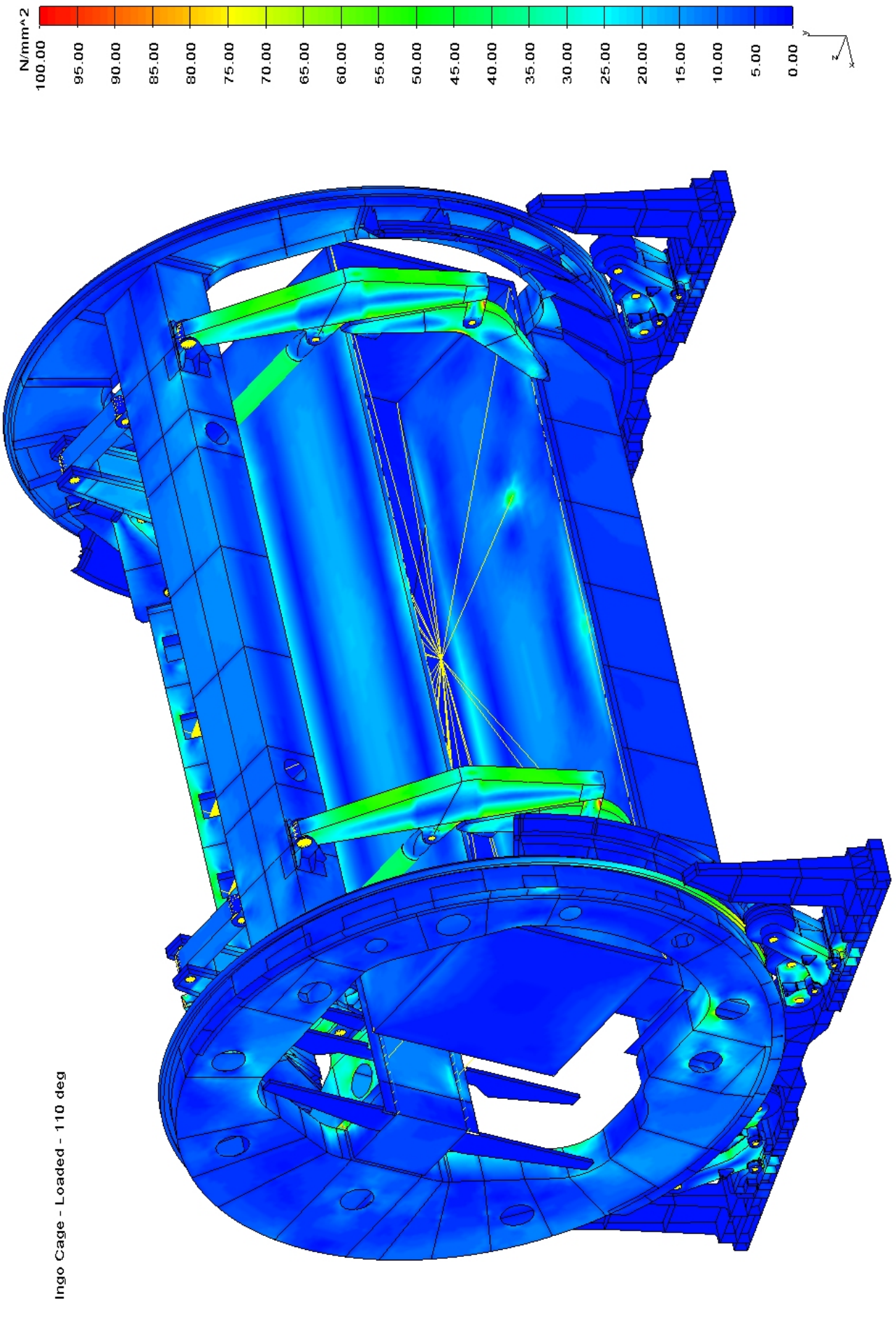
N/mm^2
100.00
95.00
90.00
85.00
80.00
75.00
70.00
65.00
60.00
55.00
50.00
45.00
40.00
35.00
30.00
25.00
20.00
15.00
10.00
5.00
0.00
Ingo Cage - Loaded - 110 deg

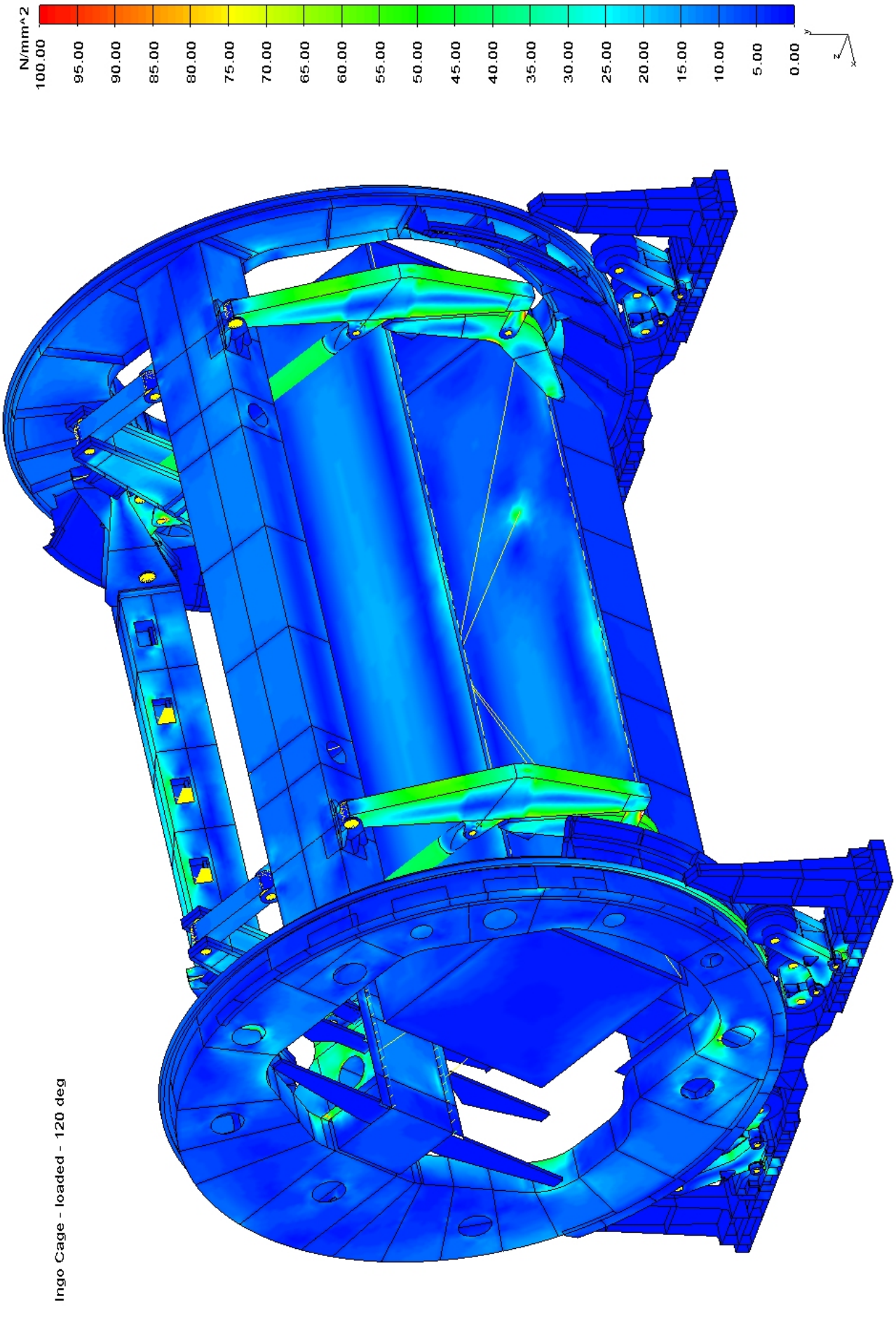
N/mm^2
100.00
95.00
90.00
85.00
80.00
75.00
70.00
65.00
60.00
55.00
50.00
45.00
40.00
35.00
30.00
25.00
20.00
15.00
10.00
5.00
0.00
Ingo Cage - loaded - 120 deg

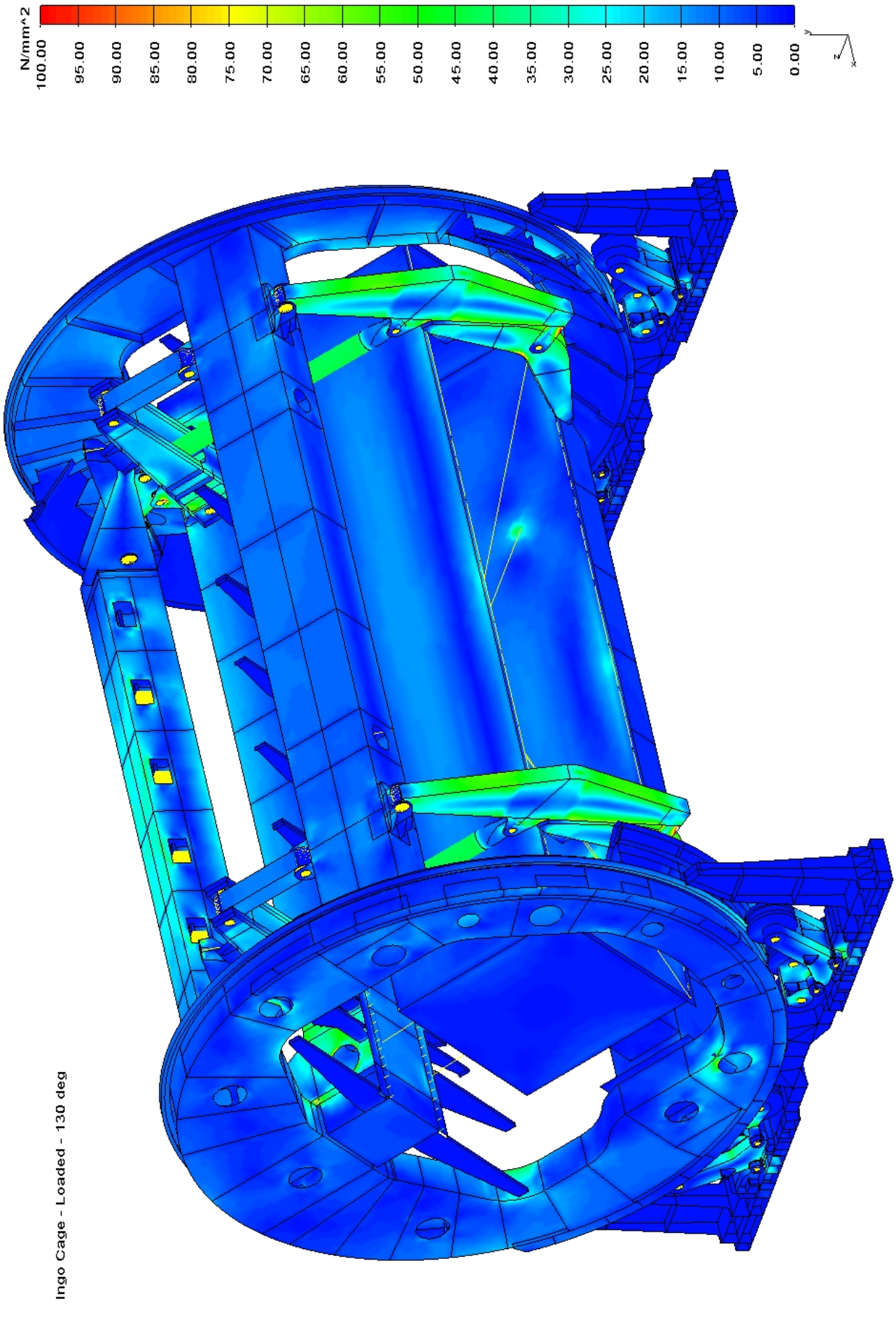
N/mm^2
100.00
95.00
90.00
85.00
80.00
75.00
70.00
65.00
60.00
55.00
50.00
45.00
40.00
35.00
30.00
25.00
20.00
15.00
10.00
5.00
0.00
Ingo Cage - Loaded - 130 deg

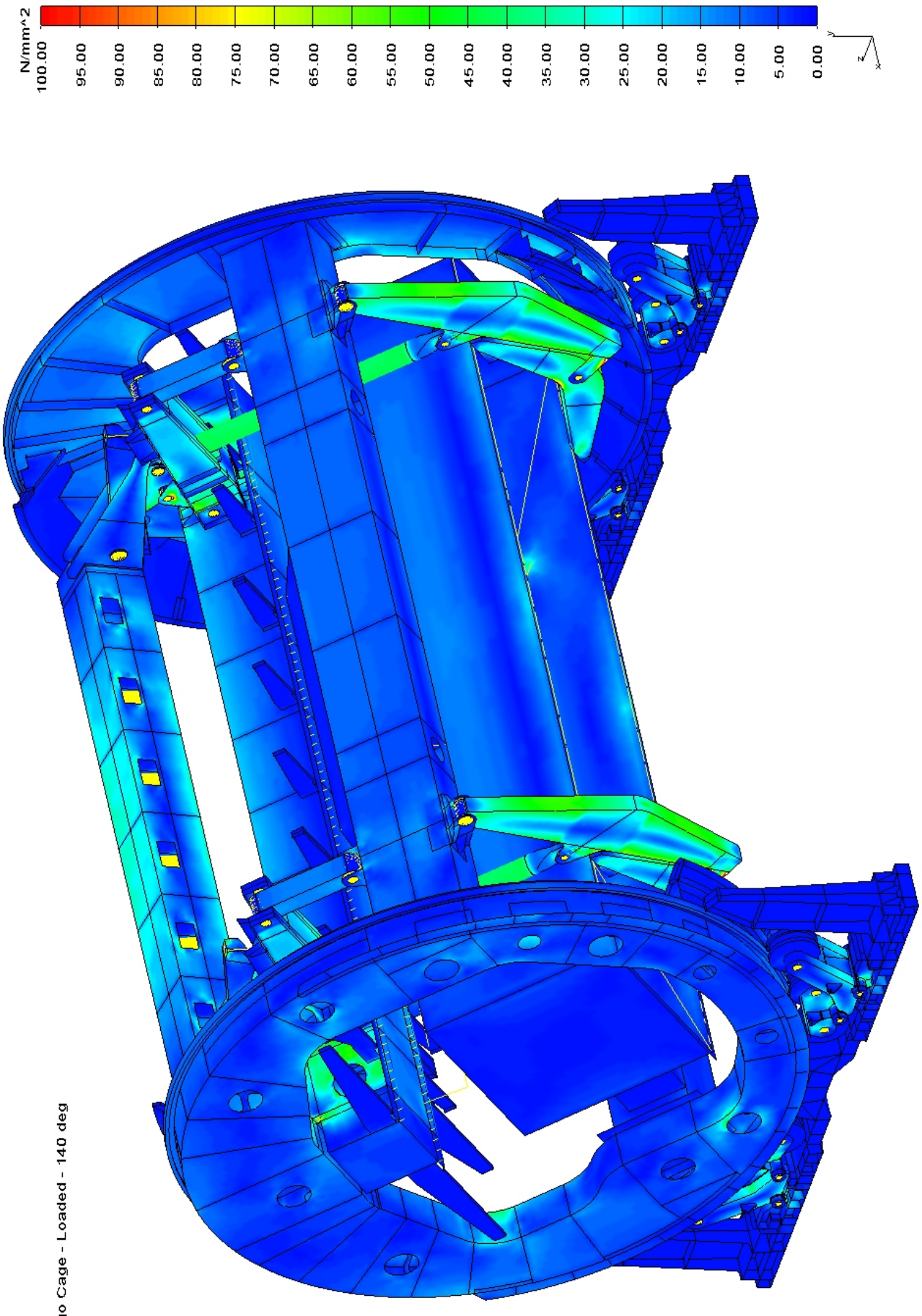
N/mm^2
100.00
95.00
90.00
85.00
80.00
75.00
70.00
65.00
60.00
55.00
50.00
45.00
40.00
35.00
30.00
25.00
20.00
15.00
10.00
5.00
0.00
Ingo Cage - Loaded - 140 deg

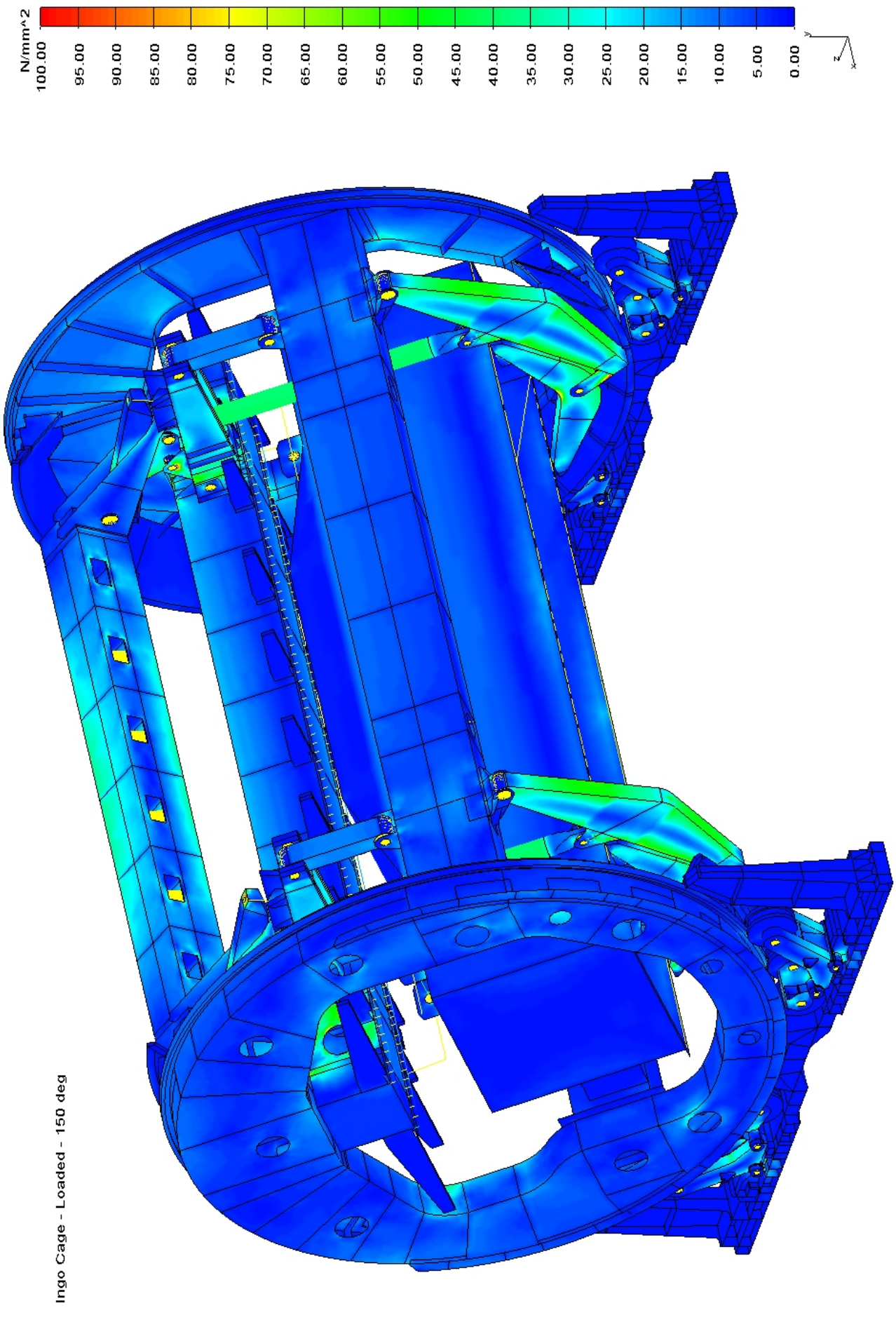
N/mm^2
100.00
95.00
90.00
85.00
80.00
75.00
70.00
65.00
60.00
55.00
50.00
45.00
40.00
35.00
30.00
25.00
20.00
15.00
10.00
5.00
0.00
Ingo Cage - Loaded - 150 deg

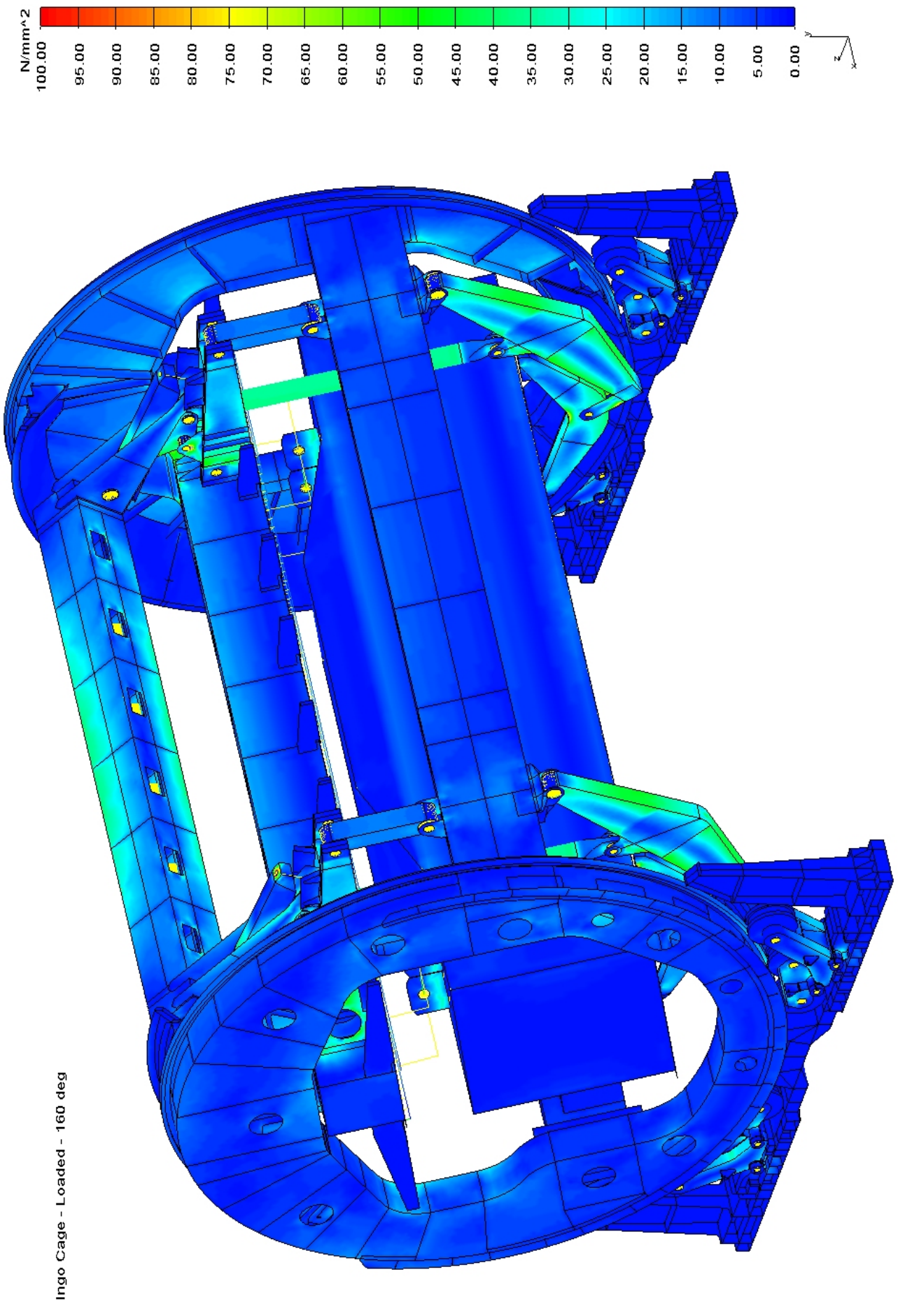
N/mm^2
100.00
95.00
90.00
85.00
80.00
75.00
70.00
65.00
60.00
55.00
50.00
45.00
40.00
35.00
30.00
25.00
20.00
15.00
10.00
5.00
0.00
Ingo Cage - Loaded - 160 deg

APPENDIX C

Material properties
ISCOR Flat steel

ISCOR flat steel

DATA SHEET:
PLATE AND STRIP TO BS 4360 : 1986
HOT ROLLED WELDABLE STRUCTURAL STEEL

FILE REFERENCE
A3.2

PRICE LIST REFERENCE:
120

General description

Iscor produces and markets hot rolled structural steel plate and strip from 1,6mm thick and upwards to the SABS 1431 specification by preference. However, plate and strip to BS 4360 : 1986 are still available. In particular, a dual certified product BS 4360 grade 43A/SABS 1431 grade 300WA is readily available. In addition, structural steel plate and strip to other national specifications are also available.

These steels are intended for structural work where no significant forming or bending must be done. The steel grade should be selected in accordance with the strength requirements as indicated in Table 3.

Iscor produces the following steel grades to the BS 4360: 1986 specification:

- Grades 40A, 40B, 40C[1], 40D[2] and 40EE[2]
- Grades 43A, 43B, 43C[1], 43D[2] and 43EE[2]
- Grades 50B, 50C[1], 50D[2], 50DD[2] and 50EE[2]

Notes:
1. *The minimum thickness available from the hot strip mill is 6,0mm.*
2. *Available as plate mill products only.*

The BS 4360 structural steel grades are all readily weldable by means of the usual metal arc processes.

Steel making

Steel is normally supplied from a basic oxygen furnace but could also be supplied from electric arc furnaces using clean internal scrap and direct reduced iron. All steel is desulphurised to maintain a high degree of cleanliness and is made fully killed and fine-grained from continuously cast slabs. Full shrouding techniques and automatic mould level control are applied to ensure superior internal and surface quality.

Chemical composition

Table 1 shows the chemical composition as specified by BS 4360: 1986. The limits are set rather wide to give the steel producer maximum scope to apply its manufacturing techniques. In order to assist customers in determining fabrication parameters, the typical analyses of the steels as made by Iscor are given in Table 2. It must be stressed that these values are given as an indication only and are in no way binding on Iscor as manufacturer. Only the specification is binding. It should also be noted that, because thicker plates cool at a slower rate during and after rolling or normalising, they will emerge at lower strength levels if the chemical composition is not enriched to counteract this effect (even though the specification does allow for some strength reduction with thickness).

When agreed at the time of ordering, BS 4360 steel grades can be supplied to maximum carbon equivalent (CE) values as indicated in the specification

MARKET DEVELOPMENT
COLD ROLLED AND AUTOMOTIVE PRODUCTS

Iscor Ltd
PO Box 2
Vanderbijlpark
1900
Toll free number
0800 005043
Tel (016) 889-7653
Fax (016) 889- 5668
E-mail address:
datasheets@iscorvdb.co.za

Effective date:
September 2000

FOR FURTHER INFORMATION, CONTACT:

A3.2
P2

TABLE 1. Chemical composition (ladle analysis, percent) as specified in BS 4360 : 1986

Grade	C max	Si	Mn max	P max	S max	Nb	V	Supply conditions
40A	0,22	0,50 max	1,60	0,050	0,050	-	-	As rolled
40B	0,20	0,50 max	1,50	0,050	0,050	-	-	As rolled
40C	0,18	0,50 max	1,50	0,040	0,040	-	-	As rolled
40D	0,16	0,50 max	1,50	0,040	0,040	-	-	Normalised
40EE	0,16	0,10 - 0,50	1,50	0,040	0,030	-	-	Normalised
43A	0,25	0,50 max	1,60	0,050	0,050	-	-	As rolled
43B	0,21	0,50 max	1,50	0,050	0,050	-	-	As rolled
43C	0,18	0,50 max	1,50	0,040	0,040	-	-	As rolled
43D[1]	0,16	0,50 max	1,50	0,040	0,040	0,003 - 0,10	0,003 - 0,10	Normalised
43EE	0,16	0,10 - 0,50	1,50	0,030	0,030	-	-	Normalised
50B[3]	0,20	0,50 max	1,50	0,050	0,050	0,003 - 0,10	0,003 - 0,10	< 12,5 mm: As rolled ≥12,5 mm: normalised
50C[3]	0,20	0,50 max	1,50	0,040	0,040	0,003 - 0,10	0,003 - 0,10	< 12,5 mm: As rolled ≥12,5 mm: normalised
50D[3]	0,18	0,10 - 0,50	1,50	0,040	0,040	0,003 - 0,10	0,003 - 0,10	Normalised
50DD[3]	0,18	0,10 - 0,50	1,50	0,040	0,040	0,003 - 0,10	0,003 - 0,10	Normalised
50EE[3]	0,18	0,10 - 0,50	1,50	0,040	0,030	0,003 - 0,10	0,003 - 0,10	Normalised

Notes:
1. *It is permissible for the steel to be supplied with no niobium or vanadium.*
2. *Several deviations from the above are permitted – refer to BS 4360 : 1986 specification for this detail.*
3. *An increase in manganese content of 0,06% above the maximum limit is permitted for every 0,01% decrease in carbon content below the maximum limit, up to a maximum manganese content of 1,60%.*

TABLE 2. Typical chemical composition (ladle analysis, percent) of Iscor's plate mill products

Grade	C[1]	Si	Mn[2]	P	S	Al	Nb	
40A	0,12	0,25	0,90	0,015	0,015	0,035	-	-
40B	0,12	0,25	0,90	0,015	0,015	0,035	-	-
40C	0,12	0,25	0,90	0,015	0,015	0,035	-	-
40D	0,12	0,25	0,90	0,015	0,015	0,035	-	-
40EE	0,12	0,25	0,90	0,015	0,008	0,035	-	-
43A	0,16	0,25	1,00	0,015	0,015	0,035	-	-
43B	0,16	0,25	1,00	0,015	0,015	0,035	-	-
43C	0,16	0,25	1,25	0,015	0,015	0,035	-	-
43D	0,16	0,25	1,25	0,015	0,015	0,035	-	-
43EE	0,16	0,25	1,25	0,015	0,008	0,035	-	-
50B	0,15	0,35	1,45	0,015	0,015	0,035	0,028	-
50C	0,15	0,35	1,45	0,015	0,015	0,035	0,028	-
50D	0,15	0,35	1,45	0,015	0,015	0,035	0,028	-
50DD	0,15	0,35	1,45	0,015	0,015	0,035	0,028	-
50EE	0,15	0,35	1,45	0,015	0,008	0,035	0,028	-

Notes:
1. *Carbon is generally 0,02% lower on all hot strip mill products.*
2. *Manganese is generally 0,20% lower on all hot strip mill products*

Mechanical properties

As can be seen from Table 3, the tensile strength requirements are the same throughout a grade range, but the impact test requirements differ in terms of the prescribed test temperatures as indicated by the suffix for each grade designation. An average impact energy value of 27 joules must be achieved on full size specimens in the longitudinal direction in all applicable cases.

TABLE 3. Mechanical properties as specified in BS4360 : 1986

Grade	Tensile strength (MPa)	Minimum yield strength (Mpa)				Minimum elongation (%) on a gauge length[4] of		Charpy V-notch impact test		
		$t \leq 16$	$16 < t \leq 40$	$40 < t \leq 63$	$63 < t \leq 100$	200 mm	$5{,}65\sqrt{S_0}$	Test temperature (ºC)	Minimum average energy (J)	Maximum thickness (mm)
40A	340 - 500	235	225	215	205	22	25	-	-	-
40B	340 - 500	235	225	215	205	22	25	20[2]	27	100
40C	340 - 500	235	225[1]	215	210	22	25	0	27	100
40D	340 - 500	235	225	215	215	22	25	-20	27	100
40EE	340 - 500	260	245	240	-	22	25	-50	27	63
43A	430 - 580	275	265	255	245	20	22	-	-	-
43B	430 - 580	275	265	255	245	20	22	20[2]	27	100
43C	430 - 580	275	265	255	245	20	22	0	27	100
43D	430 - 580	275	265	255	245	20	22	-20	27	100
43EE	430 - 580	275	265	255	-	20	22	-50	27	63
50B	490 - 640	355	345	340	325	18	20	20[2]	27	100
50C	490 - 640	355	345	340	325	18	20	0	27	100
50D	490 - 640	355	345	340	325	18	20	-20	27	100
50DD	490 - 640	355	345	340	325	18	20	-30	27	80
50EE[3]	490 - 640	355	345	340	-	18	20	-50	27	63

Notes:

1. *Minimum yield strength 230 MPa for material up to 19 mm thick.*
2. *Only if specified on order.*
3. *Minimum tensile strength 480 MPa for material over 16 mm thick.*
4. *S_0 is the original cross-sectional area*

MARKET DEVELOPMENT
COLD ROLLED AND AUTOMOTIVE PRODUCTS

Iscor Ltd
PO Box 2
Vanderbijlpark
1900
Toll free number
0800 005043
Tel (016) 889-7653
Fax (016) 889- 5668
E-mail address:
datasheets@iscorvdb.co.za

Effective date:
May 2000

FOR FURTHER INFORMATION, CONTACT:

Dimensions

The plate mill can produce products from 4,5mm to 100mm thick. The available dimensions for such plates are given in the data sheet: Plate Mill Product Dimensions (file reference A1.3).

The hot strip mill can produce products from 1,6mm to 13,0mm thick. The dimensions available are given in the data sheet: Hot Strip Mill Product Dimensions (file reference A1.1).

Tolerances

All steel is supplied with dimensional tolerances in accordance with EN 10029 : 1991 for plate and EN 10051 : 1992 for strip.

Surface inspection

All plates manufactured through the plate mill, are inspected and defects repaired in accordance with EN 10163-2 : 1991 Class B Subclass 2, unless otherwise agreed.

Ultrasonic testing

Plates may be ordered ultrasonically tested to grades B1 to B4 of BS 5996, and option B.28 of BS 4360 : 1986. (6,0 - 100mm).

Certification

All material described in this data sheet is supplied with analysis and test certificates.

Bend test

If agreed at the time of ordering, the material may be subjected to a bend test in accordance with option B.36 of BS 4360 : 1986. Attention is drawn to paragraph G5 and Tables 50 and 51 of the BS 4360 : 1986 specification, where the difference in formability between a bend test specimen and plate during fabrication is explained. Fabricators should take cognisance of this when bending operations are intended.

Weldability

When welding thick plates reference should be made to BS 5135 : 1984, '*Specification for arc welding of carbon and carbon manganese steels*' to ensure the correct welding procedures are followed.

Values of the carbon equivalent (CE) should be calculated from the values for chemical composition on the test certificates for the plates concerned.

The formula to be used is: $CE = C + \frac{Mn}{6} + \frac{Cr + Mo + V}{5} + \frac{Ni + Cu}{15}$

Supply conditions

All material described in this data sheet is supplied in terms of Price Lists 120 for hot rolled plate and strip respectively and Iscor's General Conditions of Sale.